LONDON'S GLOBAL UNIVERSITY

Developing Drug-loaded Nanogel Formulations for Intrapericardial Delivery

Hei Ming Kenneth Ho

A thesis submitted to University College London in partial fulfilment of the requirement for the degree of Doctor of Philosophy

School of Pharmacy
University College London

10 October 2022

I would like to dedicate this thesis to the Gohonzon, my mother, brother, father, and other people who have supported me throughout my PhD journey.

Declaration

I, Hei Ming Kenneth Ho, hereby confirm that the work presented in this thesis is my own. Where information has been derived from other sources, I confirm that this has been indicated in the thesis. The contents in this thesis are original and have not been submitted in whole or in part for consideration for any other degree or qualification in this, or any other University.

Hei Ming Kenneth Ho

10 October 2022

Abstract

Intrapericardial delivery is a novel route for administering localised therapy to the heart and offers advantageous pharmacokinetic profiles. Although concerns exist about invasiveness and associated complications these can be mitigated using minimally invasive techniques; however, it requires further consideration regarding the formulation of the drug being delivered for it to pass through small-bore delivery devices. Therefore, the research presented in this thesis aimed to investigate the development of nanogel formulations for use in minimally invasive intrapericardial delivery.

Propranolol-loaded chitosan-TPP nanogels were first evaluated to understand the predictability of nanogel properties. The prediction models were applied with structurally similar drugs. Relationships were found between molecular descriptors and performance parameters. Hence, the encapsulation and formation processes were drug-dependent and not simply incorporated into inter-chain voids. Moreover, the processing factors in the fabrication significantly affected the nanogels properties, which demonstrated that the scaling-up of the fabrication process is not simply via increasing the volume pro-rata. Assessment of the cytotoxicity of propranolol on epicardial cells, fibroblasts, and cardiomyoblasts revealed that propranolol is not a suitable model drug for intrapericardial delivery. Moreover, higher cytotoxic sensitivity to propranolol was observed with epicardial cells, which highlighted the importance of using epicardial cells in cell viability tests rather than more generic cell types when modelling intrapericardial drug delivery during the screening of drug formulations.

Further candidate nanogel formulations were investigated including a novel CS-GAA formulation produced at a more basic pH than the conventional chitosan-TPP nanogels (pH 4.5), which enabled the loading of the antifibrotic peptide Ac-SDKP. To quantify the peptide, it was necessary to establish an HPLC-UV assay. Unfortunately, the peptide released from the nanogels was not detectable after 24 hours during the release study conducted, of which the degradation of the peptide was likely promoted by the phosphate buffer saline. Conversely, the nanogels formulation reduced the peptide concentration needed to suppress the metabolic

activity of fibroblasts in the presence of TGF-β1. In conclusion, the research reported shows the technical feasibility of producing nanogels loaded with peptide drugs, with Ac-SDKP-loaded nanogels offering several attributes that make them potentially ideally suited for intrapericardial delivery for treating heart disease.

Impact Statement

Intrapericardial delivery is a novel route for localised delivery of drugs to the heart, offering pharmacokinetic advantages over conventional intravenous delivery. Challenges associated with the invasiveness of delivery and access techniques can be mitigated via the use of minimal invasiveness techniques, such as pericardial access devices, injections via blunt-ended needles, and infusions via catheters. However, the choice of formulations is limited by these approaches. This EPSRC-funded CDT PhD project aimed to develop a nanogel formulation that is suitable for intrapericardial delivery via the use of minimal invasiveness techniques. Nanogels are nanosized hydrogel particles, with favourable injectability, versatile architecture, and simple fabrication. In addition, the nanogels could also serve as a carrier for fragile payloads.

The research reported in the thesis provides new insights and knowledge regarding the formulation of nanogels intended for intrapericardial delivery. In particular, the predictability of the nanogels properties and the mechanism of drug loading in the nanogels were explored. Moreover, the reproducibility and scalability of the nanogels were evaluated, with important parameters in the fabrication process and formulation found in the study. A novel HPLC assay for peptide Ac-SDKP was developed with an analytical quality by design approach and a novel nanogel system was established to fabricate the nanogels in a more neutral pH environment.

The results and methods described in this thesis add extensive information and knowledge regarding the formulation of peptide-loaded nanogels and intrapericardial delivery, identifying factors crucial to obtain target properties, as well as developing novel methods for quantifying and evaluating their activity *in vitro*. Ultimately, the novel peptide-loaded nanogels described in the project could potentially be administered into the pericardium post-myocardial infarction, attenuating the cardiac injury, and improving the clinical outcome of myocardial infarction.

Acknowledgement

First and foremost, I would like to sincerely thank all my supervisors – Prof. Richard Day (Division of Medicine, University College London) and Prof. Duncan Craig (School of Pharmacy, University College London). I would not have completed the PhD without their kind guidance and continual support. I am grateful for Richard's willingness to allow me to design the project from scratch. Under his supervision, I was able to develop my independence as a researcher. I would also like to express my gratitude to Duncan for introducing me to the concept of nanogels. His insightful and constructive feedback on my work throughout the PhD was indispensable and much appreciated.

I would like to thank my fellow students and staff members in the Centre for Doctoral Training (CDT) in Advanced Therapeutics and Nanomedicine at University College London and the University of Nottingham (EP/L01646X). I have benefited much from the vibrant and friendly environment in the CDT. I am very thankful for the comprehensive support from Prof. Gareth Williams and Prof. Steve Brocchini. I appreciate the funding from the Engineering and Physical Science Research Council (EPSRC), University of Nottingham and University College London, without which the achievements in this thesis would not be possible. I am also grateful for the extra funds generously offered by the CDT to conduct some experiments on this project.

I would like to express my gratitude to Ms Zoe Whiteley, Dr Hend Abdelhakim, Ms Shorooq Abukhamees, Dr Fauzi Jalil, Dr Essam Tawfik, Mr Se Hun Chung, Mr Antony Omita, Ms Charitini Volataki, Ms Rawan Fitaihi, Ms Amal Abdulghani and other fellow members at B15/28, with whom I have many happy memories and life-long friendships at the School of Pharmacy. I am grateful for their peer support throughout my time at UCL, especially during the darkest moments of the journey and the COVID-19 pandemic. I am especially grateful to Ms Zoe Whiteley, who worked with me on innumerable evenings and weekends in the lifeless laboratory and shared the scientific knowledge, happiness, and sadness in life. I would also like to thank Dr Ho Wai (Matthew) Chin, Dr Ketevan Paliashvili, Ms Annalisa Bettini as

well as other fellow members of the Applied Biomedical Engineering Group for their kind support.

I am sincerely grateful for our “Lab Aunty” – Prof. Sue Barker, who supported me both in my work and my daily life in the early days in the School of Pharmacy. I would also appreciate the help from Dr Asma Buanz, especially when I worked with her supervising the MSc project. I have learnt a lot from her. Many thanks to Ms Satinder Sembi, Dr Collin James, and Dr Andrew Weston for their kind help in conducting the HPLC, NMR and TEM experiments. I also thank all staff members for teaching opportunities, their help, and inspiring conversations over the years, especially Ms Terry Ng and Ms Isabel Gonçalves.

I would also extend my gratitude to my close friends – Dr Lok Hin Lui, Dr Chih Yao Chung, Mr Wen Kui Liu, Dr Ke Ting Pan, Dr Moe Elbadawi and Mr Jun Jie Ong in supporting me and keeping my spirits up during the PhD journey.

Most importantly, I am incredibly grateful to my family for the love and invaluable support they have supplied me continuously through all the difficulties of the journey. I owed a debt of gratitude to my mum for her caring, support and encouragement, which give me the impetus to continue the journey and support me when I am broken. I would like to thank my brother for his kindness and for all the good times we shared and continue to share.

Lastly, I would like to thank those people who gave me a challenging time in the PhD. I treasured all difficulties and problems they brought to me very much, which became the nourishment for me to grow, be strong, independent, and persevered. Without them, I would not be the person that I am today.

UCL Research Paper Declaration Form referencing the doctoral candidate's own published work(s)

Please use this form to declare if parts of your thesis are already available in another format, e.g., if data, text, or figures:

- have been uploaded to a preprint server
- are in submission to a peer-reviewed publication
- have been published in a peer-reviewed publication, e.g. journal, textbook.

This form should be completed as many times as necessary. For instance, if you have seven thesis chapters, two of which containing material that has already been published, you would complete this form twice.

1. **For a research manuscript that has already been published** (if not yet published, please skip to section 2):

   a) **What is the title of the manuscript?**

   Access routes, devices and guidance methods for intrapericardial delivery in cardiac conditions

   b) **Please include a link to or doi for the work:**

   https://doi.org/10.1016/j.tcm.2021.04.004

   c) **Where was the work published?**

   Trends in Cardiovascular Medicine

   d) **Who published the work?** (e.g. OUP):

   Elsevier

   e) **When was the work published?**

   20 April 2021

   a) **List the manuscript's authors in the order they appear on the publication:**

   Hei Ming Kenneth Ho, Duncan Q. M. Craig, Richard M. Day

   f) **Was the work peer reviewed?**

   Yes

   g) **Have you retained the copyright?**

   Yes

   h) **Was an earlier form of the manuscript uploaded to a preprint server?** (e.g. medRxiv; if 'Yes', please give a link or doi):

   No

(If no, please seek permission from the relevant publisher and check the box next to the below statement):

☒ *I acknowledge permission of the publisher named under **1d** to include in this thesis portions of the publication named as included in **1c**.*

2. **For a research manuscript prepared for publication but that has not yet been published (if already published, please skip to section 3):**

   b) **What is the current title of the manuscript?**

   Click or tap here to enter text.

   c) **Has the manuscript been uploaded to a preprint server?** (e.g. medRxiv; if 'Yes', please give a link or doi):

   Click or tap here to enter text.

   d) **Where is the work intended to be published?** (e.g. journal names)

   Click or tap here to enter text.

   e) **List the manuscript's authors in the intended authorship order:**

   Click or tap here to enter text.

   f) **Stage of publication** (e.g. in submission):

   Click or tap here to enter text.

3. **For multi-authored work, please give a statement of contribution covering all authors (if single-author, please skip to section 4):**

   HMKH, RD and DC were involved in the overarching study design and strategy and preparation of the manuscript. HMKH performed all literature searches.

4. **In which chapter(s) of your thesis can this material be found?**

   Chapter 1

5. **e-Signatures confirming that the information above is accurate** (this form should be co-signed by the supervisor/ senior author unless this is not appropriate, e.g. if the paper was a single-author work):

Candidate: Hei Ming Kenneth Ho	**Date:** 10 October 2022
Supervisor/ Senior Author (where appropriate): Richard Day	**Date:** 10 October 2022

UCL Research Paper Declaration Form referencing the doctoral candidate's own published work(s)

Please use this form to declare if parts of your thesis are already available in another format, e.g., if data, text, or figures:

- have been uploaded to a preprint server
- are in submission to a peer-reviewed publication
- have been published in a peer-reviewed publication, e.g. journal, textbook.

This form should be completed as many times as necessary. For instance, if you have seven thesis chapters, two of which containing material that has already been published, you would complete this form twice.

1. **For a research manuscript that has already been published** (if not yet published, please skip to section 2):

   a) **What is the title of the manuscript?**

   Design of experiment approach to modelling the effects of formulation and drug loading on the structure and properties if therapeutic nanogels

   b) **Please include a link to or doi for the work:**

   https://doi.org/10.1021/acs.molpharmaceut.1c00699

   c) **Where was the work published?**

   Molecular Pharmaceutics

   d) **Who published the work?** (e.g. OUP):

   American Chemistry Society

   e) **When was the work published?**

   21 January 2022

   f) **List the manuscript's authors in the order they appear on the publication:**

   Hei Ming Kenneth Ho, Duncan Q. M. Craig, Richard M. Day

   g) **Was the work peer reviewed?**

   Yes

   h) **Have you retained the copyright?**

   Yes

   i) **Was an earlier form of the manuscript uploaded to a preprint server?** (e.g. medRxiv; if 'Yes', please give a link or doi):

   No

(If no, please seek permission from the relevant publisher and check the box next to the below statement):

☒ *I acknowledge permission of the publisher named under **1d** to include in this thesis portions of the publication named as included in **1c**.*

2. **For a research manuscript prepared for publication but that has not yet been published (if already published, please skip to section 3):**

   g) **What is the current title of the manuscript?**

   Click or tap here to enter text.

   h) **Has the manuscript been uploaded to a preprint server?** (e.g. medRxiv; if 'Yes', please give a link or doi):

   Click or tap here to enter text.

   i) **Where is the work intended to be published?** (e.g. journal names)

   Click or tap here to enter text.

   j) **List the manuscript's authors in the intended authorship order:**

   Click or tap here to enter text.

   k) **Stage of publication** (e.g. in submission):

   Click or tap here to enter text.

3. **For multi-authored work, please give a statement of contribution covering all authors (if single-author, please skip to section 4):**

   HMKH, RD and DC were involved in the overarching study design and strategy and preparation of the manuscript. HMKH performed all experimental work and data analysis.

4. In which chapter(s) of your thesis can this material be found?

   Chapter 3

5. **e-Signatures confirming that the information above is accurate** (this form should be co-signed by the supervisor/ senior author unless this is not appropriate, e.g. if the paper was a single-author work):

Candidate: Hei Ming Kenneth Ho	**Date:** 10 October 2022
Supervisor/ Senior Author (where appropriate): Richard Day	**Date:** 10 October 2022

UCL Research Paper Declaration Form referencing the doctoral candidate's own published work(s)

Please use this form to declare if parts of your thesis are already available in another format, e.g., if data, text, or figures:

- have been uploaded to a preprint server
- are in submission to a peer-reviewed publication
- have been published in a peer-reviewed publication, e.g. journal, textbook.

This form should be completed as many times as necessary. For instance, if you have seven thesis chapters, two of which containing material that has already been published, you would complete this form twice.

1. **For a research manuscript that has already been published** (if not yet published, please skip to section 2):

   a) **What is the title of the manuscript?**

   An analytical quality by design approach towards a simple and novel HPLC-UV method for quantification of the antifibrotic peptide N-acetyl-seryl-aspartyl-lysyl-proline

   b) **Please include a link to or doi for the work:**

   https://doi.org/10.1016/j.ab.2022.114793

   c) **Where was the work published?**

   Analytical Biochemistry

   d) **Who published the work?** (e.g. OUP):

   Elsevier

   e) **When was the work published?**

   22 June 2022

   l) **List the manuscript's authors in the order they appear on the publication:**

   Hei Ming Kenneth Ho, Satinder Sembi, Shorooq Abukhamees, Richard M. Day, Duncan Q. M. Craig

   f) **Was the work peer reviewed?**

   Yes

   g) **Have you retained the copyright?**

   Yes

   h) **Was an earlier form of the manuscript uploaded to a preprint server?** (e.g. medRxiv; if 'Yes', please give a link or doi):

   Yes - SSRN
   https://dx.doi.org/10.2139/ssrn.3990207

   (If no, please seek permission from the relevant publisher and check the box next to the below statement):

☒ *I acknowledge permission of the publisher named under **1d** to include in this thesis portions of the publication named as included in **1c**.*

2. **For a research manuscript prepared for publication but that has not yet been published (if already published, please skip to section 3):**

   m) **What is the current title of the manuscript?**

   Click or tap here to enter text.

   n) **Has the manuscript been uploaded to a preprint server?** (e.g. medRxiv; if 'Yes', please give a link or doi):

   Click or tap here to enter text.

   o) **Where is the work intended to be published?** (e.g. journal names)

   Click or tap here to enter text.

   p) **List the manuscript's authors in the intended authorship order:**

   Click or tap here to enter text.

   q) **Stage of publication** (e.g. in submission):

   Click or tap here to enter text.

3. **For multi-authored work, please give a statement of contribution covering all authors (if single-author, please skip to section 4):**

   HMKH, RD and DC were involved in the overarching study design and strategy and preparation of the manuscript. HMKH performed most of the experimental work and data analysis. SS and SA assisted in method validation and advised on the HPLC work.

4. **In which chapter(s) of your thesis can this material be found?**

   Chapter 5

5. **e-Signatures confirming that the information above is accurate** (this form should be co-signed by the supervisor/ senior author unless this is not appropriate, e.g. if the paper was a single-author work):

Candidate: Hei Ming Kenneth Ho	**Date:** 10 October 2022
Supervisor/ Senior Author (where appropriate): Richard Day	**Date:** 10 October 2022

Contents

List of Figures

List of Tables

List of Abbreviations

%Bi	%B increment
%Bs	Starting %B
AAV	Adeno-Associated Virus
ACE	Angiotensin Converting Enzyme
ACN	Acetonitrile
Ac-SDKP	N-Acetyl-Seryl-Aspartyl-Lysyl Proline
AIF	Apoptosis Inducing Factor
ALogP, XLogP	Theoretical n-Octanol-Water Partition Coefficient
ANF	Atrial Natriuretic Factor
Ang II	Angiotensin II
ANOVA	Analysis of Variance
Apaf1	Apoptotic Peptidase Activating Factor 1
API	Active Pharmaceutical Ingredient
apol	Sum of the Atomic Polarizability
AQbD	Analytical Quality by Design
AR	Addition Rate
ASD	Active Hydraulic Ventricular Support Drug Delivery System
α-SMA	Alpha-Smooth Muscle Actin
ATP	Adenosine Triphosphate
ATPs	Analytical Target Profiles
ATR	Attenuated Total Reflectance
B	Blocking
BAX	BCL-2 Associated X Protein
BID	BCL-2 Interacting Protein
BMMC	Bone Marrow Mononuclear Cells
BMP	Bone Morphogenetic Protein
bpol	Sum of the Absolute Value of the Difference between Atomic Polarisability of All Bonded Atoms
BrdU	Bromodeoxyuridine
CABG	Coronary Artery Bypass Graft

casp	Caspase
CC	Chitosan Concentration
CCD	Central Composite Design
CDC	Cardiosphere-Derived Cells
CI	Confidence Interval
CM	Cardiomyocytes
CP	Chitosan-Propranolol Ratio
CQA	Critical Quality Attributes
CR	Crosslinker
CS-GAA	Chitosan-glycocyamine, Guanidylated Chitosan
CT	Chitosan-TPP Ratio
CTGF	Connective Tissue Growth Factor
CVD	Cardiovascular Disease
D	Duration
D_2O	Deuterium Oxide
DA	Degree of Deacetylation
DCl	Deuterium Chloride
DHA	Docosahexaenoic Acid
DIABLO	Direct Inhibitor of Apoptosis-Binding Protein
DLS	Dynamic Light Scattering
DMEM	Dulbecco's Modified Eagle Medium
DNA	Deoxyribonucleic Acid
DOE	Design of Experiments
DSC	Differential Scanning Calorimetry
DSD	Definitive Screening Study
ECM	Extracellular Matrix
EDC	1-Ethyl-3-(3-dimethylaminopropyl)carbodiimide
EDTA	Ethylenediaminetetraacetic acid
EE	Encapsulation Efficiency
EIA	Enzyme Immunoassay
ELISA	Enzyme-linked immunosorbent assay
ELS	Electrophoretic Light Scattering
EMT	Epithelial-Mesenchymal Transition

EPR	Enhanced Permeation and Retention Effects
ERK	Extracellular Signal-Regulated Kinases
ESI	Electrospray Ionisation
FBS	Fetal Bovine Serum
FCC	Face Centred Cubic
FGF	Fibroblast Growth Factor
FR	Flow Rate
FTIR	Fourier Transform Infrared Spectroscopy
GAA	Guanidinoacetic Acid, Glycocyamine
GC	Guanidylated Chitosan Concentration
GD	Guanidylated Chitosan-Drug Ratio
GFP	Green Fluorescent Protein
GP	Genipin
GT	Guanidylated Chitosan-TPP Ratio
GV	Glass Vial Volume
H1D	Proton at Position 1 of Deacetylated Monomer
H3-6	Integration of signals from hydrogen at position 3-6, including H3, H4, H5, H6 and H6’
HAc	Proton of the Acetyl Group
HOD	Solvent Proton
HPLC	High Performance Liquid Chromatography
IC30	Thirty Percentage of Maximal Inhibitory Concentration
IC50	Half Maximal Inhibitory Concentration
ICAM-1	Intercellular Adhesion Molecule-1
ICH	International Council of Harmonisation
IGF	Insulin-Like Growth Factor
IKK-β	Inhibitor of Nuclear Factor Kappa-B Kinase Subunit Beta
IL	Interleukins
IU	International Unit
IV	Intravenous
K_{ow}	n-Octanol-Water Partition Coefficient
LC-MS/MS	Liquid Chromatography Tandem Mass Spectrometry
LDH	Lactate Dehydrogenase

LDL	Low-Density Lipoprotein
LMW	Low Molecular Weight
LOD	Limit of Detection
LOQ	Limit of Quantitation
M	Matrix solution
MAPK	Mitogen-Activated Protein Kinases
MCP-1	Monocyte Chemotactic Protein-1
MHB	Multiple Hydrogen Bond
MI	Myocardial Infarction
miRNA	Micro-Ribonucleic Acid
MLC-2v	Myosin Light Chain-2
MMP	Matrix Metalloproteinases
MMW	Medium Molecular Weight
MODR	Method Operable Design Region
MPTP	Mitochondrial Permeability Transition Pore
MRO	Multiple Response Optimisation
MS	Medial Sternotomy
MSC	Mesenchymal Stem Cells
mTOR	Mechanistic Target of Rapamycin
MTT	3-(4,5-dimethylthiazol-2-yl)-2,5-diphenyltetrazolium bromide
MWCO	Molecular Weight Cut-Off
N	Number of Theoretical Plate
nAcid	Number of Acid
Na^{+}/Ca^{2+} exchanger	Sodium-Calcium Exchanger
nBase	Number of Base
NF-κB	Nuclear Factor Keppa-Light Chain Enhancer B
nHBAcc	Number of Hydrogen Bond acceptor
nHBDon	Number of Hydrogen Bond Donor
NHS	N-Hydroxysuccinimide
NMR	Nuclear Magnetic Resonance
NRG	Neuregulin
nRing	Number of Ring

OFAT	One Factor at a Time
PAS	Phytic Acid Sodium
PB	PrestoBlue®
PBS	Phosphate Buffer Saline
PCI	Percutaneous Coronary Intervention
PDI	Polydispersity Index
PE	Pulmonary Embolism
PF	Pericardial Fluid
PI3K	Phosphoinositide 3-Kinase
PKB	Protein Kinase B
PLGA	Poly(lactic-co-glycolic) Acid
PNIPAm	Poly(N-isopropyl acrylamide)
Pyro	Sodium Pyrophosphate
Q^2	Correlation Coefficient of the Test Set
QbD	Quality by Design
R^2	Correlation Coefficient
Rf	Retention Factor
ROS	Reactive Oxygen Species
Rs	Resolution
RSM	Response Surface Methodology
SAR	Structural Activity Relationship
SD	Standard Deviation
siRNA	Small Interfering Ribonucleic Acid
Smac	Second Mitochondria-Derived Activator of Caspase
Smad	Mothers Against Decapentaplegic Homolog
SR	Stirring Rate
SS	Stirrer Size
T	Temperature
T_0	Dead Time
TAZ	Transcriptional Coactivator with PDZ-Binding Motif
TEM	Transmission Electron Microscope
TEMED	Tetramethylethylenediamine
Tf	Tailing Factor

TGA	Thermogravimetric Analysis
TGF-β	Tissue Growth Factor-Beta
TNF-α	Tumour Necrosis Factor-Alpha
TopoDiameter	Topological Diameter
TopoPSA	Topological Polar Surface Area
TopoShape	Petitjean Topological shape Index
TPP	Sodium Triphosphate Pentabasic
TV	Total Volume
Tβ4	Thymosin-β4
UK	United Kingdom
UPy	Poly(2-ureido-4[^{1}H]pyrimidinone)
USP	United State Pharmacopeia
UV-Vis	Ultraviolet-Visible Light
V	Injection Volume
VWD	Variable Wavelength Device
W/O	Water-in-Oil
WPATH	Wiener Path Number
WPOL	Wiener Polarity Number
XIAP	X-Linked Inhibitor of Apoptosis Protein
XRD	X-Ray Diffraction
YAP	Yes-Associated Protein
ZP	ζ-potential

Preface

Some of the work described in this thesis has previously been presented or published in the following conferences and peer-reviewed journals:

Developing guanidylated chitosan-TPP nanogels as a drug carrier for intrapericardial delivery.
H. M. K. Ho, R. M. Day, D. Q. M Craig. 13th World Meeting on Pharmaceutics, Biopharmaceutics and Pharmaceutical Technology. Rotterdam, The Netherland. 2022. *Poster presentation.*

Developing predictive models for optimising the properties of chitosan nanogels.
H. M. K. Ho, R. M. Day, D. Q. M Craig. PBP World Meeting Virtual Conference. Online. 2021. *Poster presentation.*

Optimisation of propranolol-loaded nanogels for targeted therapy to the heart.
H. M. K. Ho, R. M. Day, D. Q. M Craig. 10th APS International PharmSci Conference. Greenwich, United Kingdom. 2019. *Poster presentation.*

Optimisation of propranolol-loaded nanogel via design of experiment.
H. M. K. Ho, R. M. Day, D. Q. M Craig. ULLA Summer School. Helsinki, Finland. 2019. *Poster presentation.*

Peer-reviewed Publications

Ho, H. M. K., Sembi, S., Abukhamees, S., Day, R. M., & Craig, D. Q. (2022). An analytical quality by design approach towards a simple and novel HPLC-UV method for quantification of the antifibrotic peptide N-acetyl-seryl-aspartyl-lysyl-proline. *Analytical Biochemistry*, 114793.

Ho, H. M. K., Craig, D. Q., & Day, R. M. (2022). Design of Experiment Approach to Modeling the Effects of Formulation and Drug Loading on the Structure and Properties of Therapeutic Nanogels. *Molecular Pharmaceutics*.

Ho, H. M. K., Craig, D. Q., & Day, R. M. (2021). Access routes, devices and guidance methods for intrapericardial delivery in cardiac conditions. *Trends in Cardiovascular Medicine*.

Other Publications

Ho, H. M. K., Xiong, Z., Wong, H. Y., & Buanz, A. (2022). The Era of Fake Medicines: Investigating counterfeit medicinal products for erectile dysfunction disguised as herbal supplements. *International Journal of Pharmaceutics*, 121592.

Whiteley, Z., **Ho, H. M. K.**, Gan, Y. X., Panariello, L., Gkogkos, G., Gavriilidis, A., & Craig, D. Q. (2021). Microfluidic synthesis of protein-loaded nanogels in a coaxial flow reactor using a design of experiments approach. *Nanoscale Advances*, *3*(7), 2039-205

Paliashvili, K., Di Maggio, F., **Ho, H. M. K.**, Sathasivam, S., Ahmed, H., & Day, R. M. (2019). A novel adjuvant drug-device combination tissue scaffold for radical prostatectomy. *Drug Delivery*, *26*(1), 1115-1124.

Chapter 1

Introduction

Part of the contents in this chapter has already been published as the following review article.

Ho, H. M. K., Craig, D. Q., & Day, R. M. (2021). Access routes, devices and guidance methods for intrapericardial delivery in cardiac conditions. *Trends in Cardiovascular Medicine*.

1. Introduction

1.1. General Introduction

Cardiovascular diseases, including strokes and heart disease, remain the most prevalent global cause of mortality [2]. Due to the inefficient capability of the human heart to repair itself, recovery after myocardial injury remains challenging. Although there have been advancements exploring novel use of biologically active agents, including genes, growth factors, peptides, and cells to replenish myocardial cells or repair damage post-injury, these agents need to be localised in the heart to initiate cardiac protection processes and reduce off-target effects. Cardio-localised delivery is difficult to achieve via conventional delivery routes due to large distribution in other organs [3]. Intrapericardial delivery is one of the newly investigated cardio-localised delivery routes, which may offer pharmacokinetic advantages and minimal invasiveness. High myocardial concentration and low plasma concentration can theoretically be achieved simultaneously with intrapericardial drug delivery. Several studies have demonstrated that intrapericardial delivery is a feasible and suitable localised delivery method for cardioprotective agents [4–7]. To protect these agents from *in vivo* degradation and promote cellular uptake, nanoparticle delivery vehicles are often used. However, high clearance rates from plasma via the kidney, liver, and spleen are one of the major obstacles to nanoparticle formulations. Moreover, to date, research into the use of nanoparticles in intrapericardial delivery is limited and the fate, uptake, and deposition of nanoparticles are not well-understood.

This project aimed to develop a nanogel formulation suitable for minimally invasive intrapericardial delivery with a particular focus on delivering cardioprotective agents to the infarcted heart. The following introduction section is designed to present a review of related literature that lays the groundwork for this research and explains key relevant concepts that are present throughout this thesis.

1.2. Cardiovascular Disease

Cardiovascular disease (CVD) is a term used to describe the collection of diseases affecting the heart or circulatory system. It is the leading cause of death in the world and accounts for 31% of total global mortality with an estimated 17.7 million people

dying of CVD each year [8]. In the UK, a quarter of deaths (26%) are caused by CVD, with 150,000 patients dying per year [9]. Examples of the range of conditions that are defined as CVD are shown in **Table 1-1**. Ischaemic heart disease is one of the two most common types of CVD, alongside stroke ranking in the top two causes of death worldwide [2]. Ischaemic heart disease, especially myocardial infarction, will be focused on and explored in detail as follows.

Table 1-1. Summary of cardiovascular diseases, their affected organs, and causes [8].

Disease	Affected organ	Cause
Ischaemic heart disease	Heart	A disease of the coronary artery, affecting the blood supply to the cardiac myocytes
Rheumatic heart disease		Damage to cardiac myocytes and valves from rheumatic fever
Congenital heart disease		Malfunction of the heart existed at birth
Stroke	Brain	A disease affecting blood vessels of the brain and cerebral circulation
Peripheral arterial disease	Limbs	A disease of arterial vessels, affecting the blood supply in the limbs
Deep vein thrombosis and pulmonary embolism (PE)	Limbs and lung	Blockage of veins in the limbs, which may dislodge to lung and heart

1.2.1. Ischaemic Heart Disease

Ischaemic heart disease is caused by constriction of the coronary artery, limiting the blood flow to cardiac myocytes [10]. Impaired blood flood does not necessarily cause ischemia but will do so if blood flow does not meet the requirements of the tissue. Therefore, ischaemic heart disease can be subdivided into stable angina, unstable angina, and myocardial infarction. Common symptoms include chest pain, fatigue, breathlessness, and pain radiating to arms, shoulder, neck and back. Some patients may not experience any symptoms before myocardial infarction, whereas angina refers to the chest pain caused by insufficient blood flow to the heart. During stable angina, the symptoms are triggered by stress or exercise and relieved by rest, whilst symptoms appear suddenly in unstable angina and continue despite resting. Unstable angina is likely due to rupture of the plaque or thromboembolic occlusion, which may progress to acute myocardial infarction (heart attack). The difference between unstable angina and myocardial infarction (MI) is that the former does not cause cardiac damage whilst the latter causes extensive damage to the heart. Thus,

MI is the main cause of death in coronary artery disease and accounts for approximately 220,000 hospital visits in the UK each year. The mortality rate has improved, with a current 70% survival rate at present [9].

1.2.2. Aetiopathology of Cardiovascular Disease

Atherosclerosis is the leading cause of the blockage and narrowing of the coronary artery, leading to cardiac ischemia [11]. Atherogenesis refers to the process of plaque formation and involves multiple stages. The process is initiated by the infiltration of low-density lipoprotein (LDL) into the arterial endothelium. Oxidation of the entrapped LDL serves as the stimulus for inflammatory reactions, promoting expressions of endothelial adhesion molecules, which results in leukocyte infiltration. Platelets also deposit around the insult [12]. Infiltrated monocytes differentiate into macrophages, which uptake the oxidized LDL to form foam cells. Apoptosis of macrophages forms a lipid-filled necrotic lesion. Damaged endothelial cells also release cytokines, which promote smooth muscle proliferation and migration from tunica media to intima, forming a fibrous capsule around the lipid-filled lesions to stabilise the plaque. Platelet deposition and turbulent flow of the blood are created by the narrowing of the arteries and enhanced adherence of the leukocytes, promoting blood clots formation. Rupture of the plaque and formation of occlusive blood clot results in stenosis, blocking the blood flow to the cardiomyocytes [13]. Another less common cause of the narrowing of the coronary artery is coronary artery spasm, which is a temporary tightening of the muscles in the artery.

Cell death in ischaemic events was once thought of due to an unregulated necrosis process. However, it is not the only mechanism for cell death during myocardial infarction, where apoptosis also plays a role [14]. Sustained impaired blood flow to the heart initiates the ischaemic cascade as shown in **Figure 1-1**. Cardiomyocytes first switch to anaerobic glycolysis due to insufficient oxygen for adenosine triphosphate (ATP) production, leading to the accumulation of H^+ ions (acidosis). Excess H^+ ion is removed via Na^+/H^+ exchangers on the plasma membrane in exchange for Na^+, leading to elevation of intracellular Na^+ level. At a high intracellular Na^+ level, the Na^+/Ca^{2+} exchanger is less efficient to remove Ca^{2+} ions

and leads to the accumulation of Ca^{2+} ions in the cells. High cytoplasmic Ca^{2+} levels also impede the transport of Ca^{2+} ions from mitochondria to the cytoplasm, along with increased reactive oxygen species levels, leading to long-lasting mitochondrial permeability transfer pore (MPTP) opening and mitochondrial swelling and ultimately to cellular necrosis [15]. Reperfusion after the percutaneous coronary intervention (PCI) also contributes to the opening of MPTP and stimulates oxidative stress [15,16].

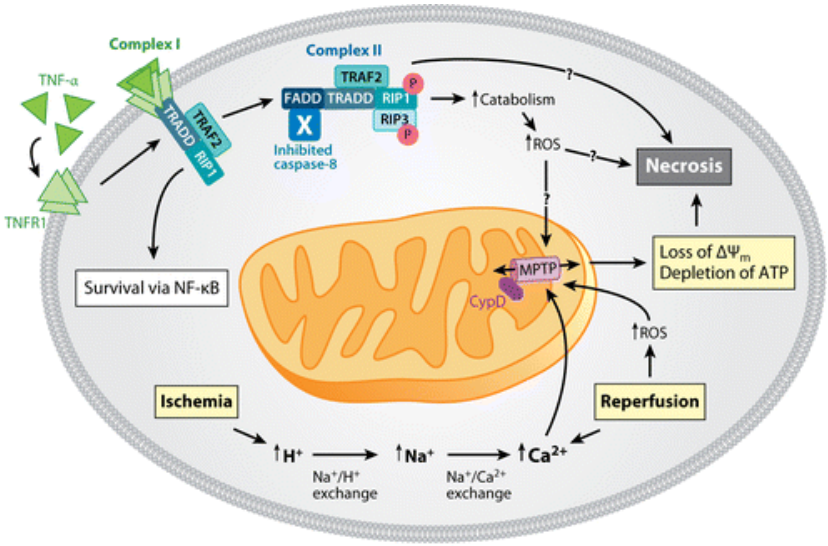

Figure 1-1. A schematic diagram showing the necrotic pathway of cardiomyocytes triggered by ischemia and reperfusion [15].

Chiong *et al.* have shown that a proportion of cell death is mediated via apoptosis as well during ischemia and reperfusion [16]. Apoptosis is a programmed cell death, which is subclassified into intrinsic and extrinsic pathways where the former is mediated via cell surface receptors and the latter via cellular organelles, such as the endoplasmic reticulum and mitochondria. Cardiomyocytes are naturally resistant to apoptosis due to low expression of Apaf1 and elevated levels of X-linked inhibitors of apoptosis protein (XIAP) [17]. Meanwhile, autophagy is likely a less important mechanism for the death of cardiomyocytes in MI, which is a highly regulated process of removal of unnecessary or dysfunctional components as a survival mechanism using double membrane autophagosomes and lysosomes for degradation. Hypoxia [18], glucose deprivation, reactive oxygen species (ROS), damaged organelles, and protein aggregates in cardiomyocytes have been shown to induce a

mammalian target of rapamycin (mTOR)-dependent autophagy [19]. Thus, it is likely to be more prevalent in the sub-lethally injured peri-infarct region and contributes to the remodelling of the heart post-infarction [16].

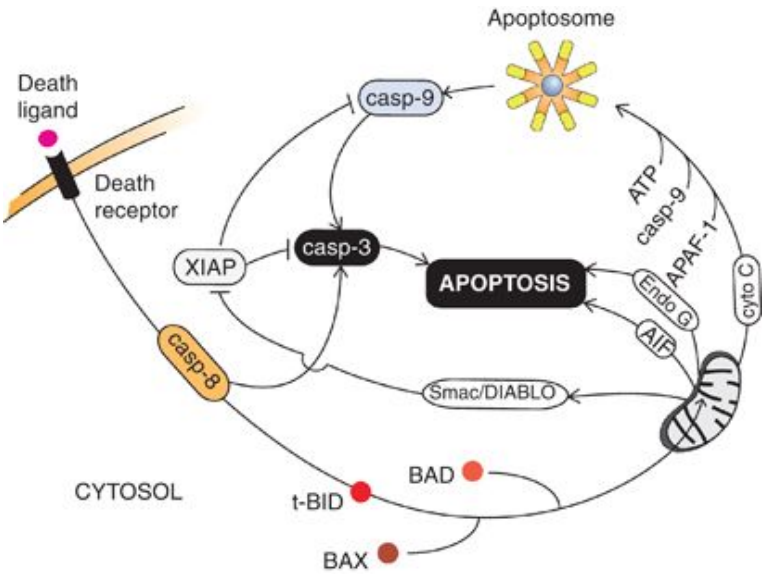

Figure 1-2. Signalling cascade in the intrinsic and extrinsic apoptosis pathways in cardiomyocytes [16]. The extrinsic apoptosis pathway is induced via the death receptor, subsequently activating the casp-8 and casp-3 downstream. The intrinsic apoptosis pathway is associated with the mitochondria, as a result of intracellular stress. It involves truncation of BID and BAX binding to mitochondria, leading to the release of cytochrome c and the formation of apoptosome with APAF-1. The casp-9 is then activated after hydrolysis of ATP and activates the executioner casp-3.

The extrinsic pathway is activated via the death receptor as shown in **Figure 1-2**, which induces the formation of death-inducing signalling complex and Caspase (casp)-8 activation, and in turn, activating casp-3 in the downstream cascade. The intrinsic pathway involves the proteolysis of BCL-2 interacting protein (BID) to truncated BID (t-BID), which activates BCL-2 associated X protein (BAX) binding to mitochondria. The interaction leads to the release of cytochrome c, Smac/DIABLO, Apoptosis-inducing factor (AIF), and Endonuclease G from mitochondria and triggers apoptosis via their downstream signalling cascades [16].

Various cell types are found in the myocardium, with abundances ranging in order from highest to the lowest – endothelial cells (45%), cardiomyocytes (30%),

fibroblasts (11%), pericytes, and mesenchymal cells (8%), macrophages and other leukocytes (6%) [20]. However, cardiomyocytes are the most susceptible to ischemia, whereas fibroblasts, endothelial cells, and resident mast cells are more resistant and have a role to play in post-MI inflammation [21]. There is a consensus that fibrosis is a three-step process, although various studies name them differently, such as inflammatory-proliferative-maturation stages [22,23] or initiating-effective-amplificative phases [24,25].

The fibrotic pathways are summarised in **Figure 1-3**. The death of cardiomyocytes in infarcted tissue zones triggers the first step, where fibroblasts increase the expression and secretion of matrix metalloproteinases (MMP) to break down the extracellular matrix (ECM) and injured tissue, activating innate immune signalling [22–24,26]. The former facilitates cell migration into the injured tissue zone [23], while the latter involves the secretion of chemotactic agents, such as chemokines and cytokines to recruit leukocytes [22,23]. The recruited immune cells clear the dead cells and ECM fragments, which allows infiltration of more neutrophils at first and macrophages and other mononuclear cells in a later stage [23]. Marked increases in the level and expression of pro-inflammatory cytokines are observed in post-MI heart failure models, such as tumour necrosis factor-alpha (TNF-α), monocyte chemotactic protein-1 (MCP-1) and interleukins (IL-6 and IL-1β) [27]. Owing to the pleiotropy of these cytokines, their exact mechanisms are not well-understood, although IL-1 is known to be responsible for inducing infiltration of leukocytes [28] and delaying the conversion of fibroblasts to myofibroblasts until the ECM fragments are cleared [29].

At the end of the first stage, inflammatory signalling is repressed due to apoptosis of the infiltrated immune cells [22]. The proinflammatory signalling is surpassed by proliferative signalling, where fibroblasts become the dominant cell type in the infarcted zone. Proliferative signals, such as transforming growth factor-beta (TGF-β), angiotensin II (Ang II) [21], and connective tissue growth factor (CTGF) [26] binding to their respective receptors, activate the downstream signalling pathways and transcriptional factors, like Mothers against decapentaplegic homolog (Smad), mitogen-activated protein kinase (MAPKs), protein kinase B (PKB), nuclear factor

kappa-light-chain-enhancer B (NF-κB), leading to the transformation of fibroblasts into myofibroblasts. Other cell types, especially epicardial and endothelial cells, also transdifferentiate into myofibroblasts [30]. The infiltration of myofibroblast occurs in the infarcted zones, regardless of the species or the regenerative capability [23], which indicates the vital role of fibrosis in cardiac repair. The myofibroblasts express and secrete massive type III collagens from the border to the centre of the infarcted zone [31], to form a collagen based matrix which increases the tensile strength and prevents ventricular rupture. The homeostasis of the ECM is regulated by MMP, and tissue inhibitors of metalloproteinases are secreted by the myofibroblasts. Transcriptional factors regulate the expression and production of the profibrotic growth factors and cytokines in cardiac fibroblasts. Neo-angiogenesis also occurs with the infiltration of endothelial cells and establishing a microvascular network to the infarcted area with the help of angiogenic growth factors to meet the need of these myofibroblasts during the repair process [22,32,33].

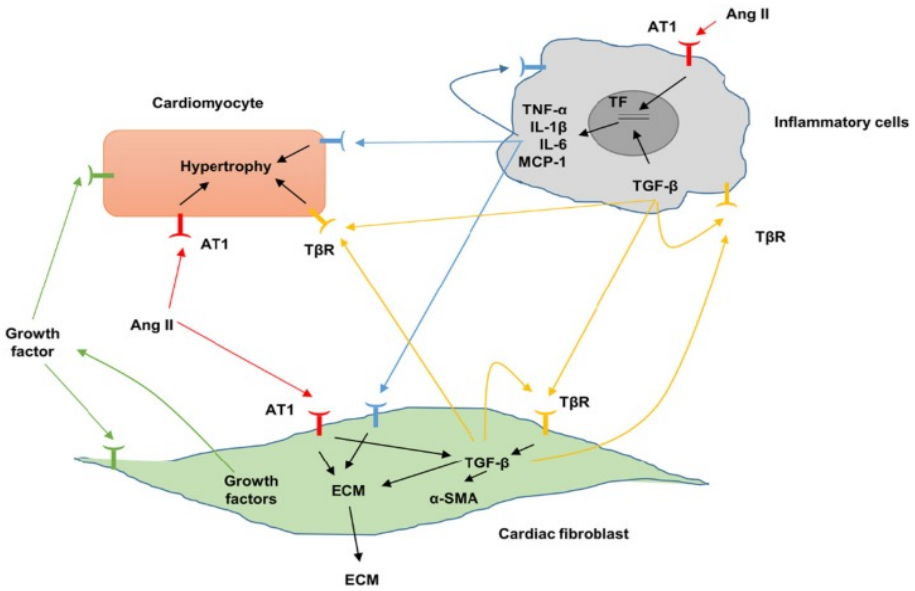

Figure 1-3. Fibrotic signalling pathways between different cardiac cell types. Secreted growth factors and cytokines from fibroblasts, endothelial and inflammatory cells can act on cardiomyocytes and fibroblasts, forming a positive feedback loop and amplifying the fibrosis response [25].

After the formation of the collagen-based matrix, fibroblasts, growth factors and matricellular proteins essential for myofibroblast survival are depleted and thus the

myofibroblasts are gradually eliminated [21,31]. However, type III collagen is continuously replaced by type I collagen in the maturation stage, where type I collagen is crosslinked via lysyl oxidases. These cross-linked collagens, i.e., mature collagen fibres, possess stronger tensile strength and contraction of the scar, which leads to the deformed geometry of the chamber and extensive remodelling in the heart [31]. This increased deposition of collagen I is known as scarring. Contrary to the normal healing process, where the myofibroblasts and collagen-based matrix are cleared from the wound, the fibrosis persists and the myofibroblasts are found in the infarcted heart even decades after the insult [34]. Persistent myofibroblasts might have a role in maintaining the ECM owing to the continuous contracting environment [31]. Therefore, chronic heart disease is one of the common complications, as the cardiac contraction and function are restricted by persistent fibrosis, deformed geometry of the chamber and extensive remodelling in the heart.

1.2.3. Current Therapies

Current treatment of myocardial infarction is categorized into acute and post-MI management. 300 mg aspirin is given as an immediate treatment for suspected MI. In the hospital setting, acute management involves coronary reperfusion therapy, either with PCI using angioplasty or fibrinolytic agents, such as alteplase, streptokinase, and tenecteplase [35]. Post-MI management involves rehabilitation training and drug treatments, such as angiotensin-converting enzyme inhibitors (ACE inhibitors), antiplatelets, beta-blockers, lipid modification drugs, and diuretics [36]. These agents prevent the spreading of the lesion, reverse the transient cardiac damage and impede fibrosis, but they could not induce the repair or regeneration of the damaged cardiac myocytes. Although the human heart is thought to be regenerated at a constant rate of 1% and 0.45% by the age of 25 and 75 respectively [37], the cardiac repairment post-injury is inefficient, generating fibrous connective tissues and scarring. Thus, chronic heart failure is a common long-term complication of myocardial infarction, due to the inability to pump blood effectively as an outcome of scarring and remodelling of the heart. There is, therefore, a need to develop therapies to stimulate the regeneration of cardiac myocytes and prevent the remodelling of the heart.

1.3. Cardiac Repair and Regeneration

Cardiac repair and regeneration aim to reverse the irreversibly damaged cardiac tissues, with the use of both stem cells and cell-free approaches. Cardiac repair and regeneration are umbrella terms, which involve inflammation reduction, survival promotion, angiogenesis, cardiomyocyte genesis, and proliferation. Cardiomyocytes are well-recognised as non-proliferative or only undergoing slow proliferation. In contrast to zebrafish [38], salamander [39], and neonatal mammals [40], which can regenerate cardiac tissues post damage, the adult human heart is thought to be regenerated at a constant rate of 1% and 0.45% by the age of 25 and 75, respectively [37]. However, the regeneration of cardiac myocytes is slow and often outpaced by fibrosis, generating fibrous connective tissues and scarring.

To achieve cardiac repair post-MI, the regeneration of new cardiomyocytes or the proliferation of surviving cardiomyocytes should be promoted. In this thesis, cell-based therapies are not the preferred option for cardiac regeneration owing to the risk of tumorgenicity and immune rejection [41]. Cell-free approaches, such as induction of cardiac proliferation with micro-RNA and other signal molecules are more of interest in this thesis. Therefore, the following review in literature is only focused on the induced proliferation of cardiomyocytes, exploring the signalling pathways, and signalling molecules involved in proliferation that has been manipulated to induce regeneration of cardiomyocyte.

1.3.1. miRNA

Micro-RNA (miRNA) is a short strand of non-coding RNA with about 22-base nucleotides, which partially pairs up with mRNA to regulate gene expression and protein expression post-transcriptionally. Several miRNAs are identified to regulate apoptosis of cardiomyocytes and cardiac regeneration. miRNA-15 family and miRNA-133 were important in cardiac repair after myocardial infarction. Neonatal rat overexpression of miRNA-195 (within the miRNA-15 family) did not lead to regeneration of cardiac myocytes post-MI, as the postnatal cardiomyocyte proliferation was inhibited [40]. Meanwhile, the overexpression of miRNA-195 also promotes cardiomyocyte enlargement and fibrosis. A study proposed that miRNA-195 overexpression in adult cardiomyocytes contributes to the loss of regenerative capacity

[40]. Another study demonstrated the depleted expression of miRNA-133 promoted cardiac regeneration in zebrafish after injury [42]. Therefore, an anti-miRNA inhibitor against these miRNAs could be developed to promote cardiac repair. Furthermore, overexpression of miRNA-21 is also found to promote cardiac fibroblast proliferation and induce cardiac fibrosis in atrial fibrillation and cardiac remodelling [43]. Therefore, by targeting the miRNA-21, cardiac fibrosis and remodelling after myocardial infarction could be minimized. Gabisonia *et al.* intramyocardially delivered miRNA-199a via an adreno-associated virus (AAV) vector into infarcted pig hearts to stimulate the expression of miRNA-199a [44]. Treated animals demonstrated improvements in contractility, reduction in scar size and increase in muscle mass, of which de-differentiation and proliferation of cardiomyocytes were successfully achieved via stimulation of endogenous cardiomyocytes. However, persistent stimulation of miRNA-199a led to sudden deaths of most of the treated animals, which indicates that the stimulation must be tightly controlled, especially the dosage. Alternatively, miRNA-199a analogues could be delivered instead of the viral vector as the miRNA-199a expressing gene would be incorporated into the host genome, while the delivery miRNA-199a analogue will have an effect for a shorter time only and will not have a permanent effect.

1.3.2. Hippo Signalling Pathway

The Hippo signalling pathway is an evolutionarily conserved signal cascade involved with controlling organ size by regulating cell proliferation and apoptosis, including inhibiting cardiomyocyte proliferation [45]. It acts through phosphorylation of transcription factors Yes-associated protein (YAP) and Transcriptional coactivator with PDZ-binding motif (TAZ), which subsequently prevent YAP and TAZ protein from translocation into the nucleus and induction of pro-proliferation gene expression. This pathway is involved in cardiac organogenesis in early cardiac development [46,47]. As such, this pathway was explored as a means of re-activating proliferation in cardiomyocytes (CM). Foetal activation of the Yap-1, a transcriptional coactivator ordinarily inactivated by the hippo pathway, induced the proliferation of postnatal cardiomyocytes in culture and the intact heart [48]. Yap-1 activation also promoted postnatal CM cellular activity, but the effect decreased with the maturation of the cells. Furthermore, a knock-out or inhibition of the Hippo pathway enhanced adult CM renewal and regeneration [47]. Hippo mutant

CM in the infarcted heart also exhibited elevated proliferation, which probably indicated that hippo signalling is a repressor for adult CM regeneration. Lastly, in mice expressed human YAP via transfection with AAV 9, activation of YAP post-MI reduced infarct size and preserved the cardiac function [48].

1.3.2.1. Neuregulin/ErbB/ERK signalling pathway

The neuregulin (NRG)/ErbB/extracellular signal-regulated kinases (ERK) signalling pathway has also been investigated for cardiomyocytes proliferation, as NRG is an epidermal growth factor and is important for cardiac development and proliferation in the embryonic heart. The signal is required for trabeculation of the ventricular wall [49], as it involves the BMP 10-controlled signalling between the endocardium and myocardium for maturation and differentiation of the trabecular cardiomyocytes [50], although activation of IGF/PI3K pathway is also required for cardiac proliferation [42]. NRG-1B raised the proportion of beating embryoid bodies and up-regulated the expression of Nkx2.5, GATA4, a-actin, MLC-2v and ANF in a time-dependent manner [51], which indicated the NRG/ErbB4/ERK pathway contributes to the differentiation of embryonic stem cells of mice, likely in early cardiogenesis. Furthermore, Bersell *et al.* elucidated that cardiomyocyte proliferation was induced by NRG-1 in culture, affecting only mononucleated cardiomyocytes to differentiate [52]. NRG-1 mediated the cardiac proliferation via activation of ErbB2-ErbB4 receptor dimers or transient induction of a basally active ErbB2 receptor in adult mice. Cardiomyocyte cell-cycle activity and cardiac regeneration were induced by injection of NRG-1, without the involvement of pluripotent progenitor cells. Reduction in scar tissue and improved cardiac function was observed two weeks post-MI in NRG-injected mice. Nonetheless, NRG-1 expression was induced in perivascular cells of adult zebrafish hearts upon injury. Overexpression of NRG-1 in injured hearts induced cardiac proliferation while reactivating the NRG-1 expression in uninjured zebrafish heart induced cardio-dedifferentiation, muscle hyperplasia, neovascularisation and ultimately cardiomegaly [53].

In conclusion, various potential drug candidates, ranging from small molecules to macromolecules like miRNA and NRG-1, have been researched and have demonstrated the ability to stimulate cardiac regeneration in *in vitro* models.

However, induction of CM proliferation in the clinical setting is limited by uncontrolled and excessive proliferation, which turns into cardiac hypertrophy, cardiomegaly, and ultimately heart failure, irrespective of which signal pathways or targets are involved such as micro-RNA, Hippo pathway proteins and cell cycle regulators [54]. The administration route and delivery system also remain a challenge to deliver these agents, with intramyocardial injection being associated with the risk of triggering ventricular arrhythmias [55]. The effect of these agents should be limited to the heart and thus delivery should be localised to the heart. Moreover, these agents are fragile and require an appropriate carrier system for protection and delivery. Hence, there is a need to develop an alternative route and optimised delivery systems to administer these agents for cardiac regeneration.

1.4. Anti-fibrosis

Fibrosis occurs in the heart regardless of the species after MI, to prevent ventricular rupture and provide mechanical support against the wall stress, which is a crucial step in wound repair. In contrast to the species with cardiac regenerative capacity, the human adult heart is unable to clear the fibrotic zone and regenerate new cardiomyocytes. Controlling the differentiation of fibroblasts and the transformation of other cells into myofibroblasts could, in theory, attenuate cardiac fibrosis and cardiac dysfunction post-MI. Currently, no licensed medication is available for preventing cardiac fibrosis [56–58]. Furthermore, the use of several cardiac regenerative drugs, such as periostin and growth factors in animal studies, also promotes cardiac fibrosis, which limits the use of these agents in the clinical setting [6,44]. Therefore, combined therapy of an anti-fibrotic drug with a cardiac regenerative drug may attenuate the cardiac fibrosis caused by cardiac regenerating drugs.

After MI, increased wall stress in the infarcted heart activates the local renin-angiotensin system, up-regulating the angiotensin II and in turn stimulating the secretion of inflammatory and profibrotic mediators such as TGF-β, IL-1B and TNF-α. These mediators promote the secretion of ECM and transformation into myofibroblast, which are the key steps in cardiac fibrosis. Therefore, the common

mechanism of action for the antifibrotic drugs is suppressing proinflammatory and profibrotic signals, i.e., secretion of these cytokines and growth factors.

1.4.1. N-acetyl-seryl-aspartyl-lysyl-proline (Ac-SDKP)

N-acetyl-seryl-aspartyl-lysyl-proline (Ac-SDKP) is a tetrapeptide cleaved from the N-terminal of thymosin-β4 (Tβ4) via hydrolysis involving meprin-α and prolyl-oligopeptidase, with the structure of the peptide shown in **Figure 1-4**. It is a naturally occurring immunomodulatory and pro-angiogenic peptide and is degraded by angiotensin-converting enzyme (ACE) into inactive fragments of Ac-SD (N-acetyl-seryl-aspartate) and KP (lysyl-proline). Hence, co-administration of ACE inhibitors, such as captopril, has been suggested to elevate the plasma concentration [59,60].

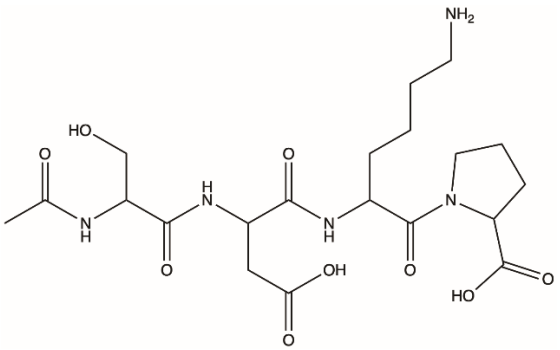

Figure 1-4. Structure of N-acetyl-seryl-aspartyl-lysyl proline. (Drawn with ChemDraw 20.1)

The exact binding site or receptor for Ac-SDKP remains unclear but the peptide is thought to possess angiogenic, anti-fibrotic, anti-inflammatory, anti-proliferative, and anti-apoptotic properties [61]. The proposed mechanisms for these properties are shown in **Figure 1-5**. Amongst all pro-fibrotic pathways, the transforming growth factor-beta (TGF-β) signalling pathway is one of the most important pathways involved in fibroblast proliferation and transdifferentiation (i.e., epithelial-mesenchymal transition). It involves the activation of Smad downstream and promotes ECM and scar formation. After myocardial infarction, the mechanical stress, and pro-fibrotic mediators, including TGF-β, activate the resident fibroblasts and transdifferentiate into myofibroblasts. In addition, angiotensin II is also worth noting, as it is a pro-inflammatory and pro-fibrotic mediator in the renin-angiotensin

system. Ac-SDKP is proposed to attenuate fibrosis via targeting the TGF-β/Smad pathway. It is also an alternative substrate to the angiotensin-converting enzyme, which is found to attenuate lung fibrosis via activation of the ACE2-angiotensin-(1-7) pathway [62]. Ac-SDKP is also found to reduce the cross-linking of collagen via downregulating the lysyl oxidase [63]. As for the anti-inflammatory properties, Zhu *et al*. demonstrated that Ac-SDKP suppresses the ICAM-1 adhesion molecule expression via TNF-α induced IKK-β dependent and NF-κB pathway. ICAM-1 is an adhesion molecule expressed on the endothelial cells, which promotes the infiltration of the immune cells [64]. Consequently, Ac-SDKP has attracted interest in the treatment of renal [65], cardiac [66,67], and lung fibrosis [68], as well as myocardial infarction [64,69,70].

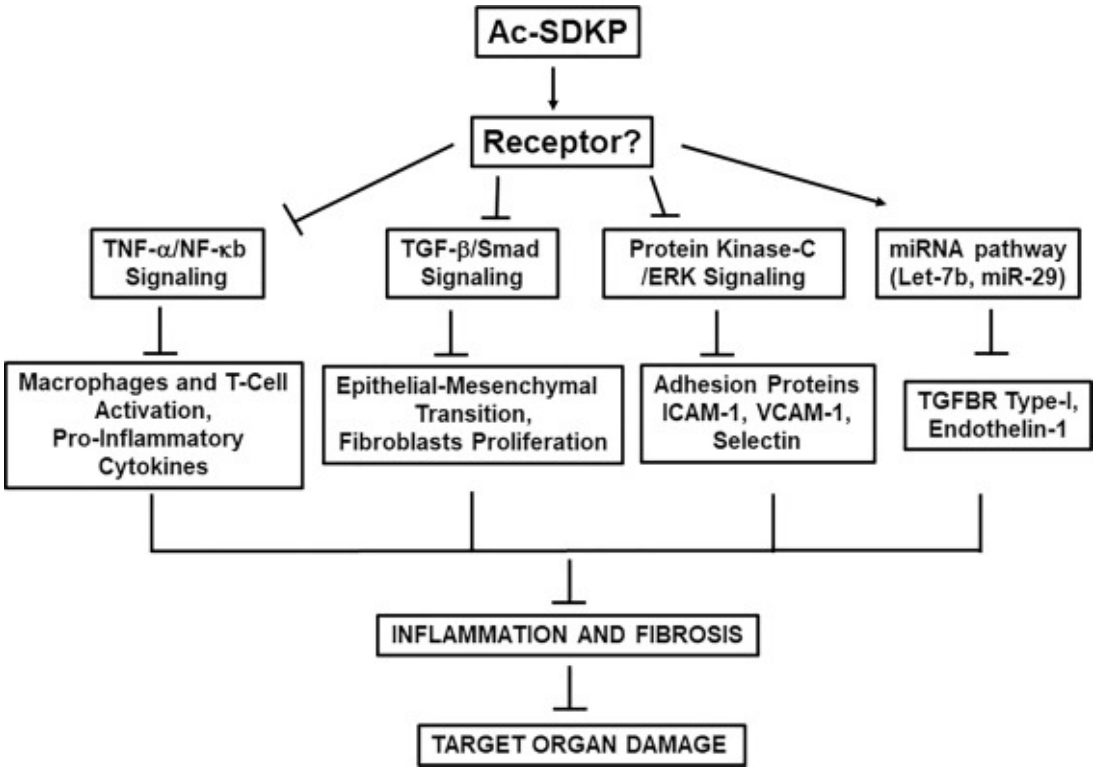

Figure 1-5. Proposed mechanisms for the anti-inflammatory and anti-fibrotic properties of Ac-SDKP [61]. The receptor remains poorly understood. The inflammation and fibrosis in organs are potentially inhibited via TNF-α/ NF-κB, TGF-β/smad, Protein kinase C/ ERK and miRNA pathways.

1.5. Anatomy of the heart

1.5.1. Structure of heart wall

The human heart wall is composed of three layers. The surface in contact with blood is called the endocardium, which is a layer of endothelial cells. The middle and thickest layer is the myocardium, which is composed of cardiac smooth muscle cells (myocytes). The pericardium is further divided into two subtypes as shown in **Figure 1-6**, namely parietal and visceral pericardium. The visceral pericardium (epicardium), is a layer of serous cells, which forms the outer layer of the heart wall [71]. The parietal pericardium is the outermost structure, which is made up of a fibrous laminar (fibrosa) and a serous laminar (serosa). The space contained by the two layers of the serous pericardium is the pericardial sac (pericardial space), which contains the pericardial fluid (PF).

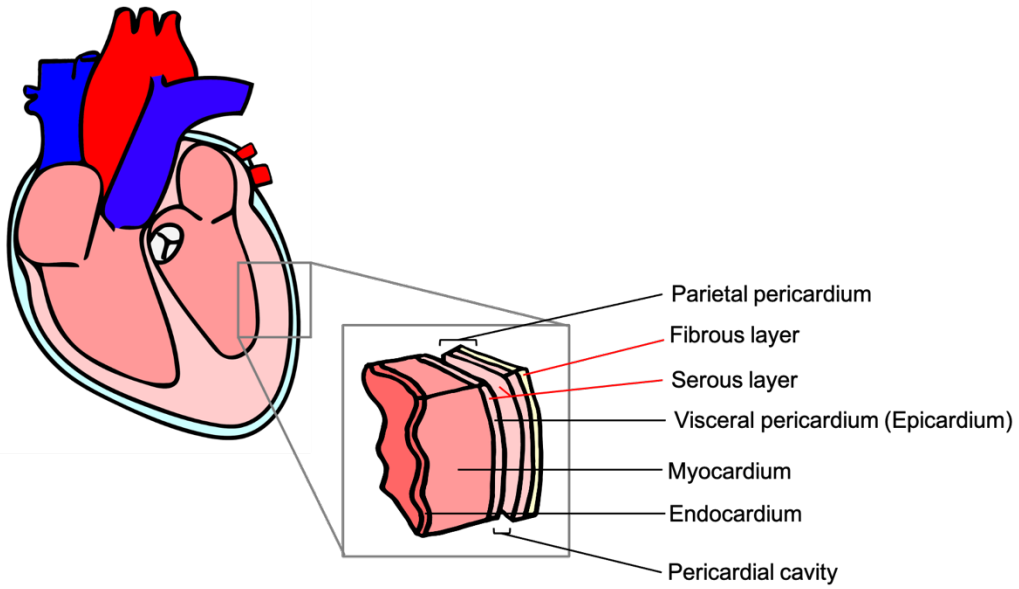

Figure 1-6. Structure of a human heart and the enlargement of a section of the human heart wall. The heart wall is composed of three layers – endocardium, myocardium, and epicardium (visceral pericardium). Epicardium is the outer layer of the heart wall, which is in connection with the serous layer of the parietal pericardium. The parietal pericardium consists of another fibrous layer which surrounds the heart, with the pericardial cavity formed in between the parietal and visceral pericardium. (Created with Adobe Photoshop Element 9)

The fibrous laminar is formed of fibrous connective tissue while the serous laminar is a monolayer of squamous epithelial cells (mesothelium). The two laminar in parietal pericardium are inseparable. The luminal membrane of the mesothelial cells is covered with microvilli projecting into the pericardial space and rare cilia, to increase the surface area for fluid transport [72]. Desmosomes, a type of intracellular junction, are present between adjacent mesothelial cells, to strengthen intercellular adhesion and form a permeability barrier [73]. The parietal pericardium enclosed the heart and the proximal portions of greater vessels, with the parietal fibrosa being continuous with the adventitia of the ascending aorta, pulmonary trunk, and superior vena [74,75]. 'Milky spot' lymphoid tissues exuding in the direction of the pericardial cavity are also scattered on the parietal pericardium. The structure is covered by a layer of mesothelial cells and is in proximity to the submesothelial lymphatic and capillary systems, providing an opening for rapid clearance of fluid [76]. Resident macrophages are also present in the submesothelial layer of pericardium for immune responses [73,77], which may have migrated from the milky spots [76].

On the other hand, the luminal surface of the visceral pericardium is a monolayer of mesothelial cells. Beneath the mesothelium, a dense network of collagen and elastic fibres is present with a thickness of several millimetres. Fibres are deposited in parallel and oriented diagonally to the heart. This configuration suggests the role of the visceral pericardium in passive stiffness and residual stress of the heart [78]. In some areas, the epicardium is adjacent to the myocardium and is separated by a thin layer of fibrous tissues, whilst near interventricular and atrioventricular grooves or around the coronary vessels, the epicardium is separated by abundant adipose tissues [79]. Although it is a continuous layer of mesothelial cells with the serous layer of the parietal pericardium [78,79], a higher proportion of cuboidal cells are present in the visceral serous laminar [77]. The thickness of the parietal pericardium is several times thicker than that of the visceral pericardium [80]. The combined thickness of normal human pericardium is 2 mm or less [81–83], which is irrelevant to the age or sex [82]. The optimal thickness of pericardium is between 2-3 mm. When the thickness is 4 mm or more at any point of the pericardium, it is considered abnormal [81,84].

1.5.2. Pericardial fluid

The function of pericardial fluid is to lubricate the membrane and ease the movement of the heart [79]. Volumetric studies of pericardial fluid in adult humans have demonstrated its volume is between 20 - 60 mL [74,85–87]. PF is predominately a plasma ultrafiltrate, with similar characteristics as pleural fluid [74,85]. It is formed by plasma ultrafiltration through epicardial capillaries, with the addition of a small amount of myocardial interstitial fluid. Blood is supplied to the pericardium via the pericardial artery branched from the descending thoracic aorta and via pericardiophrenic arteries, these being branches of the internal mammary artery. Blood is drained through the pericardiophrenic dial veins into the azygos vein and subsequently into the superior vena cava [88] or via superior intercostal veins and internal thoracic veins into the brachiocephalic veins [89].

PF has drained through the parietal pericardium lymphatic capillaries [90]. However, the mechanism of drainage is not fully understood due to the difficulty to study pericardial fluid dynamics under normal conditions [91]. Possible mechanisms of the fluid drainage into lymph are direct absorption and indirect absorption via macrophage phagocytosis [76]. The volume distribution of pericardial fluid is heterogeneous, with the largest amount located inside the atrioventricular and intraventricular sulcus, superior. and intraventricular sinus [92].

The pericardial fluid contains electrolytes, nutrients, and metabolites, with their concentrations similar to their respective plasma concentrations [85], which is consistent with the nature of pericardial fluid as the ultrafiltrate of plasma. However, a biochemical and haematological study demonstrated that the concentration of large molecules, especially lactate dehydrogenase (LDH) and albumin, were higher in the pericardial fluid than the levels measured in the ultrafiltrate of plasma [85], showing that these molecules might be leaked from adjacent pericardial and myocardial tissues. Nevertheless, proteomics analysis of the human pericardial fluid also showed that albumin is the principal protein present in the pericardial fluid [93]. However, the study showed that the LDH level in pericardial fluid (161 IU/L) was within the range of normal human plasma levels (100-260 IU/L). The discrepancy in LDH

levels between the two studies might relate to the different disease states of the patients. Enzymes were also identified in the pericardial fluid, but their profiles were not agreed upon between studies as most of the available data were obtained from cardiothoracic surgery patients, who had different disease states. The profile of enzymes was shown in **Table 1-2**. It is worth mentioning that ACE was isolated from normal pericardial fluid, which bears higher angiotensin I converting activity in PF than that in serum from patients with cardiovascular diseases [94]. The presence of ACE in PF indicates the role of pericardial fluid in metabolising active peptides. However, most of the groups sampled the pericardial fluid either from patients undergoing cardiothoracic surgery or from necropsy, limited studies were conducted on healthy living volunteers. Thus, the composition of pericardial fluid in a healthy human is difficult to define.

Biochemical markers and disease markers were also found in the pericardial fluid, with their levels varying depending on the disease states. For example, an oxidative stress marker, 8-iso-prostaglandin $F_{2\alpha}$, was elevated in pericardial fluid in patients with ischaemic and/or valvular heart diseases, with the pericardial level increasing with the severity of the heart failure [95]. Therefore, the composition of pericardial fluid is likely to vary with the condition of patients.

The white blood cell profile of normal human pericardial fluid illustrated that leukocytes were present in the pericardial fluid, with both mononuclear cells and polymorphonuclear leukocytes identified in pericardial fluid [96]. Large mononuclear cells were the largest constituents of leukocytes in pericardial fluid, followed by lymphocytes. These mononuclear cells accounted for about 74% and 26% of total cell populations, respectively. The finding is similar to the literature reported by Ben-Horin *et al.*, with lymphocytes and monocytes predominant in the differential cell counts of PF [85]. The presence of white blood cells was likely due to the inflammatory responses, as all samples were obtained from patients with different disease states.

Table 1-2. Composition of the pericardial fluid. As the fluid is formed from ultrafiltration of the plasma, nutrients, electrolytes, and metabolites are filtered into the PF. Proteins, including enzymes and albumin, were found in PF, potentially as a result of leakage from adjacent tissues or active secretion. Leukocytes are also present in PF.

Classes	Compositions	Ref
Nutrients	Glucose	[85,93]
	Triglycerides	
	Cholesterol	
Electrolytes	Phosphorus	[85,93]
	Calcium	
Metabolites	Uric acid	[85,93]
	Bilirubin	
	Creatinine	
	Urea	
Protein	Albumin	[85,93]
Enzymes	Alkaline phosphatase	[85]
	Aspartate aminotransferase	
	Amylase	
	Angiotensin-converting enzyme	[94]
	Lactate dehydrogenase	[85,93]
	MB isoenzyme of creatine kinase	[93]
	Glutamic pyruvic transaminase	
	Glutamic-oxal(o)acetic Transaminase	
	Glutamyl transpeptidase	
	Phosphocreatine kinase	
Leukocytes	Monocytes	[85,96]
	Lymphocytes	
	Polymorphonuclear leukocytes (Eosinophils, Basophils)	
	Macrophages	[96]

1.6. Cardiac localised delivery

1.6.1. Background

Localised delivery, by definition, is a form of targeted delivery where the delivered drug resides mainly at a certain site, resulting in reduced movement and absorption into the bloodstream. Two main approaches exist to maintain localised delivery – (i) delivering the drug to a naturally enclosed site, such as pericardium and myocardium in the heart, bladder, synovial space between joints, etc.; or (ii) through dosage forms where the drug has limited ability to translocate, such as patches, gels and implants [3]. Localised cardiac delivery is difficult to achieve via conventional delivery routes [3] such as intravenous (IV) and oral delivery, as these result in the drug being

introduced into the bloodstream and systemic circulation, hence being subject to typical distribution and plasma protein binding effects which render specific localisation in the heart difficult. There are three enclosed spaces in the heart where localised delivery could be achieved: the pericardium, coronary artery, and myocardium.

Intramyocardial delivery is a direct administration of materials into the myocardium, which is the thick muscle layer of the heart wall. This method is usually used in cell therapy for the delivery of stem cells or stem-cell-derived cells into the heart, where the use of intracoronary delivery is limited due to the occlusion of the artery [97]. Another use of this approach is to improve the residence time of cells in the myocardium [3]. The injections can be performed either on the endocardium or epicardium, similar to intrapericardial delivery. The epicardial approach allows accurate targeting of drugs or cells in the infarcted zone, as open surgery was performed to allow direct visualisation. In the endocardial approach, specialised catheters with electromechanical mapping systems were used to determine the site of interest [98]. Unlike the epicardial approach, the endocardial approach could be performed on high-risk populations and repeated if required [99].

Intracoronary delivery involves injection or infusion in the coronary artery, which is used preferably post-MI and with PCI [100]. Intracoronary cell delivery involves balloon catheters placed in the coronary artery, with coronary flow either maintained (non-occlusive approach) or occluded (stop-flow approach) to prevent rapid washout [97,100]. The non-occlusive approach utilises balloon catheters or other specialised catheters for sub-selective delivery, while the latter method uses balloon catheters which are temporally inflated to obstruct the coronary flow and thus minimise the washing out of cells. Cells are injected or infused at various flow rates, depending on the approach adopted, and into different vessels, where the area of interest in the myocardium is subtended from the coronary artery or collateral vessel. However, administered cells are required to transverse the endothelium and migrate into the myocardium, where the cell concentrations in the infarcted zone and border zone are higher. In common with intramyocardial cell delivery, two delivery approaches, guided delivery, and distal delivery were tested in a clinical trial for intracoronary

drug delivery. Guided delivery is a drug injection through a guiding catheter while distal delivery is a localised drug injection in a distal coronary bed via a perfusion balloon or selective microcatheter placed in the affected vessel away from the lesion [101].

1.6.2. Intrapericardial delivery

Intrapericardial delivery is the administration of pharmacological agents into the pericardium, which is a bilaminar sac surrounding the heart. It is a novel delivery route, with currently limited experimentation in animal tests and clinical trials. Indeed, the field remains at an early stage compared to its counterparts, probably due to a lack of prior understanding of the associated challenges. The access techniques will be discussed in detail in **Section 1.6.4**. Each localised delivery route has its advantages and disadvantages, which are shown in **Table 1-3**.

Table 1-3. Site of access of various localised deliveries in the heart, with ease of drug escaping into systematic circulation. The pros and cons of each delivery method were also detailed in the table [3,99].

	Intracoronary delivery	**Intrapericardial delivery**	**Intramyocardial delivery**
Site	Coronary artery	Pericardium	Myocardium
Entering systemic circulation	Yes	Minimal	Yes
Access	Easy to access (Varied between access techniques)		
Advantages	Increased and homogenous myocardial distribution	Prolonged drug half-life Minimal pericardial escape	Increase myocardial concentration Long-lasting
Disadvantages	Vessel Puncture Decreased blood flow in the artery might induce ischemia and arrhythmia Risk of occlusion and emboli when delivering large cells or viscous suspension	Pericardium opened after surgery Pericarditis Pericardial adhesion, which might induce cardiac tamponade	Perforation Limited access to certain areas e.g., septum Tissue inflammation and irritation Increased risk of cardiac arrhythmias
	Invasive / minimally invasive (depending on access techniques)		

1.6.3. Justification for using intrapericardial delivery

All cardiac localised deliveries are invasive regardless of what access techniques are being used. However, pericardial delivery possesses advantages over the other routes. Drugs or cells that have been delivered into the intrapericardial space have been shown to diffuse across the epicardium into the endocardium, penetrate the myocardium spread from the atrium to the ventricle [102,103] and achieve localised and targeted action on the heart [102–105]. Moreover, owing to the slow clearance of the pericardial fluid [76], the pericardial escape of the drug is low and thus the pericardium can act as a reservoir for the drug and prolong the half-life in the heart [106], and reduce peripheral side effects [107]. The washing-out effect observed in intracoronary delivery is reduced in intrapericardial delivery, albeit dilution by pericardial fluid would occur. Furthermore, desired drug concentration in the myocardial tissue can be achieved with a lower dose compared with other routes, such as oral, intravenous, or intracoronary delivery [105,108–110]. Nevertheless, the pericardial space contains pericardial fluid, which could solubilise the hydrophilic drugs and biologics. The pericardial space could accommodate a larger volume of materials and deliver a higher dose compared to intramyocardial injection, and act as a reservoir for prolonged release of the active pharmaceutical ingredients. Lastly, the use of intramyocardial injections was limited by ventricular arrhythmias [111], while occlusion of the coronary artery also restricted the use of intracoronary delivery [97]. In contrast, intrapericardial delivery does not interfere with the coronary flow nor inject materials directly into the myocardium, where these complications were not reported in the literature. Thus, intrapericardial delivery offers key benefits over other methods of localised cardiac delivery making it a preferred route for localised drug delivery to the heart.

Intrapericardial delivery is a double-edged sword, which offers numerous advantages as a delivery route to the heart, including favourable pharmacokinetics profiles, proximity to the myocardium, long residence time, and localised effects in the heart. Nevertheless, the invasiveness of the intrapericardial delivery is undoubtedly the key downside and should be taken into consideration. The use of minimally invasive techniques only mitigates but does not eliminate invasiveness. Therefore, it is not a delivery route that would be suitable for all sorts of cardiac conditions and drugs.

Instead, the use of the route should only be performed when the benefits outweigh the risks. Suitable conditions include pericardial diseases and conditions where there are unmet needs in the current treatments, such as myocardial infarction and arrhythmias. However, it is not designed for conditions that are not originated in the heart nor other cardiovascular conditions that can be maintained with oral or intravenous treatments, such as strokes, peripheral vascular conditions, and angina, as the risks of intrapericardial delivery outweigh the benefits. Lastly, nanoparticles and fragile drugs that are aimed to be localised in the heart could take advantage of the routes, such as proteins, growth factors, genes, and peptides, minimising the off-target effects and limiting the deposition in the heart.

1.6.4. Access routes and delivery techniques for intrapericardial delivery

Generally, there are three main approaches experimented with the delivery of pharmaceutical agents, including small molecules, peptides, and cells to the pericardium of animals and humans. The first approach, known as thoracotomy, involves an incision into the pleural space of the chest, with two subtypes – medial sternotomy accessing the pleural cavity and heart via opening the sternum, while lateral thoracotomy involves making an incision into the intercoastal space, of which the opening is widened by a rib retractor placed in between the ribs. After exposing the heart, a small incision is made on the anterior surface of the pericardium and the edges of the incision are tied with a suture to produce a square opening, forming a reservoir for the instillation of drug solutions, as shown in **Figure 1-7 (left)**. Drug solutions were then removed by suction, followed by a washout of the pericardium [112–115]. This method was usually adopted in experiments evaluating the intrapericardial delivery of anti-arrhythmic drugs as the electrodes were also placed through the pericardial opening as well as commonly in small animals like rodents [7,107,116,117]. Other designs for intrapericardial drug instillation utilised fenestrated [109] or looped catheters [105,118]. The catheter was inserted via a small incision on the pericardium, for drug delivery and pressure monitoring. The position of the catheter was secured with purse-string sutures while the pericardium was closed with a continuous locking suture to provide an airtight seal [103]. Furthermore, drug-loaded hydrogels could be delivered with a blunted needle through a micro-puncture on the pericardium [107]. The hydrogel could also be

delivered through epicardial spraying on patients undergoing coronary artery bypass graft (CABG), where the pericardium was opened for constructing the bypass graft. Before the closure of the pericardium with interrupted sutures, the amiodarone hydrogel was sprayed diffusely using a carbon dioxide driver set over the right atrial lateral wall, left atrial appendage, and transverse sinus areas are shown in **Figure 1-7 (right)** to prevent post-operational fibrillation [119,120]. Apart from fibrillation, other applications of intrapericardial delivery are discussed in **Section 1.8**.

Unfortunately, pericardial adhesion is considered an unavoidable consequence of thoracotomies, which prevents future epicardial access and limit the clinical use of thoracotomy for pericardial delivery. Pericardial adhesion refers to the sticking of the pericardium to the epicardium and is due to the damage of mesothelial cells during operation. The key steps in developing the adhesion are (1) loss of mesothelial cells, (2) accumulation of fibrin in voids, (3) loss of normal pericardial fibrinolysis, followed by (4) local inflammation [121]. Therefore, intrapericardial implants, instillation and epicardial spraying via thoracotomy might induce post-operative pericardial adhesion. Recently, new polyethylene glycol and hyaluronic acid-based products that could prevent fibrin adhesion, have become available to reduce peritoneal adhesions for clinical use, which might also prevent pericardial adhesion [122–124]. Other serious complications, like cardiac tamponade and pericardial effusion, could be caused by pericardial adhesion. In most cardiothoracic surgery, the pericardium is opened to prevent pressure from building up and cardiac tamponade. However, to form a drug reservoir, the pericardium is closed following the surgery, where reduced cardiac indices, stroke works and increased cardiac tamponade risk were observed [125].

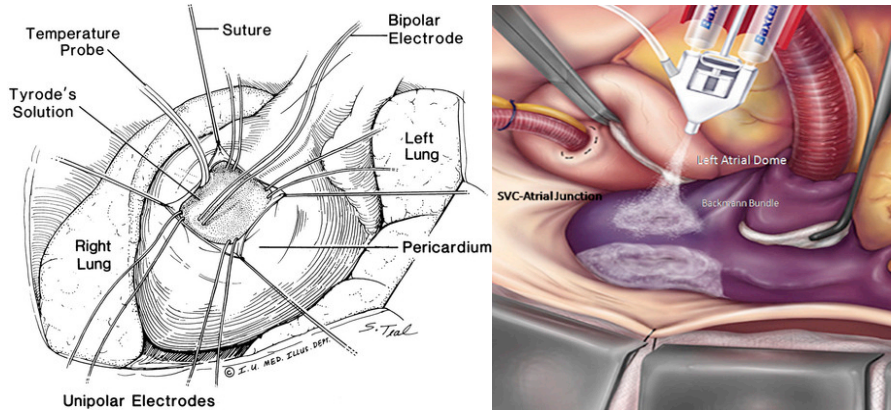

Figure 1-7. A schematic diagram showing (left) the drug instillation in the reservoir formed in pericardium [115] and (right) spraying of amiodarone hydrogel after CABG [119,120].

The second route is subxiphoid access. A small to medium-sized incision could be created on the middle line below the xiphoid, depending on the devices used [126–128]. The incision size is smaller for the needle than for the pericardial access devices. For example, an epicardial blunt-ended needle is inserted between the xiphisternum and the left costal margin for 2-3 cm. Then, the needle is lower through the infrasternal angle (15 -30^{o} angle) into the skin and directed at a swallow angle to access the pericardium over the anterior aspect of the ventricle while the needle is directed posteriorly toward the left shoulder to reach the pericardium over inferior aspect of the ventricle [129]. Alternatively, two other routes called para-apical and parasternal routes were commonly used in pericardiocentesis, but not in intrapericardial delivery, as described in **Figure 1-8**. Guidance should be performed to minimise the complications and damages, but the subxiphoid route is by far the safest under blind guidance [130].

Furthermore, several pericardial access devices are previously reported in the literature or currently on market at the time of writing, namely PerDUCER®, AttachLifter device [131] and PeriCardioScope™ (Perifect, Herzliya, Israel). In general, the core design is the same, which consists of a sheathed needle and a suction tip with a hemispheric cavity to grasp the pericardium [126,127]. A needle is housed inside a sheath tube, which is connected to a suction syringe on one end and a tapered-ended and half-moon-shaped plastic tube with a hemispheric cavity on the other. A side hole in the cavity allows access to the vacuum lumen and the insertion

of needles. The access is a two-step process, which involves (1) subxiphoid access to the mediastinal space and (2) pericardial captures, puncture and insertion of guidewire and catheter. The device is introduced into the mediastinal space via the incision on the median line below the xiphoid process [126–128], with the hemispheric cavity on the device placed against the pericardium. The pericardium is then sucked into the hemispheric cavity by the vacuum, which is isolated from the epicardium. The needle or needle-tipped catheter punctures the pericardium to create access. A guidewire is inserted through the needle or catheter into the pericardial space to direct the insertion of a drug delivery catheter [126–128,132]. The difference in terms of the features between each pericardial access device is shown in **Table 1-4**.

Table 1-4. Summary of the features of three reported pericardial access devices, with the focus on comparing the puncture part, site of puncture and pericardium lifting method.

	PerDUCER®	**AttachLifter**	**PeriCardioScope™**
Puncture part	J-tipped guidewire	External needle	Rotatable needle
Site of puncture	Inside the cavity	Outside the cavity	Inside the cavity
Pericardium lifting method	Lifted only	Lifted and rotated at 90°	Lifted only
Additional guidewire required	No	Yes	Yes

The third approach is transatrial access, which was first proposed by Uchida *et al.* in 1995 [133]. This approach first used a guiding balloon catheter advancing through the femoral vein into the right atrium. The balloon was then inflated with carbon dioxide to push against the heart wall so that a puncture on the heart wall could be created to access the pericardium under fluoroscopy. A few years later, an advanced and more clinically viable version of the device was reported by Waxman *et al.* [134]. A larger guide catheter was first introduced through the femoral introducer sheath and then positioned under fluoroscopy guidance into the right atrial appendage. A guide catheter was later positioned under fluoroscopic guidance into the right atrial appendage, followed by the withdrawal of the first catheter. A needle catheter was subsequently advanced through the guidewire and a small perforation on the atrial appendage was created using a hollow radiopaque needle mounted on its tip. Another soft and smaller transatrial guide wire equipped with a second

radiopaque marker was then inserted through the needle catheter and secured the percutaneous pericardial access, with the position in pericardial space confirmed with fluoroscopy. The insertion of the second guidewire allowed the needle catheter to be withdrawn and exchanged with an application catheter for drug injection or aspiration catheter for fluid withdrawal on the wire [134–138].

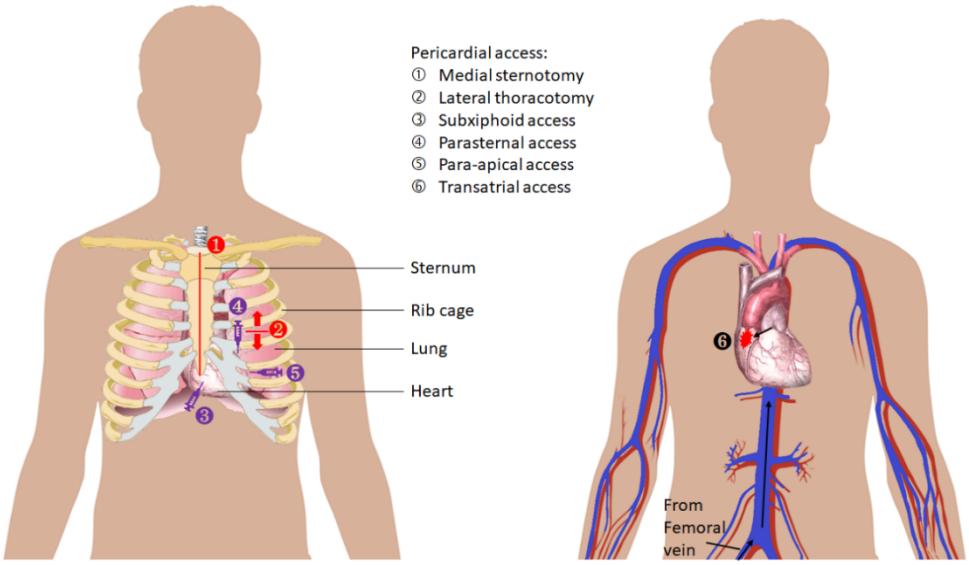

Figure 1-8. Summary of the pericardial access techniques, including both common and minor routes. (Created with Microsoft PowerPoint)

Apart from the discussed routes for pericardial delivery, two minor routes – parasternal and para-apical routes are feasible but have not been experimented with or used in studies. The para-apical approach involves needle insertion at 1-2 cm lateral to the apex beat within the 5th, 6th, or 7th intercostal space and advanced over the superior border of the rib to avoid the intercostal nerves and vessels, while a needle is inserted perpendicularly to the skin through the 5th intercostal space at the left sternal border in the parasternal approach.

Transatrial and subxiphoid access are much less invasive and more tolerable than access via thoracotomy. Transatrial access is quick and simple, which utilises standard catheters, and the process only takes 1-3 minutes after the introduction of the femoral sheath [134]. On the other hand, the subxiphoid utilises a standard Tuohy needle or dedicated pericardial access devices. The complications of pericardial access include (1) vascular and ventricular injury, (2) injury to other

organs and (3) inflammatory reaction to the epicardial access. A small incision as well as a transient, small, and minimally inflamed wound are created on the femur and the atrial wall respectively in transatrial access, but no other significant adverse events were observed [134–137,139]. Similarly, a small incision or needle puncture hole is created in subxiphoid access. Mild pericarditis and pericardial bleeding are common in subxiphoid access, but severe pericardial bleeding and pericardial inflammatory reaction reportedly occur at a low incident rate [140]. Damage to other organs during pericardial access is unusual, but complications have been reported [141].

Amongst all delivery routes discussed, medial, and lateral thoracotomy is an open-chest surgery, which allows direct visualisation of the heart. However, both techniques are lengthy, invasive, and risky for patients as a larger opening is created on the chest for direct visualisation and access to the heart. High infection rates, scarring and longer recovery time are the drawbacks of thoracotomy. Therefore, medial and lateral thoracotomies are rarely used to perform cardiothoracic surgeries and pericardial delivery is performed before the closure of the chest. The drawbacks or complications for transatrial and subxiphoid delivery are minor, relative to thoracotomy, as the size of inflammation and wound-induced are minimal, small, and reversible. The pros and cons of each access technique are presented in **Table 1-5**. Subxiphoid and transatrial routes are preferable for pericardial delivery, as they have a better balance of risk and benefit in a clinical setting. Contrarily, thoracotomies are used for cardiac surgery such as CABG, where pericardial delivery is in conjunction with and post-surgery before the chest is closed.

Table 1-5. Summary of the requirement of anaesthesia, guidance method, wound size, inflammatory responses, infection risk and recovery time for various pericardial access methods. The advantages and disadvantages of each method were also discussed.

Access method	Thoracotomy		Subxiphoid access	Transatrial access
	Medial sternotomy	Lateral thoracotomy		
Anaesthesia	General		General or local	Local
Guidance	Not required		Pericardioscopy Fluoroscopy Echocardiogram Computer tomography	Fluoroscopy
Wound size and scarring	Large	Medium to large	Small to medium size depending on devices	Small puncture on the atrial wall and thigh
Inflammatory response	Pericarditis Bone inflammation Inflammation of the wound	Pericarditis Inflammation of the wound	Pericarditis Inflammation of the wound	Transient inflammation on atrial wall and thigh
Infection risk	High		Low	
Recovery time	Long		Short	
Advantage	Direct visualisation of the pericardium	Intact chest cage (vs MS) Direct visualisation of the pericardium	Various introducer devices are available Simplest method	Rapid procedure The standard femoral vein catheterization procedure Low complication rate
Disadvantage	Cracked sternum Pericardial adhesion and tamponade Pain and a high chance of complications	Pericardial adhesion and tamponade Pain and a substantial risk of complications	Incorrect needle placement (especially under blind insertion) Puncture of other organs	Puncture of the ventricle and other organs
Suitable use	Should only be used after cardiac-thoracic surgery, in small animals like rodents or in AF studies which require the implantation of the electrodes		Can be used solely for pericardial delivery	

1.6.5. Guidance techniques for intrapericardial techniques

Apart from thoracotomies, which allow direct visualisation of the pericardium, other intrapericardial access techniques require guidance methods to confirm the position and successful entry into the pericardium. Four main types of guidance methods have been investigated in clinical trials and experimental studies to assist pericardial access. Fluoroscopy has been predominantly used in experimental studies whereas echocardiography has been the most common guidance adopted in the clinical setting for pericardiocentesis [142]. Computed tomography and pericardioscopy are relatively new techniques for assisting pericardial access, which offer advantages over echocardiography, allowing direct visualisation of needle advancement. However, limited clinical evidence and experience are available for computed tomography and pericardioscopy guidance [142]. As each guidance is distinctive in terms of working principles and operating procedures, the details of each guidance method are discussed below.

Fluoroscopy was the first imaging technique used with intrapericardial access, usually performed in conjunction with the subxiphoid approach. The technique utilises a continuous X-ray to allow real-time and dynamic visualisation of contrast media or instruments through the body. An epicardial introducer needle containing contrast medium is inserted and punctures the pericardium. Contrast medium is then injected into the pericardial space [104,143]. The access of pericardium is confirmed with tenting at the needle site [129] and a sluggish layering of contrast medium diffusing inferiorly (downwards) was observed [129,130,143]. A guidewire is then introduced into the pericardial space in exchange for the introducer needle [143].

Sosa *et al.* performed pericardial punctures in patients using an epicardial introducer needle (Tuohy-17G) via the subxiphoid route with fluoroscopic guidance [144]. The needle was advanced gently under fluoroscopic guidance until a slight negative pressure was felt. The entry of the needles into the pericardial space was confirmed by injection of diluted contrast media under fluoroscopy. Laham *et al.* also reported a successful percutaneous subxiphoid access in pigs using the same needle and a similar procedure, but with continuous positive pressure (20-30 mmHg) applied during the advancement [145].

Echo-guided pericardiocentesis was introduced by the Mayo Clinic in 1979 [146], which utilised a 2D phase-arrayed echocardiography to visualise the cardiac anatomy [147]. Callahan *et al.* advocated that the needle enters from a point where the largest fluid accumulation is the closest to the probe and the needle path is away from any vital organ [148]. The subxiphoid route is a longer route to reach the pericardium compared to the para-apical route and passes through the anterior of the liver capsule. As ultrasound does not penetrate air, the lung is also avoided in echocardiography. Therefore, the apical route instead of the parasternal route is preferred for entry under echocardiography. Two different approaches to echo guidance are available. The first technique is an echo-assisted method, as originally proposed by Tsang *et al.*, of which the path of the optimal needle trajectory is first determined using echocardiography and memorised by the operator [146]. A polyteflon (Polytef) sheathed needle is then positioned from the predetermined site and advanced to the pericardium via memorised trajectory without continuous echo monitoring. Upon entry into the pericardium, the sheathed needle is further advanced for a short distance, where the steel needle core is withdrawn to leave the polyteflon sheath in the pericardium. The position of the sheath is confirmed with the saline echo-contrast medium, where the echo-contrast effect is monitored with 2D echocardiography. A guidewire and a catheter are subsequently advanced into the sheath to create access. The second technique is an echo-guided method. The echocardiography is used to search for an optimal position and is maintained in that position throughout the procedure. The needle is attached to a multi-angle bracket mounted on the probe, inserted, and advanced under continuous echo monitoring as shown in **Figure 1-9**. When the needle tip is observed on the echocardiography, the syringe is removed and replaced with a guidewire and a catheter [149,150].

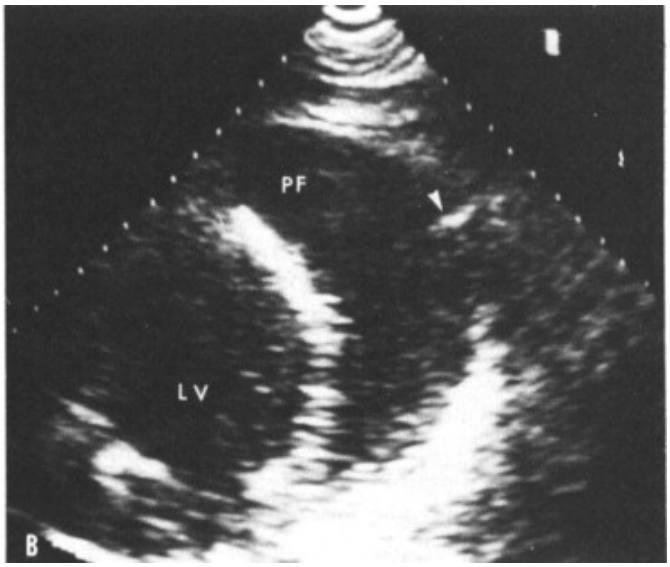

Figure 1-9. 2D echocardiogram showing the position of a needle (the white arrow) entering the pericardium of a patient with large pericardial effusion [149].

Computer tomography is a technique using computational combinations of multiple X-ray measurements from different angles to produce cross-sectional tomographic images. In general, several images are taken during the procedure to direct the needle entry. The first image of the whole thoracic cavity is taken to determine the ideal approach and entry point into the pericardium. An introducer needle is then inserted, followed by the acquisition of a new image. The orientation of the needle is then adjusted based on the second image, and the needle is subsequently advanced to the pericardium. Guidewire and catheters are advanced into the pericardium next. During the advancement of needle, guidewire, and catheter, extra images are acquired when required. After placement of the guidewire and catheter, the final image is obtained to verify the position in the pericardium. Several clinical cases have demonstrated successful computed tomography-directed pericardiocentesis [142,151–153].

Pericardioscopy is a tool for microscopic visualisation of the epicardium and pericardium, which involves the introduction of an endoscope into the pericardium for taking video and photography. In early studies, two types of endoscopes were designed for pericardial disease diagnosis – a flexible fibreglass endoscope and a rigid 110^{o} angled instrument [154]. However, only the former design was used to assist the pericardial access through PerDUCER® devices. A flexible endoscope was

applied into the mediastinal space to identify and select the suitable surface for pericardial access, with no adhesion and fat deposition on the pericardium. The position of the inserted guidewire and subsequently the catheter was also verified via the pericardioscopy [155]. Other devices such as Attachlifter and PeriCardioScope™ are incorporated with fiberscope and pericardioscope respectively on the suction head, which allows continuous visual monitoring throughout the advancement and pericardial access [131].

1.7. Pharmacokinetics of intrapericardial delivery

Delivery of pharmaceutical agents into pericardial space could achieve localised and prolonged delivery to the heart. Hermans *et al.* conducted a pharmacokinetic study on intrapericardial delivery using fluorescent proteins and conjugates [105], to identify the pharmacokinetic advantages of intrapericardial delivery over other delivery routes. The study revealed that the desired local drug concentration in cardiac tissue could be achieved with a lower dose and a lower drug plasma concentration when the active pharmaceutical ingredient is administrated intrapericardially. Moreover, various other intrapericardial drug studies also reported coherent results, with a higher drug level in cardiac tissues achieved in intrapericardial delivery compared to standard intravenous administration for anti-arrhythmic drugs, such as flecainide [108], amiodarone [109], and several beta-blockers [156–158]. Therefore, the dose of drug required to have the same response is much lower when delivered intrapericardially than intravenously. For example, the dose of sotalol and atenolol delivered intrapericardially was 10 to 30-fold lower than their intravenous dose to achieve the same anti-fibrillatory response [108]. Besides, the plasma drug levels in these studies were not detectable with the analytical technique used. A low plasma drug level is also advantageous, indicating a low level of drugs escaping from the pericardial space. Thus, intrapericardial delivery could achieve localised delivery and reduce peripheral side effects. Lastly, the slow clearance of drugs and prolonged residence time in the pericardium is also beneficial, which was discussed in detail in **Section 1.6.3**, as drug-loaded intrapericardial systems can act as a local drug reservoir to achieve prolonged delivery and local delivery.

1.7.1. Distribution

Intrapericardial drugs have been shown to diffuse and penetrate the myocardium and achieve localised and target action on the heart [102–105]. In brief, drugs were able to penetrate the epicardium into the endocardium, as well as spread from the atrium to the ventricle down the diffusion gradient [102,103]. Maslov *et al.* extensively studied the myocardial distribution, using epicardial applications of an ephedrine-loaded alginate disk and adherent poloxamer hydrogel in pigs [159]. These forms represented the directed and dispersed mode of deliveries in epicardial or intrapericardial deliveries respectively. Asymmetric distribution was observed in the heart with the alginate disc, where the ephedrine concentration was elevated in the epicardial layer of the lateral wall and apex, especially near the point of release as the transmural gradient diminished across the myocardium. In contrast, a homogenous distribution resulted in the dispersed hydrogel over the entire anterior, with the deposition in the epicardial layer of anterior, lateral, inferior, and apical walls. Anterior and lateral walls were beneath the site of application, where the drug accumulated and then spread laterally to the apical walls along the concentration gradient. Increased ephedrine level in the coronary sinus blood was also detected following the epicardial applications, but both approaches were unable to deliver ephedrine into the septum. In short, the study demonstrated that the choice of dosage form for epicardial deliveries could hugely influence the profile of myocardial drug deposition. Based on the finding, it can be deduced that epicardial implant and patch as pointed sources would have an asymmetrical deposition profile, while intrapericardial hydrogel, injection or infusion would exhibit a homogenous myocardial drug distribution. The use of dosage forms could therefore be tailored based on the application and the target site in the heart. Nevertheless, there are still plenty of uncertainties surrounding the delivery route. For example, the local concentration in the pericardium is much higher after intrapericardial delivery than in the oral or IV delivery as the clearance of the drug is slow and the volume of distribution is small. The high local drug concentration might result in the toxicity of the pericardium. In addition, the pericardial fluid contains surfactant-like prostaglandin for cardiac motion, triglyceride, and cholesterol, which might promote the dose dumping of a controlled release formulation. Therefore, further investigations are needed to understand the toxicity of the drugs at a high local

concentration in the pericardium and the effects of the contents in the pericardial fluid on drug release. The formulation has to be well-designed to minimise the risk in intrapericardial delivery.

At a micro-level, myocardial drug distribution is reported to be the outcome of the interactions between diffusive spread, transmural convection, capillary transport, and clearance of the drug [159–163]. Diffusive force is driven by the concentration gradient and augmented by the ventricular contraction and relaxation, which decreases with the distance from the source and thus the thickness of the heart tissue. Furthermore, the concentration gradient also exists between the site of administration and the distant site longitudinally [161]. In contrast, the convective force is in a counter direction to the diffusive force, which might limit the penetration of drugs. Similarly, the thickness of the heart also impacts the convection, as the hydraulic resistance in tissues builds up with the thickness. However, the convective force is usually surpassed by the diffusion force, as reflected by the fast penetration of the drug into the tissue [159]. Meanwhile, capillaries have roles to play in clearance and local pharmacokinetics at deeper tissue or sites distant from point of administration. In epicardial application, drug deposition mostly resides in the epicardium and mid-myocardium. Maslov *et al.* demonstrated that the depth of penetration was about 400 μm beneath the epicardial surface with elevated ephedrine levels detected, up to 6 mm in maximum from the alginate disc. The drug also spreads 4 cm longitudinally toward the apex and 3 cm circumstantially and unidirectionally toward the left [159].

The minimal drug deposition in the endocardium, which is the most distant from the point of administration, indicated that the transmural penetration is driven by diffusion to a large degree. However, asymmetrical distribution in the heart especially in the longitudinal and lateral directions, as well as minimal accumulation into the septum were observed in localised delivery, which illustrated that the myocardial distribution is complex and is unlikely solely due to diffusion. Maslov *et al.* identified that the drugs accumulated in the capillaries were rapidly transported to the myocardium. However, the clearance was also partly via the capillaries, and thus a substantive level was detected in coronary sinus blood. The process is driven by the coronary blood flow and hence is plausible. Therefore, it was proposed that bulk

transport in capillaries facilitates drug movement toward distal myocardial segments and around the circumference of the heart, as well as toward the lateral, apex, and inferior walls [159].

For pericardial administered nanoparticles, Segura-Ibarra *et al.* demonstrated that Cy7-PLGA nanoparticles with a diameter of 190 nm were predominately distributed superficially and unevenly on the epicardium, with a half-life of about 2.5 days. However, the payload could penetrate inside the myocardium readily, with a longer half-life of ~7.5 days. The distribution of payload was influenced by the anatomy and physiology of the heart. The study demonstrated that the payload encapsulated by nanoparticles administered intrapericardially exhibited enhanced myocardial distribution and longer retention time [84].

1.7.2. Metabolism and Excretion

Pericardial fluid is cleared slowly via the lymphatic and epicardial capillaries [164]. Although the mechanism is not well understood, pericardial drugs in the fluid are therefore likely to be cleared through lymphatic and epicardial capillary drainage via passive diffusion. Due to the presence of enzymes in the pericardial fluids, drug molecules can be modified before excretion through the lymphatics. However, the profile of enzymes expressed on the pericardial mesothelial cells and secreted in the pericardial fluid is not well understood, with some of the enzymes present in the pericardial fluid discussed in **Section 1.5.2**. However, these enzymes might relate to a particular disease state and their roles in metabolism are unknown. It is worth noting that the presence of ACE in the pericardial fluid is known to metabolise the peptide Ac-SDKP and shorten the half-life and residence time in pericardial fluid. Therefore, the clearance of the drugs is dependent on the physicochemical properties of the drugs, including enzyme stability, molecular size, hydrophilicity, and solubility in the fluid [88]. Large molecules including proteins, are not readily cleared owing to the slow passive diffusion into lymphatics and thus have a longer half-life and residence time. For example, pericardial administration of atrial natriuretic peptide offered a fivefold longer residence time compared to intravenous administration [165]. Nonetheless, as discussed above, drugs that entered the epicardium and myocardium are likely transported as well as cleared via the

capillary, draining into the coronary sinus blood. Therefore, the drug concentration in coronary sinus blood was elevated [159]. As capillary transport and clearance are dynamic processes as the blood flow through the heart, the extent of drugs cleared from the heart through capillary transport is not clear. The uncertain clearance of drugs could limit the use of the approach in a clinical setting. Thus, further studies on drug clearance, especially on macromolecules, in the pericardium are crucial for the future developments of intrapericardial delivery.

The clearance of small molecules in the pericardial fluid is dependent on the physicochemical properties of the molecules. Small water-insoluble drugs, such as 5-fluorouracil, are reported to have a prolonged pericardial residence time and half-life. 5-fluorouracil is sparingly soluble which exhibited a ten-fold longer half-life in the pericardial fluid than in plasma (168 vs 16 minutes) in the case of a breast cancer patient with pericardial involvement [106]. On the contrary, small hydrophilic drugs have either similar or shorter residence time and half-life than in plasma. For instance, the half-life for intrapericardial metoprolol (Log K_{ow} 1.88) was 14.4 minutes, slightly longer than the half-life of the intravenous counterpart of 11.1 minutes [156], while procainamide (Log K_{ow} 0.88) had a five- to eight-fold shorter pericardial clearance than plasma. Similarly, the pericardial half-life of procainamide was 30 - 41 minutes, much shorter than that in plasma (180 minutes). The short half-life of intrapericardial procainamide was likely due to the rapid diffusion of procainamide out of pericardial space or rapid diffusion of procainamide from the plasma into the pericardial space [85,166].

1.8. Dosage forms used for intrapericardial delivery in MI

A variety of drugs have been delivered into the pericardial space to promote cardiac regeneration, as shown in **Table 1-6**. For instance, Uchida *et al.* delivered heparin sulphate and fibroblast growth factors (FGF) into the pericardium via a catheter placed transatrially [133]. This study demonstrated angiogenesis from the epicardium towards the subepicardial infarcted area as well as myocardial salvage in a canine model of myocardial infarction. In another study, intrapericardial delivery of FGF-2 was found to promote myocardial angiogenesis and improve myocardial perfusion and function in the ischaemic area without significant side effects [125].

Polizzotti *et al.* have investigated intrapericardial periostin-loaded Gelfoam implants [5]. Periostin is a secreted extracellular matrix protein that has been shown to stimulate cardiomyocyte proliferation and angiogenesis post-MI [4]. Gelfoam (Pfizer, New York, NY, USA) is made of gelatine purified from porcine skin, which is non-toxic, non-immunogenic, and biodegradable. It triggers the non-fibrotic fibrosis *in vivo* and forms a fibrin-loaded hydrogel. Gelfoam loaded with a recombinant peptide of periostin stimulated cardiomyocyte mitosis and enhanced angiogenesis in a pig model of myocardial infarction compared to direct injection of recombinant periostin peptide alone [5]. Ladage *et al.* also developed an injectable slurry of Gelfoam loaded with periostin peptide for the treatment of myocardial infarction [6]. However, periostin peptide treatment was associated with myocardial fibrosis at one week and 12 weeks post-treatment, which is likely to limit the clinical application.

In addition to drug therapies, intrapericardial cell delivery has also been studied to promote cardiac regeneration. Cells have been delivered in either a suspension, such as Hypothermosol which is a hypothermic preservation media for the preservation of cells and tissues [167], or in biodegradable polymer scaffolds. Blázquez *et al.* reported an intrapericardial injection of porcine cardiosphere-derived cells (CDC) into a porcine infarct model to modulate the microenvironment for promoting cardiac repair [167]. Changes in immunological parameters were observed, which modulated the inflammatory environment of the infarcted heart and thus promoted cardiac repair indirectly. However, no direct improvement in cardiac function was observed in pigs upon receiving intrapericardial CDC compared to the control group. Nonetheless, Branco *et al.* demonstrated that Bone Marrow Mononuclear Cells (BMMC) delivered via an intrapericardial infusion were able to diffuse into and penetrate the myocardium, with the BMMC concentration higher in the infarcted region. This finding suggests that interactions with local factors in the infarcted area may promote cell migration and/ or cell survival of BMMC [104].

Table 1-6. Summary of the intrapericardial drug delivery system used to modulate the infarcted heart or induce cardiac regeneration post-myocardial infarction. The details of the API, carrier of the formulation, species and outcome of the animal studies were detailed in the table.

Drug or cell (dosage form)	Solvent/ carrier	Species	Outcome
Transatrial access			
CDC (injection)	Hypothermosol	Pig	- Altered the phenotypes of resident lymphocytes and TH1 cytokines in pericardial fluid, modulating the inflammatory environment of the infarcted heart [167]
Heparin sulphate and bFGF (injection)	Normal saline	Dog	- Reduced percentage weight of the infarct ventricle and increased vascular number, predominantly in the subepicardial area - Neo-angiogenesis from epicardium toward subepicardial infarcted area [133]
Heparin and FGF-2 (injection)		Pig	- Increased myocardial vascularity, left-to-left angiographic collaterals, and left circumflex blood flow post intrapericardial delivery of FGF-2 [125]
Subxiphoid access			
BMMC	Saline	Pig	- Diffused penetrations of BMMC in the myocardium [104]
Thoracotomy			
Docosahexaenoic acid (DHA)	Normal saline with ethanol	Pig	- Reduced infarct sizes in infarct model - Reduced ventricular fibrillation score during ischemia and related mortality rate [168]
eGFP vector and MSC (injectable)	Gelform particles	Pig	- The presence of MSC and expressed eGFP in the myocardium [7]
IGF-1	Saline	Sheep	- Increased ejection fraction post-heart failure [169]
Nitro-glycerine (instillation)	ASD	Rat	- Vasodilation and improved cardiac function - Prevented serum myoglobulin level elevation, and decreased ST-elevation post-MI [170]
Periostin (implants)	Gelform patches	Pig	- Improved survival, cardiac function and left ventricular wall thickness in infarct zone post-MI - This led to substantial fibrosis in the heart [6]

Gelform discs	Mice	-	Increased cardiomyocyte cell cycle activity and angiogenesis infarct border zone [5]

1.9. Nanogels

As discussed above, the common formulations employed in pericardial delivery are drug solutions, implants, patches, particles, and hydrogels [5,7,107,115,171]. Implants, patches, hydrogel spray and microparticles require thoracotomy for administration, as they require a larger opening and direct access into the pericardium. Therefore, only drug solutions, nanosized particles and hydrogels could be delivered via the needles or catheter systems in subxiphoid and transatrial access, which are the preferred methods. For hydrogels, it is a general requirement that *in situ* gelation takes place inside the pericardium after the injection as crosslinked hydrogels are difficult to pass through the lumen, especially with the narrow-gauged needles or catheters [107]. However, *in situ* crosslinked hydrogel might be of a challenge as it requires a loop catheter, which creates a contained space via vacuum for the *in-situ* crosslinking. Moreover, its rheological properties have to be optimised such that it will not affect the heart contractions and induce pericardial adhesion. For solutions, the quantity of the drugs delivered is restricted by the solubility of the drugs and the volume of the solution. Thus, not every drug could be practically delivered in solution forms, restricting the choice of drugs applied in pericardial delivery. To prevent a huge disruption of the pericardial fluid homeostasis, intrapericardial pressure and volume, a pump and drainage system could be used. However, this method required intrathoracic tubing and a stoma on the thoracic cavity, which associates with infection risks and complications. Therefore, the use of nanogels in intrapericardial delivery is proposed to overcome these limitations and promotes intracellular uptakes.

1.9.1. Overview of nanogels

Nanogels, also known as hydrogel nanoparticles, are nanosized particles comprised of a network of hydrophilic polymers (hydrogel). They are mostly spherical but could sometimes be irregular in shape. They also have a three-dimensional hydrophilic structure containing voids that allow encapsulation of active pharmaceutical ingredients, ranging from small molecule drugs to macromolecules such as peptides, proteins, and genes. They are formed by crosslinking hydrophilic natural and/or synthetic polymers either physically or chemically and possess strong

water-holding ability without self-dissolution or self-disintegration. Key properties of nanogels, including size, surface potential, polydispersity, porosity, mechanical robustness, and degradability can be optimized by the chemical composition and fabrication process, resulting in versatile architectures ranging from simple homogenous particles, as shown in **Figure 1-10**, to co-axial multi-laminar particles (e.g., core-shell particles).

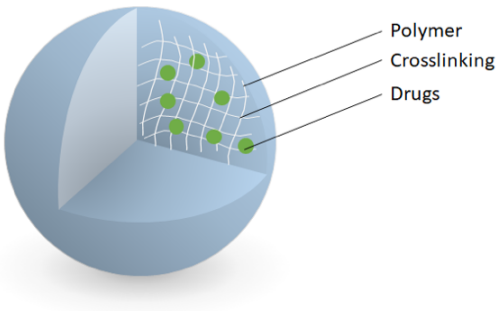

Figure 1-10. A schematic diagram showing the structure of a homogenous nanogel. The polymer chains were crosslinked to form a nanosized 3D matrix, of which the drugs were encapsulated. (Created with Microsoft PowerPoint)

Nanogels possess similar advantages as other polymer drug delivery systems, including protecting the drug cargo from metabolism. Therefore, this approach is useful for protecting fragile therapeutics, such as proteins, enzymes, and genes, as well as prolonging the circulation half-lives of the APIs. Besides, nanogels could also be deployed to encapsulate the toxic APIs, protecting the body from the drugs, maximizing the therapeutic window, and minimizing the side effects. Moreover, like other polymeric carriers, the properties of the nanogels, including size, surface potential, polydispersity, porosity, hardness, and degradability could be optimized with the polymer, the chemical composition of the formulations as well as the fabrication processes. In common with other nanocarriers, targeted delivery could be achieved passively via enhanced permeation and retention effects (EPR) or actively via the ligands conjugated on the polymer. Thus, cellular uptake and intracellular trafficking of the nanogels are feasible [172].

As discussed above, intrapericardial delivery is undoubtedly invasive. The use of minimally invasive techniques, such as the use of needles and catheters, could

mitigate the invasive drawback but could also restrict the dosage form available for the route. Therefore, only solutions, suspensions, emulsions, and injectable hydrogels could be administered through the narrow lumen of needles and catheters. Nanogel formulation is a suspension of nanoparticles in an aqueous vehicle, which has similar injectability as the solvent. Thus, the use of nanogels offers multiple advantages, which make them ideal for intrapericardial delivery - desirable injectability of a solution, protection of the payload from the degradation of other polymeric delivery systems and the ability of nanoparticles for target delivery and intracellular uptake. Noteworthy, nanogels remain in the early stage of development, with no nanogels formulations applied in the clinical setting.

1.9.2. Nanogels fabricated with chitosan and its derivatives

One of the commonly used polymers for nanogel fabrication is chitosan. It is a linear polycationic polysaccharide derived from chitin, which is found in the cell wall of fungi, exoskeletons of arthropods, and shells in crustaceans [173–175]. Chitosan is a co-polymer of randomly distributed D-glucosamine and N-acetylglucosamine via β (1-4)-glycosidic bonds as shown in **Figure 1-11**. It is produced from partial deacetylation of chitin - poly-(N-acetylglucosamine), via an alkaline treatment. Chitosan is economic, biodegradable, biocompatible, non-toxic and mucoadhesive [176]. Besides, owing to the polycationic nature, a variety of chitosan is available with differing polymer sizes (molecular weight and repeating units), degree of deacetylation and possibility of modification, allowing the materials to be optimised according to the need for biological applications [177]. Other chitosan derivatives, such as glycol chitosan, carboxymethyl chitosan and chitosan oligosaccharide, are also used for nanogel fabrication. Functionalisation of chitosan, such as conjugation at the amine, free radical formation at hydroxyl group, and ring-opening oxidation, changes the physicochemical properties of chitosan and thus can form nanogels using a different mechanism. Properties of functionalised chitosan depend on the group conjugated at the amine. Hydrophobic groups, including mercaptohexadecanoic acid [178], benzoic acids [179], caffeic acids [179], cinnamic acid [179] and deoxycholic acid [180], were grafted on the chitosan, which made the polymer more hydrophobic and less hydrophilic.

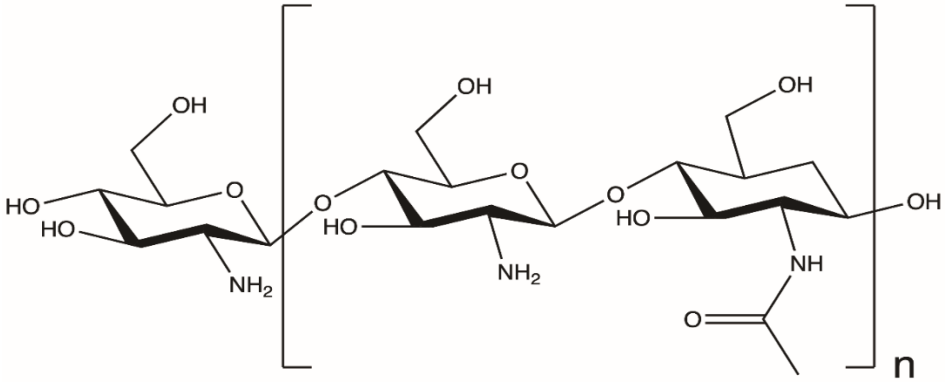

Figure 1-11. Structure of chitosan. It is a copolymer of randomly distributed D-glucosamine and N-acetylglucosamine via β (1-4)-glycosidic bonds. (Created with ChemDraw 20.1)

1.9.3. Chitosan-derived nanogel fabrication methods

1.9.3.1. Mixing

Mixing, in generalisation, is a process of mass transport and brings different solutes into contact. The use of mixing in nanogel fabrication brings the polymer and crosslinkers in the solution to contact with each other, which increases the contact surface between two chemical entities and increases the probability of colliding with each other for interactions. Therefore, the mixing process helps to spread the solutes, form a homogenous solution as well as drive the interactions between solutes, in terms of reaction rate. Mixing is the most extensively used method in producing chitosan nanogels. The simplest and most convenient method employed for mixing is stirring, where the chitosan or its derivatives solution is stirred with the crosslinkers solution. A more advanced and controllable technique, microfluidics, can be used in nanogel fabrication. Microfluidics is a manipulation of fluids in a geometrically confined space with a sub-millimetre scale where the capillary penetration governs the mass transport. Microfluidics provides precise control and a large surface-to-volume ratio, which allows effective mass transfer, improving the mixing efficiency in contrast to stirring. Besides, it is a continuous manufacturing process, which could minimise the batch-to-batch variation and can be scaled up easily.

1.9.3.2. Microemulsion and nanoemulsion templating

Micro-/nanoemulsion templating is an advanced method for fabricating nanogels. Micro-/nanoemulsion is a thermodynamically stable colloidal system containing micron/ nano-sized droplets. This technique utilises the architecture of the droplets as a template for nanogel fabrications, which requires two immiscible fluids and surfactants to form emulsion droplets, followed by the addition of crosslinkers. The advantage of using micro-/nanoemulsion templating is that the fabrication is routine and simple, but the process is inefficient, which requires massive quantities of surfactants and solvents for fabrication, as well as an extra step to remove the surfactants. The templating method used to produce chitosan nanogels is a water-in-oil approach. Water-in-oil (W/O) micro-/nanoemulsion is micro/nano-sized aqueous droplets suspended in an oil phase. The droplets are usually used as micro-/nanoreactors for crosslinking polymer in a confined space, a mild and controlled condition. For example, chitosan and derivatives contained microemulsion and crosslinkers microemulsion was prepared by dissolving chitosan (and its derivatives) and crosslinkers e.g., genipin [181,182], tartaric acid, and poly(ethylene glycol) dicarboxylic acid (via EDC and NHS coupling) respectively in n-hexanol and cyclohexane [183]. Surfactant Triton X-100 was added dropwise into the microemulsion and thus the microemulsions were mixed under stirring. Nanogels were precipitated by ethanol and separated by centrifugation.

1.9.3.3. Radical polymerisation

Radical polymerisation is mostly used for co-polymer nanogels comprised of polyacrylic acid, polyacrylamide, and derivatives. Free radical polymerization is started by an initiator, which is a strong oxidizing agent, plasma, or radiation. The first step involves the transfer of radicals to the monomer, generating free radical monomers. The polymer is formed by the addition of the non-radical monomers (alone or comonomers) to the free radical monomers or chains. Monomers must contain an electron-rich allyl group for radical polymerisation. Highly controlled methods for radical polymerization are available [184]. However, as chitosan does not naturally contain any vinyl group for free-radical polymerization, it has to be activated to form free radicals or functionalised with a vinyl group, before free radical copolymerisation. Therefore, copolymerisation with acrylic acid is a more

common approach. Duan *et al.* reported self-assembly nanogels composed of a copolymer of chitosan and poly(N-isopropylacrylamide) (PNIPAm) for delivery of oridonin [185]. Chitosan formed a free radical by reacting with a free radical initiator ammonium persulfate. N-isopropylacrylamide, the building unit for PNIPAm, and the crosslinker - N, N-methylene bisacrylamide were then added and copolymerised with the chitosan free radicals. The copolymer was eventually sonicated to form nanogels.

1.9.3.4. Self-assembly

Self-assembly of nanogels is an approach where the polymers are self-interacting with each other to form a network and condense into nanosized particles. The majority of the self-assembly nanogels require the polymers to be amphiphilic. Most chitosan-based self-assembly nanogels require functionalisation of chitosan or its derivatives which have both cationic and anionic moieties such as O-carboxymethyl chitosan. Amide linkages between the amine group of chitosan and the carboxylic acid group from organic acids also introduced the hydrophobic moiety on the polymer, such as mercaptohexadecanoic acid [178], EDTA [186], benzoic acid [179], caffeic acids [179], cinnamic acid [179], and deoxycholic acid [180]. When the functionalised chitosan is dropped into the polar medium, such as under aqueous conditions, the hydrophobic groups on chitosan tend to interact with themselves, to minimize the exposure to polar solvent. As for chitosan with both cationic and anionic moieties, these moieties will interact with each other and form a polymer network, and the interactions between these moieties are pH dependent. Thus, the polymer network condenses into a nano-sized particle and encapsulates the drugs present in the solution.

1.9.4. Crosslinking in nanogels fabricated with chitosan and its derivatives

Crosslinking can be subdivided into physical and chemical crosslinking, where chemical crosslinks involve covalent bonds. Meanwhile, physical crosslinks are formed by non-covalent interactions, such as electrostatic interactions (including hydrogen bonds) and hydrophobic interactions.

1.9.4.1. Physical crosslinking

Ionic gelation is the most extensively used method in producing nanogels, with charged polyelectrolyte polymers crosslinked by oppositely charged ions. Ionotropic gelation refers to the polyelectrolyte complexation, in which a polycation interacts with polyanions to form nanogels and vice versa [187]. Chitosan is a good example of illustrating ionic and ionotropic gelation. Chitosan is usually crosslinked via ionic gelation with sodium triphosphate pentabasic (TPP) and glycerol β-phosphate, between the positively charged amine group and the negatively charged phosphate group. Furthermore, it can also form nanogels with polyanions, including alginate and hyaluronic acid. The electrostatic interactions between polymer and crosslinkers are strong. However, there is a fine balance in crosslinking, where precipitation will occur if the interaction is too strong. Conversely, the 3D conformational structure could not be maintained in dissolution if the interaction is too weak [188]. Although hydrogen bonding is a type of weaker electrostatic interaction, hydrogen bonds have a significant role in crosslinking especially in temperature-responsive nanogel, but not in chitosan-based nanogels. For example, *Chen et al.* developed thermal responsive nanogels made of poly(2-ureido-4[^{1}*H]pyrimidinone* (UPy) functionalised polyethylene glycol methacrylate-co-*N*-isopropyl acrylamide) [189], of which the nanogels were crosslinked by the multiple hydrogen bond (MHB) arrays between the 2-ureido-4[^{1}*H]pyrimidinone* groups grafted on the polymers. Furthermore, Ding *et al.* established DNA-*g*-polycaprolactone nanogels for siRNA delivery, where the siRNA was used to crosslink the DNA brush grafted on the polycaprolactone, via the MHB arrays between the complementary sequence on the DNA brushes and siRNA [190].

Furthermore, polymer chains can be crossly linked by hydrophobic interactions. As nanogels are hydrophilic, crosslinking via hydrophobic interactions could only happen when the polymer is amphiphilic, i.e., a hydrophobic group was grafted onto the polymer, or the polymer is a copolymer having both hydrophilic and hydrophobic moieties. Thus, the polymer would be self-assembled into nanogels under aqueous conditions by the electrostatic or hydrogen bonds between hydrophilic moieties, as well as the hydrophobic interactions between the hydrophobic moieties and weak Van der Waal's forces between the polymers. Duan

et al. also reported self-assembly nanogels composed of a copolymer of chitosan and PNIPAm for delivery of oridonin. Therefore, this type of crosslinking is mostly used in the self-assembly of nanogels [185].

1.9.4.2. Chemical crosslinking

Chemical crosslinking involves covalent bonding between polymers. For example, chitosan can be crosslinked by glutaraldehyde and genipin (GP) as shown in **Figure 1-12**. Genipin is a natural crosslinker, extracted from gardenia fruits, that may crosslink various polymers including proteins, collagen, gelatine, and chitosan [181]. However, the crosslinking mechanism of genipin is pH-dependent, with genipin undergoing ring-opening polymerisation before crosslinking to chitosan under basic conditions. Genipin reacts with the amine group on chitosan to form heterocyclic amines, and subsequently associates to form crosslink networks. Therefore, the crosslinked bridge is shorter in acidic conditions (usually a dimer, trimer, or tetramer) than in basic conditions with 7-88 monomer units [191]. Pujana *et al.* reported that a chitosan nanogel was successfully prepared via reverse microemulsion and genipin crosslinking [181], with a mono-distribution of particle sizes. Glutaraldehyde, a dialdehyde, is a cold-sterilant that are commonly used in hospitals. It is capable of crosslinking proteins or amine-containing polymers. Crosslinking is formed between the amine group on chitosan and the dialdehyde group on glutaraldehyde. It was the most used crosslinker for covalent bond formations, but its use is associated with toxicity, and it is an irritant to the eyes, mucous layers, and skin. Other chemical crosslinkers are also bi-functional, including diisocyanate, diepoxy [43], dialdehyde [192], and dicarboxylic acid [183] were used to covalently crosslink chitosan.

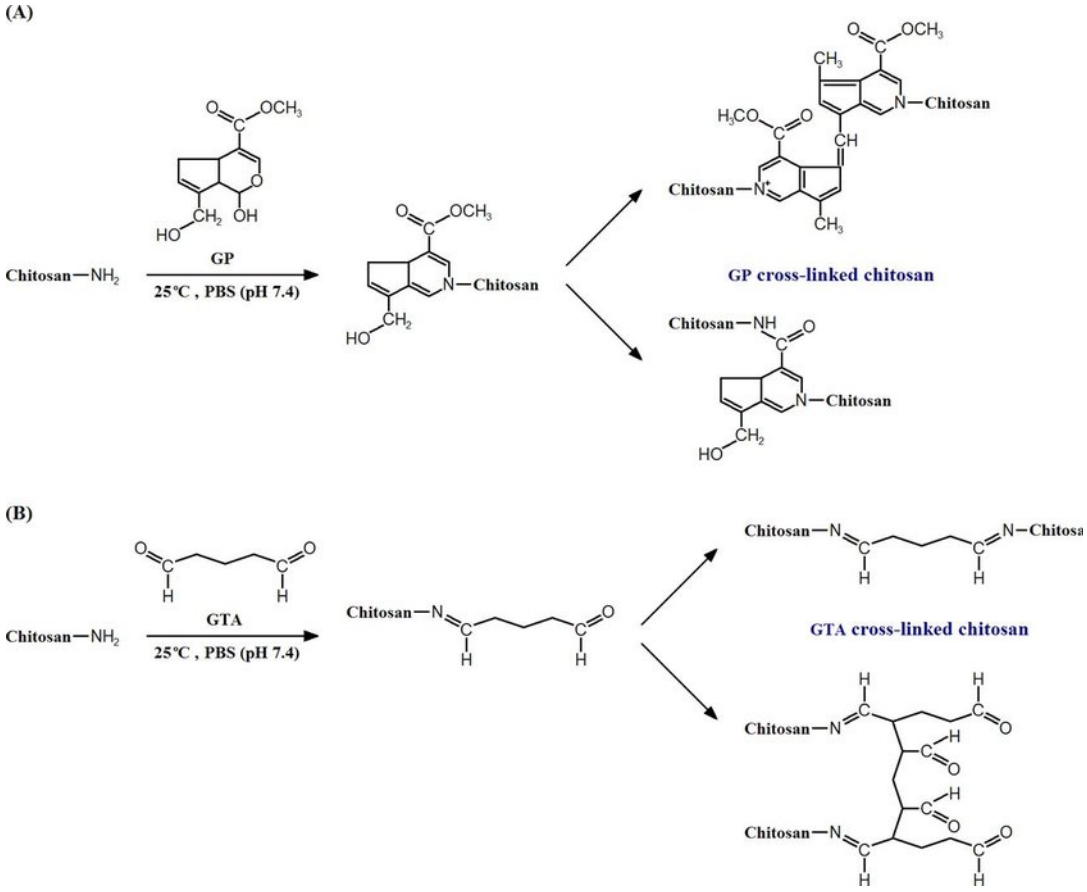

Figure 1-12. Cross-linking scheme of chitosan with (A) genipin and (B) glutaraldehyde [193].

1.9.5. Chitosan-TPP nanogels

Chitosan-TPP nanogels were used as the drug carrier system for this project, which is formed by crosslinking chitosan with TPP. Chitosan offers several advantages for nanogels fabrication as it is economic, biocompatible, biodegradable, and non-toxic, and with a variety of possible chemical modifications and intrinsic properties such as polymer size and degree of acetylation, where the formulation could be optimised [193]. Moreover, chitosan is a polycation, which could be used to complex with genes or other anionic peptides or proteins. The use of cationic polymer can also facilitate the intracellular uptakes of the nano-carrier [194,195]. On the other hand, TPP is non-cytotoxic, which is a better choice than the toxic counterpart glutaraldehyde. Any residual glutaraldehyde could also possess issues *in vivo*, as it could crosslink with other amine-containing proteins, cells, and tissues, leading to damage. The use of non-toxic and biodegradable materials could minimise an

immune response against the carrier and allow the removal of empty nanocarrier from the body.

In terms of the fabrication process, they can be fabricated with stirring [196] or microfluidics [197]. This method allows even distribution of crosslinkers in the solution and prevents instantaneous gelation. They are also relatively simple compared to other fabrication methods, especially via chemical crosslinking using glutaraldehyde, and radical polymerisation in the production of PNIPAm nanogels. Moreover, chitosan-TPP nanogels are generally safe and have been researched extensively in the literature for various applications [198–206]. They are also capable to deliver a wide range of payloads. For example, small molecule drugs, photosensitizers, proteins, and genes were successfully delivered to cells and animals with the use of chitosan-TPP nanogels as a carrier [197,202,203,205–208]. Furthermore, crosslinking chitosan and TPP provides mechanical strength, compatibility, and durability to the nanogels. These nanogels could be modified by coating and surface modifications, offering a versatile architecture for different applications. For example, alginate and polysorbate 80 were used in coating the chitosan-TPP nanogels for transmucosal delivery [209] and brain delivery [201] respectively. Thus, the chitosan-TPP nanogels could be easily modified to tailor for the delivery purpose.

1.10. Aim of the thesis

Throughout the above literature review, it is clear that there are significant unmet clinical needs in the treatment of myocardial infarction to achieve the repair and regeneration of damaged cardiomyocytes. Although various active agents such as peptides, proteins, genes, and cells have been explored elsewhere there is a need to establish effective localised delivery to the heart. Intrapericardial delivery is a novel delivery route that offers numerous advantages over other delivery routes. Owing to the invasiveness of the access routes, minimally invasive techniques using needles and catheters are preferable, but this introduces limitations onto the choice of formulations, where the formulations need to be compatible with these devices. Nanogels are potentially an ideal formulation for minimally invasive pericardial

delivery as they could be injected via the small bore of needles and catheters, promote intracellular uptakes, and offer protection to the payloads from degradation.

To address this hypothesis, the overarching aim of the project was to develop a novel nanogel suitable for the delivery of drugs into the pericardium via minimally invasive techniques for the treatment of myocardial infarction. The intention was to develop new insight into the fabrication process and drug encapsulation in nanogels, where the properties of nanogels could be tuned and predicted, and potentially utilise these nanogels for drug delivery into the pericardium. The initial aim of the project was to establish the set-up, fabrication process, and characterisation methods for the chitosan-TPP nanogels. The subsequent aim was to identify parameters influencing the properties of nanogels, optimise the nanogels formulation and fabrication condition, and develop insights into drug encapsulation in the nanogels. After obtaining an optimised nanogels formulation, the aim shifted to evaluate the cytotoxicity of the nanogels and to utilise the epicardial cells as an *in vitro* testing platform for intrapericardial delivery. During the *in vitro* cell studies with epicardial cells and other cells, the model drug - propranolol was found to be cytotoxic and thus peptide Ac-SDKP was used as the new payload. Thus, the aim progressed to develop a novel HPLC method suitable for formulation development purposes to assay the peptide. The final aim of the project was to develop a novel nanogel formulation for the delivery of an anti-fibrotic peptide to the pericardium that is intended to attenuate cardiac fibrosis and inflammation post-myocardial infarction.

1.11. Key Objectives

- To optimise the fabrication process and formulation for the chitosan-TPP nanogels using propranolol as a model drug.
- To evaluate the possibility of applying the Design of Experiments (DOE) models in other drugs and investigate the drug encapsulation mechanism in the nanogels.
- To evaluate the cytotoxicity of the nanogels via cell studies and explore the potential of using epicardial cells as an *in vitro* testing platform for intrapericardial delivery.

- To develop a novel HPLC method that is suitable for pharmaceutical assessment for the anti-fibrotic peptide Ac-SDKP via an analytical quality by design (AQbD) approach.
- To develop a novel guanidylated chitosan-TPP nanogels for delivering the anti-fibrotic peptide Ac-SDKP.

1.12. Thesis overview

The thesis is structured into the following chapters.

Chapter 2 – Fabrication of propranolol-loaded chitosan-TPP nanogels via stirring and characterisations of raw materials and nanogels

Four propranolol-loaded chitosan-TPP nanogels formulations were prepared by stirring. This chapter aims to determine whether the fabrication setup, fabrication method, assay methods, and lyophilisation were suitable for this project. Moreover, the nanogels were characterised using a variety of analytical techniques to determine the properties and performance of the nanogels formulation. Solid state characterisation techniques were tested on the raw materials and freeze-dried nanogels to understand the properties of these materials.

Chapter 3 – Modelling the effects of formulation, processing factors and drug loading on the structure and properties of nanogels

This chapter focuses on developing a tuneable nanogel system with predictable properties using a DOE approach. The effects of the formulation, drug loading, and the processing factors in fabrications on the nanogels properties were determined. Optimal formulation and fabrication conditions were identified. The mechanism of drug loading in the nanogels and the predictability of the DOE models on other drugs were explored.

Chapter 4 – Determining the cytotoxicity of the propranolol-loaded nanogels using *in vitro* cell cultures

This chapter focused on the delivery of the propranolol-loaded nanogels *in vitro*. The cytotoxicity of the propranolol and propranolol-loaded nanogels was established in the epicardial cells, cardiomyoblasts and fibroblasts.

Chapter 5 – Developing an HPLC-UV method for quantification of the antifibrotic peptide N-acetyl-seryl-aspartyl-lysyl-proline

Despite the antifibrotic tetrapeptide N-acetyl-seryl-aspartyl-lysyl-proline (Ac-SDKP) having multiple potential clinical applications, a simple quantification method for the peptide, which was compatible with the phosphate buffer as the matrix, was lacking. Current quantification methods involve extensive sample preparations and are not compatible with the samples in phosphate buffer saline, where *in vitro* drug release test is performed in. This chapter focuses on developing and validating a novel and simple HPLC-UV method for the quantification of Ac-SDKP.

Chapter 6 – Developing guanidylated chitosan-TPP nanogels as a novel drug carrier for intrapericardial peptide delivery

This chapter focuses on developing a new nanogel system with guanidine grafted chitosan to increase the solubility at physiological pH and minimise the degradation of peptides due to pH during fabrication. Formulations in **Chapters 2** and **Chapter 3** were also found to precipitate in the *in-vitro* drug release study, which raised questions about how stable the nanogels are in the pericardial fluid and how to prevent the agglomeration of nanogels. To address this, functionalised chitosan is formed by replacing the amine group on chitosan with a physiologically cationic group, which in theory creates stronger interactions with the crosslinker and improves the stability of the nanogels. Several properties and performances of the nanogels formulation were measured to compare with the nanogel formulation fabricated with the unfunctionalised chitosan. Based on the correlation established in **Chapter 3**, where size correlated with LogP of the payload, a structurally similar molecule, lisinopril, was used as the model drug to establish the optimal experimental condition. Ac-SDKP were then used for the nanogel fabrication and the nanogels were tested as a treatment to attenuate cardiac fibrosis post-MI.

Chapter 7 – Conclusion and Future Works

This chapter provides a summary of the main conclusions that can be drawn from the experiments performed during this project and highlights areas of the research that require further investigation.

Chapter 2

Fabrication of Propranolol-loaded Chitosan-TPP Nanogels via Stirring and Characterisations of Raw Materials and Nanogels

2. Fabrication of propranolol-loaded chitosan-TPP nanogels via stirring and characterisations of raw materials and nanogels

2.1. Introduction

Chitosan and sodium triphosphate pentabasic (TPP) nanogels are the most extensively explored systems, as it only requires mild fabrication conditions to form nanogels via ionic gelation as described in **Section 1.9.4.1**. Both chitosan and TPP were non-toxic materials, where chitosan is a linear polycationic polysaccharide derived from chitin found in the cell wall of fungi, exoskeletons of arthropods, and shells in crustaceans [173–175]. As it is a biodegradable and biocompatible, non-toxic, and mucoadhesive material [176], it is suitable for drug delivery. TPP is also non-toxic and the interaction with the chitosan is spontaneous. Owing to these advantageous properties of easy fabrication and biocompatibility, chitosan-TPP nanogels were used as the starting point of the project, as the first formulation to be investigated.

Nanogels were fabricated using magnetic stirring in this project, where the efficient mixing or stirring of the chitosan and TPP solutions was achieved by the flow motion generated by the rotating magnetic stirrer, as shown in **Figure 2-1**. The TPP solution, which is miscible with the chitosan solution, is added dropwise into the chitosan solution under stirring, and thus the two solutions are mixed continuously. Stirring was chosen as the manufacturing technique as the technique is less labour intensive. Moreover, a few processing factors could be optimised, such as stirring speed and temperature. On the other hand, only small volumes of nanogels could be produced using a vortex while the stirring rate is also fixed, which makes the vortex a less attractive method for nanogels production. Despite the widespread use of magnetic stirring in nanogels production, the mechanism of the mixing was not well understood and explored in literature. Thus, the mechanism of mixing for nanogel fabrications is first explored with fluid mechanics in this chapter.

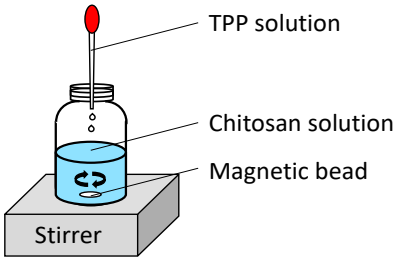

Figure 2-1. Illustration of the set-up of magnetic stirring used in the fabrication of the nanogels. TPP solution was added dropwise using a pipette into the chitosan solution under constant stirring. The TPP solution droplets were dispersed by the vortex generated from the rotating magnetic bead, which allowed chitosan and TPP dispersed in the solution. The mixing and crosslinking occurred spontaneously and formed the nucleus. Particles grew with more crosslinking. The diameter of the magnetic bead used should be smaller than the diameter of the container. (Created with Microsoft PowerPoint)

Nanogel fabrication is governed by two key components – the mixing and gelation process. To describe the mixing processing, the flow of solutions under magnetic stirring may be described by the Rankine Vortex model, which is a simple mathematical model of a potential vortex in a viscous fluid [210]. In brief, there are two different flow regions in the model - a rigid inner core vortex and a free (irrotational) vortex in the model, as shown in **Figure 2-2**. The radius R is the radius of the forced vortex and subsequently the radius of the solid body – the stirrer, while the radial distance r denotes the distance from the vortex core, with the maximum equivalent to the radius of the cylindrical container. V_θ is the tangential velocity of the flow. In the inner core, where the radial distance $r < R$, the rigid body rotation takes place, which means the motion resembles the solid-body motion (i.e., Rotation) in the core vortex. On the other side, the tangential velocity correlates with the radius r inversely in the free vortex. Moreover, a break appears at $r = R$ in the Rankine model [211]. The reason for using the Rankine model to describe the mixing process is that the stirring system of nanogels fulfilled the descriptions for the model. For instance, chitosan solution is viscous, although the viscosity is dependent on the molecular weight of the chitosan and the concentration used. Moreover, the vortex is generated by the rotation of a solid body (i.e., magnetic bead) and the solution is stirred in a cylinder larger than the radius of the rotating object. Noteworthy, the

model is simple and capable of accurately describing the geometry of the vortex in a 2D manner. However, the stirring of solutions happened in a 3D space in reality. Thus, the flow also exhibits a toroidal motion, where a downward jet is formed on the axis of the vortex and upward streams are at the outer walls [210]. The toroidal flow also helps mix the solutions in the vertical axis - z.

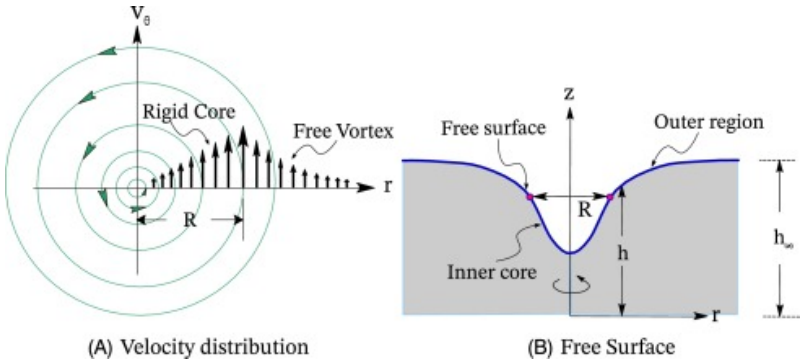

Figure 2-2. Illustration showing (a) the velocity distribution and (b) the free surface of the vortex in the Rankine model. (Adapted from [212])

The second important process is gelation, which is governed by the interaction between the chitosan and the crosslinkers. Several types of ionic gelation were discussed in **Section 1.9.4.1**. In this project, chitosan is a cationic polymer while the crosslinkers - TPP, carry the opposite charge. The two components interact via electrostatic interactions, and thus the gelation only happened when the two components were at a close distance. The gelation process of nanogels could simply be described by nucleation. When the TPP solution is added dropwise into the chitosan solution under stirring, the mixing happens simultaneously. On a molecular level, chitosan is spatially and molecularly dispersed in the solution before the addition of TPP. When TPP is added gradually, the concentration of TPP in the mixture slowly increases, while the concentration of chitosan reduces due to dilution. At diluted concentrations, the two components are still dispersed in space and thus the probability of the interaction is low. When more TPP solutions are added, the two components are closer in space as the TPP concentration is higher, leading to a higher probability for ionic interactions and forming a nucleus. Moreover, the gelation process is also controlled by the diffusion, as the chitosan and the crosslinker's movements are governed by the concentration gradient. Thus, the diffusivities of these components are also crucial in the process, which is dependent

on the temperature and the dynamic viscosity of the solution according to the Stoke-Einstein equation – **Equation 2-1**, with the assumption that they are spherical. When the distance between the two components is close enough, the gelation process will then be initiated. The nucleus is formed and the nanogels are grown from this nucleus [213]. Combining the Rankine model with the gelation process, it is known that the velocity decays with the distance from the edge of the rotating object in the free vortex. Therefore, the gelation is likely to take place in this region as chitosan and TPP could have sufficient time to diffuse and interact.

$$\boldsymbol{D = \frac{K_B T}{6\pi\eta r}} \qquad \textbf{Equation 2-1}$$

Where D is the diffusion coefficient, K_B is Boltzmann's constant, T is the temperature, η is the dynamic viscosity and r is the radius of the spherical particle.

After exploring the mechanism of mixing in stirring, the first part of this study was to fabricate several chitosan-TPP nanogels using the stirring method, to evaluate if the fabrication method, assay method for propranolol and the set-up were fit-for-purpose. Propranolol was used as the model drug and four formulations were designed. Their properties in the solution state were then characterised, namely hydrodynamic size (Size), polydispersity index (PDI), zeta-potential (ZP), encapsulation efficiency (EE), and viscosity. Moreover, it is also crucial to understand the properties of the raw materials that were used in nanogels production, minimizing the variations in the properties of nanogels due to changes in the raw materials. Therefore, some solid-state characterization techniques were performed, including thermal analysis, X-ray diffraction (XRD), and Fourier-transformed infrared spectroscopy (FTIR).

The properties of the lyophilised nanogels were also determined. Similar to other biopharmaceuticals, the formulation was commonly lyophilised to remove water for long-term storage, unless the formulation is freshly prepared before use. Lyophilisation of nanogels is practical, which also mitigates multiple disadvantages shared between nanogels solution, emulsions, and suspensions. The solution-based formulations are bulky to transfer and difficult to store. In addition, the use of aqueous vehicles also made them susceptible to microbial growth and contamination

as well as hydrolysis, leading to a shorter expiry date. Despite the repulsion between the cationic charge on the nanogel particles, they could still aggregate and precipitate in the solution under long-term storage. Therefore, the nanogels are freeze-dried and were also characterized by solid-state characterisation techniques to evaluate their stability and properties after freeze-drying. It is vital to understand if lyophilisation would alter the nanogels. Noteworthy, these characteristics did not resemble the stability and properties in the solution state. Therefore, the lyophilised nanogels were resuspended in water and the nanogel properties were recharacterized.

In short, the overarching aim of this chapter was to evaluate if the assay method, fabrication set-up and method were suitable for producing chitosan-TPP nanogels, using propranolol as a model drug. The second aim was to characterize the raw materials and the nanogels to understand their properties. Nanogels were also freeze-dried as it is a frequent practice for long-term storage. Therefore, the lyophilised nanogels were characterised using solid state techniques while the properties of the nanogels were determined after the resuspension of the lyophilised counterparts, to evaluate if the lyophilisation process alters the nanogel properties.

2.2. Materials and Method

2.2.1. Materials

Low molecular weight (LMW) and medium molecular weight (MMW) chitosan were purchased from Sigma Aldrich (St Louise, MO, USA) with a molecular weight of 50-190 and 190-310 kDa respectively according to the manufacturer. Sodium triphosphate pentabasic (TPP) was purchased from Fluka (Buchs, Switzerland) while propranolol hydrochloride (Propranolol), deuterium oxide, and deuterium chloride were acquired from Acros Organics (Geel, Belgium). Glacial acetic acid was obtained from Fisher Scientific (Waltham, MA, USA). Sodium hydroxide pellets were acquired from VWR (Radnor, PA, USA). All chemicals were at analytic grade and used as supplied. Deionised water was obtained from PURELAB® Chorus 2+ machine (ELGA LabWater, High Wycombe, UK). 0.22 μm syringe filters were purchased from Merck Millipore (Darmstadt, Germany).

2.2.2. Propranolol-loaded nanogels fabrication

Propranolol-loaded chitosan nanogels were prepared by the ionic crosslinking method, adapted from the method reported by Al-Kassas *et al.* [208]. Low and medium molecular weight chitosan was first dissolved in 1% acetic acid solution until it formed a clear solution, followed by adjustment of the pH to pH 4.5 with 0.1M sodium hydroxide solution. Chitosan solutions were filtered through a 0.22 µm syringe filter before use. Propranolol HCl was weighed and dissolved in the chitosan solution before the addition of the TPP solution. Meanwhile, various amounts of TPP were dissolved in deionised water to prepare different concentrations and the TPP solutions were also filtered with a 0.22 µm syringe filter. An equal amount of TPP solution was added to the chitosan solution under stirring at room temperature. The solution was then stirred at 600 rpm for 1 hour. Various chitosan concentrations (CS), chitosan-TPP ratio (CT) and chitosan-propranolol ratio (CP) were used, and nanogels were prepared using four formulations shown in **Table 2-1**. The prepared nanogels were then kept in a fridge at 4 ^{o}C for further characterisation. All nanogels were prepared and tested in triplicate.

Table 2-1. Formulations of propranolol-loaded chitosan nanogels using both LMW and MMW chitosan and their measured properties. Three formulations were fabricated with LMW chitosan - F1 was the optimal condition from **Chapter 3**, while the formulations F2 and F3 were predicted using the models to obtain sizes of 100 and 200 nm respectively and the lowest PDI. Thus, different CS and CT were used in the formulation. Only one formulation was fabricated with MMW chitosan – F4, as the properties of nanogels fabricated using the F2 and F3 formulations with MMW chitosan were different from those prepared with LMW chitosan. Thus, only one formulation for MMW chitosan was selected. Results were obtained from three independent experiments (n = 3) and represented as mean ± SD.

Sample	**Experiment conditions**			**Size (nm)**	**PDI**	**ZP (mV)**	**EE (%)**
	CS (%)	**CS/TPP ratio**	**CS/prop ratio**				
LMW chitosan							
F1	0.1	3	0.5	75.5 ± 2.2	0.210 ± 0.013	31.4 ± 1.3	66.0 ± 0.9
F2	0.15	3	0.5	97.0 ± 1.5	0.247 ± 0.009	34.3 ± 1.4	69.0 ± 6.5
F3	0.3	5	0.5	186.8 ± 2.0	0.461 ± 0.009	40.9 ± 1.4	66.1 ± 6.2
MMW chitosan							
F4	0.1	3	0.5	113.6 ± 5.8	0.215 ± 0.009	20.9 ± 7.2	58.9 ± 5.2

2.2.3. Characterisation techniques for raw materials and freeze-dried nanogels

2.2.3.1. Thermogravimetric analysis

The analysis was conducted on a Discovery TGA (TA Instruments, New Castle, DE, USA). Approximately 3 mg of sample was added in a tared aluminium pan (TA Instruments, New Castle, DE, USA). The samples were then heated from 40 ºC to 400 ºC at a temperature ramp of 10 ºC/min. Experiments were conducted at a nitrogen purge flow rate of 25 mL/min. Data were analysed using Trios software (TA Instruments, New Castle, DE, USA).

2.2.3.2. Differential scanning calorimetry

3 - 5 mg of sample was added to an aluminium pan, which was sealed with a non-hermetic lid (Tzero, TA instrument, New Castle, DE, USA). A hole was punctured in the lid to release the vaporized solvent and moisture during heating. The analysis was carried out using a Q2000 differential scanning calorimeter (TA Instruments, New Castle, DE, USA). The calorimeter was calibrated for temperature using an indium standard before the experiment. The sample was heated directly from 0 ºC to 200 ºC at a temperature ramp of 10 ºC/min and under a flow of 50 mL/min nitrogen gas. Data were recorded with the TA Advantage software package and analysed using TA Universal Analysis.

2.2.3.3. Fourier transform infrared spectroscopy (FTIR)

Analysis was performed with a Spectrum 100 FTIR spectrometer equipped with an attenuated total reflectance (ATR) sampling accessory (Perkin Elmer, Waltham, USA) in the range of 650 - 4000 cm^{-1} and with a resolution of 1 cm^{-1}.

2.2.3.4. Solid X-ray diffraction

XRD patterns were recorded using a Copper-source Miniflex 600 (Rigaku, Tokyo, Japan) over a range of 2θ from 3 - 40º. The voltage and current used were 40 kV and 15 mA. Data was collected at a g step of 0.02º and a scan rate of 5º/minute.

2.2.4. Characterisation techniques for raw materials only

2.2.4.1. Degree of deacetylation determination for chitosan using ^{1}H nuclear magnetic resonance spectroscopy

The degree of deacetylation (DA) was determined based on a method adapted from Lavertu *et al.* [214]. ^{1}H NMR spectrums were obtained using a 400 MHz NMR spectrometer (Bruker, Billerica, MA, USA), at the temperature of 60 ^{o}C. The relaxation time was set at 30 seconds. 10 mg of chitosan samples were dissolved in 2 mL of 2% deuterium chloride (DCl) in deuterium oxide (D_2O) and the solutions were then transferred into a 5 mm glass NMR tube. Results were analysed using TopSpin software (Bruker, Billerica, MA, USA), with the integrals of the peaks being automatically determined. The deacetylation degree was calculated using **Equation 2-2**. The experiment was repeated three times and the results were presented as mean ± SD.

$$\boldsymbol{DA}(\%) = \frac{\boldsymbol{H1D}}{(\boldsymbol{H1D}+\frac{\boldsymbol{HAc}}{\boldsymbol{3}})} \times \mathbf{100}\% \qquad \textbf{Equation 2-2}$$

where the integral for the peak of proton *H1* of the deacetylated monomer is denoted as *H1D* and that of the peak of the three protons of the acetyl group is denoted as *HAc*.

2.2.4.2. Particle size analysis by laser diffraction

Particle size distributions of the LMW and MMW chitosan powders were measured using a Malvern Mastersizer 3000 particle analyser using an Aero S dispersion unit (Malvern Panalyticals, Malvern, United Kingdom). The samples were initially riffled to condition the line, and then 1 g of each sample was used for measurement (n = 3). Span was calculated based on **Equation 2-3**.

$$\textbf{Span} = \frac{\boldsymbol{D90-D10}}{\boldsymbol{D50}} \qquad \textbf{Equation 2-3}$$

where D10, D50 and D90 were the diameters of the particles at 10%, 50% and 90% percentile based on a volume distribution.

2.2.5. Characterisation techniques for nanogels only

2.2.5.1. Transmission electron microscopy

The shape and morphology of the nanogels were characterised using an FEI CM120 Bio Twin Transmission Electron Microscope (TEM) (Hillsboro, Oregon, United State). One drop of the nanogel sample was dropped onto 200-mesh carbon lacey-coated copper grids and stained with 1% uranyl acetate solution, followed by air-drying at room temperature for a few minutes. The excess solution was removed using filter paper. Particle size distribution was performed using Image J (NIH, Bethesda, MA, USA).

2.2.5.2. Dynamic light scattering (DLS) and electrophoretic light scattering (ELS)

The Z-average particle diameter and polydispersity index of the nanogels were measured using a Zetasizer Ultra (Malvern Panalyticals, Malvern, United Kingdom) at room temperature using a backscatter angle of 173^{o}. A disposable polystyrene cuvette was employed in the analysis. Zeta potentials were measured using U-shaped capillary cells (DTS 1070, Malvern Panalyticals, Malvern, United Kingdom). The results were measured in triplicate obtained from three independent experiments.

2.2.5.3. Encapsulation efficiency of propranolol in chitosan-TPP nanogels

Measurement of EE of propranolol was adapted from the method reported by Al-Kassas *et al.* [208]. Instead of separating the nanogels via centrifugation solely, 0.5 mL of the propranolol-loaded nanogel solutions were loaded into a 0.5 mL Amicon diafiltration tube (MWCO 3000; Merck Millipore, Billerica, MA, USA). The solutions were then centrifuged using at 14000 X g for 30 minutes at 4 ^{o}C using a refrigerated mini centrifuge (Heraeus Fresco 17, Thermo Scientific, Waltham, USA), the filtrate was isolated and assayed by a UV-Vis spectrometer (Jenway 6305, Vernon Hills, IL, USA). The wavelength was set at 280 nm and drug concentrations were calculated using a pre-determined calibration curve, as shown in **Figure 2-3**. %EE was calculated using **Equation 2-4**. The experiment was repeated three times and the results were presented as mean ± SD.

$$\mathbf{EE} = \frac{D_{Theoretical} - D_{Free}}{D_{Theoretical}} \times 100\% \qquad \textbf{Equation 2-4}$$

where $D_{Theoretical}$ refers to the amount of propranolol added to the solution while D_{Free} refers to the amount of propranolol present in the aliquot after centrifugation.

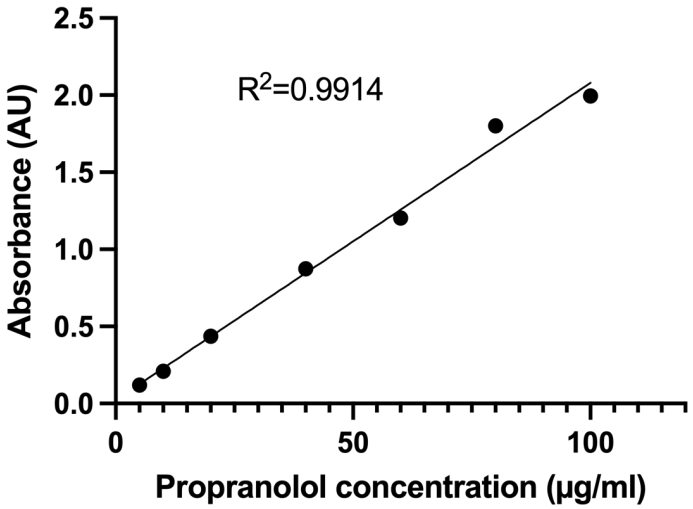

Figure 2-3. Calibration curve of the propranolol hydrochloride. Each data point was presented as a mean value from experiments in triplicates (n = 3). Error bars were too small to be observed.

Encapsulation efficiency was measured via an indirect method in this study, in brief, the proportion of the unencapsulated propranolol in solution was measured. However, this method has a limitation, where the drug was assumed to be either encapsulated or in solution. Degradation was not taken into consideration, and thus the encapsulation efficiency could be exaggerated if the drug was degraded. Moreover, the drug could be adsorbed onto the plastic surfaces, which would also be considered encapsulated in this method. Usually, encapsulation efficiency could be measured via a direct method, where the nanogels were broken up and the drug content was measured. However, no suitable solvent was found in the preliminary study to break up the nanogels, which made the direct measurement of encapsulated drugs unpractical.

2.2.5.4. Viscosity measurements of the nanogels

The density of the nanogel samples was obtained before the viscosity measurement. Kinematic and dynamic viscosities of the selected propranolol-loaded nanogels were measured with an automated rolling ball micro-viscometer (AMVN, Anton Paar, Graz, Austria) at 25 ^{o}C, with 5 replicates at each measurement. A 1.6 mm glass capillary with 1.5 mm stainless steel balls was used for the measurement. All samples were analysed at different tube inclination angles of 50^{o}, 60^{o} and 70^{o}.

2.2.6. Drug release of propranolol-loaded in Chitosan/TPP nanogels

Dissolution tests were performed in 50 mL phosphate buffer saline (PBS) (10 mM, pH 7.4) solution with continuous stirring at 37 ^{o}C over 72 hours. 2 mL of the nanogels solutions were loaded into a cellulose dialysis bag (MWCO 3500, volume/cm = 1.91; Fischer Scientific, Waltham, MA, USA) with both ends tied, followed by submerging into PBS. 1 mL aliquots were withdrawn at certain time points and an equal volume of fresh preheated PBS solution was added to maintain a constant volume. Propranolol was assayed by UV-vis spectroscopy using a UV-Vis spectrometer (Jenway 6305, Vernon Hills, IL, USA) as described above. Drug concentrations were calculated using pre-determined calibration curves as shown in **Figure 2-3**. The experiment was replicated independently three times and the results were presented as the mean value ± standard deviation.

2.2.7. Resuspension of lyophilised nanogels

A solution at pH 4.5 was first prepared by adding hydrochloric acid to the PBS solution. Lyophilised propranolol-loaded LMW and MMW chitosan nanogels were resuspended at a concentration of 3.33 mg/mL in the solution under ultrasonication for 30 minutes. The properties of the resuspended nanogels were determined. The difference between the nanogels before lyophilisation and after resuspension of lyophilised nanogels was determined with a two-way ANOVA using GraphPad Prism 15, with the Šidák post-hoc test for comparisons within nanogels fabricated from the same chitosan grade.

2.3. Results and Discussion

2.3.1. Fabrication of nanogels

Nanogels were successfully fabricated in all formulations, with the nanogels properties shown in **Table 2-1**. The size of all nanogels was smaller than 200 nm, while the PDI ranged from 0.210 to 0.461, showing the nanogels were moderately polydisperse. The zeta potential of the nanogels was between 20 mV and 40.9 mV, which demonstrated that the propranolol-loaded nanogels are cationic in charge and had good colloidal stability. The LMW chitosan nanogels had higher zeta potential than the MMW chitosan nanogels, resulting in better colloidal stability. Lastly, the encapsulation efficiency was about 60% only, which indicated the encapsulation was not efficient, likely due to the repulsion between propranolol and chitosan.

2.3.2. Characterisation techniques for raw materials and freeze-dried nanogels

Only two formulations of nanogels were freeze-dried and characterised. Unless otherwise specified in the text, the propranolol-loaded LMW and MMW chitosan nanogels described below denoted F1 and F4 nanogels respectively. The formulation was identical in these nanogels, with the only difference being the chitosan grade used. Therefore, they were suitable for comparing the effects of the chitosan grade. As for the drug-free nanogels, they were fabricated with the same formulation and experimental condition without propranolol.

2.3.2.1. Thermogravimetric analysis

The TGA thermogram of raw materials used in chitosan-TPP nanogel fabrication is shown in **Figure 2-4**. The thermogram demonstrated that all materials were thermally stable until 200 ^{o}C, with less than 10% weight loss observed under 200 ^{o}C. The results indicated that all raw materials and all samples are stable to heat up to 200 ^{o}C in the differential scanning calorimetry (DSC) study.

TPP has high thermal stability, with minimal weight loss observed after heating to 400 ^{o}C, owing to the high melting point of 622 ^{o}C. A small weight loss of 1.0% under 120 ^{o}C, which was likely the moisture adsorbed on the power. Contrarily, a full loss was observed for propranolol HCl after heating over 300 ^{o}C, which indicated that the drug is more sensitive to heat. No water loss was observed in

propranolol under 120 ºC, where the minimal moisture content correlated to the hydrophobicity of the drug. LMW and MMW chitosan exhibited a multi- and two-step profile, with the initial weight loss starting at around 40 ºC and ending at around 85 ºC, owing to the vaporization of adsorbed and bound water from the chitosan [215]. To figure out the moisture content in chitosan quantitatively, TGA analysis was performed in triplicate. Weight losses of 9.6 ± 0.2% and 9.6 ± 0.1% were observed for LMW and MMW chitosan respectively under 120 ºC, which indicated that moisture adsorbed or bound to chitosan accounted for about a tenth of the total weight. The second stage was associated with a rapid and dramatic drop in weight that occurred at 280 ºC and continue up to 320 ºC, with about half of the weight loss as shown in the drug-loaded MMW chitosan nanogels. It was due to the thermal degradation of the chitosan. The finding is consistent with the results reported in the literature [216]. The degradation was higher for LMW chitosan than in MMW chitosan, which demonstrated the thermal stability was higher in MMW chitosan, probably due to higher molecular weight and stronger intermolecular interactions. However, as chitosan is a natural polymer, the intrinsic features of the molecule, especially the degree of deacetylation, would affect the water contents and thus the total weight loss as well as degradation temperature. Therefore, some discrepancies between LMW and MMW chitosan, as well as between the measured result and literature are expected.

In contrast, multiple and similar decomposition stages were observed for the drug-free nanogels fabricated with LMW and MMW chitosan. About 5% weight loss under 120 ºC was observed for both drug-free nanogels, which indicated that a small amount of bound water remained in the freeze-dried samples or moisture was adsorbed on the lyophilised nanogels. The second decomposition at about 200 ºC was due to degradation. In contrast, the weight losses under 120 ºC were much higher in the drug-loaded nanogels, with 11.6% and 14.6% weight loss in propranolol-loaded LMW and MMW chitosan nanogels respectively. The results revealed the moisture content accounted for a substantial proportion of the total weight of the lyophilised samples. Higher water content in drug-loaded nanogels is likely due to propranolol disrupting the intermolecular interactions between polymer and crosslinkers. Subsequently, the polymers and crosslinkers interacted with the

water and retained the water. The MMW chitosan nanogels had higher moisture due to the stronger interaction with water. The higher the molecular weight, the larger the surface area for interaction, and thus the stronger the interaction.

Similarly, the propranolol-loaded MMW chitosan nanogels were more thermally stable than the LMW counterpart, with lower weight loss over 120 °C. The widening difference in weight loss between the two nanogels when the temperature increased, demonstrated the propranolol-loaded LMW chitosan nanogels were more susceptible to the high temperature. It is likely due to weaker interactions between chitosan and crosslinker in LMW chitosan nanogels. In short, the results indicated that the thermal stability of lyophilised nanogels varied with the chitosan grades that the nanogels were fabricated from.

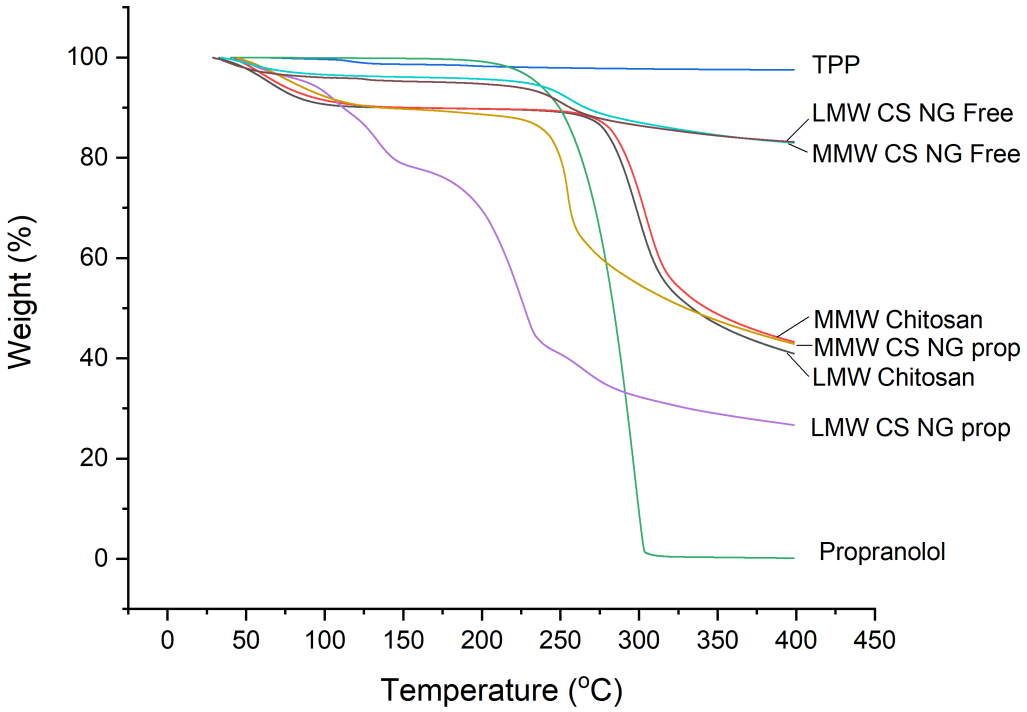

Figure 2-4. TGA thermogram of the raw materials and freeze-dried nanoparticles. F1 of the propranolol-loaded LMW chitosan-TPP nanogels was characterised. Chitosan, drug-loaded and drug-free nanogels demonstrated multi-stage degradations, while propranolol demonstrated a sharp degradation at 200 °C. No degradation was observed for TPP within the temperature range.

2.3.2.2. Differential scanning calorimetry

DSC thermograms of propranolol hydrochloride, TPP, LMW and MMW chitosan, freeze-dried drug-free and drug-loaded nanoparticles using a single heating method are shown in **Figure 2-5**. Propranolol shows a sharp melting peak at 164.5 ºC, which confirms its crystalline nature as reported in the literature [217]. No melting peak is observed for LMW and MMW chitosan, which demonstrated that the materials are mostly amorphous. Board peaks at 107.3 and 99.0 ºC in LMW and MMW chitosan respectively were likely due to vaporization of the moisture adsorbed or bound to chitosan. The peak temperature was lower in MMW chitosan than in LMW chitosan, which demonstrated more loosely bound water was present in the former. TPP exhibits two endothermic peaks at 112.6 ºC and 190.5 ºC. A larger temperature range (up to 300 ºC) is required to see the full profile as an endothermic peak is observed at around 200 ºC. The first peak at 112.6 ºC was likely due to the evaporation of bound water. Similar to chitosan, a broad peak was observed at 68.1 and 72.0 ºC in the drug-free nanogels fabricated with LMW and MMW chitosan respectively, which was shifted from 99.0 and 107.3 ºC in the LMW and MMW chitosan. The peak likely corresponds to water, which is less bound in the freeze-dried nanogels than in chitosan. The broad peak was less obvious in propranolol-loaded nanogels, which indicated that the water is also held but to a lesser degree. The peaks at 161.6 and 117.0 ºC in propranolol-loaded LMW and MMW chitosan nanogels probably correspond to the propranolol, which was shifted from 164.5 ºC. The slight shift of the peak in LMW chitosan nanogels was due to the presence of other components in the formulation, while the peak intensity was smaller due to a much lower content of propranolol present in the sample. The peak in MMW chitosan nanogels was likely shifted from 164.5 to 117.0 ºC, which echoed the TGA results showing the lower thermal stability of the propranolol-loaded MMW chitosan nanogels.

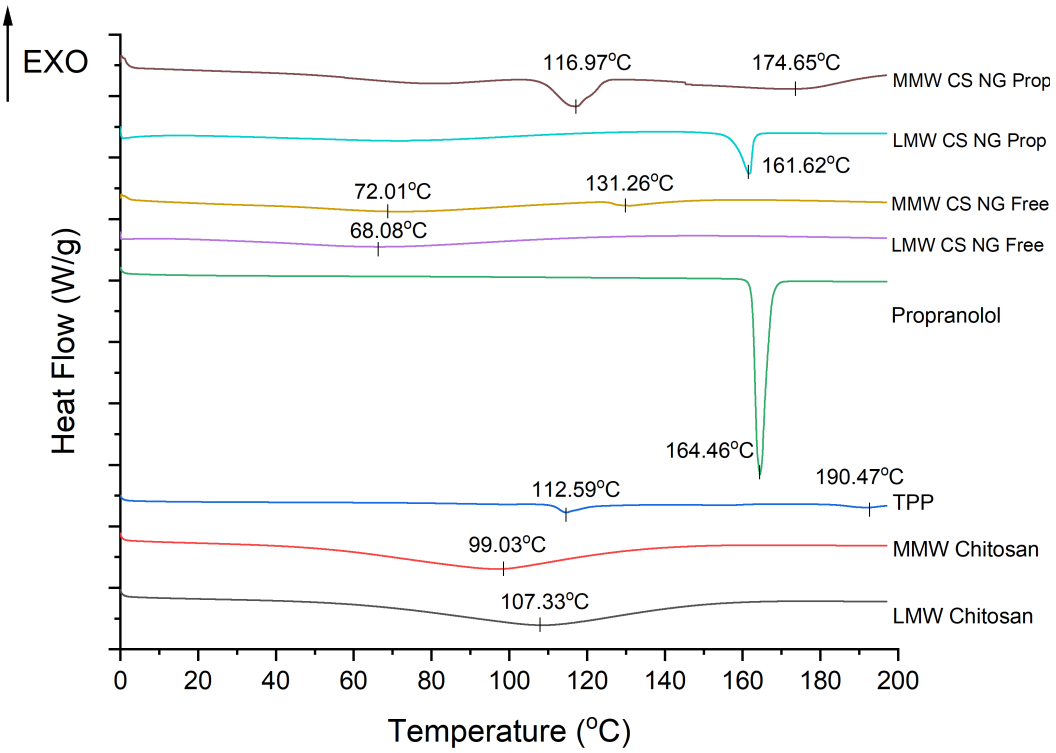

Figure 2-5. DSC thermogram of the propranolol hydrochloride, TPP, LMW chitosan, freeze-dried drug-loaded and drug-free nanoparticles using a single heating method.

2.3.2.3. Fourier transform infrared spectroscopy

Figure 2-6 shows the IR spectrum of the individual components of the nanogels, as well as both propranolol-loaded and drug-free nanogels fabricated with LMW and MMW chitosan. In the spectra of LMW chitosan, strong bands around 3290 and 3356 cm^{-1} are associated with O-H and N-H stretching and intramolecular hydrogen bonds, while the peak at around 2870 cm^{-1} corresponds to asymmetric C-H stretching. Slight shifts of peaks were observed in the MMW chitosan. Similar bands at 3288, 3371 and 3414 cm^{-1} were observed in the freeze-dried chitosan nanogels which also correspond to these intramolecular hydrogen bonds. The symmetric C-H stretching was not obvious in the spectra, as no peak was observed around 2900 cm^{-1}. N-acetylation of chitosan was confirmed with the band at 1642-1650 cm^{-1} and 1323-1420 cm^{-1}, which are the C=O stretching of amide and C-N stretching of amide respectively, as well as the peak at around 1590 cm^{-1} which corresponds to the N-H bending. The strong bands at 1027-1067 cm^{-1} are associated with the C-O stretching. The spectra agree with the results reported in the literature [218,219].

In the IR spectrum of propranolol, a band at 3277 cm^{-1} corresponds to the O-H stretching with intramolecular hydrogen bonds, but the N-H stretching with intramolecular hydrogen bonds was less obvious at 3221 cm^{-1} in the spectrum. A peak at 796 cm^{-1} corresponds to the naphthalene in propranolol while the aryl alkyl ether is associated with the peak at 1266 cm^{-1} [215]. C=C stretching in naphthalene is observed with a sharp peak at 1578 cm^{-1}. The spectrum obtained agrees with other literature [220]. As for TPP, the band at 3326 cm^{-1} corresponds to the O-H stretching while the band at 1135 and 1209 cm^{-1} is associated with O-P=O and P=O stretching, respectively [221]. A sharp peak at 1094 cm^{-1} corresponds to P-O stretching. The sharp peak at 1255 and 1269 cm^{-1} were present in the drug-free and propranolol-loaded nanogels respectively, which are indicative of the P=O bond in TPP within the nanogel structure, albeit shifted from 1209 cm^{-1} in TPP alone as a result of the interaction with chitosan [197]. Drug-free nanogels fabricated with LMW chitosan exhibited sharper peaks at 1558 and 1648 cm^{-1} compared to the LMW chitosan, which showed that the complexation of LMW chitosan with TPP is likely to influence the chemical interaction between chitosan. In contrast, the peaks at 1522 and 1638 cm^{-1} in drug-free nanogels fabricated with MMW chitosan were less sharp than its counterpart fabricated with LMW chitosan, which illustrated the complexation between MMW chitosan and TPP was less strong compared to LMW chitosan and TPP. Moreover, the C-O stretching of either group in chitosan was observed at 1087cm^{-1}, which shifted to 1009-1069 and 1018-1019 cm^{-1} in the drug-free and propranolol-loaded nanogels. The shift was similar to the reported literature [197]. Moreover, several distinct peaks for propranolol at 776, 795, and 1269 cm^{-1} were present in propranolol-loaded nanogels, which were not observed in the drug-free nanogels. In conclusion, the IR spectrum confirms the presence of the individual components in the nanogels and structural change of the nanogels after encapsulation and loading of propranolol was not observed.

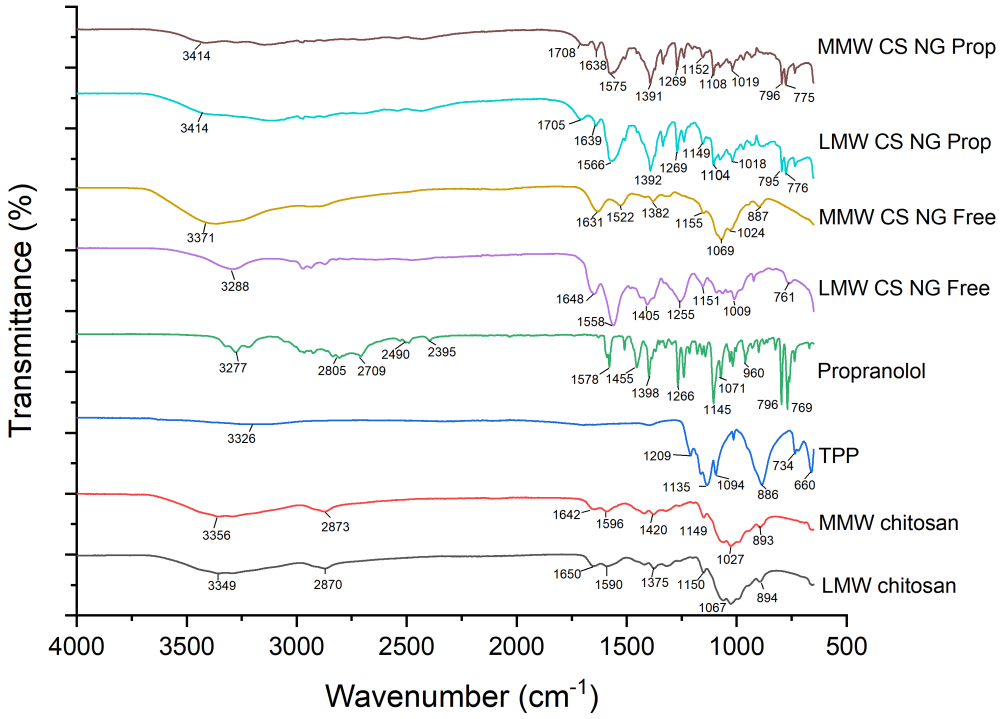

Figure 2-6. FTIR spectrum showing the components of the formulation individually, freeze-dried unloaded nanogels and the propranolol-loaded nanogels.

2.3.2.4. X-ray powder diffraction

The physical forms of raw materials and nanogels were assessed by XRD, with the results shown in **Figure 2-7**. Propranolol is a crystalline material, with strong peaks at 2θ = 8.3°, 12.8°, 21.2° and doublets at 16°, 19° and, 25°. The result agrees with the study by Fernandes *et al.* [217]. X-ray diffraction patterns of both LMW and MMW chitosan exhibited broad peaks at 2θ = 10° and 2θ = 20°. The result is also in agreement the with XRD analysis of chitosan reported in the literature and indicates that the chitosan has a low degree of crystallinity rather than being amorphous [222,223]. TPP is crystalline, with sharp peaks observed in the diffractogram. However, it has two crystalline forms – phase I and II [224]. Phase I hydrates quickly in the atmosphere and is the stable form at high temperatures while phase II hydrates less readily and is thermodynamically stable at low temperatures [224]. Three peaks at 2θ = 23.7°, 24.1° and 24.7° are observed in the diffractogram, which are the characteristic peaks for phase II TPP [225]. With the IR result shown above, the presence of two phases in the sample is demonstrated. However, only small

bands are observed at the 2θ of around 22° and 29° in the XRD diffractogram, which indicates the majority of TPP is in phase II form, with only a small amount of phase I present.

The nanogels exhibited a mixture of amorphous and crystalline materials, especially in the propranolol-loaded nanogels. Nanogels fabricated with LMW and MMW chitosan exhibited similar diffractograms. Two board peaks observed in chitosan disappeared, which is in agreement with the previous literature [226,227]. No Bragg reflection but two small board peaks were observed at $2\theta = 10°$ and $2\theta = 18°$ in drug-free nanogels, with much smaller intensity compared to unreacted chitosan. The disappearances indicated that the crosslinked chitosan was amorphous, and the crystallinity was lost due to the crosslinking with TPP, as a structure with a dense network of TPP crosslinked chitosan was formed [228]. However, only the former halo was present in the propranolol-loaded nanogels. Additional peaks with low intensities were observed at $2\theta = 13$, 16, 22, and 23° in both propranolol-loaded LMW and MMW chitosan nanogels, which are likely due to a small amount of propranolol crystal present. However, they were shifted slightly from those in the diffractogram of propranolol. The intensity of these peaks was weaker than those observed in propranolol crystals due to the smaller amount of propranolol present in the nanogels. Hence, the freeze-dried propranolol-loaded nanogels were a solid dispersion of amorphous crosslinked chitosan-TPP structure and crystalline propranolol.

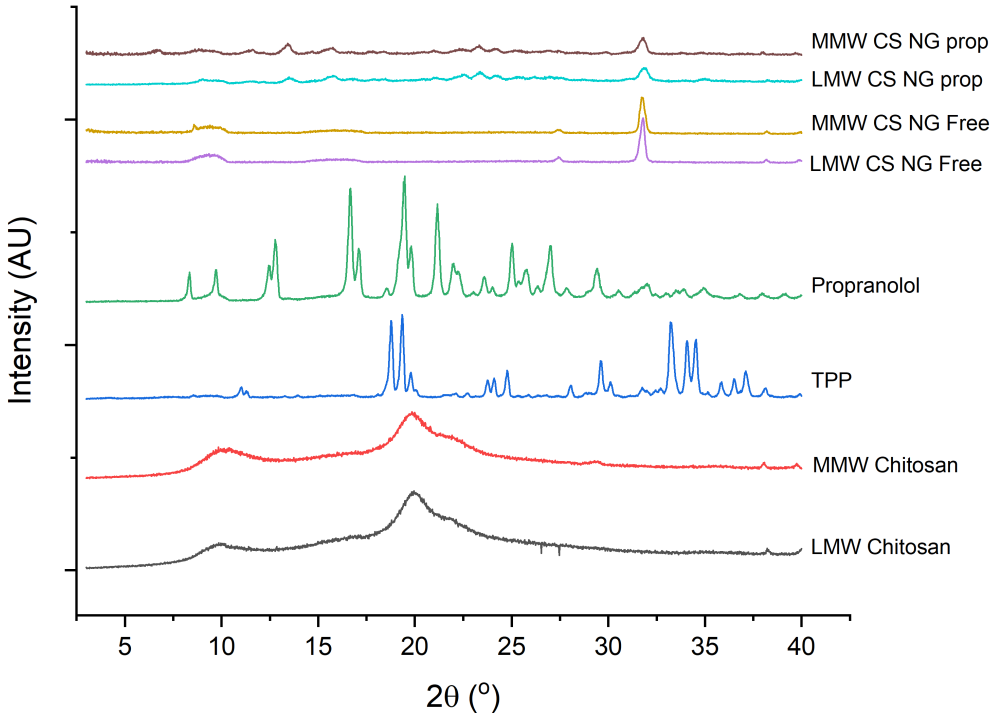

Figure 2-7. X-ray powder diffraction patterns of the various raw materials used in chitosan-TPP nanogels fabrication.

2.3.3. Characterisation techniques for raw materials only

2.3.3.1. Determination of deacetylation efficiency of chitosan using ^{1}H nuclear magnetic resonance

Various temperatures and relaxation times were used in the NMR to obtain a decent quality NMR spectrum. First, measurements were performed at elevated temperatures as the peak of H1D overlapped with the solvent peak HOD at room temperature. Shifting toward downfield for all assignations of chitosan peaks is observed in **Figure 2-8**, when the temperature increases from 25 °C to 50 °C, and a further shift was observed when temperature increased to 60 °C. Apart from the shift in peaks, no other peak was observed in the spectrum at a higher temperature, which elucidated that the shifting was not due to degradation at a higher temperature. As the solubility of chitosan increased at a higher temperature [229], the possible explanation for the shift is that chitosan interacts more with water and less with chitosan itself. Thus, the protons are de-shielded and a downfield shift with all peaks of the assignment was observed.

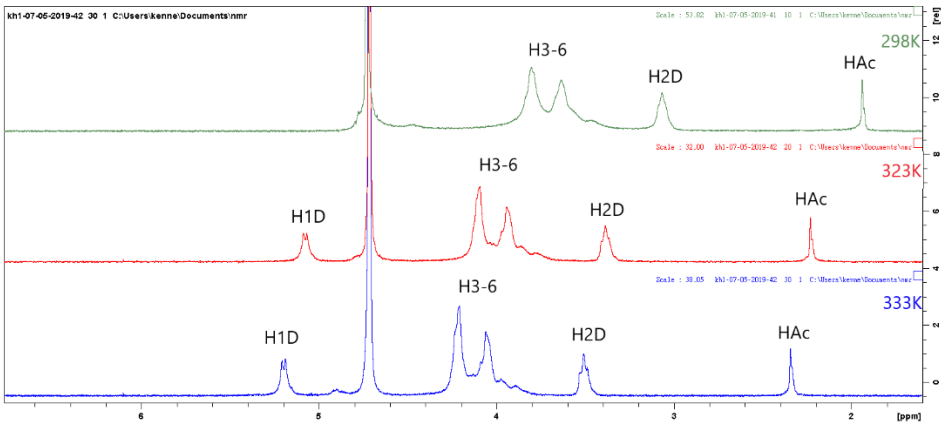

Figure 2-8. ^{1}H NMR spectrums of low molecular weight chitosan were performed at three different temperatures 298 K (25ºC), 323 K (50ºC) and 333 K (60ºC), where H3-6 referred to the integration of signals from hydrogen at position 3-6, which included H3, H4, H5, H6 and H6'.

On the other hand, different relaxation times were used in NMR measurement, as shown in **Figure 2-9**. No major change in chemical shifts of peaks was observed between NMR spectrums measured with 2 s and 30 s relaxation time. However, the peaks measured with 30 s relaxation time were sharper than the counterpart measured with a relaxation time of 2 s.

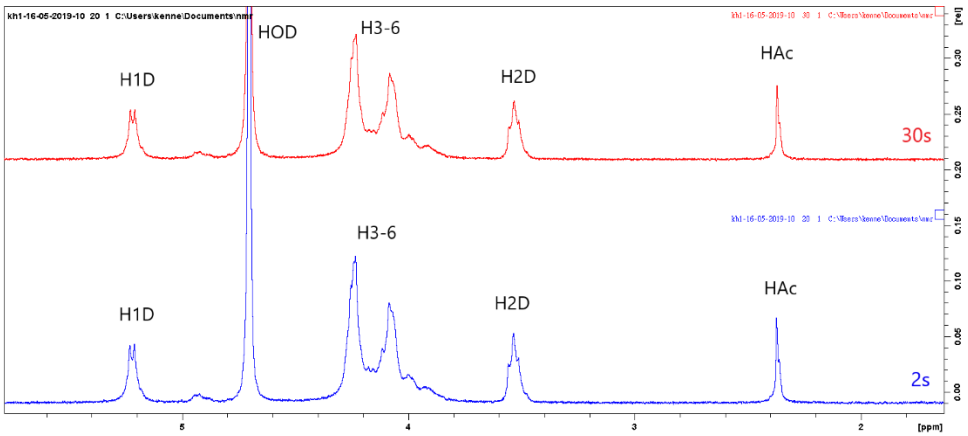

Figure 2-9. An overlay of the ^{1}H NMR spectrums was obtained for the medium molecular weight chitosan at 60 ºC, with different relaxation times of 2 s (blue) and 30 s (red). Chemical shifts of the peaks were not varied amongst the three runs.

Therefore, the measurement was performed at 60 ºC and 30-second relaxation time on the LMW and MMW chitosan to quantify the DA of chitosan, with the spectrum

presented in **Figure 2-10** and **Figure 2-9** respectively. The solvent (HOD) proton resonated at 4.7040 ppm and the chemical shifts of other protons in chitosan presented similarly. Chitosan peaks were assigned based on the reported literature [214,230,231]. H3-6 is the collection of signals from protons at H3-6 and 6', with a peak at a chemical shift of 4.2093 ppm being the signal for H3, 4 and 6. The peak at a chemical shift of 4.0579 ppm was a signal from H5 and 6'. H1D was a doublet as there is only one hydrogen (H2) interacting with the H1 proton, with chemical shifts of 5.2070 and 5.3138 ppm. H2D is a triplet, with 2 neighbour hydrogens H1 and H3. The degree of deacetylation was calculated using the integrals of the peak of H1 of deacetylated monomer (H1D) and the integral of the three protons in the acetyl group (HAc) via **Equation 2-2** [214]. DA for LMW and MMW chitosan was calculated as 84.0 ± 0.8% and 89.4 ± 0.8% respectively, which indicated that most of the amine groups were free and the chitosan in 1% acetic acid should readily be crosslinked with TPP.

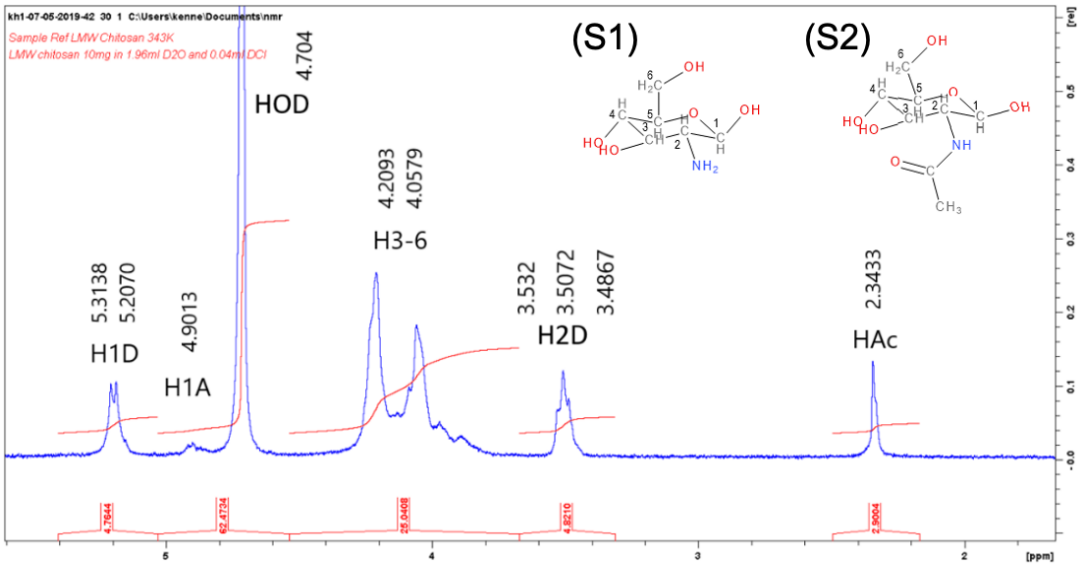

Figure 2-10. A ^{1}H NMR spectrum of the low molecular weight chitosan at 60 °C with the structures of deacetylated monomer (S1) and acetylated monomer (S2) of chitosan, with the position of carbon in the ring labelled.

2.3.3.2. Particle size analysis by laser diffraction

The particle size distributions (PSD) obtained from a different grades of chitosan raw materials are presented in **Table 2-2** and **Figure 2-9.** The D [v,0.1] represents the fine end of the particle size distribution, the D [v,0.5] represents the mean particle size

while the D [v,0.9] represents the coarse end of the particle size distribution. The D [4,3] refers to the volume mean diameter while the span is an indication of how far the 10% and 90% quantile are apart but normalised with the midpoint. The LMW chitosan had lower mean D[v,0.1], D [v,0.5], D [v,0.9] and D [4,3] than the MMW chitosan. The span was calculated to describe how far apart the finest and the coarsest part of the particle size distribution is and normalise it against the mid-point of the distribution, as shown in **Equation 2-3**. Span of LMW chitosan was approximately two times of the MMW counterpart, which indicated that the particle size distribution was much wider in the LMW chitosan powder than in MMW chitosan powder.

Table 2-2. Mean D [v,0.1], D [v,0.5], D [v,0.9] and D [4,3] of the LMW and MMW chitosan powders. Span was calculated to describe the difference between the finest and coarsest parts of the particle size distribution. The results were presented as mean ± SD from triplicates (n = 3).

Sample	D [v,0.1] (μm)	D [v,0.5] (μm)	D [v,0.9] (μm)	D [4,3] (μm)	Span
LMW chitosan	20.5 ± 0.3	165.0 ± 4.6	551.7 ± 23.7	232.7 ± 9.0	3.22 ± 0.16
MMW chitosan	209.7 ± 6.1	504 ± 6.4	968.7 ± 3.8	551.0 ± 5.6	1.51 ± 0.03

LMW chitosan with MW 50-190 kDa according to the manufacturer had smaller particle sizes than MMW chitosan, which has a molecular weight of 190-310 kDa. However, the range of particle size population was higher in LMW chitosan than in MMW chitosan, as reflected in the higher span, which quantifies distribution width. Therefore, a wider particle size distribution and a less steep cumulative distribution curve are observed and shown in **Figure 2-11**.

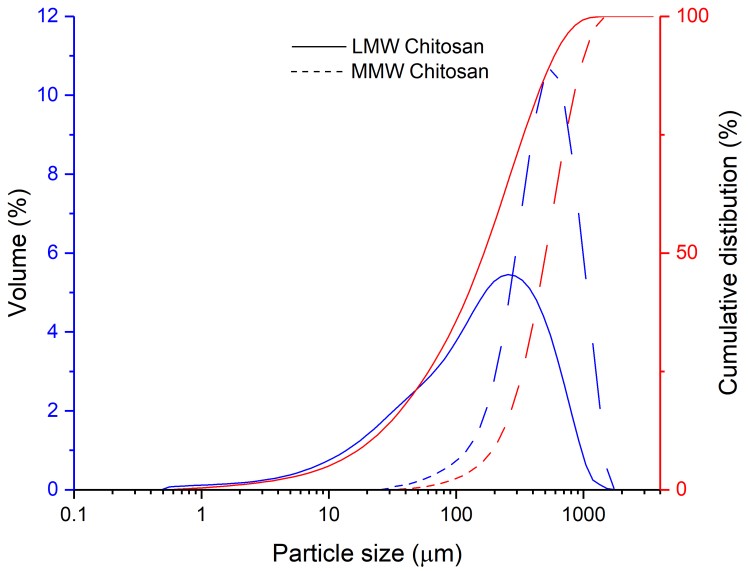

Figure 2-11. Volume size distribution curves (in solid line) and cumulative distribution curves (in dotted line) for LMW and MMW chitosan.

2.3.4. Characterisation techniques for nanogels only

2.3.4.1. Transmission electron microscopy (TEM)

TEM images of the propranolol-loaded nanogels fabricated with LMW and MMW chitosan were shown in **Figure 2-12 (a) and (c)** respectively, while their size distribution is shown in **Figure 2-12 (b) and (d)**. Both LMW and MMW nanogels appeared as spherical or oval objects. The average size of the propranolol-loaded LMW nanogels at the dried state was 67.6 ± 18.4 nm as presented in **Figure 2-12 (b)**, which is close to the measured Z-average of 75.5 ± 2.2 nm. Z-average is defined as the harmonic intensity averaged particle diameter according to ISO 13321; in other words, cumulants mean hydrodynamic size measured in DLS. However, the quality of the TEM images was substandard. The average size of the propranolol-loaded LMW nanogels was only based on 10 particles, as only 10 particles are visible from the background, which are circled in red in **Figure 2-12 (a)**. Thus, the size distribution was not reliable as the particle count was not sufficient. The greyish cloud-like materials in the background were likely the undried polymer.

Regarding the propranolol-loaded MMW chitosan nanogels, the measured size was much bigger than those fabricated with LMW chitosan, as the scalebar was shorter in **Figure 2-12 (c)** for the same distance. As the quality of the TEM image was better

and the background was clearer than the previous image, more particles could be measured. Thus, the size distribution was calculated from 75 particles, with a diameter of 283.0 ± 74.6 nm. However, the particle size of the same sample measured with Zetasizer was 113.6 ± 5.8 nm. The discrepancy between the two values was likely because the size measured in the TEM image was the diameter at the dry state, while the size measured with Zetasizer was the hydrodynamic size, where particles were suspended in water with an assumption of the spherical particles. The wide particle size distribution in the TEM images demonstrated that the TEM samples were not sufficiently dried and thus some nanogels may not be fully dried and may appear larger than others [197]. Paradoxically, the drying of the nanogels can also promote aggregates to form, which could explain why plenty of larger particles as observed on the TEM.

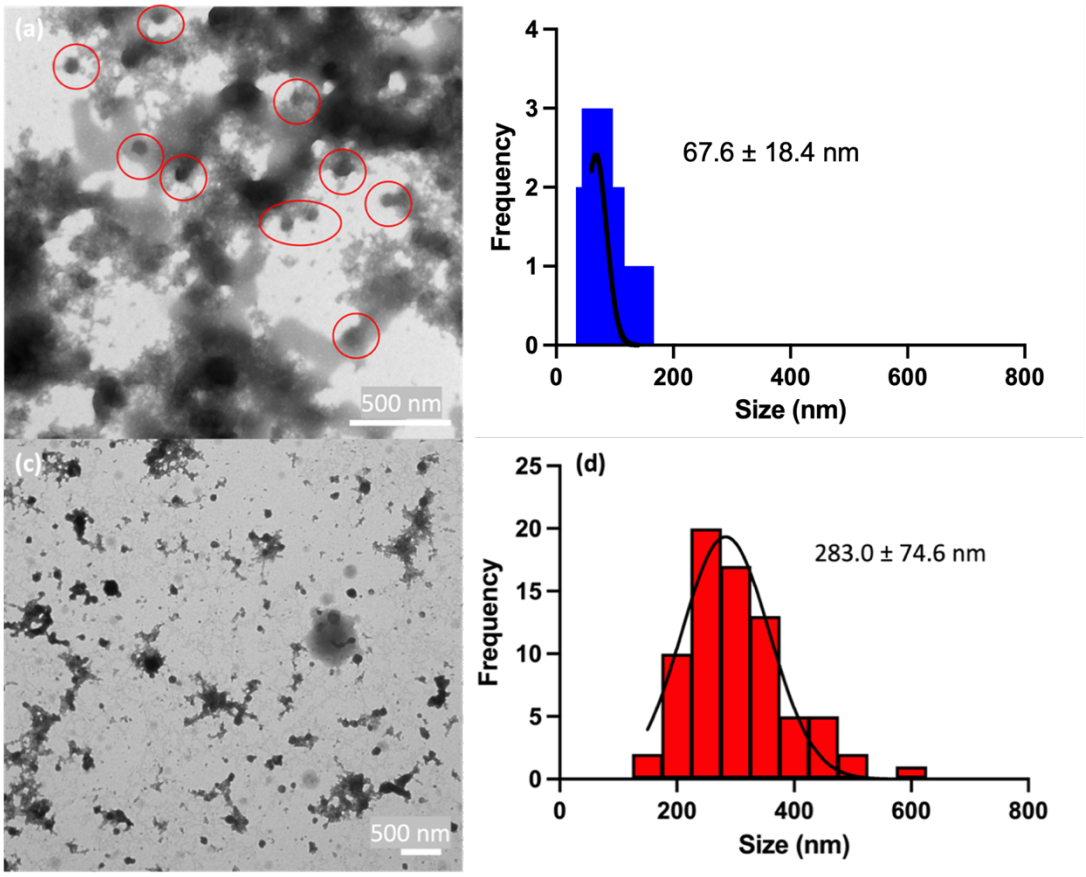

Figure 2-12. (a) A TEM image of the propranolol-loaded nanogels fabricated with LMW chitosan. (b) The PSD of the LMW chitosan nanogels is based on the diameters measured using Image J on the particles that could be identified (circled in red) in the TEM image. (c) A TEM image of the propranolol-loaded nanogels fabricated with MMW chitosan and (d) its particle size distribution based on the TEM image.

2.3.4.2. Viscosity of nanogels

One of the advantages of using nanogels as a formulation is the favourable injectability, which is related to the ease of administration of a dosing solution and is partly dependent on the viscosity of the formulation [232]. Thus, it is important to determine the viscosity of the nanogels formulations. A ball-rolling micro-viscometer was used to measure the viscosity of the formulations, as this viscometer is simple, easy to use and requires only a small volume of sample. Moreover, the viscosity of the nanogels could not be determined in a parallel plate rheometer, as a suitable plate was lacking. Microfluidic viscometer (e.g., Rheosense) could not be used for the nanogels solution

either as filtration through a 0.22 µm filter is required to prevent blockage of channels, which might also remove the bigger-sized nanogels.

In the ball-rolling micro-viscometer, the shear rate is influenced by the tube inclination angle, so the shear-dependent flow behaviour can be tested. The dynamic and kinematic viscosities of F1, F2, and F3 reduced with the higher inclination angles as shown in **Figure 2-13**, which indicates these LMW chitosan formulations might be shear thinning, whereas the MMW chitosan nanogels F4 might be slightly shear thickening, as the kinematic and dynamic viscosity increased with the inclined tube angle. F1 formulation has higher viscosities than F2 formulations, even though the former used a lower concentration of LMW chitosan. A further decrease in viscosity was observed in F3, which indicates that an increase in LMW chitosan concentration might reduce viscosity. However, the limitation of the ball-rolling technique is that the shear stress across the capillary was not uniform. Therefore, the shear-thinning or shear-thickening properties of these formulations were estimated but could not be concluded based on the results, as the correlation between the shear rate and the inclination angle could not be established.

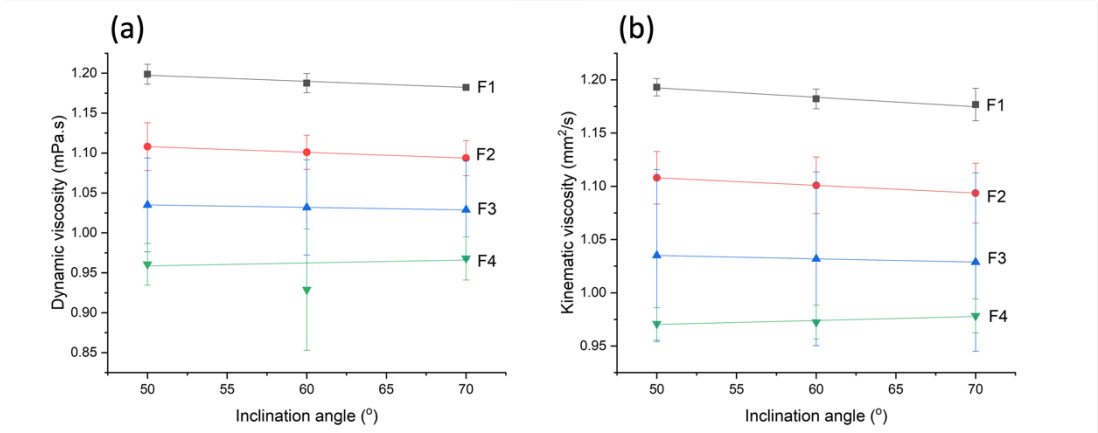

Figure 2-13. (a) Dynamic and (b) kinematic viscosities of the nanogel formulations F1-3 and F4 at different inclination angles. F1 and F4 were the propranolol-loaded nanogels fabricated with the formulation - CC of 0.1% and CT of 3 using LMW and MMW chitosan respectively. F2 was propranolol-loaded nanogels fabricated with LMW chitosan at 0.15% CC and CT of 3, while F3 was fabricated at 0.3% CC and CT of 0.5. CP was fixed at 0.5 for all formulations.

2.3.5. Drug release studies

The *in vitro* drug release test determined the dissolution profile and bioavailability of the loaded drugs. The use of PBS (pH 7.4) is to stimulate the release at physiological pH. A burst release of encapsulated propranolol in the first 2 hours can be observed in **Figure 2-14**. A significant release of around 20% propranolol was observed within the first 10 minutes, followed by a slow increase until 8 hours, when most of the drugs were released from the carrier. After 8 hours, the concentrations from some formulations levelled off. Similar release profiles were observed between nanogels F1 to F3, which indicated that these nanogels were likely to release propranolol comparatively even though the size and PDI of nanogels were different. It is likely due to the precipitation and aggregation of chitosan nanogels in PBS. The solutions turned turbid and opaque due to the presence of precipitates. Precipitation of chitosan might also destroy the architecture of the nanogels, and thus propranolol inside the void of nanogels could leach out, which might account for the rapid and burst release. Besides, as both propranolol and chitosan are cationic, there is lacking interaction between polymer and propranolol to retain the propranolol and slow the release down. The number of precipitates present in the dialysis bag was likely to be dependent on the concentration of chitosan and therefore the amount of chitosan present, with the lowest amount of precipitate observed in F1 and the highest amount of precipitate observed in F3 for LMW chitosan.

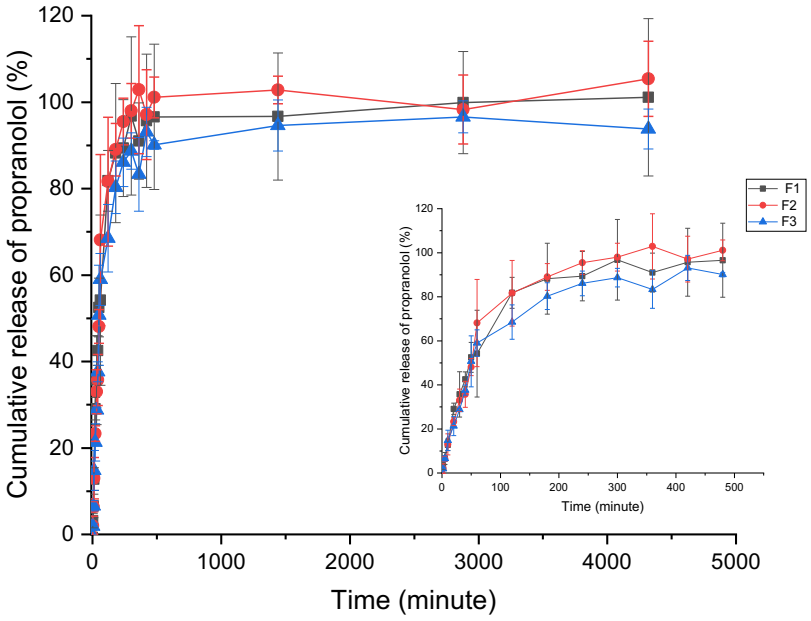

Figure 2-14. *In vitro* propranolol release over 72 hours (large) and the zoom-in of the first 8 hours (small) from various propranolol-loaded nanogels fabricated using LMW chitosan, where F1, F2 and F3 nanogels were fabricated with different formulations. Data are obtained from three independent experiments and represented as mean ± SD.

Comparing the nanogels fabricated with different chitosan grades, similar release profiles were observed between LMW (F1) and MMW (F4) nanogels in **Figure 2-15**, which indicated that the nanogels were likely to release propranolol in an equivalent way even different grades of chitosan were used. A significant release of around 20% propranolol was observed in both nanogels within the first 10 minutes, followed by a slow increase until 8 hours, when most of the drugs were released from the carrier. Therefore, the release mechanism of propranolol from the nanogels remained unchanged, despite different chitosan grades used for fabrication. Interestingly, both solutions turned turbid and opaque due to the presence of precipitates. Therefore, the results indicated that the precipitation of chitosan at physiological pH was unavoidable, even when LMW chitosan was used.

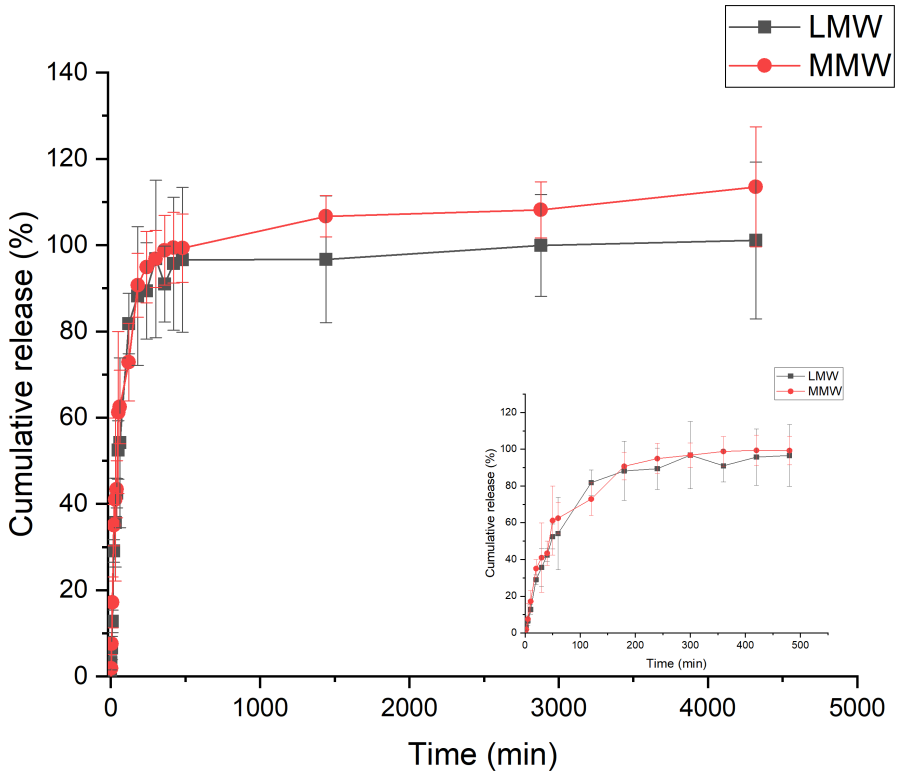

Figure 2-15. *In vitro* propranolol release from the nanogels fabricated with both LMW and MMW chitosan over 72 hours (large) and the zoom-in of the first 8 hours (small). The nanogels were fabricated using the same formulation but with different grades of chitosan. Data are obtained from three independent experiments and represented as mean ± SD.

2.3.6. Resuspension of lyophilised nanogels

Lyophilised propranolol-loaded LMW and MMW chitosan nanogels were resuspended in a buffer at pH 4.5 under ultrasonication for 30 minutes. Nanogel properties were measured and shown in **Figure 2-16**. The ANOVA demonstrated that all nanogels properties – size, PDI, ZP and EE were statistically significantly different before freeze-drying and after resuspension of lyophilised nanogels. The size of the resuspended nanogels was much bigger, with a 4-fold increase. In addition, the resuspended nanogels were also more polydisperse than the original nanogels before freeze-drying. The PDI was double and quadruple in the LMW and MMW nanogels, respectively. The results indicated that the nanogels were aggregated in the resuspended solution, where the aggregation could not be broken with ultrasonication. Thus, the aggregation of nanogels after freeze-drying was likely

irreversible. The ZP of both LMW and MMW nanogels were increased, which was likely due to the aggregation of nanogels, increasing the charge density. Interestingly, the encapsulation efficiency was improved in both nanogels. It is also likely related to the aggregation of nanogels, as larger particles could allow more propranolol to be entrapped. In conclusion, the lyophilisation of nanogels might lead to an irreversible aggregation of the nanogels and they could not be broken up by ultrasonication effectively. The results elucidated that the lyophilisation was not suitable for these nanogels as a long-term storage method. Chitosan-TPP nanogels samples should be prepared freshly before any further experiment or assay, which would limit their potential clinical uses.

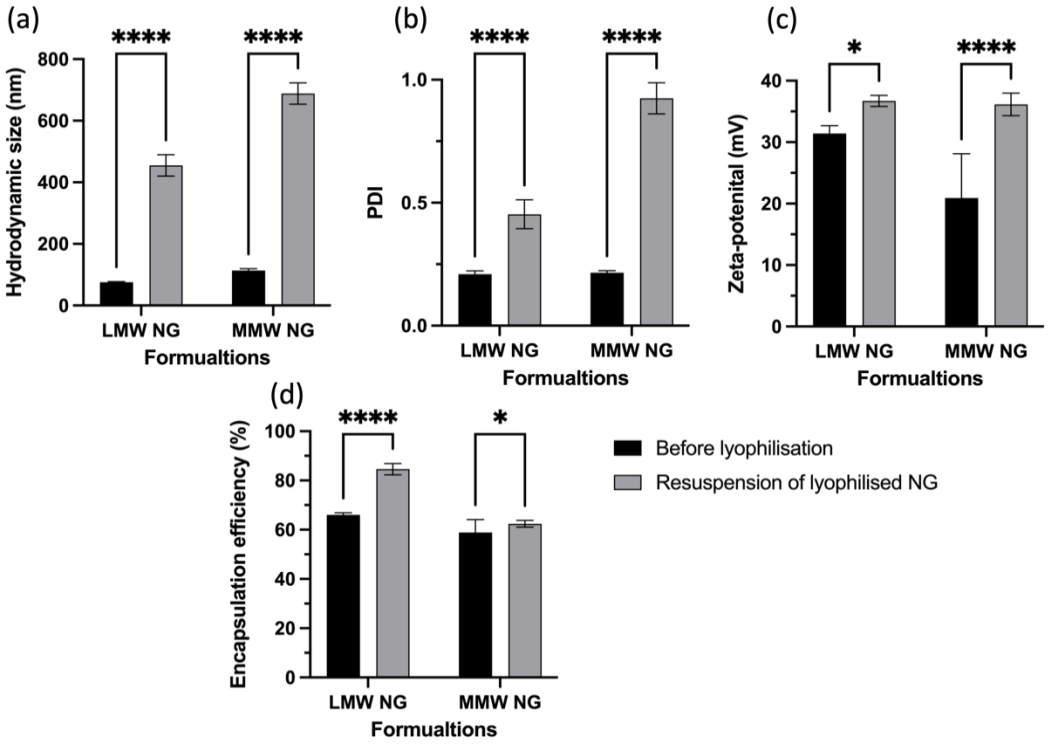

Figure 2-16. (a) Size, (b) PDI, (c) zeta potential and (d) encapsulation efficiency of the propranolol-loaded LMW and MMW chitosan nanogels before freeze-drying and after resuspension from the lyophilised samples and sonication.

2.4. Conclusion

In this study, four nanogels were fabricated with different formulations, varying the chitosan concentration, chitosan-TPP ratio, chitosan-propranolol ratio and chitosan grade. The properties of nanogels, including the hydrodynamic size, polydispersity,

zeta potential, encapsulation efficiency, and viscosities were measured for these nanogels. The results demonstrated that the setup of the experiment was fit-for-purpose, in which nanogels could be fabricated using it. Thus, the set-up would be used in the next experimental chapter.

Two samples F1 and F4, which shared the same formulation but were fabricated with different chitosan grades, were freeze-dried. Their lyophilised samples and raw materials were then characterised using various analytical techniques to understand the stability in the solid state. They were also resuspended in a buffer at pH 4.5 under ultrasonication. However, all nanogels properties of resuspended nanogels were significantly different from the respective nanogels in solution before freeze-drying. The results elucidated that lyophilisation led to the irreversible aggregation of the nanogels. Fresh samples should be prepared before any experiment and assay.

Overall, the set-up was shown to be fit-for-purpose, while the characterisation performed highlighted various properties of nanogels to be controlled, which are crucial for a successful nanogel formulation. However, the mechanism of drug loading in the nanogels is currently not understood. Parameters such as the formulation, drug loading, and processing factors could also potentially affect these properties. Therefore, these areas are explored in more detail in the next experimental chapter.

Chapter 3

Modelling the Effects of Formulation, Processing Factors and Drug Loading on the Structure and Properties of Nanogels

Part of the contents in this chapter has been published as the following research article.

Ho, H. M. K., Craig, D. Q., & Day, R. M. (2022). Design of Experiment Approach to Modelling the Effects of Formulation and Drug Loading on the Structure and Properties of Therapeutic Nanogels. *Molecular Pharmaceutics*.

3. Modelling the effects of formulation, processing factors and drug loading on the structure and properties of nanogels

3.1. Introduction

Controlling the parameters of nanoparticles is crucial for any nanoparticle formulation, including nanogels. The size and surface charge of nanoparticles are especially important as these parameters impact the solubility, biodistribution, stability, cytotoxicity, cellular uptakes, and clearance of the nanoparticles. For instance, the uptake of nanoparticles into cells is dependent on the size, shape, surface hydrophobicity, and charge of the nanoparticles, although the permeability varies between different cells [233]. The particles have to be in a size range generally between 10 to 500 nm, and up to 5 μm, to be engulfed via micropinocytosis [233]. Nanoparticles taken up via clathrin-mediated endocytosis tend to have diameters in the region of 100 nm, while those involved in caveolae-mediated endocytosis are typically 60-80 nm in size [234]. Furthermore, Tang *et al.* showed that only cationic nanoparticles suspended in a culture medium were ingested by endocytosis, suggesting the importance of nanoparticle surface charge in cellular uptake [235]. Cationic nanoparticles have a strong interaction with the negatively charged cytomembrane, facilitating the entry of nanoparticles into the cell. These nanoparticles are usually taken up via clathrin-mediated endocytosis [194,195]. For instance, chitosan-TPP nanogels are successfully taken up into lung epithelial cells (A549) and intestinal epithelial cells (Caco2) predominantly via this mechanism [236,237]. For systemic clearance, nanoparticles <10 nm are cleared quickly by renal filtration and are not reabsorbed into the blood, whilst nanocarriers between 50 – 200 nm are often unable to escape from blood capillaries [238].

Stability is another key parameter for nanoparticle formulation. Suspended nanoparticles are a colloid system and thus tend to flocculate, coagulate, and sediment, which leads to increased particle size and affects cellular uptakes and clearance. To maintain stability, nanoparticles may be stabilised via steric and electrostatic repulsion. In chitosan-TPP nanogels, the nanoparticles are stabilised by

electrostatic repulsion and zeta potential is an indication of the potential stability of the colloidal system. Particles with zeta potential more positive than 30 mV or more negative than -30 mV are considered stable, and the nanoparticles are unlikely to flocculate due to the repulsion between nanoparticles [239]. In short, successful delivery of nanogels requires optimal size and charge, and thus the fabrication process needs to be optimised.

Design of Experiments (DOE) is a popular method for optimising pharmaceutical formulation development. It allows a systematic evaluation of the effect of multiple factors in the variation of the response measured and reduces the number of experimental runs. However, the drawback is that the process is driven by experiments and is labour-intensive, as DOE models are constructed based on the input parameters, and any changes in the input factors require the construction of a new model. Thus, a model is usually reported for a particular drug and delivery system. The prediction ability of these models with new drug payloads is rarely explored in literature and therefore is poorly understood. Indeed, the drugs are commonly thought to be encapsulated in the voids between polymer chains and thus the drug choice is often assumed to be of limited influence if that drug is of a size and solubility to allow incorporation into the nanogel voids. Here, this view was challenged by exploring both the development of predictive models using a DOE approach and the possible generalisability of both the approach and the model to a range of drugs. A predictive understanding of the effects of composition on nanogel performance parameters will both aid the formulator and aid in understanding the role of drug structure on both incorporation and nanogel architecture.

The mechanism of drug loading in chitosan-TPP nanogels is not well understood. It is thought that the drugs are loaded in the voids formed between the crosslinked chitosan matrix during the gelation process. If the loading mechanism is purely entrapment during the gelation process, the nanogel properties should be governed by the formulation, such as the polymer and crosslinker concentrations. Thus, different drugs could be loaded into the nanogel without alteration of the nanogel properties, as long as the drugs fit into the voids of the nanogels, and the prediction models remain valid for different drugs. Since these nanogels are fabricated via

electrostatic interactions between chitosan and TPP, it is expected that the drug molecules could also potentially impact the gelation process, altering the interaction between the drug, chitosan and TPP. Thus, the structure of drugs, drug properties and pH are important. It is hypothesized that drugs are loaded via both physical entrapment and through interaction with the nanogel carrier during the gelation process, where the drug electrostatically interacts with either oppositely charged chitosan or TPP. Other interactions such as weak *Van der Waal's* force and hydrophobic interaction could also play a role in the interactions. Thus, it is expected that the properties vary when the properties of the drug change.

To verify this hypothesis, propranolol was used initially as a model drug for nanogel fabrication. Response surface models were constructed for the unloaded and drug-loaded systems to predict the properties of propranolol-loaded chitosan-TPP nanogels, namely size, PDI, ZP, and EE. Seventeen experimental runs were performed to build a three-factor, three-level face-centred cubic central composite model in which chitosan, chitosan-TPP ratio, and chitosan-propranolol ratio were varied. The models were then verified by an individual test group, before identifying the optimal conditions. The optimal condition was selected and explored experimentally with twelve other drugs without structural similarity to propranolol and six beta-blocker drugs with close structural relationships to propranolol, of which the latter are expected to similarly interact with the polymer or crosslinker. In this way, it is possible to establish whether the models may be applied to other drugs and if so whether structural similarity is a requirement for such extrapolation.

To describe a drug molecule, one of the common representations is the molecular descriptor. It is defined as an algorithm-generated mathematical representation of structural or physicochemical properties of molecules [240], which can be classified based on either the dimensionality or information content. The former classifies descriptors into 0D to seven-dimensional (7D) descriptors, whereas the latter classifies them into constitutional, topological, geometric, and electronic descriptors [241]. The classifications overlap extensively and are not mutually exclusive. Thus, molecular descriptors discussed in this study will be based on the constitutional and topological properties for clarity. Constitutional descriptors are calculated from

molecular formulae, such as molecular weight atom and bond count whereas topological and structural descriptors, including counts of fragments and functional groups, are calculated from the two-dimensional (2D) structure. Geometric spatial and electronic descriptors are derived from the three-dimensional (3D) structure [241]. Numerous open-source and commercial software exist for computing these molecular descriptors, including PaDEL [242], MORDRED [243], CDK [244], Dragon [245], RDKit [246], and etc. As a proof-of-concept study, these drugs were described in terms of 15 basic molecular descriptors, which include the number of acids (nAcid), bases (nBase), rings (nRing), hydrogen bond acceptors (nHBAcc), hydrogen bond donors (nHBDon), the sum of the atomic polarizability (apol), the sum of the absolute value of the difference between atomic polarisability of all bonded atoms (bpol) in the molecule, Wiener path number (WPATH), Wiener polarity number (WPOL), topological polar surface area (TopoPSA), topological diameter (TopoDiameter), Petitjean topological shape index (Toposhape), two logarithms of n-octanol/water partition coefficient ALogP and XLogP. The constituent descriptors, especially the number of chemical groups, were selected to evaluate the chemical groups responsible for the interactions with the carriers and to identify the mode of loading in the nanogels, where the polarity and polarizability were picked to evaluate the effects of other interactions, such as *Van der Waal's* force and hydrophobic interaction. The topological shape and size descriptors were selected to evaluate whether the size and shape of the drugs impact drug entrapment since the drugs are loaded into the voids of the nanogels. The relationship between nanogel properties and molecular descriptors of drugs was determined via multiple linear regressions, logarithmic, exponential and quadratics correlations. This facilitates our understanding of how a drug may influence entrapment and nanogel structure, intending to establish the generalisability of the DOE modelling approach across a wide range of drug structures and increase our understanding of the mechanism of drug loading in nanogels. Notably, the development of predictive models for optimising the properties of drug delivery systems is an incredibly useful and well-established approach within the field. In this particular case, we focus on two as yet unexplored applications of performance modelling. Firstly, the formulation of nanogels is a complex and as yet poorly predictable process whereby each system is explored on a largely individual basis due to the absence of a

validated methodology for performance prediction, hence there is a clear requirement and novel application for such approaches for these systems. Secondly, the effect of drug incorporation on performance and properties is a critical area which has as yet again not received systematic study, hence the intention is to develop methodologies whereby the effects of incorporation of the active agent may be developed at least, in the present case, for structurally related molecules, with the intention of this providing a basis for studies into a broader range of active pharmaceutical ingredients.

Lastly, the chapter finished off with a systemic screening of processing parameters in the fabrication process. The properties of nanogels were demonstrated to be dependent partially on the formulation and the properties of the drugs encapsulated in the nanogels in the above studies. However, the predictability of the zeta potential and encapsulation efficiency was found to be weak in these models and the percentage differences between the predicted and experimental size and PDI were occasionally larger than 10%. These observations revealed that there are other factors responsible for governing these performance parameters. Therefore, other factors such as the processing factors in the fabrication process were explored. Understanding the effects of these processing factors is important in the manufacture of nanogels, as they could impact the scale-up, robustness of the fabrication method and reproducibility of the products. To evaluate the effects of the fabricating factors respective to the stirring, eight processing factors were selected, namely, temperature (T), the total volume of the solution (TV), stirring rate (SR), the addition rate of crosslinker solution (AR), duration (D), glass vial volume (GV), stirrer size (SS), and blocking (B). In conjunction with the chitosan grade and crosslinker choice, these ten factors were screened with a definitive screening design approach. The optimal fabrication condition was also identified in the design, followed by an investigation of the scaling-up of the nanogels fabrication via increasing the volume pro-rata at this condition. This is the first study that systematically demonstrated the impacts of the processing factors in fabrication on the properties of nanogels and investigated the scaling-up of nanogels.

3.2. Materials and Method

3.2.1. Materials

Sodium pyrophosphate, paracetamol, metoclopramide hydrochloride, metoprolol tartrate, lidocaine hydrochloride, theophylline, ofloxacin, metronidazole, acebutolol, pindolol, and esmolol hydrochloride were also acquired from Sigma Aldrich (St Louise, MO, USA). Caffeine was purchased from Fluka (Buchs, Switzerland) while quinine anhydrous, lisinopril dihydrate, verapamil hydrochloride, and betaxolol were acquired from Acros Organics (Geel, Belgium). Pirfenidone and atenolol were purchased from Tokyo Chemical Industry (Tokyo, Japan). Chlorpheniramine maleate was acquired from the LKT laboratory (St Paul, MN, USA). Stirrers with three assorted sizes and two glass vial volumes were used in the DSD, with the dimensions shown in **Table 3-1**.

Table 3-1. The dimensions of various stirrers and glass vials were used in the definitive screening design.

Stirrer	**Length (mm)**	**Width (mm)**	**Thickness (mm)**
Small	12.82 ± 0.02	4.76 ± 0.01	4.71 ± 0.06
Medium	15.12 ± 0.05	4.75 ± 0.01	4.62 ± 0.01
Large	19.92 ± 0.02	6.02 ± 0.02	6.19 ± 0.27
Glass Vial Volume (mL)	**External Diameter (mm)**	**Height (mm)**	**Glass Wall thickness (mm)**
14	23.18 ± 0.06	58.37 ± 0.07	1.05 ± 0.02
28	27.46 ± 0.03	71.69 ± 0.15	1.09 ± 0.01

3.2.2. Propranolol-loaded nanogels fabrication

Propranolol-loaded chitosan nanogels were prepared by the method detailed in **Section 2.2.2**. A range of nanogels was prepared by varying these factors according to the experimental matrix shown in **Table 3-2, Table 3-3 and 3-5**.

3.2.3. Central composite design

Response surface methodology was used to determine the optimal condition for preparing propranolol-loaded nanogels. A face-centred cubic (FCC) central composite design (CCD) was used in the optimisation, which was formed by three factors, namely the chitosan concentration (CC), the chitosan-TPP mass ratio (CT) and the chitosan-propranolol mass ratio (CP), at three levels as shown in **Table 3-2.** A total of seventeen experimental runs were denoted as the training set and were

performed in triplicate to construct the response surface model, as shown in **Table 3-3**. The composite matrix was constructed using JMP 15 (SAS Institute, Cary, NC, USA). Four properties of nanogels (Size, ZP, PDI, and EE), which contribute to being a successful drug carrier, were determined as the dependent variables.

Noteworthy, the results were obtained from three independent experiments for each fabrication condition. However, only a single value for each datapoint can be input into the software for modelling. Thus, the mean value for each condition was used as the input. As a result, standard deviation (SD) was not included in the model.

Table 3-2. Non-codified levels for each factor used in the central composite design.

		Non-Codified level		
Factor	**Symbol**	**Low (-)**	**Mid (0)**	**High (+)**
Chitosan concentration (%w/v)	(CS)	0.1	0.2	0.3
Chitosan-TPP ratio	(CT)	0.010	0.015	0.020
Chitosan-propranolol	(CP)	0.1	0.2	0.3

A stepwise least square regression was used to fit the polynomial model to the data individually for each dependent variable. A 5-fold cross-validation was performed to validate the model for all dependent variables. A one-way analysis of variance (ANOVA) test and lack of fit test was conducted to determine the statistical significance and goodness of fit for the model respectively, at a confident interval (*CI*) of 95%. Response surfaces were plotted to visualise the relationship between independent and dependent variables. A p-value <0.05 is considered statistically significant.

Table 3-3. The experimental design matrix was constructed for the CCD design, with various independent and dependent variables. The result of the dependent variables was based on three independent experiments and was presented as the average only.

Sample	Independent variables			Dependent variables			
	CC (%w/v)	CT	CP	Size (nm)	Zeta potential (mV)	PDI	Encapsulation efficiency (%)
1	0.2	3	0.375	135.3	23.45	0.243	23.3
2	0.2	5	0.25	135.6	29.53	0.367	40.6
3	0.2	5	0.375	132.3	28.01	0.378	11.7
4	0.2	5	0.375	138.6	29.95	0.352	18.6
5	0.1	5	0.375	65.6	24.57	0.288	30.7
6	0.1	3	0.5	69.8	25.73	0.233	35.1
7	0.3	5	0.375	208.1	26.49	0.481	18.7
8	0.2	5	0.375	135.2	30.59	0.327	16.5
9	0.2	5	0.5	146.4	29.62	0.323	20.9
10	0.1	7	0.25	59.4	18.67	0.342	19.7
11	0.3	3	0.25	194.4	24.38	0.343	21.7
12	0.3	7	0.25	198.6	31.58	0.498	14.5
13	0.3	7	0.5	206.2	31.02	0.507	16.4
14	0.2	7	0.375	132.0	32.23	0.461	18.0
15	0.1	3	0.25	65.0	18.11	0.217	26.7
16	0.3	3	0.5	190.8	24.69	0.345	19.6
17	0.1	7	0.5	56.8	25.25	0.313	25.8

3.2.4. Multiple response optimisation

Multiple response optimisation was employed to determine the optimal condition for fabricating propranolol-loaded nanogels, as the dependent variables might contradict each other. The desirability function approach, first proposed by Harrington [247] in 1965 and later advocated by Derringer and Suich [248], is one of the most widely used methods in multiple response optimization. It transformed the response variables (y_i) into an individual desirability function $d_i(y_i)$, with a number assigned between 0 and 1. $d_i(y_i) = 0$ indicates a completely undesirable response while $d_i(y_i) = 1$ represents the most desirable response. Individual desirability functions were transformed using JMP 15 software to minimise the particle size and PDI while maximising the EE and ZP. Individual desirability functions were then combined into overall desirability, as shown in **Equation 3-1**.

$$\boldsymbol{D = \sqrt[i]{(d_1(y_1) \times d_2(y_2) \times \ldots \times d_i(y_i)}}$$ **Equation 3-1**

where $d_1(y_1)$ and $d_2(y_2)$ denote the individual desirability function for factors 1 and 2, respectively. i is the total number of factors and $d_i(y_i)$ is the individual desirability function of factor i.

The running conditions with the highest overall desirability were deemed as the optimal condition and were determined by JMP 15. Nanogels were then fabricated under the optimal conditions in triplicate, with the dependent variables measured experimentally and compared with the predicted values to validate the models. Nanogels produced were then freeze-dried and characterised.

3.2.5. Test set validation and final formulations

To determine the predictive accuracy of the models, an independent test set with 13 formulations was used with the properties of nanogels measured experimentally and compared with the predicted value from the model. The experimental conditions for the formulations in the training set were generated randomly and the test set is reported in **Table 3-4**. Finally, nanogels were also fabricated under experimental conditions predicted by the validated models to obtain 100 and 200 nm in size, with the secondary aim to minimise the PDI. Owing to the low predictability of the ZP and EE models, these parameters were measured but not compared with the predicted values.

Table 3-4. The parameter investigated, experimental findings and predicted results of the test set for evaluating the predictive accuracy of the CCD models. The experimental results were presented as the mean value only in this table from three independent experiments (n = 3). Percentage differences between the actual and predicted results were also calculated.

	Experiment conditions			Size (nm)			PDI			ZP (mV)			EE (%)		
	CC (%w/v)	C/T	C/P	Exp	Pred	%Diff	Exp	Pred	%Diff	Exp	Pred	%Diff	Exp	Pred	%Diff
1	0.15	4	0.25	114.4	103.0	-10.0	0.268	0.281	4.9	27.4	23.8	4.9	14.9	26.2	75.8
2	0.25	4	0.375	138.1	168.8	22.2	0.283	0.353	24.7	25.4	27.8	24.7	15.4	21.5	39.6
3	0.25	6	0.25	131.1	170.9	30.4	0.318	0.434	36.5	25.1	30.4	36.5	9.5	18.3	92.6
4	0.1	4	0.5	98.9	70.1	-29.1	0.156	0.246	57.7	29.5	25.4	57.7	19.6	28.6	45.9
5	0.15	3	0.375	118.1	99.4	-15.8	0.245	0.248	1.2	26.0	25.4	1.2	15.4	27.8	80.5
6	0.3	6	0.5	179.8	206.2	14.7	0.422	0.476	12.8	29.4	29.2	12.8	8.5	16.0	88.2
7	0.15	3	0.25	119.3	99.4	-16.7	0.253	0.248	-2.0	26.3	23.1	-2.0	31.4	27.8	-11.5
8	0.2	4	0.5	113.0	135.9	20.3	0.268	0.317	18.3	23.1	29.3	18.3	9.7	23.9	146.4
9	0.2	6	0.375	107.6	135.6	26.0	0.289	0.391	35.3	24.0	30.2	35.3	25.2	20.7	-17.9
10	0.1	6	0.5	60.7	65.1	7.2	0.146	0.306	109.6	24.8	26.0	109.6	18.5	25.4	37.3
11	0.15	7	0.375	115.8	94.1	-18.7	0.355	0.382	7.6	26.1	28.2	7.6	13.8	21.4	55.1
12	0.25	3	0.25	133.8	162.7	21.6	0.263	0.312	18.6	25.0	25.8	18.6	18.3	23.1	26.2
13	0.3	4	0.5	194.4	201.6	3.7	0.397	0.388	-2.3	28.4	25.3	-2.3	18.8	19.2	2.1

3.2.6. Application of the validated model with other drugs

To determine the possibility of applying the validated models to other drugs, nanogels were fabricated at the optimal condition identified above. Chitosan nanogels loaded with other drugs were prepared by the same method discussed, except for atenolol. Atenolol-loaded chitosan nanogels were prepared with the respective amount of atenolol dissolving in the chitosan before pH adjustment, as the atenolol is not in a salt form, of which the pH of the chitosan solution would increase upon the addition of atenolol after the pH adjustment. Drugs with and without structural relationships were grouped and analysed separately.

Owing to the poor predictability of the models, the zeta potential of the nanogels was measured but not predicted. To describe each drug molecule, fifteen basic molecular descriptors were selected and are shown in **Table 3-5**, which are subdivided into constitutional, topological descriptors, and molecular properties. These molecular descriptors of the drugs were calculated with PaDEL [242]. The correlations between molecular descriptors and the properties of nanogels were determined with linear regression using JMP 15, with the correlation coefficient (R^2) aimed above 0.7.

Table 3-5. Selected molecular descriptors of the drugs with and without structural similarity to propranolol.

Drugs	MW	nAcid	nBase	nHBa	nHBd	nHetero Ring	apol	Bpol	WPath	WPol	XLogP	AlogP	Topo-shape	Topo-PSA	Topo-diameter
Propranolol	259.2	0	1	3	2	0	44.866653	25.533347	792	25	4.053	-1.0098	2	41.49	11
Drugs without structural similarity to propranolol															
Caffeine	194.1	0	0	5	0	2	26.751930	20.108070	258	25	-0.625	-0.4311	2	58.44	6
Chlorpheniramine	274.1	0	1	2	0	1	45.209067	24.490933	718	25	4.288	0.6514	2	16.13	9
Lidocaine	234.2	0	1	3	1	0	42.311446	27.648554	556	23	2.848	1.166	1	32.34	9
Lisinopril	405.2	2	2	8	4	1	64.940583	38.743417	2362	40	1.106	-4.3984	2	132.96	13
Metoclopramide	299.1	0	1	6	2	0	46.393446	29.324554	902	29	1.144	0.0496	1	67.59	11
Metronidazole	171.1	0	0	3	1	1	22.267137	14.394863	193	15	0.017	0.2875	1	81.19	6
Ofloxacin	361.1	1	1	8	1	3	52.080860	32.839140	1484	51	1.49	-0.2260	4	73.32	12
Paracetamol	151.1	0	0	3	2	0	22.785137	11.456863	166	11	1.079	-1.0852	1	49.33	7
pirfenidone	185.1	0	0	2	0	1	30.356723	14.963277	293	19	2.753	0.1195	2	20.31	7
Quinine	324.2	0	1	3	1	1	55.007032	31.452968	1286	42	2.662	-0.5136	2	45.59	12
Theophylline	180.1	0	0	5	1	2	23.658344	16.601656	211	22	-0.435	-0.967	2	69.3	5
Verapamil	454.3	0	1	5	0	0	78.266134	51.845866	3698	55	4.71	0.1993	2	63.95	18
Drugs with structural similarity to propranolol															
Acebutolol	336.4	0	1	6	3	0	55.758204	35.761796	1568	31	1.747	-2.1004	1	87.66	15
Atenolol	266.3	0	1	5	3	0	43.915446	26.924554	890	21	0.678	-1.6098	1	84.58	13
Betaxolol	307.4	0	1	4	2	0	54.522997	36.195003	1427	24	2.772	-0.6800	2	50.72	16
Esmolol	295.2	0	1	5	2	0	49.137825	32.780175	1212	24	2.296	-0.9014	1	67.79	15
Metoprolol	267.2	0	1	4	2	0	46.575825	31.822175	906	21	2.034	-0.7944	1	50.72	14
Nadolol	309.2	0	1	5	4	0	52.231411	32.092589	1168	31	1.774	-0.925	2	81.95	12
Pindolol	248.2	0	1	4	3	1	41.779860	25.100140	687	22	1.62	-1.4302	2	57.28	10

3.2.7. Screening the effects of parameters in the fabrication process

To evaluate the effects of the process factors in the fabrication, a definitive screening study (DSD) was used to screen and optimize the important fabricating factors that size, PDI, ZP, and EE. Seven independent fabricating variables were screened in the study, namely temperature (T), total volume (TV), stirring speed (SR), addition rate of TPP solution (AR), duration of stirring (D) glass vial size (GV) and size of the magnetic stirrer (SS). As these factors are continuous factors except the glass volume, they were modelled in three levels. Glass volume was considered as a categorical factor in this study, as no medium-sized glass vial (21 mL) was available. Moreover, three additional factors were included in the design. Blocking (B), chitosan grade (CS) and choice of crosslinkers (CR) were added to the design to evaluate if any of these factors affect the properties of nanogels. Blocking was introduced to eliminate the influence of extraneous factors, in which the experiment was divided into two. In this study, the blocking was to balance out the effect of inter-day on the fabrication, in which nanogels in each block were fabricated on a separate day. Moreover, chitosan grade and choice of crosslinkers were added to the study to evaluate the effect of different material attributes on the properties of nanogels. As chitosan is a natural polymer, its properties, including solubility and charge density, vary between manufacturers, batches, grades, origin, molecular weight, and deacetylation efficiency. Therefore, it is important to understand the effect on nanogel properties when different chitosan was used. To simplify the variations in chitosan, two batches of chitosan were purchased from the same manufacturer and were classified as different chitosan grades based on the molecular weight – LMW and MMW. However, the limitation of this approach is that it is impossible to identify the exact parameters of chitosan impacting the nanogel properties. Regarding the choice of the crosslinkers, only two crosslinkers were used in the DSD with their structures shown in **Figure 3-1**, namely sodium pyrophosphate (Pyro) and sodium triphosphate (TPP), where pyrophosphate is a synonym for diphosphate. Therefore, it would be interesting if these structurally alike crosslinkers similarly interacted with chitosan or not. Blocking, chitosan grade and choice of crosslinker belonged to categorical factors, and thus they were modelled at two levels only. The optimal fabrication condition identified in **Section 3.2.4** was kept as the formulation in this study.

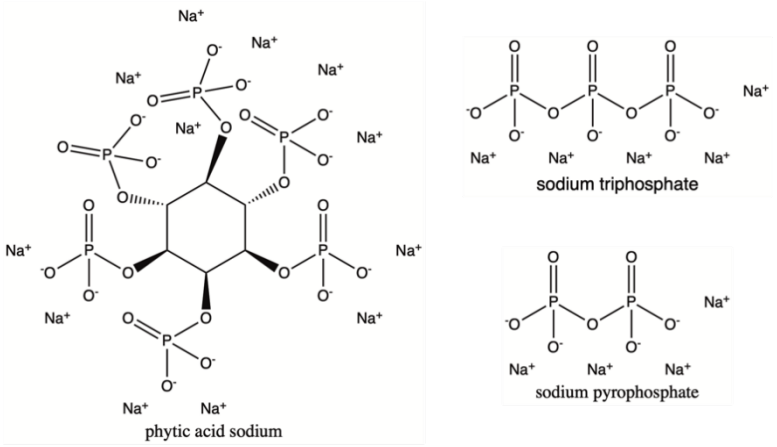

Figure 3-1. Structures of various phosphate-containing crosslinkers used during the fabrication of the nanogels in this study, namely phytic acid sodium, sodium triphosphate pentabasic and sodium pyrophosphate. (Created with ChemDraw 20.1)

A total of twenty-six experimental runs were performed according to the composite matrix shown in **Table 3-6** in triplicate to construct the definitive screening design (DSD), where the composite matrix was constructed using JMP 15 (SAS Institute, Cary, NC, USA). The definitive screening design was then fitted by the Effective Model Selection for DSD methodology, which was performed automatically in JMP 15. The main effects and second-order effects were first estimated individually and then combined to form the model parameter estimates.

The identified factors were then used in the optimisation step. A stepwise least square regression was used to fit the polynomial model to the data individually for each dependent variable. A 5-fold cross-validation was performed to validate the model for all dependent variables. A one-way analysis of variation (ANOVA) test and lack of fit test was conducted to determine the statistical significance and goodness of fit for the model respectively, at a confidence interval (*CI*) of 95%. Response surfaces were plotted to visualise the relationship between independent and dependent variables. A p-value < 0.05 is considered statistically significant. The optimal fabrication was obtained via multiple response optimisation, as discussed in **Section 3.2.4**.

Table 3-6. Processing factors in the nanogels fabrication and dependent variable and the experimental design matrix of DSD design.

Processing factors										Nanogels properties			
B	**T (°C)**	**TV (mL)**	**SR (rpm)**	**AR (mL/min)**	**D(hr)**	**CS**	**CR**	**GV (mL)**	**SS (mm)**	**Size (nm)**	**PDI**	**ZP (mV)**	**EE (%)**
1	25	10	300	0.5	1	MMW	TPP	14	20	130.4	0.235	33.1	28.8
2	25	7	300	2	1	LMW	TPP	28	12	129.5	0.266	17.01	31.4
1	25	10	300	2	1.5	MMW	Pyro	14	12	240.9	0.29	30.1	34.0
1	25	4	300	2	2	LMW	TPP	14	20	139.6	0.257	38.84	33.2
2	25	4	300	0.5	2	MMW	Pyro	28	20	195.2	0.282	35.9	38.3
1	25	10	450	0.5	2	LMW	Pyro	28	12	158.3	0.282	31.74	37.0
1	25	10	600	2	1	LMW	Pyro	28	20	148.7	0.275	25.02	33.1
2	25	4	600	1.25	1	LMW	Pyro	14	20	99.2	0.224	26.36	29.7
2	25	4	600	0.5	1	MMW	TPP	28	12	152.2	0.261	35.76	36.0
2	25	4	600	2	2	MMW	Pyro	14	12	163.7	0.301	29.4	29.8
2	25	10	600	0.5	2	LMW	TPP	14	16	199.1	0.318	38.47	16.6
1	37.5	4	300	0.5	1	LMW	Pyro	14	12	153.7	0.289	25.29	35.1
1	37.5	7	450	1.25	1.5	MMW	TPP	28	16	142.6	0.237	36.09	28.7
1	37.5	7	450	1.25	1.5	LMW	Pyro	14	16	105.5	0.258	24.8	31.0
1	37.5	10	600	2	2	MMW	TPP	28	20	203.9	0.303	24.29	28.8
2	50	10	300	0.5	1	LMW	TPP	28	20	255.5	0.355	33.69	29.9
2	50	4	300	2	1	MMW	Pyro	28	16	155.1	0.272	37.39	34.7
1	50	4	300	0.5	2	MMW	TPP	14	12	146	0.282	30.81	32.4
2	50	10	300	1.25	2	MMW	TPP	28	12	170.8	0.258	33.58	29.6
2	50	10	300	2	2	LMW	Pyro	14	20	138.8	0.269	32.69	31.1
1	50	4	450	2	1	MMW	TPP	14	20	110	0.218	28.44	35.7
1	50	10	600	0.5	1	MMW	Pyro	28	12	100	0.244	22.03	33.2
2	50	10	600	2	1	LMW	TPP	14	12	107.3	0.229	19.73	31.0
1	50	4	600	0.5	1.5	LMW	TPP	28	20	175	0.243	26.18	41.9
1	50	4	600	2	2	LMW	Pyro	28	12	161.5	0.292	31.81	31.1
2	50	7	600	0.5	2	MMW	Pyro	14	20	112.5	0.254	28.34	40.7

3.2.8. Scaling up of the nanogels fabrication

Nanogels were fabricated at 4 different total volumes ranging from 2 to 20 mL, at the optimal fabrication conditions and formulation identified in **Section 3.2.4 and 3.2.7**. The total volume is defined as the sum of volumes for chitosan solution and TPP solution. 4 mL was used as the total volume (i.e., 2 mL of chitosan solution mixed with 2 mL TPP solution) in the studies described in **Section 3.2.4 and 3.2.7** and thus was used as the control. Size, PDI, ZP and EE of the nanogels were measured as discussed previously in **Sections 2.2.5.2 and 2.2.5.3**. A one-way ANOVA test with Dunnett's post-hoc test was used to compare if the properties of nanogels at different volumes were different to the control.

3.3. Results and Discussion

3.3.1. Central composite design (CCD)

3.3.1.1. Statistical analysis

A one-way analysis of variation (ANOVA) and lack of fit test was performed on the response surface models for each individual dependent variable to determine the statistical significance and the goodness of fit for these models on the training set. The null hypothesis of the ANOVA is that these models have no correlation to the training data set and thus do not have predictive capacity. The results of the ANOVA and lack of fit tests are reported in **Table 3-7**. *p*-values obtained in the ANOVA test for all the models were smaller than 0.05, demonstrating the significance of the correlations between the training set and the models. Furthermore, the *p*-values in the lack of fit tests for all models were larger than 0.05, which indicate these models were a good fit for the training set data. Thus, these models can predict the properties of nanogels.

Table 3-7. ANOVA and lack of fit test results for the CCD models for various independent variables. The significance of each term used in constructing the model was also reported. Statistical significance was set as Prob. > F being smaller than 0.05.

Independent variables	Source of variations	Degree of freedom	Sum of squared	Mean squares	F value	Prob.> F	Significance
Size	**Model**	4	46804.498	11701.200	649.0404	<0.001	**Significant**
	CC	1	46444.225		2576.256	<0.0001	Significant
	CT	1	0.529		0.529	0.0293	Not significant
	CC X CT	1	182.405		10.118	0.0079	Significant
	CT^2	1	177.738		9.859	0.0085	Significant
	Residual	12	216.342	18.000			
	Lack of fit	4	49.794	12.449	0.5980	0.6746	**Not significant**
	Pure error	8	166.548	20.819			
PDI	**Model**	3	0.117	0.039	56.7929	<0.001	**Significant**
	CC	1	0.061		88.579	<0.001	Significant
	CT	1	0.055		79.523	<0.001	Significant
	CC X CT	1			2.277	0.1552	Not significant
	Residual	13	0.009	0.001			
	Lack of fit	5	0.006	0.001	3.2981	0.0654	**Not significant**
	Pure error	8	0.003	0.000			
EE	**Model**	2	0.032	0.0162	3.9079	0.0448	**Significant**
	CC	1	0.022		5.347	0.0365	Significant
	CT	1	0.010		2.468	0.1385	Not significant
	Residual	14	0.058	0.004			
	Lack of fit	6	0.003	0.000	0.0686	0.9979	**Not significant**
	Pure error	8	0.055	0.007			
ZP	**Model**	6	251.138	41.856	13.2271	0.00003	**Significant**
	CC	1	66.641		21.060	0.0010	Significant
	CT	1	50.060		15.820	0.0026	Significant
	CP	1	19.721		6.232	0.0316	Significant
	CC X CT	1	22.616		7.147	0.0234	Significant
	CC X CP	1	26.082		8.242	0.0166	Significant
	CC^2	1	66.017		20.862	0.0010	Significant
	Residual	10	31.644	3.164			
	Lack of fit	8	28.035	3.504	1.9420	0.3839	**Not significant**
	Pure error	10	3.609	1.805			

Where CC is chitosan concentration, CT is chitosan-TPP ratio and CP is chitosan-propranolol ratio.

3.3.2. Effect of formulation composition on the nanogels

3.3.2.1. Z-average and polydispersity index

Size is one of the crucial factors controlling the performance of nanogels in cellular uptake [233]. Z-average is measuring the hydrodynamic size of the nanoparticles, which is a better indication of the size of the nanogels in solution than the size measured in TEM as the latter is measured at a dried state. All nanogels in the seventeen formulations from the training set were found to be within a range from 56.8 to 208.1 nm. These nanoparticles were in the range for endocytic uptakes. Chitosan concentration, the interaction effect between chitosan concentration and chitosan-TPP ratio and the quadratic effect of chitosan-TPP ratio were found to have significant effects on the size of nanogels. Although the effect of the individual term for the chitosan-TPP ratio was not significant, it had to be included in the model as its interaction and quadratic terms were included.

The size of the nanogels increased with the chitosan concentration as shown in **Figure 3-2 (a)**. However, the observed trend is opposite to the results reported by Al-Kassas *et al.* [208], in which the "one factor at a time" (OFAT) optimisation approach was used to prepare propranolol-loaded chitosan-TPP nanogels. Nanogels fabricated in their study with 0.1% chitosan were much larger than those prepared from 0.2% and 0.3% chitosan. Moreover, the size of the nanogels prepared in this study was smaller than those reported by the Al-Kassas group. The discrepancy in nanogel sizes between the two studies is probably due to a different grade of chitosan being used, with low molecular weight chitosan used in this study while medium molecular weight chitosan being used by Al-Kassas *et al*. As the chitosan concentration increases with the viscosity, of which the crosslinking between chitosan and TPP are inefficient at high chitosan concentrations, eventually forming larger particles [249]. Furthermore, an interaction between chitosan concentration and the chitosan-TPP ratio was identified in the response surface model, which demonstrated that the nanogels formed were bigger at high chitosan concentration and high chitosan-TPP ratio. It is likely due to more chitosan and TPP being available, and thus more crosslinking was formed.

$$\boldsymbol{Size = -15.5125 + 562.125 \times CC + 11.535 \times CT - 1.6425 \times CT^2 + 23.875 \times CC \times CT}$$ **Equation 3-2**

On the other hand, polydispersity index is a less crucial factor in endocytosis in contrast to the size, as endocytosis is still feasible for chitosan-TPP nanogels even though a wide range of nanoparticles with different sizes were present [236,237]. Ma *et al.* successfully delivered large (> 400 nm) and polydisperse (PDI = 0.5) chitosan-TPP nanoparticles to human colorectal Caco2 cell lines [237]. However, from a pharmaceutical perspective, a successful nano-formulation should be stable, safe and effective. The preparation method should also be robust. Thus, the population of the nanocarriers should be as homogenous as possible. The PDI is a measure of the homogeneity of the nanoparticles in terms of size distribution [250], which is a value between 0 to 1 for the Malvern Zetasizer series. Hence, the smaller the PDI, the more uniform the size of the nanogels. A high PDI value (> 0.7) denotes a broad size distribution of the nanoparticles, which might indicate agglomeration of the nanoparticles or the presence of other contaminants.

PDI of the training set formulations was between 0.217 and 0.507, of which only four amongst these formulations were considered polydisperse (PDI > 0.4) and the rest of the formulations were moderately dispersed. The response surface model is shown in **Figure 3-2 (b)**, where chitosan concentration and chitosan-TPP ratio were identified to have a significant effect on the PDI of the nanogel formulations. The findings are similar to the trend observed in the study performed by Hosseinzadeh *et al.* [251]. It is likely due to more crosslinking formed at high chitosan concentration and high TPP concentration (i.e., Chitosan-TPP ratio), forming larger particles and agglomerating. Therefore, with larger particles being formed, the distribution of size for the nanogels was broadened and higher PDI was observed. However, their interaction was not significant, albeit it was estimated in the stepwise regression, which indicated that the nanogels are more polydisperse at high chitosan concentration and chitosan-TPP ratio, with no synergetic effect observed between these two factors.

$$\boldsymbol{PDI = 0.0128 + 0.781 \times CC + 0.037 \times CT}$$ **Equation 3-3**

3.3.2.2. Zeta potential

The nanogels are formed by ionic gelation between cationic chitosan and anionic TPP, where chitosan is used in excess compared to TPP. Therefore, nanogels are generally positively charged at acidic conditions with pH < 6, where the amine group on the chitosan are protonated. The ZP of nanogels is an important influencer on the colloidal stability of the nanogels, as the agglomeration of nanogels is attenuated by the electronic repulsion [251,252]. Nanogels with ZP values of 30 mV are generally stable in suspension due to the sufficient electronic repulsion between particles [253]. Zeta potentials of the nanogels from the training set as shown in **Table 3-4**, were in a range of 18 to 32 mV, which indicated that only a quarter of the nanogels formulations were stable due to the surface charge in the suspension.

All selected factors were found to have significant effects on the ZP of the nanogels. Positive coefficients were associated with the chitosan concentration and chitosan-propranolol ratio in **Equation 3-4**, which indicated that the ZP of nanogels increased with these parameters. As chitosan and propranolol consist of amine groups and are positively charged at pH 4.5, increasing chitosan and propranolol concentration will result in more positive charges on the nanogels particles. At high chitosan concentrations, the crosslinking between chitosan and TPP is ineffective, and thus the ZP is higher at high concentrations [249]. In contrast, TPP is an anionic molecule, of which increases in the chitosan-TPP ratio will lead to decreasing amount of TPP for crosslinking and reduction of the negative charge on nanogels, thus the ZP is inversely correlated to the chitosan-TPP ratio. These findings were in good agreement with the study conducted by Al-Kassas *et al.,* using the OFAT approach [208]. The DOE approach is more advanced and allows interactions and quadratic effects to be identified, compared to the OFAT approach. Therefore, several additional were identified influencing the zeta potential of the nanogels in the RSM model. A quadratic effect of the chitosan concentration is demonstrated in **Figure 3-2 (c) and (d)**, which illustrates that there is a maximum concentration for chitosan at 0.25% to achieve the highest zeta potential. Interactions between chitosan concentration and chitosan-TPP ratio as well as between chitosan concentration and chitosan-propranolol ratio were identified in the model, which demonstrated the

relationships amongst these factors, and the effect of chitosan concentration on the zeta potential is dependent on the other two factors.

$$\boldsymbol{ZP = -4.358675 + 198.113375 \times CC + 40.1244 \times CP - 0.562675 \times CT - 400.41 \times CC^2 - 144.25 \times CC \times CP + 8.406875 \times CC \times CT}$$

Equation 3-4

3.3.2.3. Encapsulation efficiency

Another crucial property of nanogels is their ability to encapsulate therapeutic molecules. The EE of propranolol in the nanogels formulation was between 10% to 40%, as shown in **Table 3-3**, which indicates the encapsulation process of propranolol was inefficient. On the contrary, Al-Kassas *et al.* reported that the EE in their study was over 85% [208]. The discrepancy is probably related to the nanogels formed using low molecular weight chitosan in this study. Chitosan concentration and chitosan-TPP ratio were found to have inverse effects on the EE, with low EE observed under high chitosan concentration and low chitosan-TPP ratio (i.e., high TPP concentration), as shown in **Figure 3-2 (e)**. It is likely due to the inefficient crosslinking at these conditions. Moreover, Whiteley *et al.* used a similar central composite design to predict the encapsulation efficiency of lysozyme in nanogels fabricated via microfluidics [197]. The EE of lysozyme in nanogels was higher, with at least 54% of the drug input. One likely reason to account for the discrepancy in encapsulation efficiency is that the molecular weights of propranolol and lysozyme are massively different at 259.34 Da and 14.3 kDa respectively, even though both are carrying a positive charge. Propranolol is, therefore, more likely to leach out from the nanogels, as compared to lysozyme. Moreover, the study identified different key factors on EE, which also revealed that the encapsulations of payloads are different between microfluidics and stirring.

$$\boldsymbol{EE = 0.3968470588 - 0.471 \times CC - 0.016 \times CT}$$

Equation 3-5

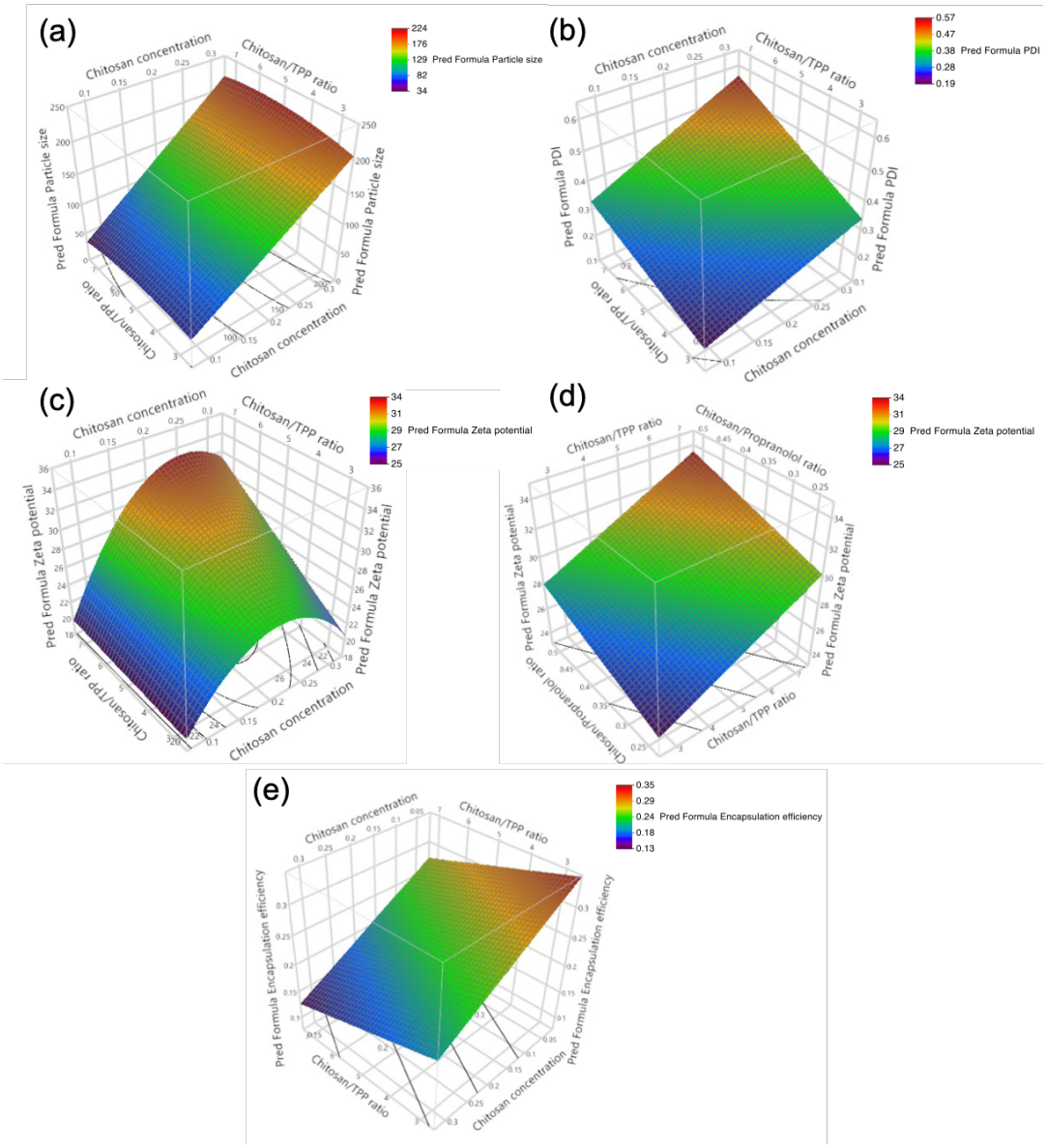

Figure 3-2. Response surface models predicting the effect of CC and CT ratio on (a) Z-average, (b) PDI and (e) EE. As the response surface and contour plots are only able to compare 2 factors at once, the model of ZP was presented in (c) and (d), showing the effect of CC against CT and CT ratio against CP respectively on ZP.

3.3.3. Multiple response optimisation

The optimal fabricating condition was determined by multiple response optimisation (MRO) as shown in **Figure 3-3**, aiming to achieve the highest EE and ZP, and the lowest size and PDI. The optimal running condition for nanogels production is at 0.10% chitosan concentration, a chitosan-TPP mass ratio of 3 and a chitosan-propranolol mass ratio of 0.5, as shown in **Figure 3-3**. The predicted size, PDI, ZP, and EE of nanogels produced at the optimal condition were 69.2 nm, 0.217, 25.3 mV, and 30.1% respectively while the measured results of the nanogels were 75.5 nm, 0.210, 31.4 mV, and 66.0%. The measured values were 9.1%, 2.8%, 24.1%, and 122.3% different from the predicted values, respectively. The high discrepancies between the measured and predicted values for EE demonstrate that the model did not give a good prediction and was dependent on the training set.

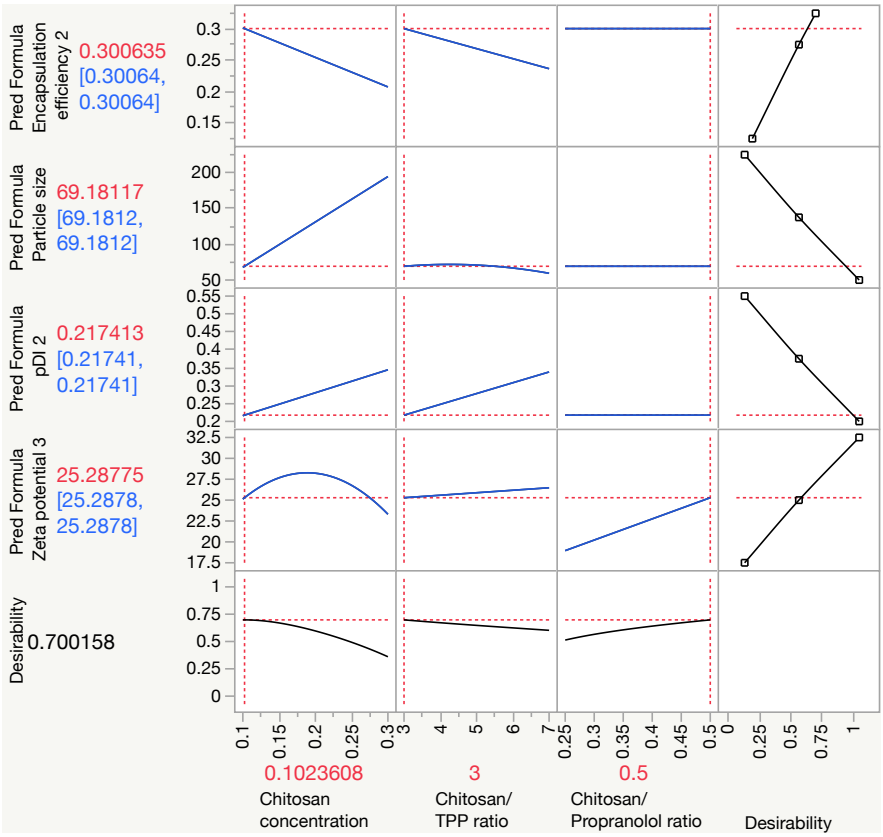

Figure 3-3. Prediction tool shows the relationship between the parameters and the properties of nanogels. The optimal condition for nanogel fabrications was shown on the x-axis (in red), whereas the corresponding nanogels properties were estimated and shown on the y-axis (in red).

3.3.4. Test sets and final formulations

Thirteen test set formulations were performed to determine the prediction accuracy of the models, with the measured and predicted results shown in **Table 3-4**. The regression coefficients of the test set (Q^2) were compared to those of the training set (R^2) for each parameter of nanogels. Good fitting is reflected on R^2 close to 1, while a similar R^2 and Q^2 indicate that the model was working independently from the training data set, which indicates the power of model prediction. Size and PDI models were good with a relatively high Q^2 value (> 0.6) compared to R^2 as shown in **Figure 3-4**, indicating high predictive accuracy. As these models work independently from the training data set, the model and mathematical equation could be used for prediction. Conversely, the models for ZP worked only on the training set and had limited predictive accuracies. An opposite trend is observed for the test set compared to the training set. Therefore, the model for ZP should not be used for prediction and as the criteria for final formulation. The R^2 and Q^2 for the EE model were low, which suggested that the model is not a good representation of the EE within the design space, nor it has a good prediction ability. Therefore, only the hydrodynamic size and PDI of the nanogels were predicted as shown in **Table 3-4** whilst the ZP and EE were only measured. The results elucidated the importance of verifying the models with test sets as the constructed models do not necessarily have the power of prediction.

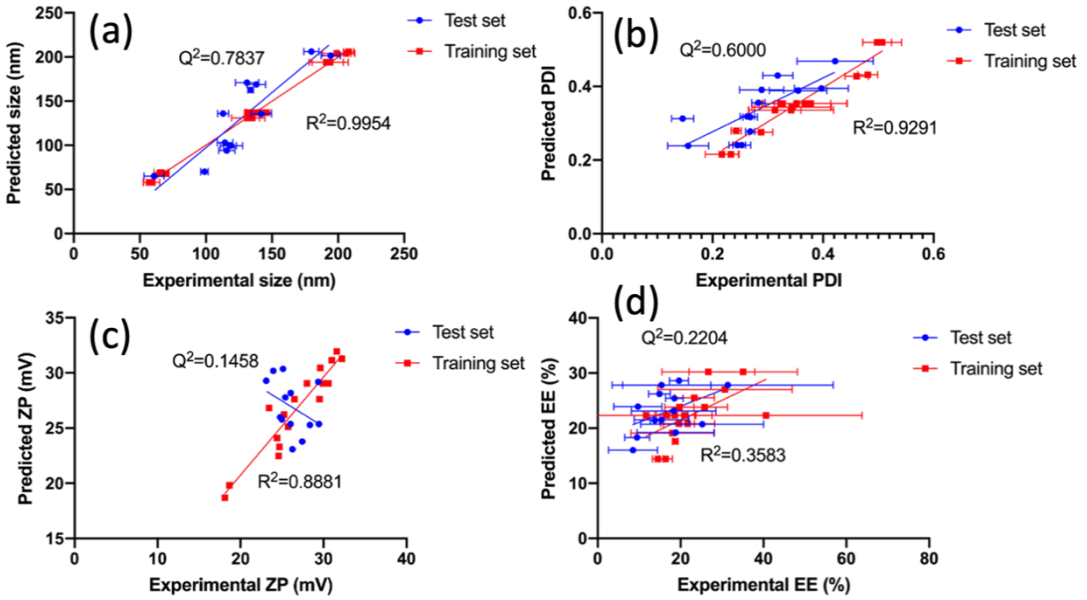

Figure 3-4. Correlations between measured and predicted values for the prediction of (a) size, (b) PDI, (c) ZP and (d) EE for the training set (in red) and test set (in blue) formulations. The coefficients of determination of the training set (R^2) and test set (Q^2) were determined to find out the degree of correlation between the experimental and predicted nanogels properties. R^2 close to 1 indicated a good fitting, while the proximity of R^2 and Q^2 demonstrated good predictability.

3.4. Application of the prediction models to other drugs

Nanogels were fabricated at the optimal condition identified in the model using a total of nineteen other drugs, where the drugs are divided into two groups based on the molecular similarity to propranolol. The measured size, PDI and zeta potential of the nanogels fabricated using structural distinct drugs with propranolol were shown in **Figure 3-5**. Dunnett's test was applied to the measured size, PDI and zeta potential of the nanogels fabricated with different drugs, which illustrated that the properties of the nanogels were different and were dependent on the choice of drugs. Moreover, the percentage differences between the predicted and measured size of nanogels ranged between 10% to 41%, whilst the counterpart in PDI was between 5% and 59%. The discrepancy between the predicted and measured values elucidated that the model does not apply to other drugs, and DOE optimisation should be performed when a different drug is used. These drugs are structurally distinct from each other (i.e., no structural activity relationship), possess different functional groups and thus are likely to interact

with chitosan and TPP in nanogels differently, influencing the properties of the nanogels. Albeit the distinct results from the propranolol-loaded nanogels, all other nanogels were between 70 and 120 nm in size and the PDI were between 0.2 and 0.4. The zeta potential of the nanogels was above 20 mV, which indicated that the nanogels were less stable than the propranolol-loaded nanogels but possessed some degree of colloidal stability. The results indicated that the size, PDI and ZP were different but remained in similar magnitudes, indicating properties of nanogels are partly dependent on the formulation.

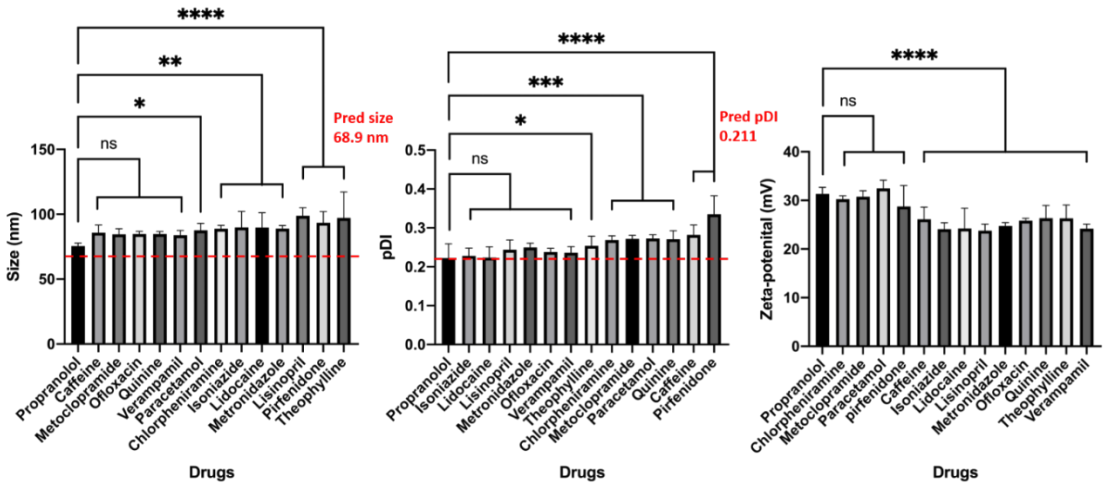

Figure 3-5. Measured size, PDI and ZP of the nanogels fabricated with a variety of drugs with no structural similarity with propranolol. The red dashed lines represented the predicted value from the model. Analysis of Variance (ANOVA) was performed to determine the significant difference between nanogels loaded with propranolol and other drugs. The error bar represents the standard deviation. * p-value < 0.05, ** p-value < 0.01, *** p-value < 0.001 and **** p-value < 0.0001. ns refers to a p-value > 0.05. All samples were fabricated at the optimal conditions, with chitosan concentration at 0.1% (w/v), a chitosan-TPP ratio of 3 and a chitosan-drug ratio of 0.5.

To investigate whether drugs with molecular similarities behaved differently, seven beta-blocker drugs with structure-activity relationships (SAR), including propranolol, were tested. All beta-blocker drugs had similar structures, the same number of acid and base groups, and pKa of pH ~ 9. Thus, at pH 4.5, the drugs were ionised and likely interacted with anionic TPP in the nanogels. However, there are also repulsions

between cationic chitosan and drugs, which could limit the encapsulation and decrease the drug loading. As the drugs and TPP are polar and possess a hydrogen acceptor and donor, these interactions are likely to play a role in drug loading. Multiple linear regressions and non-linear fittings were conducted to evaluate the correlations between the selected molecular descriptors and nanogel properties, which was shown in **Table 3-8**. Metoprolol was not included in the fittings, as the drug comes as a tartrate salt of which tartrate could also crosslink in chitosan nanogels [254]. Thus, the extra crosslinking may mask the effect of the drug itself. As the sample sizes were too small with only seven beta-blockers, these drugs were not sub-grouped into training and test sets.

Table 3-8. Estimated correlation coefficients (R^2) between selected molecular descriptors and properties of nanogels were calculated by the Row-wise method. $R^2 < 0.5$ referred to weak effect, $0.5 < R^2 < 0.7$ indicated moderate effects whilst $R^2 > 0.7$ indicated strong correlation. The estimated correlations with $R^2 > 0.7$ were highlighted in red. A negative value in R^2 indicated an inverse correlation and vice versa.

Drugs	Properties of nanogels		
	Size	PDI	ZP
Acebutolol	108.41	0.269	19.15
Atenolol	121.44	0.261	28.29
Betaxolol	104.17	0.274	20.64
Esmolol	89.27	0.243	27.90
Metoprolol	97.76	0.204	18.88
Nadolol	98.77	0.216	27.71
Pindolol	96.61	0.235	27.88
Propranolol	82.23	0.231	28.92

Molecular descriptors	Properties of nanogels		
	Size	PDI	ZP
nAcid	0	0	0
nBase	0	0	0
nHBd	0.4006	-0.3888	0.0986
nHBa	0.5786	0.3091	-0.4141
nRing	-0.4544	-0.4630	0.1544
nHeteroRing	-0.1207	-0.2456	0.2273
apol	0.1495	0.3918	-0.8015
bpol	0.1955	0.4989	-0.7985
WPATH	0.2508	0.5515	-0.8425
WPOL	-0.0846	-0.1859	-0.4219
XLogP	-0.7985	-0.1870	0.0087
ALogP	-0.5275	-0.3334	0.2914
TopoPSA	0.6740	0.1363	-0.1791
TopoDiameter	0.3126	0.7367	-0.7042
TopoShape	0.0444	-0.1610	-0.1702

Several strong linear correlations were estimated by the Row-Wise method, between some molecular descriptors and properties of nanogels. As the number of acids and bases in all tested beta-blockers are the same, the correlation coefficients were 0. Correlations with strong effects were estimated between XLogP and size, as shown in

Figure 3-6. Both ALogP and XLogP are atom-additive approaches to calculate the partition coefficient (LogP) theoretically, where XLogP is an enhanced modification of ALogP. The correlation coefficient (R^2) between the size and XLogP was 0.64 and the *p*-value was 0.0313, which demonstrated that the correlations were moderately strong and statistically significant. Hence, the nanogels are likely to be smaller in size when a beta-blocker with higher XLogP is used. As LogP is a measure of hydrophobicity, higher XLogP indicates higher hydrophobicity. Therefore, the observation elucidates that the nanogels size reduced with the hydrophobicity of beta-blockers. Another strong correlation was estimated between PDI and topological diameter (TopoDiameter), indicating a potentially strong influence of graph-theoretical sizes on the PDI of the nanogel as TopoDiameter is a measure of the maximum atom eccentricity. However, the *p*-values for the ANOVA and lack of fit were 0.0589 and 0.7043 respectively, which indicated that the relationship was well-fitted but was statistically insignificant. Other multiple correlations were estimated between the sum of all atomic polarizability (apol), the sum of the absolute value of the difference between atomic polarizabilities of all bonded atoms in the molecule (bpol), Wiener path number (WPATH), TopoDiameter with zeta potential. Apol and bpol are two measures of the polarizability of the drug, while WPATH is a topological descriptor, which is defined as the sum of the lengths of the shortest paths between all pairs of vertices in the chemical graphs [255]. The Wiener index helps to identify the branching, cyclicity and centricity of the compounds. The first three correlations were statistically significant, with a *p*-value of 0.0302, 0.0313, and 0.0173 respectively, whereas the correlation between TopoDiameter and ZP was not. All regression coefficients were over 0.6, which demonstrated that these correlations were moderately strong. The result revealed that the polarizability and molecular topography of the drug could potentially affect the zeta potential of the nanogels.

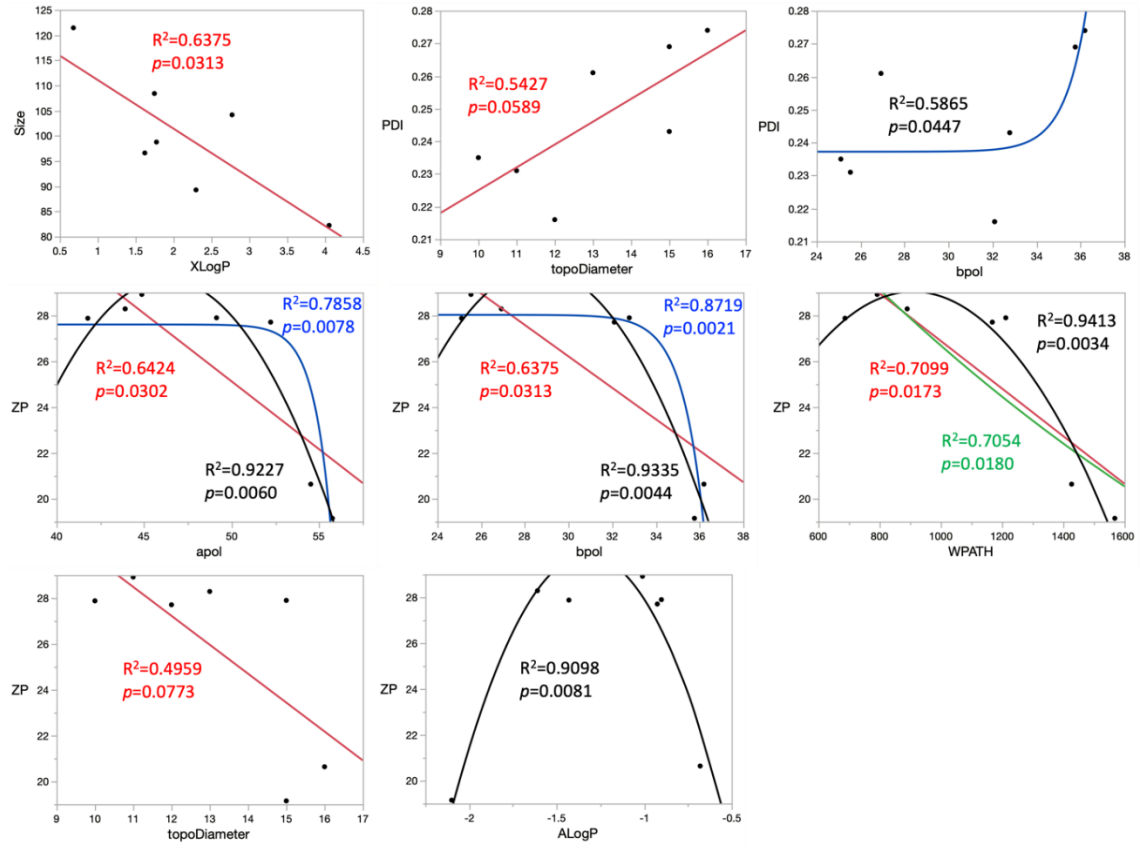

Figure 3-6. Linear regression and non-linear correlation plots between the nanogel properties and the selected molecular descriptors. Linear, logarithmic, exponential, and quadratic fittings were plotted in red, green, blue, and black respectively, with the correlation coefficient (R^2) and *p*-value for each fitting shown in the respective colour.

Non-linear correlations, such as logarithmic, exponential, and quadratic correlations were also fitted between the molecular descriptors and the nanogel properties. As with the linear regressions, the correlation coefficient for nAcid and nBase was 0. Interestingly, the exponential correlation between PDI and bpol was significant despite the moderate effect of the correlation, with a *p*-value of 0.0447 and an R^2 of 0.5865. The result revealed that the polarizability of the drugs impacted the PDI of the nanogels, potentially in an exponential growth fashion. Moreover, the interactions between apol, bpol, WPATH, and ZP could be fitted in other relationships, as shown in **Table 3-9**, with the quadratic correlations between these molecule descriptors and ZP deemed as the best fitting ($R^2 > 0.9$). However, the vertex of the quadratic fit could not be confirmed with the existing data set and thus is likely to be overfitted. Exponential fitting between apol and ZP, as well as bpol and ZP, were also good, with

p-values of 0.0078 and 0.0021, respectively. Hence, the result showed that these two factors could have negative exponential effects on the ZP, instead of linear relationships. Contrary, the exponential fit was invalid for WPATH and ZP, as there are invalid arguments. The quadratic fit was the best fit amongst all relationships, with the highest R^2. Both linear and logarithmic correlations were comparable and slightly above 0.7. With the existing data set, there is likely a quadratic correlation between the WPATH and ZP. Last but not least, a new correlation between ALogP and ZP was found in the quadratic fit, with a *p*-value of 0.0081 and an R^2 of 0.9098. The result indicates that hydrophobicity also influenced the ZP and the colloidal stability of the nanogels.

Table 3-9. Correlation coefficients (R^2) between selected molecular descriptors and properties of nanogels were calculated for each non-linear fitting method. The correlations with $R^2 > 0.7$ and *p*-value < 0.05were highlighted in red while the correlation with $R^2 < 0.7$ and *p*-value < 0.05 were highlighted in purple.

Fits		Logarithm			Exponential			Quadratic		
		Properties of nanogels								
		Size	PDI	ZP	Size	PDI	ZP	Size	PDI	ZP
Molecular descriptors	nAcid	0	0	0	0	0	0	0	0	0
	nBase	0	0	0	0	0	0	0	0	0
	nHBd	0.1437	0.1638	0.0010	0.0429	0.2881	0.0255	0.4358	0.4197	0.0513
	nHBa	0.3098	0.0915	0.1737	0.1945	0.1425	0.3345	0.3863	0.1078	0.2707
	nRing	0.2226	0.2266	0.0269	0.2065	0.2144	0.0238	0.2065	0.0573	0.0238
	nHeteroRing	0.0197	0.0546	0.0269	0.0146	0.0603	0.0517	0.0146	0.0603	0.0517
	apol	0.0125	0.1357	0.6367	0.1066	0.3594	0.7858	0.1777	0.3406	0.9227
	bpol	0.0243	0.2304	0.6261	0.0815	0.5865	0.8719	0.0390	0.5143	0.9335
	WPATH	0.0468	0.2848	0.7054	Invalid	Invalid	Invalid	0.0693	0.4290	0.9413
	WPOL	0.0131	0.0431	0.1836	0.0334	0.0204	0.1564	0.6451	0.0414	0.1805
	XLogP	0.6193	0.0348	0.0000	0.4521	0.0604	0.0518	0.6779	0.0369	0.2255
	ALogP	0.2828	0.1156	0.0095	0.2280	0.0387	0.0112	0.2925	0.4658	0.9098
	TopoPSA	0.4407	0.0165	0.0335	0.1023	0.2159	0.5063	0.4604	0.0325	0.0666
	TopoDiameter	0.0874	0.5306	0.4877	0.0201	0.5045	0.5498	0.1925	0.5859	0.6019
	TopoShape	0.0001	0.0321	0.0224	0.0015	0.0277	0.0271	0.1677	0.1996	0.2101

To summarise, the results indicate that the properties of the payload impacted the properties of nanogels. Interaction between the drugs and other components of nanogels is most likely to play a vital role in determining the nanogels properties in addition to the formulations. Thus, the loading of drugs in nanogels is not purely a simple entrapment inside the void. Drugs with diverse sizes and shapes could still be

encapsulated in the nanogels but altered the nanogel properties. Furthermore, most of the topological size and shape descriptors selected failed to influence the nanogel properties, which also supported the finding. Interestingly, since the structural difference between drugs is small for drugs with structural activity relationships, hence the interactions between nanogel and drugs remain similar. The constitutional descriptors selected did not impact the nanogel properties, which demonstrated that the hydrogen bonds and the heterocyclic and aromatic rings were not the key interactions or groups between the drugs and the carrier. Instead, the hydrophilicity, polarity and polarizability of the drugs were more important, which were found to impact the nanogel properties. With these correlations, the DOE models established could potentially be applied to similar drugs, to estimate the nanogels properties. In practice, for example, if the target payload is expensive or has limited availability, cheaper drugs with a SAR could be used to optimise the formulation and the optimum conditions could then be applied to the target payload.

As a proof-of-concept study, there are several limitations to this approach. First, only a small number of molecular descriptors were selected compared to approximate 1800 descriptors computed by PaDEL. Therefore, future use of machine learning could help identify molecular descriptors that have stronger and more non-linear correlations with the properties of nanogels, as well as from a larger pool of molecular descriptors. Despite the limitations, this study revealed that the established DOE models could be applied to similar drugs with the help of molecular descriptors. It also provided a deeper understanding of how drugs are loaded in nanogels as well as how payloads could impact the properties of nanogels.

3.4.1. Screening the effects of processing factors in nanogels fabrication

3.4.1.1. Definitive Screening Design (DSD)

The factors with linear effects were first screened in the definitive screening design for each nanogel property (size, PDI, ZP and EE), followed by the factors with quadratic and interaction effects. The processing parameters were estimated to have effects on nanogel properties using the profilers shown in **Figure 3-7**. Temperature, the total volume of the solution, stirring speed, grade of chitosan and choice of crosslinkers were estimated to impact the size of the nanogels, while temperature and

the choice of crosslinker also influenced the PDI of nanogels. Furthermore, ZP was likely to be dependent on the chitosan grade and interestingly the size of the stirrer. Nevertheless, the addition rate of the crosslinker and glass vial volume was expected to affect the encapsulation efficiency in the nanogels. These results revealed that these processing factors could also impact the nanogels properties, in addition to the formulation composition and drug loading.

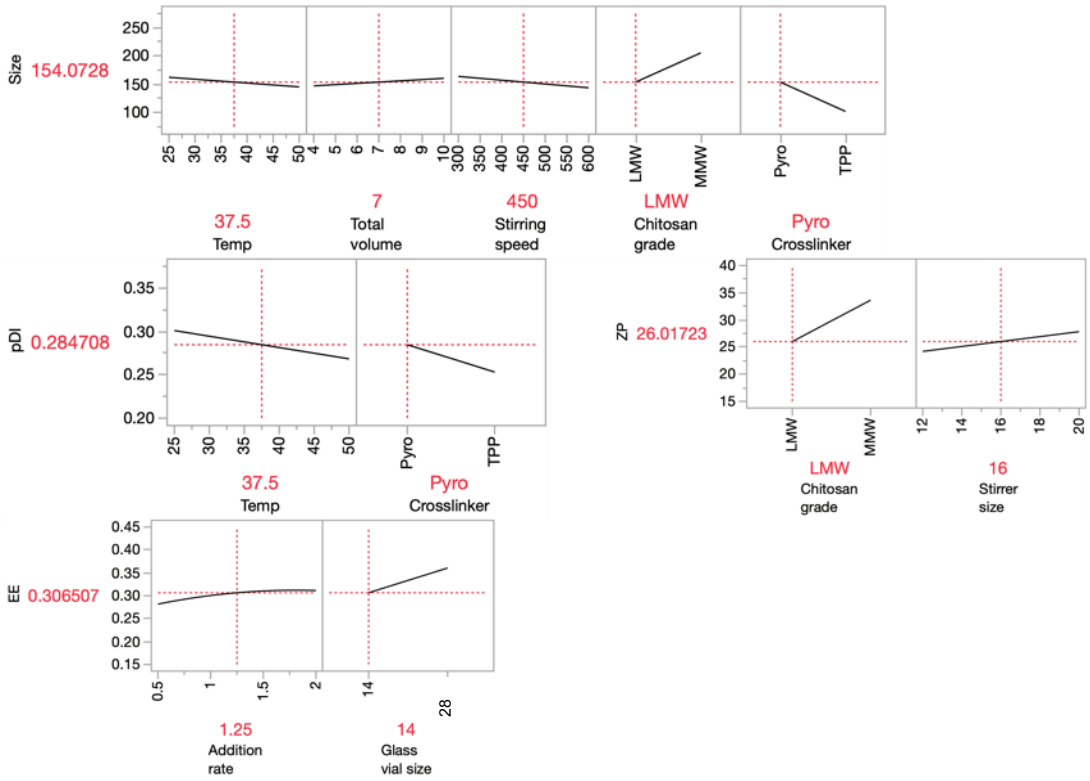

Figure 3-7. Profilers show the effect of the factors identified from the DSD on each nanogels property. The predicted correlation was present as the solid black line. At the experimental conditions mentioned on the x-axis of the profiler and in red, the corresponding predicted nanogel properties were in red on the y-axis of the profiler.

3.4.1.2. Response surface methodology

The estimated parameters were then used to construct a model via stepwise regression, with a 5-fold cross-validation. For size, two interactions (T x CR and T x SR) and total volume (TV) were removed from the model to avoid overfitting. A one-way analysis of variation (ANOVA) and lack of fit test was then performed on the linear regression models for each individual dependent variable to determine the statistical significance and the goodness of fit of these models on the training set. The null hypothesis of the ANOVA is that the nanogel properties do not correlate

with the parameters. The results of the ANOVA and lack of fit tests are reported in **Table 3-10**. *p*-values obtained in the ANOVA test for all the models were smaller than 0.05, demonstrating the significance of the correlations between the training set and the models. Furthermore, the *p*-values in the lack of fit tests for all models were larger than 0.05, which indicate these models were a good fit for the training set data. As discussed above in **Section 3.3.4**, a good fit with the training data does not indicate good predictability. A test set is usually performed to determine the predictability, but it was not performed in this study as the final aim of the study focused on identifying the optimal condition only, instead of predicting the properties. In short, the results indicated that the models were well-fitted to the data set and the correlations between the processing factors and the properties of nanogels were significant. Hence, an optimal condition was obtained from the multiple response optimisation.

Table 3-10. ANOVA and lack of fit test results for the DSD models for various independent variables. The significance of each term used in constructing the model were also reported. Statistical significance was set as Prob. > F being smaller than 0.05.

Independent variables	Source of variations	Degree of freedom	Sum of squared	Mean squares	F value	Prob.> F	Significance
Size	**Model**	5	37432.870	7486.570	43.225	<0.0001	**Significant**
	T	1	2526.010		14.584	0.0011	*s*
	SR	1	2180.853		12.591	0.0020	*s*
	CS	1	16225.800		93.682	<0.0001	*s*
	CR	1	16416.877		94.785	<0.0001	*s*
	T X CS	1	1978.637		11.424	0.0030	*s*
	Residual	20	3764.03	173.20			
	Lack of fit	14	2848.699	203.478	1.984	0.2046	**Not significant**
	Pure error	6	615.334	102.556			
PDI	**Model**	2	0.013	0.007	14.076	0.0001	**Significant**
	T	1	0.006		12.274		*s*
	CR	1	0.006		13.526		*s*
	Residual	23	0.011	0.000			
	Lack of fit	3	0.000	0.000	0.062	0.9764	**Not significant**
	Pure error	20	0.011	0.001			
EE	**Model**	2	0.0024	0.012	8.119	0.0021	**Significant**
	AR	1	0.007		4.727	0.0402	*s*
	GV	1	0.019		12.692	0.0017	*s*
	Residual	23	0.0341	0.001			
	Lack of fit	3	0.003	0.001	0.5524	0.6524	**Not significant**
	Pure error	20	0.031	0.002			
ZP	**Model**	2	421.314	210.657	11.650	0.0003	**Significant**
	CS	1	373.803		20.673	0.0001	*s*
	SS	1	72.002		3.982	0.05810	*ns*
	Residual	23	415.884	18.082			
	Lack of fit	3	29.797	9.932	0.5145	0.6770	**Not significant**
	Pure error	20	386.087	19.304			

Where T is temperature, SR is stirring rate, CS is chitosan grade, CR is crosslinker choice, AR is addition rate, GV is glass vial volume and SS is stirrer size.

3.4.2. Effect of processing factors on the nanogels properties

3.4.2.1. Z-average

The nanoparticles in **Table 3-6** were in a range of 100-250 nm, despite the fabrication conditions varying dramatically. The results echoed the previous observations in the sections above, which also demonstrated the size of the nanogels were partially dependent on the formulations, where the formulation of the nanogels was fixed in this study. Thus, the sizes of nanogels remained similar. In the definitive screening design, temperature, stirring rate, grade of chitosan, and choice of crosslinker were found to have significant effects on the Z-average of nanogels, as presented in **Table 3-10**. The interaction between temperature and chitosan grade (T x CS) also significantly impacted the size.

In macroscopic terms, the propranolol nanogels were fabricated by mixing chitosan and crosslinker solutions under stirring, where the fluid motion and mixing of the two solutions could be described by the Rankine vortex model [210]. The model involved a swirling flow of viscous fluid, which was the chitosan solution with the forced vortex generated in the centre and a free vortex surrounding it. Nevertheless, in microscopic terms, the mixing and gelation process is still governed by diffusion and could also be described as nucleation. Thus, the nanogels properties are likely dependent on how well the chitosan and crosslinker solutions are mixed under stirring.

The size of nanogels decreased with temperature and stirring speed, as shown in **Figure 3-8 (a)**. At high stirring speed and high temperature, the sizes of nanogels are reduced. The vortex increased with the stirring speed, which improved the turbulence and subsequently the mixing effect of the two solutions. Thus, the chitosan was more readily available to interact with the crosslinker, resulting in more nucleation and smaller particles being formed. Similar results were observed by Hussain *et al.* for this stirring speed range, where the particle size of chitosan TPP nanoparticles decreased with the stirring speed varying from 200 to 700 rpm [256]. However, the group also found that the effect of stirring speed on the nanoparticle size was a V-shape or quadratic effect. Thus, the size of nanoparticles increased

when the stirring speed further increased from 700 rpm to 1000 rpm. This observation was likely due to the poor mixing effect when the vortex was too deep and reached the impeller. The power was absorbed by the liquid and the mixing was inefficient. Another possible explanation was that the shearing generated at these stirring speeds was too weak to break up the agglomerated nanoparticles, as the fluid was in a circular motion only. Hence, larger particle size was observed. At high temperatures, the viscosity of the chitosan solution reduced at high temperature in particular, which allowed better mixing between the crosslinker solution and chitosan solution and resulted in a larger surface area between the chitosan and crosslinker. In addition, the diffusibility of the chitosan and crosslinkers were increased under high temperature. More nucleation was present and thus the size of the nanogels was smaller. Interestingly, the result demonstrated an opposite trend to the study conducted by Kamat *et al.,* where the nanoparticles obtained at 4 ^{o}C were smaller in size and had a narrower distribution compared to 27 and 35 ^{o}C [213]. The difference in observations might be due to the different fabrication processes of the nanogels. Kamat *et al.* fabricated the nanogels in the pipette tips without stirring at a microlitre scale, while nanogels were produced by stirring in this study with a millilitre scale. Thus, temperature influenced the nucleation stage in the former study, while the temperature was likely impacting the mixing of the two components before nucleation in this study.

Choice of crosslinkers was also found to impact the size, with nanogels formed with pyrophosphate being larger than those formed by TPP. It is likely due to alterations of the crosslinking between chitosan and crosslinkers. Pyrophosphate is a diphosphate carrying only four negative charges while TPP refers to triphosphate, which bears five negative charges. Hence, the electrostatic interactions between chitosan and pyrophosphate are weaker than those between chitosan and TPP. As a consequence, the nanogels were less contracted due to electrostatic interaction. In addition, the coordination of the crosslinkers was thought to be different between the pyrophosphate and TPP, where a TPP molecule arranged in a V-shape and interacted with the amine group on chitosan to form two crosslinks per molecule. In contrast, pyrophosphate interacted with anime groups on chitosan and formed one crosslink per molecule [257]. Furthermore, the chitosan-pyro nanogels retained colloidal

stability even at a high pyro concentration, while chitosan-TPP nanogels would form aggregates and coagulate when the TPP concentration was high. Thus, the size of chitosan-TPP nanogels was larger than the chitosan-pyro nanogels [258]. Lastly, chitosan grade was found to impact the size, with LMW chitosan producing smaller nanogels than MMW chitosan. It is probably related to the higher viscosity of the MMW chitosan solution than that of the LMW chitosan solution. Thus, the LMW chitosan was mixed better than the MMW chitosan solution and subsequently produced smaller nanogels.

$$\boldsymbol{SIZE = 216.8 - 0.069SR - 0.863 \times T - 3 \times CS\begin{pmatrix} LMW & 9.517 \\ MMW & -9.517 \end{pmatrix} + 0.08 \times T \times CS\begin{pmatrix} LMW & 9.517 \\ MMW & -9.517 \end{pmatrix} + CS\begin{pmatrix} LMW & -25.209 \\ MMW & 25.209 \end{pmatrix} + CR\begin{pmatrix} Pyro & 25.357 \\ TPP & -25.357 \end{pmatrix}}$$

Equation 3-6

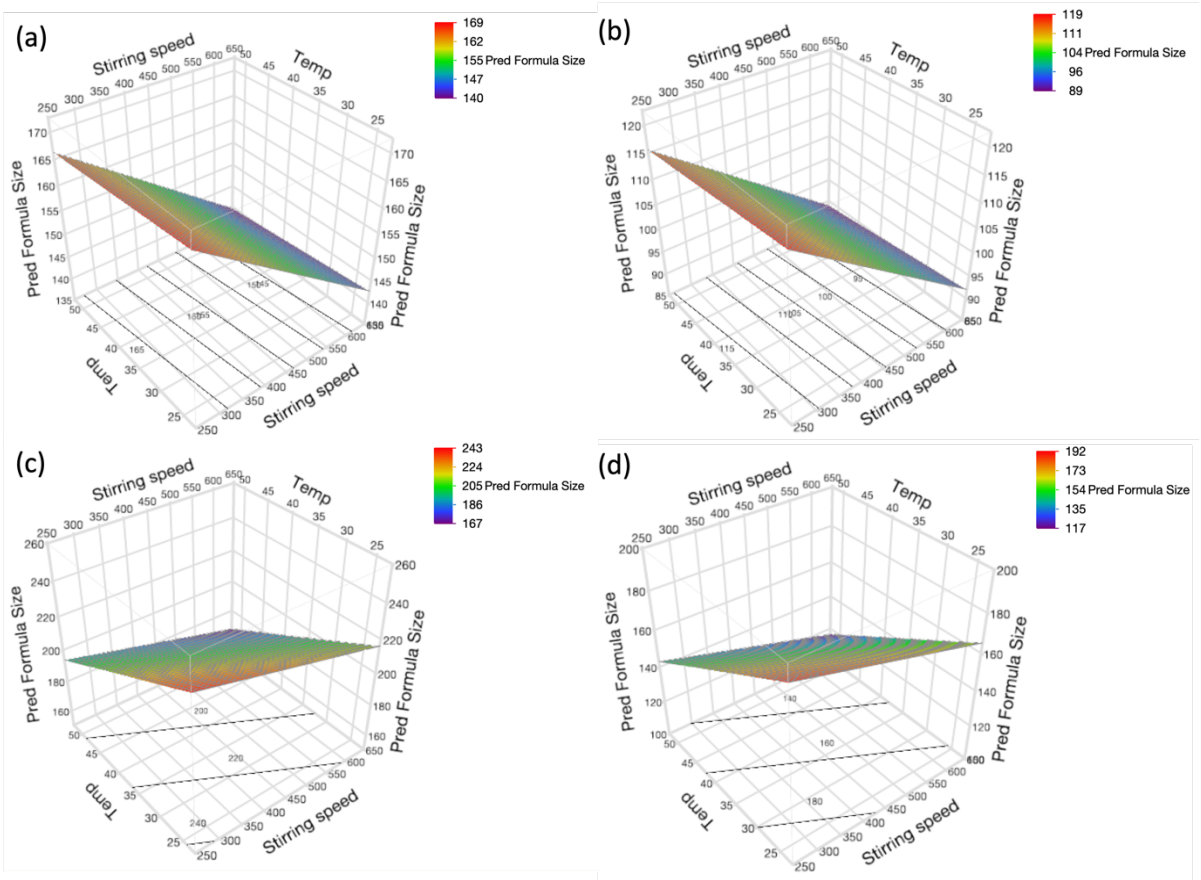

Figure 3-8. Response surface models predicting the effect of temperature and stirring rate on the size of the nanogels at four different combinations of chitosan grade and crosslinkers, as the response surface plots, could show the continuous factors only. Thus, the surface plots were presented in 4 combinations, namely (a) LMW chitosan and pyrophosphate, (b) LMW chitosan and TPP, (c) MMW chitosan and pyro, and (d) MMW chitosan and TPP.

3.4.2.2. PDI

From a pharmaceutical perspective, a successful nano-formulation should be stable, safe, and effective, and the preparation method should be robust. Thus, the population of the nanocarriers should be as homogenous as possible. The PDI is a measure of the homogeneity of the nanoparticles in terms of size distribution [250], which is a value between 0 to 1 for the Malvern Zetasizer series. Hence, the smaller the PDI, the more uniform the size of the nanogels. A high PDI value (> 0.7) denotes a very broad size distribution of the nanoparticles, which might indicate agglomeration of the nanoparticles or the presence of other contaminants.

PDI of the nanogels shown in **Table 3-3** was between 0.218 and 0.355, of which all formulations were considered moderately dispersed. Temperature and crosslinker choice were the only processing factors found to affect the PDI of the nanogels, as shown in **Table 3-10**. At high temperatures, the mixing was improved as the viscosity of the chitosan solution and crosslinker solution was lowered. Furthermore, the diffusibility of both chitosan and crosslinkers was higher. The nucleation was more, and the particles were smaller in size. Thus, the particle size distribution was narrower at high temperatures, and thus the PDI decreased with temperature. Moreover, the choice of crosslinkers was equally important, with higher polydispersity obtained with pyrophosphate than with sodium triphosphate. It is probably related to the stronger interaction between chitosan and TPP compared to that with pyrophosphate. The particles are more contracted by the electrostatic force and thus the particle size distribution was narrower, resulting in lowering the PDI.

$$\boldsymbol{PDI = 0.318 - 0.001 \times T + CR\begin{pmatrix} Pyro & 0.016 \\ TPP & -0.016 \end{pmatrix}} \qquad \textbf{Equation 3-7}$$

3.4.2.3. Zeta potential

The nanogels are formed by ionic gelation between cationic chitosan and anionic crosslinkers, where chitosan is used in 3-fold of the crosslinkers. Therefore, nanogels are generally positively charged at acidic conditions with pH < 6, where the amine group on the chitosan are protonated. The ZP of nanogels is an important influencer on the colloidal stability of the nanogels, as the agglomeration of nanogels is attenuated by the electronic repulsion [251,252]. Nanogels with ZP values of 30 mV are generally stable in suspension due to the sufficient electronic repulsion between particles [253]. Zeta potentials of the nanogels from the data set as shown in **Table 3-3**, were in a range of 17 to 38 mV, which indicated that around half of the nanogels formulations were colloidally stable due to the surface charge repulsions in the suspension.

Only the grades of chitosan were found to have significant effects on the ZP of the nanogels. Stirrer size was first estimated to affect the ZP of nanogels but failed the statistical test in the end. The chitosan grade was classified as a categorical data set

in this study, as the chitosan was different in terms of molecular weight and deacetylation efficiency. The higher ZP in nanogels fabricated with MMW chitosan was likely due to the higher deacetylation efficiency, as shown in **Section 3.2.2**. Deacetylation efficiency indicated the proportion of free anime groups on the chitosan, which would be protonated at the fabricating pH. Thus, the higher the deacetylation efficiency, the more pronated the chitosan. Thus, the MMW chitosan was more cationic than LMW chitosan at pH 4.5 and the surface charge was neutralised by the anionic crosslinker to a lesser degree, resulting in higher ZP.

$$\boldsymbol{ZP = 22.617 + 0.454 \times SS + CS\begin{pmatrix} LMW & -3.805 \\ MMW & 3.805 \end{pmatrix}} \qquad \textbf{Equation 3-8}$$

3.4.2.4. Encapsulation efficiency

The EE of propranolol in the nanogels formulations after varying the fabrication factors was between 16% to 40%, as shown in **Table 3-3**, which were similar to those reported in **Section 3.3.2**. The results indicated the encapsulation process of propranolol was not altered by varying the fabricating factors, and thus the encapsulation efficiency remained similar. In conjunction with the previous chapter, the encapsulations were inefficient, as a consequence of the charge repulsions between the cationic chitosan and propranolol. The addition rate of crosslinker solution and glass vial volume were found to have proportional effects on the EE, with high EE observed at a high addition rate and when a large container was used. It is likely due to the faster the addition rate, the more TPP or pyrophosphate available for crosslinking. Hence, the gelation process was faster, and more propranolol could interact with the TPP or pyrophosphate at the beginning of the gelation stage, which enhanced the encapsulation efficiency in the nanogels. Interestingly, the encapsulation efficiency was also dependent on the glass vial volume, with nanogels fabricated in the larger glass vial (volume = 28 mL) possessing higher encapsulation efficiency. Glass vial volume was considered as a categorical data set, as the radius and height of the glass vial changed simultaneously for the larger glass vials and no intermediate size was found between the two vial sizes. The higher encapsulation efficiency using a larger vial is probably related to the vortex mixing, where the radius (r) of the container plays an important role. The velocity of the flow decreased with $1/r^2$ outside the vortex. The larger the radius of the vial, the slower the velocity

and thus more time was available for propranolol to interact with the crosslinkers and encapsulation during the gelation process.

$$EE = 0.295 + 0.024 \times AR + GV \begin{pmatrix} 14 & -0.027 \\ 28 & 0.027 \end{pmatrix} \quad \textbf{Equation 3-9}$$

3.4.3. Comparison between different chitosan grades and crosslinkers

The training sets and test sets were reported in **Sections 3.3.2 and 3.3.4** to construct the response surface profile and verify the models, where LMW chitosan was used. The same formulations were repeated with MMW chitosan under the same condition. Instead of constructing another response surface model, the results from the training set and test set were grouped as a single data set, followed by a statistical test to determine the differences between the properties of nanogels fabricated with different chitosan grades. The properties of the nanogels fabricated using both LMW and MMW chitosan were summarised in **Table 3-11**.

Table 3-11. Nanogels were fabricated using different chitosan grades with the formulations in the training and test sets, with the details of experimental conditions shown for each formulation. Properties of the fabricated nanogels were measured and reported as mean ± SD, based on three independent results (n = 3).

Experiment conditions			LMW chitosan				MMW chitosan			
Chitosan conc. (%w/v)	**Chitosan/ TPP ratio**	**Chitosan/ Propranolol ratio**	**Size (nm)**	**PDI**	**ZP (mV)**	**EE (%)**	**Size (nm)**	**PDI**	**ZP (mV)**	**EE (%)**
0.2	3	0.375	135.3 ± 5.5	0.243 ± 0.009	23.45 ± 2.64	23.3 ± 12.3	201.4 ± 15.5	0.365 ± 0.051	31.80 ± 0.34	37.8 ± 5.2
0.2	5	0.25	135.6 ± 5.3	0.367 ± 0.076	29.53 ± 1.36	40.6 ± 27.7	193.1 ± 5.4	0.356 ± 0.055	35.87 ± 2.09	36.6 ± 3.1
0.2	5	0.375	132.3 ± 2.7	0.378 ± 0.066	28.01 ± 0.97	11.7 ± 11.4	197.1 ± 7.9	0.395 ± 0.048	34.69 ± 1.45	37.6 ± 2.2
0.2	5	0.375	138.6 ± 4.5	0.352 ± 0.062	29.95 ± 1.76	18.6 ± 10.1	217.1 ± 12.7	0.413 ± 0.036	35.33 ± 2.19	36.3 ± 3.2
0.1	5	0.375	65.6 ± 5.2	0.288 ±0.021	24.59 ± 7.43	30.7 ± 20.2	101.7 ± 4.7	0.302 ± 0.024	31.50 ± 5.07	55.2 ± 3.2
0.1	3	0.5	69.8 ± 1.4	0.233 ± 0.015	25.73 ± 3.34	35.1 ± 20.6	122.5 ± 3.5	0.279 ± 0.012	32.38 ± 2.56	55.1 ± 9.2
0.3	5	0.375	208.1 ± 3.9	0.481 ± 0.018	26.49 ± 7.00	18.7 ± 10.8	295.8 ± 20.5	0.518 ± 0.038	37.49 ± 1.40	35.4 ± 2.8
0.2	5	0.375	135.2 ± 4.8	0.327 ±0.037	30.59 ± 2.32	16.5 ± 9.3	191.3 ± 3.1	0.330 ± 0.007	35.02 ± 3.67	42.7 ± 7.6
0.2	5	0.5	146.4 ± 3.7	0.323 ±0.028	29.62 ±1.46	20.9 ± 11.8	204.7 ± 10.6	0.367 ± 0.053	34.14 ± 8.61	38.4 ± 4.2
0.1	7	0.25	59.4 ± 6.1	0.342 ± 0.077	18.67 ± 4.38	19.7 ± 10.3	109.6 ± 1.7	0.426 ± 0.030	37.10 ± 1.88	38.7 ± 4.5
0.3	3	0.25	194.4 ± 3.7	0.343 ± 0.072	24.38 ± 0.73	21.7 ± 12.1	295.3 ± 26.5	0.502 ± 0.083	32.35 ± 2.39	39.0 ± 5.2
0.3	7	0.25	198.6 ± 10.8	0.498 ±0.026	31.58 ± 1.57	14.5 ± 7.3	342.8 ± 35.3	0.555 ± 0.020	38.39 ± 2.52	35.2 ± 3.1
0.3	7	0.5	206.2 ± 6.7	0.507 ±0.035	31.02 ± 2.45	16.4 ± 8.3	348.5 ± 14.0	0.561 ± 0.029	41.03 ± 8.48	47.9 ± 4.7
0.2	7	0.375	132.0 ± 12.6	0.461 ± 0.021	32.23 ± 3.55	18.0 ± 12.1	183.4 ± 8.8	0.423 ± 0.048	34.77 ± 8.48	35.4 ± 4.6
0.1	3	0.25	65.0 ± 1.8	0.217 ± 0.030	18.11 ± 8.10	26.7± 16.2	123.5 ± 1.3	0.274 ± 0.005	34.31 ± 3.13	41.0 ± 5.6
0.3	3	0.5	190.8 ± 12.9	0.345 ±0.069	24.69 ± 1.19	19.6 ± 10.3	307.9 ± 24.7	0.544 ± 0.112	34.52 ± 0.67	43.4 ± 6.8
0.1	7	0.5	56.8 ± 4.4	0.313 ± 0.047	25.25 ± 5.86	25.8 ± 13.7	110.1 ± 8.6	0.413 ± 0.068	35.90 ± 4.68	46.1 ± 4.9
0.15	4	0.25	114.4 ± 5.9	0.268 ± 0.008	27.44 ± 4.48	14.9 ± 2.6	187.5 ± 569	0.327 ± 0.026	38.78 ± 1.40	72.4 ± 3.9
0.25	4	0.375	138.1 ± 7.0	0.283 ± 0.012	25.42 ± 3.76	15.4 ± 6.6	198.3 ± 40.5	0.343 ± 0.067	35.52 ± 2.10	70.7 ± 4.4
0.25	6	0.25	131.1 ± 8.8	0.318 ± 0.027	25.12 ± 3.77	9.5 ± 3.0	254.5 ± 36.3	0.574 ± 0.320	38.89 ± 2.16	75.8 ± 4.1

0.1	4	0.5	98.9 ± 2.8	0.156 ± 0.037	29.46 ± 3.23	19.6 ± 2.3	165.6 ± 4.3	0.291 ± 0.004	37.01 ± 1.51	71.4 ± 4.7
0.15	3	0.375	118.1 ± 4.9	0.245 ± 0.015	26.03 ± 1.84	15.4 ± 11.9	241.6 ± 2.1	0.456 ± 0.007	36.01 ± 1.13	70.8 ± 3.7
0.3	6	0.5	179.8 ± 5.7	0.422 ± 0.069	29.36 ± 2.72	8.5 ± 5.9	348.7 ± 10.2	0.543 ± 0.026	40.83 ± 2.66	74.6 ± 3.9
0.15	3	0.25	119.3 ± 8.4	0.253 ± 0.016	26.26 ± 1.29	31.4 ± 25.4	168.9 ± 12.1	0.298 ± 0.025	36.58 ± 0.83	74.9 ± 3.7
0.2	4	0.5	113.0 ± 4.2	0.268 ± 0.013	23.10 ± 4.66	9.7 ± 5.8	209.5 ± 21.7	0.366 ± 0.061	40.28 ± 1.38	74.0 ± 5.2
0.2	6	0.375	107.6 ± 5.9	0.289 ± 0.040	23.95 ± 6.26	25.2 ± 14.8	198.+ ± 9.7	0.336 ± 0.010	37.05 ± 2.12	78.0 ± 9.0
0.1	6	0.5	60.7 ± 7.6	0.146 ± 0.020	24.79 ± 2.49	18.5 ± 2.1	103.2 ± 3.8	0.333 ± 0.037	36.07 ± 3.53	72.2 ± 5.1
0.15	7	0.375	115.8 ± 6.1	0.355 ± 0.052	26.06 ± 7.11	13.8 ± 1.1	171.4 ± 14.8	0.395 ± 0.048	41.94 ± 3.27	69.4 ± 6.8
0.25	3	0.25	133.8 ± 2.1	0.263 ± 0.013	24.99 ± 3.72	18.3 ± 10.2	223.1 ± 16.5	0.412 ± 0.033	31.11 ± 0.51	67.9 ± 3.0
0.3	4	0.5	194.4 ± 7.3	0.397 ± 0.049	28.36 ± 2.30	18.8 ± 9.3	385.7 ± 24.7	0.589 ± 0.110	41.33 ± 1.16	71.2 ± 2.2

Significantly different in PDI (p = 0.0027), hydrodynamic size, zeta potential, and encapsulation efficiency (p < 0.0001) were observed for nanogels fabricated with different chitosan grades, with the result of the F-test and t-test shown in **Table 3-12**. Interestingly, these results suggest that different grades of chitosan have effects on all the properties of nanogels, whereas the result in **Section 3.3.2** demonstrated the effect of chitosan grades on the size and ZP of nanogels. The difference is probably related to the poor ability of the definitive screening design to identify the marginal effects. By comparison, nanogels produced using LMW chitosan are smaller in size (131.5 ± 8.1 nm) and less poly-disperse (0.330 ± 0.015) than those fabricated under the same condition using MMW chitosan, where the size and PDI of the MMW chitosan-TPP nanogels were 213.4 ± 14.4 nm and 0.410 ± 0.017, respectively. However, the encapsulation in the LMW chitosan fabricated nanogels is less efficient (20.0 ± 1.4%) than those prepared by the MMW chitosan (54.8 ± 3.0%). It is likely due to a smaller size in nanogels fabricated with LMW chitosan, which has a smaller capacity to accommodate the drug. Moreover, the zeta potential of nanogels is lower when LMW chitosan (26.57 ± 0.62 mV) is used for fabrication, compared to those of MMW chitosan (363.26 ± 0.54 mV). The finding showed that the nanogels produced with LMW chitosan are more prone to agglomeration, compared to their counterparts made from MMW chitosan.

Table 3-12. F-test and T-test results comparing the effect of using different chitosan for fabrication on the properties of the nanogels formed. *p*–value < 0.05 was deemed statistically significant. The results demonstrated the differences in nanogel properties were statistically significant when different chitosan was used for fabrication.

		F-test to compare variances			**T-test**							
Properties	**CS**	**F**	***p*-value**	**Sig.**	**Mean**	**SD**	**Mean difference**	**SE difference**	**T**	**df**	***p*-value**	**Sig.**
Size (nm)	LMW	3.174	0.0027	Yes	131.5	8.1	-81.9	16.5	4.967	45	<0.0001*	Yes
	MMW				213.4	14.4						
PDI	LMW	1.305	0.4786	No	0.330	0.016	-0.080	0.023	3.40	58	0.0012	Yes
	MMW				0.410	0.023						
ZP (mV)	LMW	1.280	0.5106	No	26.57	0.62	-9.69	0.82	11.79	58	<0.0001	Yes
	MMW				36.27	0.54						
EE (%)	LMW	4.915	<0.0001	Yes	20.0	1.4	-34.8	3.3	10.49	40	<0.0001*	Yes
	MMW				54.8	3.0						

* T-test was conducted with Welch's correction as F-test to compare variances with the group is significant.

Altering the crosslinkers could also impact the properties of nanogels. Apart from the two crosslinkers used above, phytic acid sodium (PAS, aka. inositol hexaphopshate) was used as the crosslinkers in nanogels, which potentially allow the non-linear and non-planar crosslinking between the chitosan chains, constructing a more complex three dimensional structure. In addition, the number of phosphate groups in PAS was double of the TPP and triple of the pyrophosphate, which allows more crosslinking to be formed per crosslinking molecule. The structure of these crosslinkers is shown in **Figure 3-1**.

A one-way ANOVA was performed on the size, PDI, and the zeta potential of the nanogels fabricated with different crosslinkers. The result revealed that there were differences in size, PDI, and the zeta potential of nanogels fabricated with various crosslinkers ($p < 0.001$). The nanogels fabricated with PAS were the largest, while those with TPP were the smallest. The large size of particles was fabricated with PAS as it has the highest molecular weight, indicating that the number of molecules available for crosslinking for the same mass of crosslinker was fewer. Therefore, the number of nuclei was fewer, and the particles grew larger. In contrast, pyrophosphate carried lower charges and interacted differently with chitosan [257], which contracted the nanogels less and resulted in larger particles compared to chitosan-TPP nanogels.

In terms of polydispersity, there was no significant difference between nanogels fabricated with TPP and PAS. However, the nanogels fabricated with pyrophosphate were significantly more polydisperse than those with TPP or PAS. It is likely due to the weaker ability of pyrophosphate to contract the nanogels, resulting in larger size distribution. Furthermore, the lowest and highest ZP were measured in pyrophosphate and PAS nanogels respectively. The ZP of nanogels was likely related to the charge and molecular weight of the crosslinkers. Each Pyro, TPP and PAS molecule carries four, five and, twelve negative charges, but their molar masses were 265.90, 367.86, and 932.82 g/mol, respectively. Thus, under the same mass ratio of the chitosan-crosslinker ratio, more pyrophosphate was available for crosslinking and neutralising the positive charges on chitosan. Conversely, the PAS

has the highest charge and molecular weight, resulting in a fewer number of molecules for crosslinking. Despite PAS carrying the highest number of charges, the number of molecules available for crosslinking and neutralising the positive charge of chitosan was the lowest amongst all crosslinkers. Thus, the overall net charge on the nanogel was the highest.

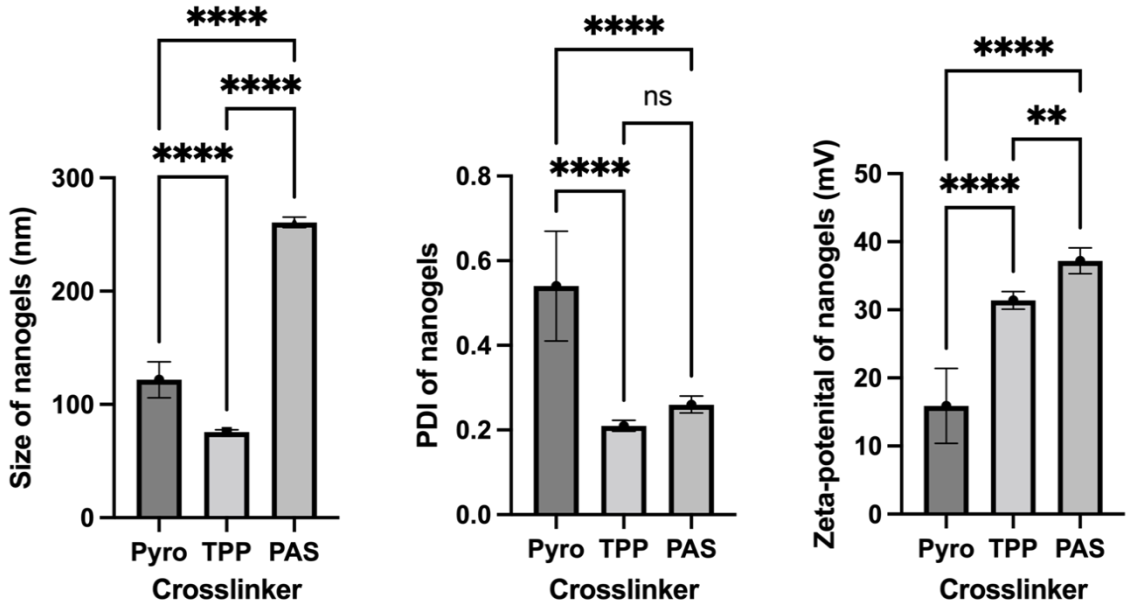

Figure 3-9. Size, PDI and ZP of nanogels fabricated with different crosslinkers. ** *p*-value = 0.042, while **** *p*-value < 0.001. The results showed the size, PDI and zeta-potentials of the nanogels fabricated with various crosslinkers were different.

3.4.4. Multiple response optimisation

Unlike the central composite design used in **Section 3.3.2**, both screening and response surface methodology could be performed with a single model of definitive screening design, as discussed in **Sections 3.4.1 and 3.4.2**. Thus, an optimal fabricating condition could also be determined by multiple response optimisation (MRO), based on the established correlations. The MRO aimed to maximise EE and ZP and lower Z-average and PDI. The profilers in **Figure 3-10** summarised all correlations between nanogel properties and the processing factors. A horizontal line in the profiler indicated no correlation between the nanogel properties and the respective processing factors, whereas a slope indicated a linear relationship. Each response was converted into a desirability function ranging between 0 and 1 as

discussed in **Section 3.2.4**. They were shown in the last column in **Figure 3-10** for each response. The optimal fabrication for nanogels production was shown in red on the x-axis, of which the overall desirability of the optimal condition was shown as 0.749. The optimal condition utilised MMW chitosan and TPP, with an additional rate for TPP solution at 2 mL/min. The solution was then stirred at a temperature of 50 ^{o}C, stirring speed of 600 rpm. The volume of the glass vial used was 28 mL while the stirrer size was 20 mm. The predicted properties of nanogels fabricated at this condition were presented in red and shown on the y-axis, which was 132.7 nm, 0.237, 35.5 mV, and 36.9% for the predicted size, PDI, ZP, and EE, respectively. However, the measured results of the nanogels were 113.6 ± 5.8 nm, 0.215 ± 0.009, 20.9 ± 7.2 mV, and 58.9 ± 5.2%, which were -16.8%, -10.2%, -69.9%, and 59.6% different from the predicted values, respectively. The high discrepancies between the measured and predicted values for ZP and EE indicated that other factors that were not included in the models impacted these properties, even though more factors in processing factors were included. Alternatively, the results might demonstrate that the encapsulation efficiency and zeta potential could not be effectively predicted and was partly random. In short, an optimal fabrication condition was obtained from the DSD, with the experimental size and PDI close to the predicted value. ZP and EE were not effectively predicted, as high differences between the measured and predicted values were obtained.

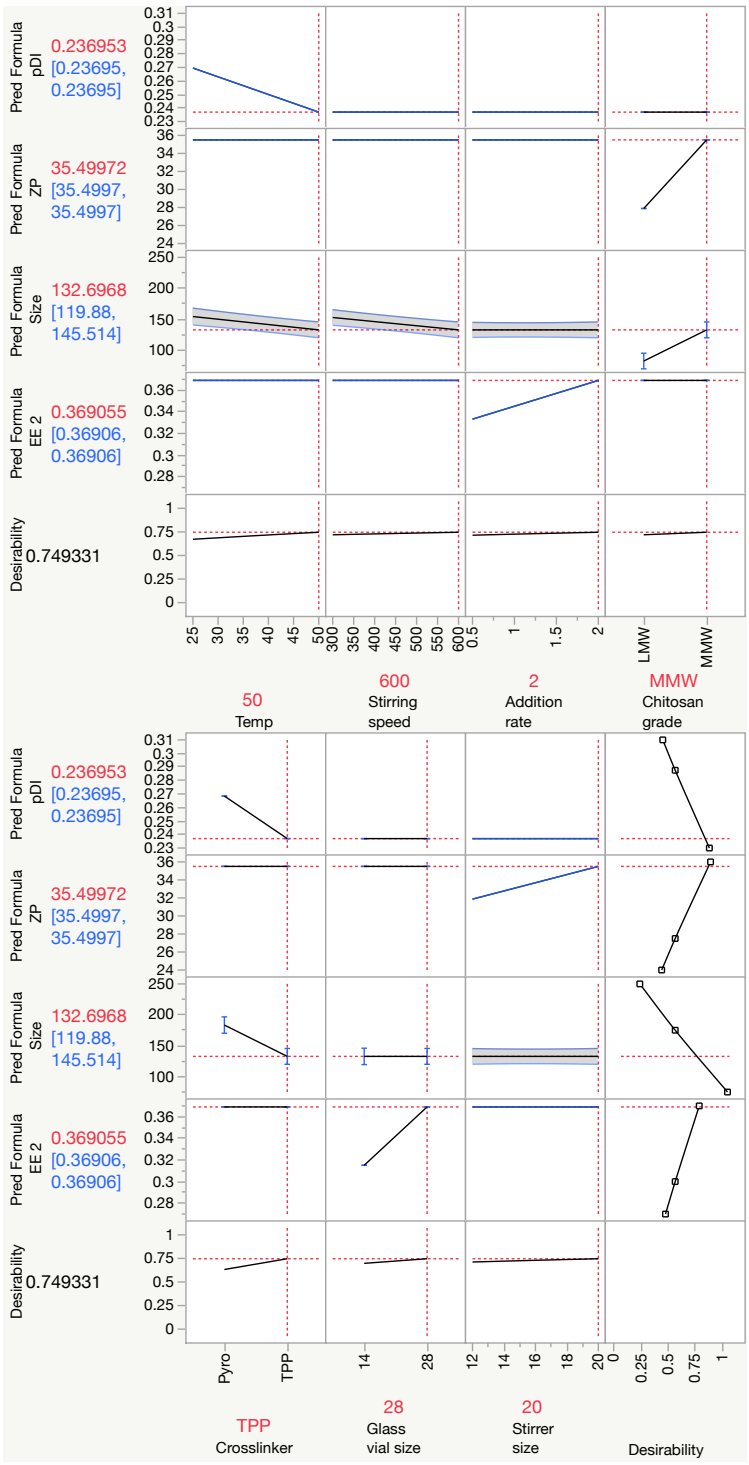

Figure 3-10. The prediction tool shows the relationship between the parameters and the outcome and the optimal condition for nanogel fabrications. The predicted correlation was present as the solid black line in the profiler. At the experimental conditions mentioned on the x-axis of the profiler and in red, the corresponding predicted nanogel properties were in red on the y-axis of the profiler. The overall desirability was shown as 0.749 for this experimental condition, against the prerequisite criteria set for each nanogel property.

3.4.5. Scaling-up of the nanogels fabrication

After determining the formulation and fabricating condition, the scaling-up process of the nanogels was investigated. As the total volume was not estimated to impact the nanogels properties in the definitive screening design, it is expected that the nanogels could be scaled up by increasing the volume pro-rata. The optimal fabrication conditions and formulation identified above were used to fabricate the nanogels. 4 volumes of total volume ranging from 2 to 20 mL were used. Total volume refers to the sum of volumes for chitosan solution and TPP solution in a 1:1 ratio, where 4 mL was used in all studies above and as the control. Size, PDI, ZP and EE of the nanogels were measured and shown in **Figure 3-11**.

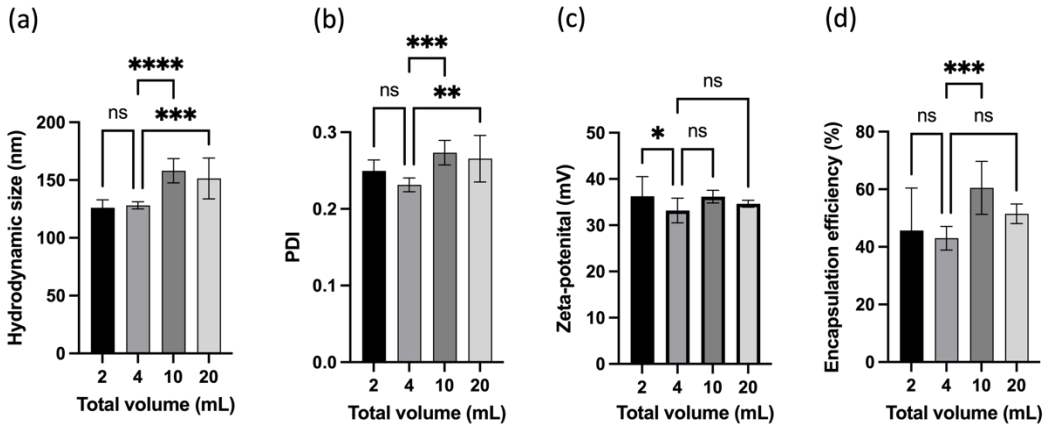

Figure 3-11. Properties of nanogels fabricated with different total volumes at the optimal formulation and fabrication condition. The ANOVA demonstrated a significant difference in the measured properties when different total volumes of nanogels were used for fabrication. The results of multiple comparisons between sub-groups were denoted in the figure. ns denoted not significant, * referred to $p < 0.05$, ** $p < 0.01$, *** $p < 0.001$while **** $p < 0.0001$.

A one-way ANOVA with Dunnett's multiple comparison test was performed to determine the difference in the nanogel properties when the total volume varied. When the total volume increased from 4 mL to 10 and 20 mL, the size and PDI of the nanogels also increased significantly. Conversely, when the total volume decreased from 4 mL to 2 mL, the difference in size and PDI was insignificant. Interestingly, the zeta potential of the nanogels showed an opposite trend, where the

zeta potential of the nanogels did not change with increasing total volume but increased with scaling down. No difference was observed between nanogels fabricated at 2 and 20 mL. However, the encapsulation efficiency was increased when the total volume changed from 4 to 10 mL. In short, the results demonstrated that changing the volume pro-rata in nanogels fabrication also altered the nanogels properties, despite the use of an identical fabrication condition and formulation. Thus, nanogels fabrication could not be scaled up by increasing the volume pro-rata.

3.5. Conclusion

The effect of formulation, drug loading and the processing factors in the fabrication of the properties of propranolol-loaded nanogels were evaluated using the DOE approach. First, the effect of the formulation in terms of chitosan concentration, chitosan-TPP ratio and chitosan-propranolol ratio were determined against the hydrodynamic size, PDI, ZP, and EE of the nanogels. The optimal formulation of 0.1% chitosan concentration, a chitosan-TPP ratio of 3 and a chitosan-propranolol ratio of 0.5 was predicted. The measured Z-average and PDI of the nanogel were similar to the predicted values. However, ZP and EE were not predicted as the predictability of these models were weak, indicating the importance of performing a test set. To evaluate the application of these prediction models to different drugs, the nanogels loaded with other drugs were fabricated at the optimal condition in the model with twelve structurally distinct and six structurally similar drugs. All measured properties were distinct from the predicted value but were of similar magnitude, which indicated that the DOE models must be refined when a new drug is used and the nanogels properties were partly related to the formulations. Nevertheless, relationships were found between structurally related drugs and performance parameters, indicating that encapsulation and nanogel formation processes are indeed drug-dependent and are not simply a matter of incorporation into inter-chain voids. The interactions between the nanogels and drugs are important mechanisms for encapsulation, which also govern the properties of nanogels. Finally, the processing factors in the nanogel fabrication were also shown to impact the properties of nanogels, which demonstrated that the scaling-up process of the nanogels fabrication process is not simply via increasing the volume pro-rata. Lastly, the optimal fabricating condition for nanogels utilised MMW chitosan and

TPP. The additional rate for TPP solution was set at 2 mL/min while the solution was then stirred at a temperature of 50 ^{o}C, stirring speed of 600 rpm. The volume of the glass vial used was 28 mL while the stirrer size was 20 mm.

In short, the effects of the drug loading, formulation, and processing factors on the nanogel properties were systematically evaluated in this chapter. The optimal formulation and fabricating conditions were also established, where nanogels were successfully prepared accordingly. Although nanogels could be produced with controllable and predicted properties, it is pivotal that these materials are biocompatible, especially in a localised environment of the pericardium. The cytotoxicity effect of these materials is not well understood and thus this area is explored in more detail using location-specific cells in the following experimental chapter.

Chapter 4

Determining the cytotoxicity of the propranolol-loaded nanogels using *in vitro* cell studies

4. Determining the cytotoxicity of the propranolol-loaded nanogels using *in vitro* cell studies

4.1. Introduction

Intrapericardial delivery is a novel delivery route and thus no existing *in vitro* cell model is reported at the time of writing. Therefore, all studies, as shown in **Table 1-6**, were performed directly on animals without performing any *in vitro* cytotoxic essay in advance. As such, there is an unmet need to develop a suitable *in vitro* cell model for the delivery route, to facilitate the development of intrapericardial therapies. During the intrapericardial delivery, the first layer of cells in contact with the pericardial fluid and drugs is the pericardium, thus understanding the likely cytotoxicity on the epicardium is particularly crucial for this route. The next layer is the myocardium, composed of cardiomyocytes. Cardiomyocytes are the target cell type for the payload and thus it is important to evaluate the cytotoxicity of the nanogels with them. However, due to cardiomyocytes being unavailable for this project, H9c2 cardiomyoblasts were used instead of cardiomyocytes. Hence, these cells were selected to model the cellular interactions following intrapericardial delivery. Although L929 fibroblasts are derived from subcutaneous connective tissue originating from the areolar of rats, they have been used extensively as a cell line to determine cytotoxicity according to the ISO 10993-5 standard, and thus they are also used for comparison in this study [259].

This chapter focuses on determining the cytotoxicity of the propranolol-loaded nanogels using *in vitro* cell studies with epicardial cells, H9c2 cardiomyoblasts and L929 fibroblasts. Propranolol-loaded nanogels were fabricated according to the optimal conditions and formulation established in **Chapter 3**. First, the cellular toxicity of the propranolol-loaded nanogels, drug-free nanogels and propranolol was established on epicardial cells. Finally, the cytotoxicity of the nanogels was assayed in the three cell lines described above to determine if epicardial cells are more sensitive and more suitable to be an *in vitro* model for determining the cytotoxicity in the intrapericardial route than other cell lines such as L929 and H9c2.

4.2. Materials and Method

4.2.1. Materials

High glucose Dulbecco's Modified Eagle's Medium with Glutamax (DMEM), fetal bovine serum (FBS), 5% streptomycin-penicillin solution and 0.05% trypsin-EDTA solution were purchased from ThermoFisher Scientific (Gibco; Waltham, MA, USA). Trypan blue was purchased from Sigma Aldrich (St Louis, MO, USA). T75 cell culture flasks and clear flat-bottomed 96-well plates were purchased from Grenier Bio-One (Kremsmünster, Austria). T225 cell culture flasks were purchased from Coning (Hartford, CT, USA).

4.2.2. Propranolol-loaded nanogels fabrication

Propranolol-loaded chitosan nanogels were using the optimal experiment condition established in **Chapter 3**. The optimal fabrication condition was identified as the chitosan concentration fixed at 0.1% w/v while the chitosan-TPP ratio and chitosan-propranolol ratios were 3 and 0.5, respectively. Thus, a TPP solution of 0.333 mg/mL was prepared by dissolving the respective amount of TPP in HPLC grade water and was then filtered with a 0.22 μm syringe filter. MMW chitosan was used in this study, with the chitosan first dissolved in 1% acetic acid solution until it formed a clear solution, followed by adjustment of the pH to pH 4.5 with 0.1M sodium hydroxide solution. Chitosan solution was filtered through a 0.22 μm syringe filter before use. Propranolol HCl was weighed and dissolved in the chitosan solution before the addition of the TPP solution. An equal amount of TPP solution was added dropwise to the chitosan solution under stirring at 2 mL/min. The temperature of the solution was maintained at 50 ^{o}C, while the solution was stirred at 600 rpm for 1 hour. The prepared nanogels were then kept in a fridge at 4 ^{o}C when the cytotoxicity tests were not performed on the same day. All nanogels were prepared and tested in triplicate.

4.2.3. *In vitro* cell culture

Cells were grown in T75 flasks unless otherwise specified in the individual section. They were incubated in a PHCbi carbon dioxide incubator (MCO-170AICD; PHC, Tokyo, Japan) at 37 ^{o}C and 5% carbon dioxide. When confluency of 70-80% was

reached, the cells were first washed with PBS and then passaged by treating with 1.5 mL of a 0.05% trypsin-EDTA solution for 5 minutes. 5 mL of complete medium was added to suspend the cells and inhibit the activity of trypsin, followed by centrifugation at 1,000 x g for 5 minutes (Eppendorf; Hamburg, Germany). The cell pellet was resuspended in a complete medium and divided 1:3 - 1:4 into fresh flasks.

4.2.3.1. *H9c2 cardiomyoblasts*

The rat cardiomyoblast cell line (H9c2) was a kind gift from Prof. Gareth Williams (UCL School of Pharmacy, London). The cells were cultured in a T75 and T225 flask pre-treated with 0.2% gelatine solution. The cells were cultured in a complete medium, consisting of Dulbecco's modified Eagle's medium-high glucose with Glutamax (DMEM) and supplemented with 10% (v/v) heat-inactivated fetal bovine serum (FBS), and 1% (v/v) antimycotic-antibiotic solution (100x). Attention was given to the cell morphology over consecutive passages, which can be altered with increasing passage numbers [260]. The passage number of H9c2 used in the study was between 4 and 11.

4.2.3.2. *Epicardial/mesothelial cells and L929 fibroblast cells*

Rat epicardial/mesothelial cells were a kind gift from Dr Caroline Pellet-Many (Royal Veterinary College, London). The cells were isolated from rats, as described by Wada *et al.* and Eid *et al.* [261,262]. On the other hand, L929 cell lines are immortalised subcutaenous fibroblasts from mice. Both cells were cultured in a complete medium consisting of Dulbecco's modified Eagle's medium-high glucose (DMEM) with 2 mM glutamate and supplemented with 10% (v/v) heat-inactivated fetal bovine serum (FBS), and 1% (v/v) streptomycin-penicillin solution (100X). Epicardial cells between passages 1 and 5 were used while the passage number of L929 was between 9 and 13 in this study.

4.2.4. Inverted light microscopy

Imaging of the cells was performed using an EVOS® FL imaging system (ThermoFisher Scientific, Waltham, MA, USA). The flask containing cells and medium was placed on the microscope stage and imaged at 20X and 40X magnifications.

4.2.5. Cell viability assays

Three different cell viability assays were performed for propranolol and propranolol-loaded nanogels on epicardial cells, namely PrestoBlue® assay, 3-(4,5-dimethylthiazol-2-yl)-2,5-diphenyltetrazolium bromide (MTT) assay, and Bromodeoxyuridine (BrdU) assay. Both MTT and PrestoBlue® assays determine cell viability in terms of cell metabolic activity. Therefore, the response from the assay is conventionally determined as cell viability in literature with two assumptions. First, a positive correlation was assumed between cell metabolic activity and the number of cells. Secondly, the tested agent does not suppress metabolic activity. As the effect of propranolol on the cell metabolic activity was unknown, the metabolic activity was used as the response in the section below. On the other hand, BrdU measured cell proliferation via measuring the incorporation of BrdU in cell division.

Time-dependent and concentration-dependent cytotoxicity of propranolol and propranolol nanogels was investigated. Cells were seeded into flat-bottomed 96-well plate tissue culture plates at a density of 10,000 cells per well for MTT, PrestoBlue®, and BrdU assays. The cells were allowed to equilibrate in the wells for 24 hours before incubation with the nanogels and propranolol. The propranolol and nanogels were first dissolved in a complete culture medium and then filtered through a 0.22 μm syringe filter for sterilisation. After 24 hours, the old culture medium was removed and replaced with 100 μL of the complete medium containing nanogels or propranolol at various concentrations and incubated for 24, 48 and 72 hours. The concentration range for propranolol, drug-free nanogels and propranolol-loaded nanogels were 0.010-2.500, 0.005-1.333, and 0.007-1.670 mg/mL respectively, where the solutions were prepared by serial dilutions.

However, only PrestoBlue® was performed when comparing the sensitivity of various cell lines, as the test was simpler to perform compared to the MTT assay given that more cell lines were experimented with. PrestoBlue® offers some advantages over MTT, including living cell viability monitoring, a simpler and faster procedure than MTT assay, as the cell lysis step was not required. Boncler *et al*. demonstrated that the MTT assay and PrestoBlue® (fluorometric assay) showed comparable results [263]. Data from the tests were analysed using GraphPad Prism

15. The data sets were first normalised. Statistical significance of differences between formulations was evaluated by two-way ANOVA using the Bonferroni post-hoc test. The significance level was set at *p*-value < 0.05.

4.2.5.1. PrestoBlue® assay

PrestoBlue® (PB) cell viability reagent is a resazurin-based cell viability reagent that allows live-cell viability determination. In brief, as the reagent was supplied as a 10X solution, it is diluted 10-fold with the media to a 1X solution. 100 µL of the diluted solution was added to the 96-well plate with cells and incubated at 37 ºC for 2 hours. The excitation wavelength was set at 560 nm whiles the fluorescence at 590 nm was measured using a SpectraMax M2e spectrophotometer (Molecular Devices Inc., Sunnyvale, CA, USA).

$$\boldsymbol{Cell\ metabolic\ activity}\ (\%) = \frac{\boldsymbol{F590_{sample} - F590_{background}}}{\boldsymbol{F590_{control} - F590_{background}}} \times \mathbf{100}\%$$

Equation 4-1

4.2.5.2. MTT assay

(3-(4,5-Dimethylthiazol-2-yl)-2,5-diphenyltetrazolium bromide (MTT) assay monitors the metabolic activity of the cells. It is used as a cell viability measurement where the metabolic activities are proportional to the number of viable cells present. MTT assay was performed using a CellTiter 96 Non-radioactive cell proliferation assay kit (Promega, Madison, WI, USA). The assay kit was performed as described in the protocol by the manufacturer. In brief, the media with the testing agents (100 µL) were retained in the well after incubation for 24-72 hours. 15 µL of the dye solution was added to each well. The plate was then incubated at 37 ºC for 4 hours, followed by the addition of 100 µL of the solubilisation/stop solution. The plate was then incubated at 37 ºC overnight to dissolve the formazan. Absorbance at 570 nm was measured using a SpectraMax M2e spectrophotometer (Molecular Devices Inc., Sunnyvale, CA, USA). Reference wavelength at 630 nm was also monitored. The background was also measured with empty wells containing the media, dye solution and solubilisation/stop solution.

$$\boldsymbol{Cell\ metabolic\ activity}\ (\%) = \frac{\boldsymbol{A570_{sample} - A570_{background}}}{\boldsymbol{A570_{control} - A570_{background}}} \times \mathbf{100}\%$$

Equation 4-2

4.2.5.3. ELISA for BrdU incorporation assay

Bromodeoxyuridine (BrdU) incorporation in the cells during DNA synthesis was determined using a commercial cell proliferation assay kit (Roche Diagnostics, Mannheim, Germany, Cat. No. 11647229001). The kit was performed as directed by the protocol provided by the manufacturer. In brief, after incubating with the test agents in a volume of 100 µL per well for 24 hours, 10 µL of BrdU solution was added to the wells and subsequently re-incubated for 2 hours. The labelling medium was first removed by tapping off. 200 µL of FixDenat solution was then added to each well, followed by incubation at ambient temperature for 30 minutes. After fixing the cell, the FixDenat solution was removed by tapping and 100 µL of the anti-BrdU-POD solution was added and incubated for another 90 minutes. Subsequently, the antibody conjugates were removed by tapping and the wells were rinsed with PBS solution 3 times. The washing solutions were removed and 100 µL of the substrate was finally added. After 30 minutes, the absorbances at 370 nm (target wavelength) and 470 nm (reference wavelength) were measured by a SpectraMax M2e spectrophotometer (Molecular Devices Inc., Sunnyvale, CA, USA).

4.3. Results and Discussion

The optimal fabricating condition was determined by multiple response optimisation (MRO) in **Section 3.2.4**, aiming to achieve the highest EE and ZP, and the lowest Z-average and PDI. The optimal fabrication for nanogels production utilised MMW chitosan and TPP, with an additional rate for TPP solution at 2 mL/min. The solution was then stirred at a temperature of 50 ^{o}C and a stirring speed of 600 rpm. The volume of the glass vial used was 28 mL while the stirrer size was 20 mm. The measured results of the nanogels were 113.6 ± 5.8 nm in size, with PDI of 0.215 ± 0.009, ZP of 20.9 ± 7.2 mV, and EE of 58.9 ± 5.2%.

4.3.1. Morphology of the cells under a light microscope

The morphology of the cells was observed and imaged using an inverted light microscope. **Figure 4-1** shows the morphology of epicardial/ mesothelial cells, H9c2 and L929 cells when cultured under control conditions. The epicardial/ mesothelial cells appeared as polygonal "cobblestone' morphology as shown in **Figure 4-1**, which became a continuous epithelial monolayer at confluency. The morphology of the cells corresponds with descriptions reported by Eid *et al.* and Wada *et al*. [261,262]. The morphology of H9c2 cells is highly dependent on the passage number, with the cells changing from spindle to ameboid in shape. Witek *et al*. reported that H9c2 cells remain spindle-shaped for the first 5 passages, whilst the nuclei were enlarged, and the cell appeared ameboid shape after ten passages [260]. In **Figure 4-1 (b)**, H9c2 cells were at passage 3. They appeared mostly spindle shape and the nuclei remained small, echoing the findings of Witek *et al*. L929 exhibited heterogeneous morphology, with cells appearing in spindle-like, epithelial-like, stellate and round shapes [264], as shown in **Figure 4-1 (c)**.

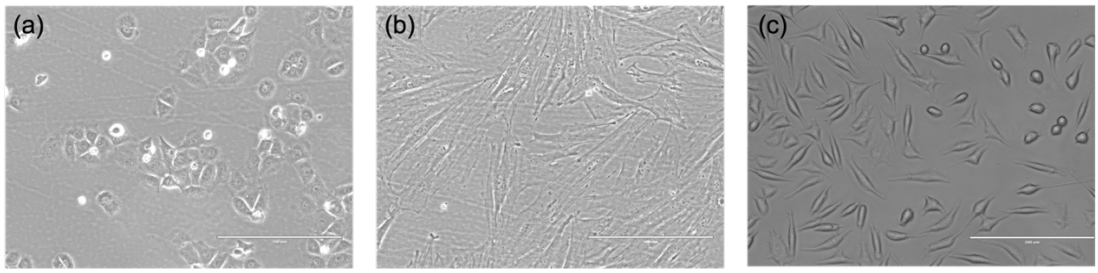

Figure 4-1. Light microscopy of (a) epicardial/ mesothelial cells, (b) H9c2 cardiomyoblasts and (c) L929 fibroblasts. The former two were sub-confluent while the L929 was confluent. The magnification was at 20X, while the scalebar was at 200 μm.

4.3.2. Biocompatibility of propranolol-loaded nanogels

Intrapericardial delivery is a novel administration route, so most of the reported studies investigated the route via animal testing [5–7,169,170]. No *in vitro* cell model has been previously described in the literature. However, animal studies are expansive in terms of maintenance, animal costs and require personal, project licenses and ethical approval, leading them not suitable for screening drugs and formulations. *In vitro* cell studies are thus useful for these purposes, owing to a much

lower maintenance cost and simple procedures. Therefore, the biocompatibility of the nanogels was tested with the epicardial cells, L929 and H9c2 cells *in vitro*.

4.3.2.1. Time and dose-dependent suppression of metabolic activity on epicardial cells

To investigate the cellular effects of propranolol, drug-free nanogel and propranolol-loaded nanogel on epicardial cells, the cells were incubated with increasing concentrations of propranolol (0.005 to 2.500 mg/mL, equivalent to 33 to 8375 μM), drug-free nanogel (0.005 to 1.333 mg/mL) and propranolol-loaded nanogel (0.007 to 1.667 mg/mL) for 24 hours, as shown in **Figure 4-2**. The viability of epicardial cells was determined using the MTT assay, which is based on measuring cell metabolic activity. The assay shows that the metabolic activity of the propranolol-treated epicardial cells was 70% of the control cells (< 33.8 μM, which is equivalent to 10 μg/mL). However, the metabolic activity dropped to below 20% of the control cells at and above 67.6 μM (20 μg/mL) These data indicate there was a dose-dependent effect on cell metabolism for propranolol on the epicardial cells.

IC50 is defined as the concentration of the test compound where the response is halved, indicating the potency of the test compound. Thus, in the context of metabolic activity measured by MTT assay; it is the concentration of the compound at which the cell metabolic activity is reduced by 50% compared to untreated cells. It was established by plotting the metabolic activity of the cells at a range of concentrations of propranolol. The IC50 for propranolol was 0.005, 0.008 and 0.011 mg/mL after incubations for 24, 48 and 72 hours respectively, which are equivalent to 17.0, 27.0 and 37.2 μM. The IC50 decreased with the incubation times with propranolol, where the lowest IC50 was determined after 72 hours of incubation. In contrast, the IC50 at 24 hours was the highest, which indicated that the suppression of the metabolic activity of the epicardial cells was dependent on the incubation time. The longer the incubation with propranolol, the more inhibitory effect on the metabolic activity of the epicardial cells. The identified IC50 for propranolol was lower than the reported values for other cell lines in the literature, where the anti-tumour properties of propranolol were shown [265]. For example, Wei *et al*. showed that propranolol inhibited the growth of 8505C and K1 thyroid cancer cells *in vitro*, where the IC50 were 200 and 280 μM, respectively [266]. Bota *et al*. reported the

IC50 for propranolol on HUVEC and BJ fibroblast were 81.94 and 148.32 μg/mL, respectively [267].

Nevertheless, the drug-free nanogels exhibited no effect on the metabolism of the epicardial cells at concentrations below 0.667 mg/mL after they were incubated for 24, 48 and 72 hours, as the cell metabolic activity remained above 70%. However, the nanogel was cytotoxic to the cells at 1.333 mg/mL. Furthermore, the cell metabolism of the epicardial cells was lower at 72 hours across all concentrations than at 24 and 48 hours, but the IC50 calculated were remarkably similar. Thus, the decrease in cell metabolism was possibly due to depletion of nutrients and accumulation of waste during the long incubation time, instead of time-dependent cytotoxicity. The cytotoxicity of the nanogels only happened at high concentrations (0.667 mg/mL), indicating the biocompatibility of the nanogels. The cytotoxicity of free nanogels could be related to the cationic surface charge of nanogels damaging cell membranes at high concentrations.

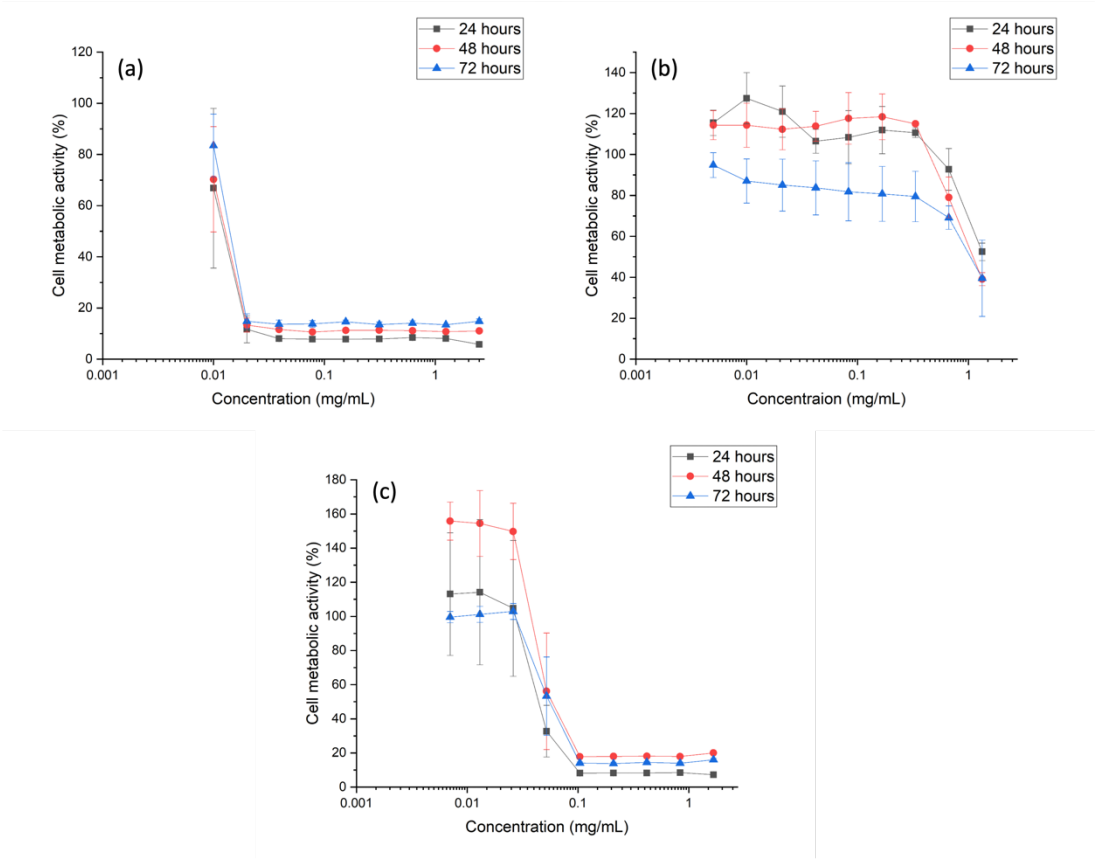

Figure 4-2. Metabolic activity of the epicardial/ mesothelial cells under incubation with (a) propranolol, (b) drug-free nanogels and (c) propranolol-loaded nanogels for 24-72 hours. Concentration on the x-axis means the amounts of propranolol or freeze-dried nanogels per mL in the complete media, which were used to incubate with the cells. PBS was used as the control sample in this experiment. Epicardial/ mesothelial cells were tested as the epicardium is the layer directly in contact with the nanogels during intrapericardial delivery. Therefore, the effects on the epicardial/ mesothelial cells were crucial and first explored in the study. The metabolic activity of the epicardial/ mesothelial cells decreased when the concentration of propranolol and propranolol-loaded nanogels increased. However, in figure (c), the cell metabolic activity increased from 24 to 48 hours, which was likely due to cells grown in number at low nanogels concentrations, promoting the overall cell metabolic activity. The metabolic activity remained relatively constant unless a high concentration of drug-free nanogels was used.

In conjunction with propranolol, the propranolol-loaded nanogels displayed both dose-dependent and time-dependent inhibition of the metabolic activity of the epicardial cells. Interestingly, the inhibitory effect of propranolol-loaded nanogels was inversely dependent on the incubation time, which was opposite to the observation in the propranolol incubated cells. The metabolic activity inhibition was higher at 48 and 72 hours than at 24 hours, whereas the former two were similar in terms of the profile. The baseline cell metabolic activity at 48 and 72 hours was at about 20%, which was higher than that measured at 24 hours, indicating that the surviving cells were replicating and dividing after the exposure to propranolol. Thus, the cell metabolism and the IC30 increased. Most importantly, the dose-dependent inhibitory effect of metabolic activity was established on propranolol-loaded nanogels. It is likely due to the payload - propranolol. However, the IC50 calculated was 0.050, 0.044 and 0.052 mg/mL for 24-, 48-, and 72-hour incubations. However, these concentrations were the total weights of freeze-dried propranolol-loaded nanogels per mL, which could not be used as a direct comparison. Thus, after adjustment, the equivalent concentration of propranolol in these nanogels were 0.030, 0.026 and 0.031 mg/mL, which were much lower than those identified for propranolol. The IC50 for propranolol were identified as 0.005, 0.008 and 0.011 mg/mL for 24-, 48- and 72-hour incubations, which were approximately one-sixth, one-third, and a quarter of the equivalent results of propranolol-loaded nanogels. The IC30 also increased with the incubation times of the propranolol-loaded nanogels, indicating the recovery of the metabolic activity in the survived cells over the 72 hours. In short, these results reveal the inhibitory effect of the cell metabolism was reduced when propranolol was fabricated in the nanogels, demonstrating the advantage of using the biocompatible nanogels as drug carriers.

The propranolol and propranolol-loaded nanogels were tested with cell proliferation assays - BrdU, to evaluate the effect of propranolol nanogels on cell proliferation. BrdU is a synthetic nucleoside analogue that can be incorporated into the newly synthesized DNA molecules of the dividing cells and thus measures cell viability in terms of cell division. The IC50 of propranolol at all incubation times were 0.088, 0.079 and 0.770 mg/mL for 24, 48 and 72 hours respectively, demonstrating the cell division of epicardial cells started to recover at 72 hours. Interestingly, the IC50 for propranolol-loaded nanogels were lower than the drug only across all incubation

times, which demonstrated that the propranolol-loaded nanogels impacted the cell division to a larger degree than the propranolol itself. In summary, although various IC50 was determined for propranolol and propranolol-loaded nanogels using different assays, all results indicated that propranolol and propranolol-loaded nanogels were likely suppressing the cell proliferation and metabolic activity in the epicardial cells at concentrations likely to be used in the clinical setting.

Table 4-1. IC50 and IC30 were calculated for the propranolol, drug-free nanogels and propranolol-loaded nanogels on the epicardial cells at three different incubation times.

Samples	**Assay method**	**IC50 (mg/mL)**			**IC30 (mg/mL)**		
		24 hours	**48 hours**	**72 hours**	**24 hours**	**48 hours**	**72 hours**
Propranolol	MTT	0.005	0.008	0.011	0.004	0.007	0.010
	BrdU	0.088	0.079	0.770	0.076	0.075	0.639
Propranolol-loaded nanogels	MTT	0.050	0.044	0.052	0.042	0.039	0.050
	BrdU	0.073	0.006	0.115	0.073	0.006	0.047
Drug free nanogels	MTT	0.800	0.700	0.750	0.650	0.800	1.000

4.3.2.2. Sensitivity of different cell lines on the metabolic inhibition from propranolol-loaded nanogels

The metabolic activity of the epicardial cells and two other cell lines H9c2 and L929 determined using the PrestoBlue® assay on the propranolol-loaded nanogels. These nanogels were incubated with the cells using the same concentration ranges for 24-72 hours. The response was first normalised before performing the two-way analysis of variance (ANOVA), Then, the analysis was performed between the metabolic activity of epicardial cells, H9c2 and L929 cells, to evaluate if the responses were different between the cell types. The result indicated that there was a difference in the cell metabolic activity between different cell types after exposing to propranolol-loaded nanogels at all incubation times ($p < 0.0001$). Propranolol-loaded nanogels exhibited both time-dependent and dose-dependent inhibitions of the metabolism for all cell types, with the metabolic activity of epicardial cells being the lowest amongst all cells regardless of the incubation time.

A Turkey's post hoc test was performed to compare the cell metabolic activities in different cell types at each propranolol concentration. The analysis showed that the cell metabolic activity measured in epicardial cells was significantly lower than those measured in H9c2 cells in the concentrations between 0.007 to 0.209 mg/mL, 0.013 to 0.209 mg/mL at 24- and 48-hour incubation times respectively ($p < 0.001$). There were also significant differences between the metabolic activities of both cells at 0.026, 0.104 and 0.209 mg/mL after 72 hours of incubation. On the other hand, the significant difference in cell metabolic activity was only observed at nanogels concentrations of 0.026 to 0.209, 0.013 to 0.104 and 0.104 mg/mL after 24-, 48- and 72-hour incubation respectively with the propranolol-loaded nanogels. At concentrations above 0.835 mg/mL, there was no significant difference between the cell metabolic activity across all cell types. The results demonstrated that the epicardial cells were more susceptible than the H9c2 and L929 to the inhibitory effect of propranolol on the cell metabolism at nanogels concentrations ranging from 0.007 to 0.418 mg/mL, but the susceptibility decreased with the incubation time. The surviving cells were able to recover from the inhibitory effect of propranolol over time.

The cell metabolism inhibitory profile of propranolol on L929 and H9c2 cells were comparable for 24- and 48-hour incubation times at propranolol-loaded nanogels concentrations lower than 0.013 mg/mL or above 0.835 mg/mL. The cell metabolic activities of both cells were different at 0.026 and 0.104-0.418 mg/mL at 24 hours, 0.026-0.209 mg/mL at 48 hours, and 0.007-0.014 mg/mL at 72 hours. However, no trend could be deduced from the results to demonstrate if L929 or H9c2 were more sensitive.

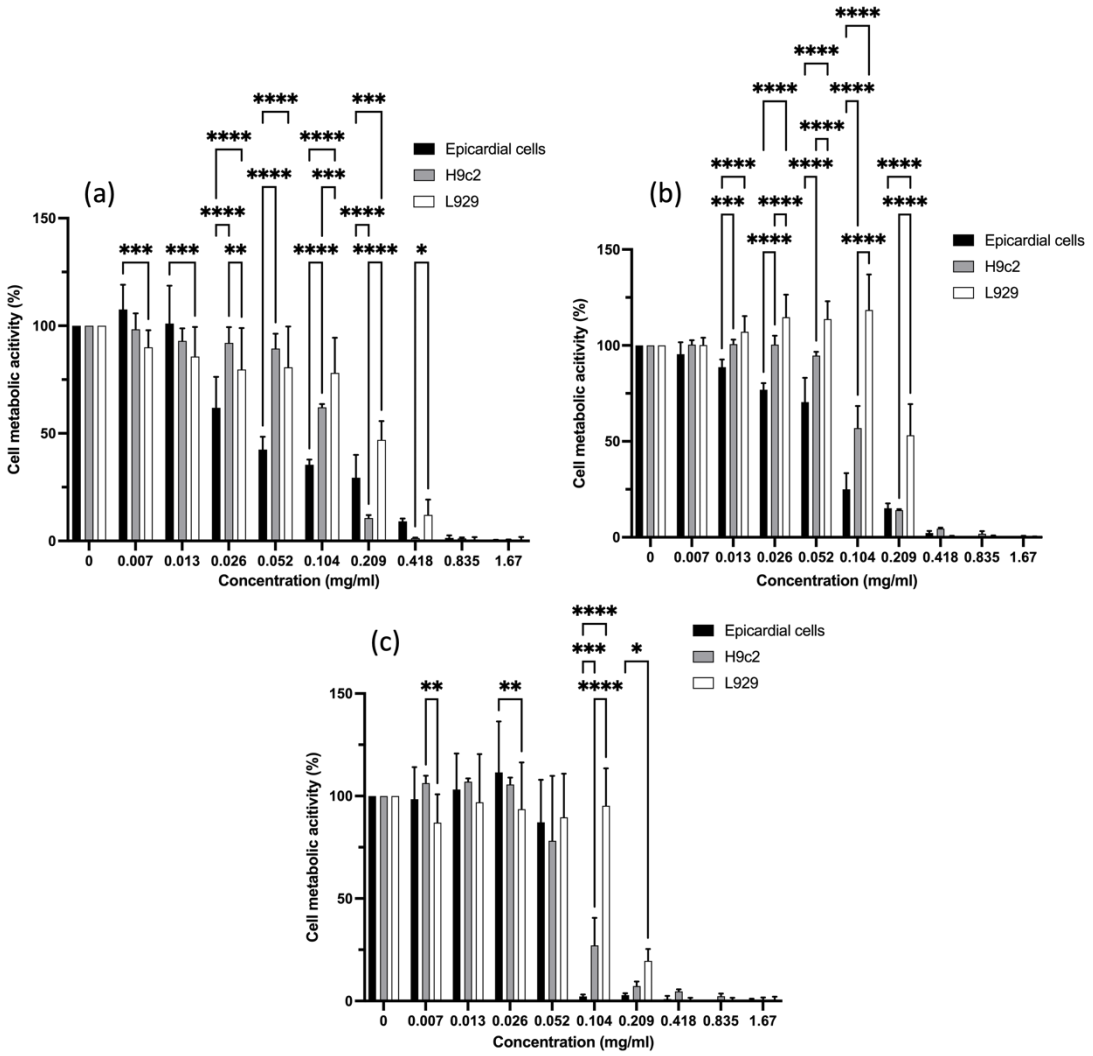

Figure 4-3. Cell viability of epicardial cells, H9c2 cells, and L929 cells under incubation with various concentrations of propranolol-loaded nanogels for (a) 24, (b) 48, and (c)72 hours. 2-way Analysis of variance (ANOVA) was performed to determine the significant difference in the cell viability between the different cell types, where Tukey's test was used to compare the difference in cell viability after exposure to propranolol-loaded nanogels between the epicardial cells, H9c2 and L929 cells at each concentration. * $p < 0.05$, ** $p < 0.01$, *** $p < 0.001$ and **** $p < 0.0001$.

The IC50 was determined from a sigmoidal curve fitted to **Figure 4-3**. The IC50 and IC30 were the lowest in the epicardial cells, followed by the H9c2 and L929 cells across all incubation times, as shown in **Table 4-2**. The results revealed that the epicardial cells were the most sensitive to the metabolic inhibitory effect of propranolol-loaded nanogels, which indicated that the use of epicardial cells is likely

to offer better sensitivity than other cell lines for intrapericardial delivery. The IC50 and IC30 of the propranolol-loaded nanogels decreased with the incubation times in H9c2 and L929, indicating the inhibition of the metabolic activity was increased over time in these cells. In short, the cell viability and proliferation assay using the epicardial cells could be performed to screen drugs and formulations suitable for intrapericardial delivery before conducting animal studies, minimizing the unnecessary toxicity on the animals.

Table 4-2. IC50 and IC30 of propranolol were determined on the epicardial cells, H9c2 cardiomyoblasts, and L929 fibroblasts at different incubation times.

Cells	IC50 (mg/mL)			IC30 (mg/mL)		
	24 hours	48 hours	72 hours	24 hours	48 hours	72 hours
Epicardial cells	0.004	0.075	0.062	0.023	0.114	0.069
H9c2 cardiomyoblasts	0.121	0.113	0.071	0.151	0.148	0.093
L929 fibroblasts	0.227	0.209	0.194	0.304	0.201	0.204

4.4. Conclusion

In this study, propranolol-loaded nanogels were fabricated using the optimal formulation and fabrication conditions established in **Chapter 3**. The effects of propranolol, drug-free nanogels and propranolol-loaded nanogels on cell metabolism and proliferation were assayed on the epicardial cells. The result indicated that propranolol inhibited the cell metabolic activity and proliferation of the epicardial cells. More importantly, the results demonstrated that the use of nanogels attenuated the inhibitory effect of propranolol on the cells. Lastly, the inhibitory effect of propranolol on the metabolism of epicardial cells, H9c2 and L929 cells were tested to evaluate if epicardial cells are more sensitive than other cell types. The results indicated a significantly higher inhibition of the metabolic activity in epicardial cells than H9c2 and L929 after the exposure to propranolol-loaded nanogels. The results demonstrated epicardial cells might be applied to cytotoxicity assays to screen drugs and formulations suitable for the route in the future. As a result, a new drug has to be sought to replace propranolol as the payload of the nanogels. An anti-fibrotic peptide Ac-SDKP was selected, but a quantitation method that is compatible with the nanogel formulation and high peptide concentrations is required as a prerequisite for

the formulation development. Therefore, a new quantitation method for the peptide is developed and validated in the next chapter.

Chapter 5

Developing an HPLC-UV Method for Quantification of the Anti-fibrotic Peptide N-acetyl-seryl-aspartyl-lysyl-proline

Part of the contents in this chapter has been published as the following research article.

Ho, H. M. K., Sembi, S., Abukhamees, S., Day, R. M., & Craig, D. Q. (2022). An analytical quality by design approach towards a simple and novel HPLC-UV method for quantification of the antifibrotic peptide N-acetyl-seryl-aspartyl-lysyl-proline. *Analytical Biochemistry*, 114793.

5. Developing an HPLC-UV method for quantification of the antifibrotic peptide N-acetyl-seryl-aspartyl-lysyl-proline

5.1. Introduction

N-acetyl-seryl-aspartyl-lysyl proline (Ac-SDKP) is a tetrapeptide, with the structure shown in **Figure 1-4**. It is a candidate drug for potentially attenuating damage post-MI and promoting cardiac repair due to its anti-fibrotic, anti-inflammatory, and angiogenic properties. The proposed mechanism of action, synthesis, degradation, and potential clinical applications of the peptide are discussed in **Section 1.4.1**. Owing to the short half-life of the peptide (4.5 minutes in circulation) [268], pericardial delivery of Ac-SDKP using the nanogel delivery system could localise delivery and prolong the residence time of the peptide in the heart.

Given the potential clinical applications of the peptide, a reliable analytical method is required to facilitate the formulation of the peptide-loaded nanogel, as well as to assess the associated *in vivo* release profile. The charge and pH plot of the peptide is shown in **Figure 5-1**, with the isoelectric point estimated at roughly 3.1 [269]. The molecular weight of the peptide is 487.5 g/mol while the XLogP is -5.369. Thus, it is likely that the peptide can be quantified with the HPLC using the ordinary C18 column as other polar small molecules.

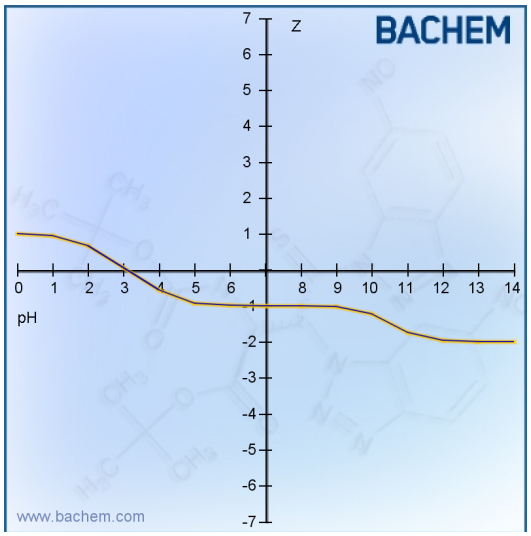

Figure 5-1. The isoelectric point of the peptide Ac-SDKP. The figure was generated using the peptide calculator from Bachem (Bubendorf, Switzerland) [269].

Although a limited number of quantitative assays for the peptide or its analogue have been reported, these techniques either involve enzyme immunoassays (EIA) [270,271] or liquid chromatography-tandem mass spectrometry (LC-MS/MS) [272–275]. Pradelles *et al.* first described an EIA for Ac-SDKP in 1990, using acetylcholinesterase-Ac-SDKP conjugate as the tracer, rabbit antiserum, and mouse anti-rabbit IgG antibody-coated 96-well plate. However, the limitation of this method was a lack of specificity, resulting in cross-reactivity with Ac-SDKP-like materials [271]. Junot *et al.* reported an improved EIA assay for the amidated analogue of the peptide, with successful quantification of the peptide analogue in the mouse plasma samples without interference from the endogenous Ac-SDKP. The detection limit in mouse plasma was 1 nM, which is equivalent to 0.5 ng/mL [270]. The same group also published a liquid chromatography-electrospray mass spectrometry (LC-ESI-MS) method for quantifying the Ac-SDKP peptide in human plasma and urine from health volunteers receiving intravenous Ac-SDKP injection or captopril. However, the recovery in plasma was only 64% and the limit of quantitation was 5 ng/mL, as the plasma samples were first extracted using methanol. Detection in urine samples dropped from 88% within the range of 2.5 to 25 ng/mL to 15% at 1000 ng/mL, indicating an upper detection limit exists using this method for higher concentrations of Ac-SDKP in the samples [275]. Therefore, to overcome these limitations, Inoue *et al.* reported an LC-ESI-MS/MS method to

quantify Ac-SDKP in human plasma samples obtained from haemodialysis patients, with a wider detection range of 0.5 to 100 ng/mL and a lower limit of quantitation (LLOQ) of 0.1 ng/mL. Several stable isotope tetrapeptides were used as the internal standard, whilst the samples were extracted via solid-phase extraction before LC-MS/MS [274]. The same group further developed an online solid-phase extraction liquid chromatography-tandem mass spectrometry for high-throughput analysis of the Ac-SDKP peptide in human plasma samples. The LLOQ and range remained unchanged in the new method [272]. Mesmin *et al.* performed a head-to-head comparison of the LC-MS/MS and EIA method in quantifying the amidated analogue of the peptide in human biological samples and concluded that the LC-MS/MS method offered higher sensitivity and lower assay variability than the EIA [273].

The above methods provide high sensitivity assays for Ac-SDKP but require specialist equipment and non-trivial experimental procedures. Both the LC-MS/MS methods and EIA methods are designed for quantifying Ac-SDKP in biological samples, where the concentration is low and intensive sample preparations are required. The use of high concentrations of analyte might overload the extraction column or the separation column in LC-MS/MS or the EIA plates, so the response could be non-linear, which makes these approaches undesirable to detect analytes with high concentrations. In addition, *in vitro* drug release is routinely performed in pharmaceutical developments to simulate drug release in the body, where phosphate buffer is commonly used as the medium. However, phosphate buffer is not compatible with the LC-MS/MS, owing to its non-volatile nature. Thus, this chapter aimed to develop and validate a simple and selective HPLC-UV assay method for the detection of the peptide Ac-SDKP, which is suitable for supporting the development and evaluation of nanogels formulations containing the peptide at concentrations commensurate with therapeutic doses, ranging from 400 µg/kg to 3.2 mg/kg per day [67,276]. Moreover, the method has to be suitable for quantifying Ac-SDKP without extensive sample preparation.

The HPLC method was developed using an analytical Quality by Design (AQbD) approach. Quality by design (QbD) is defined by the International Council of

Harmonisation (ICH) Q8 (R2) guideline as a systematic approach to development that begins with predefined objectives and emphasizes product and process understanding and process control, based on sound and quality risk management [277]. However, it does not explicitly discuss the requirements for analytical method development. ICH Q9 and Q10 guidelines focus on the risk management and control strategy respectively [278,279], while the ICH Q11 guideline detailed the implementation of QbD in the API synthesis process [280]. While neither of these guidelines is designed for analytical method development, several papers have discussed the implementation of the QbD life cycle in analytical method development, i.e., Analytical Quality by Design (AQbD) [280–284]. These authors also applied the approach to HPLC method developments according to the ICH Q8 (R2) guideline [285,286]. Aligned with QbD, AQbD applies a similar approach as the typical QbD life cycle, despite the use of different tools and terminology. In brief, the AQbD life cycle includes analytical target profiles (ATPs), critical quality attributes, (CQA), risk assessment, method optimisation and development with the design of experiment (DOE), method operable design region (MODR), control strategies, continuous method monitoring and continual improvement [280,287]. The use of AQbD could offer more flexibility for the analytical method but does require a robust quality system and a deep understanding of the process, product, and analytical method [287]. Therefore, the HPLC method, robustness and ruggedness were tested at the beginning of the method development stage to ensure the efficiency of the method throughout the product life cycle, followed by method validation according to the ICH Q2 (R1) guideline.

5.2. Materials and Method

5.2.1. Materials

Peptide Ac-SDKP was synthesised by the Chinese Peptide Company (Hangzhou, PRC), with a purity of 90-94%. Acetonitrile (ACN) was purchased from Fisher Scientific (Waltham, MA, USA) and HPLC grade water was obtained from PURELAB® Chorus 2+ machine (ELGA LabWater, High Wycombe, UK). Potassium phosphate monobasic and phosphoric acid were purchased from Sigma Aldrich (St Louis, MO, USA). Amber HPLC vial caps were purchased from Fisher

Scientific (Waltham, MA, USA), while the 200 µL conical glass vial insert was purchased from Agilent (Santa Clara, CA, USA). Steritop™ vacuum bottle-top filter and Amicon Ultra filter (MWCO 3000 Da, 0.5 mL) were purchased from Merck Millipore (Darmstadt, Germany).

5.2.2. Instrumentation and chromatographic conditions

Chromatographic analysis was performed on an Agilent 1260 Infinity liquid chromatography system (Santa Clara, CA, USA), equipped with a Variable Wavelength Detector (VWD). The column used in the study was a Zorbax Eclipse Plus C18 column (Agilent, Santa Clara, CA, USA), with a particle size of 5 µm, dimensions of 4.6 mm internal diameter and 250 mm in length. The VWD was set at a wavelength of 220 nm and detector sensitivity of 0.1 AUFS. Various flow rates (FR), gradient program, temperature (T), injection volume (V) and pH of the buffer (pH) were used, based on the experimental design matrixes. 1 mg/mL standard solution of Ac-SDKP in water was prepared and used for the screening and response surface methodology studies.

5.2.3. Preparation of buffer component of the mobile phase

Phosphate buffer was prepared at a concentration of 10 mM by dissolving 1.36 g potassium phosphate monobasic in 1 L HPLC grade water, with the pH adjusted to 2.5 or 3.0 (± 0.05) with the phosphoric acid solution. The buffer was filtered through a 0.22 µm polyethersulfone Steristop™ vacuum bottle-top filter. The buffer was then used immediately upon preparation or stored under refrigeration in borosilicate glass bottles for a maximum period of 24 hours.

5.2.4. Sample preparation

The verification standard was prepared by dissolving the Ac-SDKP standard in HPLC grade water at 1 mg/mL. Drug-free matrix solution was prepared by diafiltration of chitosan-TPP nanogels, where 0.5 mL of the nanogel solution was centrifuged with the Amicon Ultra filter (MWCO 3,000) at 14,000 rpm while PBS was prepared as discussed above. Samples in PBS and matrix solutions were

subsequently prepared by dissolving the respective amount of Ac-SDKP in the PBS and matrix solution.

5.3. HPLC method development by an AQbD approach

5.3.1. Identification of analytical target profiles

The analytical target profiles (ATPs) set the criteria to be achieved in the measurement. The proposed method is intended to be an analytical method for quantifying the peptides present in pharmaceutical dosage forms (i.e., Chitosan-TPP nanogels in this study) and phosphate buffer saline (PBS) using a reversed-phase HPLC equipped with an autosampler and a quaternary pump. In routine, the method is designed to determine the peptide released in the PBS during the *in vitro* drug release study and to quantify the unencapsulated peptide in the chitosan-TPP nanogel formulations. Four key outputs in HPLC measurement were identified in the ATPs, namely capacity factor (Rf), resolution between the peak of analyte and the closest adjacent peak (Rs), tailing factor for the peak of analyte (Tf), and theoretical plate count (N). The acceptable criteria for these outputs are derived from the ICH Q2 (R1) guideline, with Rf and Rs ≥ 2, Tf ≤ 1.5 and N $\geq 2{,}000$.

5.3.2. Determining critical quality attributes

The critical quality attributes (CQA) are the method parameters that impact the ATPs. Thus, these factors should be controlled to achieve the pre-determined criteria in the ATPs. HPLC CQA usually include mobile phase ratio, pH of the buffer, diluent, column selection, organic modifier, injection volume, flow rate, buffer strength and elution methodology [280].

5.3.3. Risk assessment

Risk assessments were performed throughout the method development cycle. Initial risk assessment was deployed to identify and assess the risks at the beginning of the method development, as these risks could impact the efficiency of the HPLC method established. The cause-effect relationships between the CQA and the ATPs were illustrated using an Ishikawa fishbone diagram, which was visualised with MindManager 12 (Mindjet, Austin, TX, USA).

5.3.4. Definitive screening design

A definitive screening design (DSD) was used for identifying key independent variables impacting the ATPs. The eight screened factors included blocking, starting solvent B concentration ($\%B_s$), solvent B concentration increment ($\%B_i$), flow rate (FR), temperature (T), injection volume (V), the run time (t), and pH of the buffer. A total of 22 experimental runs, as shown in **Table 5-1**, were performed in triplicate to construct the DSD, where the composite matrix was constructed using JMP 15 (SAS Institute, Cary, NC, USA). The design was then fitted by Effective Model Selection for DSD methodology, which was performed automatically in JMP 15 (SAS Institute, Cary, NC, USA). The main effects and even order effects were first estimated individually and then combined to form the model parameter estimates. Since the DSD was used for the screening only, the factors estimated to have effects were selected as the independent parameters for the response surface methodology below.

Table 5-1. Independent and dependent variable and the experimental design matrix of DSD design. The outputs were reported as the mean value from three independent experiments (n = 3).

Screened parameters							Outputs				
Block	$\%B_s$	$\%B_i$	t (min)	FR (mg/mL)	T (°C)	V (mL)	pH	Rf	Rs	Tf	N
1	3	1	15	1	45	10	2.75	1.917	6.484	1.84	5709
1	4	1	10	1	25	10	2.5	1.698	5.882	1.42	4243
1	5	1	15	1.5	35	10	2.5	1.982	4.991	1.28	5939
1	3	10	12.5	1.5	25	10	3	1.540	4.786	1.33	10279
1	5	10	10	1.5	25	20	2.75	2.096	6.490	0.98	4425
1	4	5.5	12.5	1.25	35	15	2.75	1.270	5.183	1.44	4437
1	5	10	15	1	25	20	2.5	3.508	5.070	1.57	4858
1	3	10	10	1	35	20	3	0.634	5.591	1.19	4225
1	4	10	15	1.5	45	20	3	0.851	5.195	2.01	4098
1	5	1	12.5	1	45	20	2.5	1.178	5.390	1.21	4697
1	3	1	10	1.5	45	10	3	1.137	4.693	1.21	4413
2	5	1	15	1.5	25	15	3	2.747	5.613	1.08	2630
2	4	5.5	12.5	1.25	35	15	2.75	3.030	5.606	1.14	2397
2	5	1	10	1.25	45	20	3	1.905	5.514	2.19	3214
2	3	1	15	1	25	20	3	2.339	6.491	0.96	9589
2	5	10	10	1.5	45	10	2.5	1.504	5.774	1.61	13200
2	3	1	10	1.5	25	20	2.5	1.427	5.285	1.42	4560
2	5	10	15	1	45	10	3	0.769	4.637	1.65	4383
2	3	5.5	15	1.5	45	20	2.5	1.168	5.146	0.87	3418
2	3	10	15	1.25	25	10	2.5	1.140	5.791	0.86	6975
2	5	5.5	10	1	25	10	3	0.492	5.747	1.39	7133
2	3	10	10	1	45	15	2.5	0.538	6.029	1.32	7173

5.3.5. Response surface methodology

5.3.5.1. Experimental design

Response surface methodology (RSM) was used to determine the optimal condition for the chromatographic analysis of Ac-SDKP. A three-level face-centred cubic (FCC) central composite design (CCD) was used in the optimisation, which was formed by five pivotal independent variables as identified from the DSD, namely starting solvent B concentration ($\%B_s$), solvent B concentration increment ($\%B_i$), flow rate (FR), temperature (T), and pH of the buffer. Four key criteria set in the

ATPs, namely Rf, Rs, Tf, and N, were determined as the dependent variables. The injection volume (V) and running time were fixed at 20 µL and 15 minutes to minimise the number of factors in the model, as a run-time of 15 minutes allows a sufficient time to elute the analyte even at a low percentage of solvent B. The injection volume was fixed at 20 µL to maximise the ranges of detection and quantitation. It is known that any alteration does not hugely affect the capacity factor and theoretical plate number, and thus selectivity and efficiency are maintained. Thus, it is used for fine adjustment on the optimal condition, especially when column overloading happened. Lowering it could further reduce the tailing and improve the resolution. The design matrix to construct the RSM, as shown in **Table 5-2**, comprised 21 running conditions and was constructed using JMP 15 software, where each running condition was repeated in triplicate and reported as an average value. Prediction profilers were plotted using the same software. Wash runs were performed in between two different running conditions to equilibrate the column, where a blank solution was run at the set solvent compositions, temperature, and flow rate of the next running condition for 10 minutes.

A stepwise least square regression was used to fit the polynomial model to the data individually for each dependent variable. A 5-fold cross-validation was performed to validate the model for all dependent variables. A one-way analysis of variance (ANOVA) test and lack of fit test was conducted to determine the statistical significance and goodness of fit for the model respectively, at a confidence interval (*CI*) of 95%. Response surfaces were plotted to visualise the relationship between independent and dependent variables. A p-value < 0.05 is considered statistically significant. The response surface and contour plots were plotted using the same software.

Table 5-2. Independent and dependent variables and the experimental design matrix of CCD design. The outputs were reported as the mean value from three independent experiments (n = 3).

Input parameters						Output			
Pattern	**%B_s (%)**	**%B_i (%)**	**pH**	**FR (mg/mL)**	**T (^oC)**	**Cf**	**Rs**	**Tf**	**N**
−−−++	3	1	2.5	1.5	45	1.936	5.853	2.25	3213
000A0	3.5	5.5	2.75	1.5	35	1.750	5.203	1.48	3444
+−+++	4	1	3	1.5	45	1.220	4.710	1.76	3362
−+−−+	3	10	2.5	1	45	1.588	5.680	1.86	8021
+++−+	4	10	3	1	45	1.143	5.205	1.73	6262
++−−−	4	10	2.5	1	25	1.568	5.439	1.22	6154
A0000	4	5.5	2.75	1.25	35	1.463	5.131	1.55	3819
−−+−+	3	1	3	1	45	1.903	5.341	2.18	3350
−++++	3	10	3	1.5	45	1.558	4.997	1.73	4522
00a00	3.5	5.5	2.5	1.25	35	1.746	5.387	1.72	4087
−++−−	3	10	3	1	25	1.872	5.007	1.04	7275
0a000	3.5	1	2.75	1.25	35	1.891	5.352	1.66	2725
00000	3.5	5.5	2.75	1.25	35	1.706	5.263	1.56	4378
−−++−	3	1	3	1.5	25	2.711	5.177	0.99	2187
−−−−−	3	1	2.5	1	25	3.018	6.139	1.32	2997
000a0	3.5	5.5	2.75	1	35	1.612	5.488	1.64	4789
0000a	3.5	5.5	2.75	1.25	25	2.042	5.454	1.07	3872
a0000	3	5.5	2.75	1.25	35	1.968	5.537	1.57	4078
00000	3.5	5.5	2.75	1.25	35	1.698	5.260	1.55	3699
++−++	4	10	2.5	1.5	45	1.318	5.434	1.73	4866
0000A	3.5	5.5	2.75	1.25	45	1.453	5.516	1.93	4558
−+−+−	3	10	2.5	1.5	25	2.171	5.364	1.11	5198
+−−−+	4	1	2.5	1	45	1.359	5.661	2.15	3628
+−+−−	4	1	3	1	25	1.725	5.113	1.05	2589
0A000	3.5	10	2.75	1.25	35	1.581	5.105	1.47	5537
00A00	3.5	5.5	3	1.25	35	1.647	4.779	1.42	4228
++++−	4	10	3	1.5	25	1.637	4.920	0.93	4267
+−−+−	4	1	2.5	1.5	25	2.024	5.511	1.13	2575

Key: - means low level, 0 refers to intermediate level whilst + refers to the high level. A and a refer to the two axial points.

5.3.5.2. Multiple response optimisation

Multiple response optimisation (MRO) was used to identify the optimal chromatographic condition using the desirability function approach as described in **Section 3.2.4**. The running condition with the highest overall desirability was

considered the optimal condition as determined by JMP 15 (SAS Institute, Cary, NC, USA). The peptide was analysed under the optimal chromatographic conditions in triplicate, with the dependent variables measured experimentally and compared with the predicted values to validate the models.

5.3.5.3. Optimal running condition

The optimal condition for quantifying the peptide Ac-SDKP was performed with an Agilent Zorbax Eclipse Plus reverse phase C-18 column with a dimension of 4.6 x 250 mm, 5 µm particle size (Santa Clara, CA, USA) to verify the model, at the column temperature of 25 ºC. The peptide was eluted using a gradient method as shown in **Table 5-3**, at a flow rate of 1 mL/min with 10mM phosphate buffer at pH 2.5 and acetonitrile used as the mobile phase. Injection volume was originally set at 20 µl in the MRO but was reduced to 10 µL, minimising the mass overloading. A post-time of 5 minutes at 97% solvent A and 3% solvent B was used after each run to re-equilibrate the column.

Table 5-3. HPLC gradient program.

	Composition	
Time (min)	**% Solvent A (Phosphate buffer)**	**% Solvent B (ACN)**
0	97	3
15	90.3	9.7

5.3.6. Control strategy

A control strategy, which is a method to maintain the important process parameters and material attributes within the method operable design region, is implemented after the HPLC method development [280]. The analytical control strategy was established according to the ATPs, through understanding the limits of the method operable design region, which were identified from the robustness test. The purity of the peptide and other materials used in the method was tested routinely. The method was also tested at the intermediate stage with a higher limit to understand the processing capacity.

5.3.7. Continuous method monitoring and continual improvement

Continuous monitoring of the method performance and quality consistency was monitored by tracking the system suitability data [280]. Moreover, regular maintenance of the HPLC instrument and computers was performed. Other related apparatus used in this study, including the pH meter, weighing balance, and pipettes, were maintained and calibrated. The software was also routinely updated [282,285].

5.4. Method validation

The method was validated according to the ICH Q2 (R1) guideline [288], utilising a reported template for best practice [289]. System suitability, linearity, accuracy, repeatability, selectivity, and robustness were evaluated during method validation, with the validation methods discussed individually as follows.

5.4.1. Specificity

Specificity is the ability of the method to determine the analyte from other components in the sample matrix [290], which is usually demonstrated by the complete separation of the peak of the analyte from other peaks present in the chromatogram of the sample matrix. Therefore, 10 µL of the verification standard, samples in PBS and matrix samples, PBS, blank (water), and drug-free matrix were introduced into the system to evaluate the specificity of the method.

5.4.2. System suitability

System suitability testing was performed with a 1 mg/mL validation standard solution on two different HPLC systems. A total of 6 injections of the sample were injected. The capacity factor, resolution, tailing factor, and theoretical plates were present as the average, whilst relative standard deviations (RSD) for retention time and peak area were determined.

5.4.3. Linearity and range

Calibration standard solutions were prepared at 8 various concentrations ranged from 0.25 mg/mL to 2 mg/mL. A further 6 concentrations were prepared via serial 2-fold dilutions of six repeats to prepare concentrations ranging from 3.9 µg/mL to 0.125

mg/mL. Three individually prepared solutions at each concentration were prepared. Linear regression was employed to determine the correlation. The acceptable criteria of the R-squared (R^2) are $R^2 \geq 0.999$. The range was determined on the linear region of the calibration curve.

5.4.4. Limit of detection and limit of quantitation

The lower limit of detection (LOD) and lower limit of quantitation (LOQ) was determined from the calibration curve, according to **Equation 5-1** and **Equation 5-2**.

$$\boldsymbol{LOD = \frac{3.3\sigma}{S}} \qquad \textbf{Equation 5-1}$$

$$\boldsymbol{LOQ = \frac{10\sigma}{S}} \qquad \textbf{Equation 5-2}$$

Where σ was the standard deviation of the response and S was the slope of the calibration curve.

5.4.5. Accuracy and quantitative matrix effects evaluation

Spiked samples were prepared at 3 concentrations - 0.75, 1.0, 1.5 mg/mL, using both phosphate buffer and matrix solutions. Matrix solution was prepared by diafiltration of chitosan-triphosphate nanoparticles, where 0.5 mL of the nanoparticle solution was centrifuged with the filter at 14,000 rpm. Three individually replicates at each concentration were prepared and analysed. The mean, standard deviation, RSD, and percentage recovery were evaluated, and the acceptance criteria are within 90-110%. Evaluation of the matrix effects was performed by comparing the slopes of the curves constructed by PBS and placebo, with the slope of the calibration curve in water. A one-way ANOVA was performed on GraphPad Prism 9 to determine if the matrix effect was statistically significant, where a *p*-value < 0.05 is considered statistically significant.

$$\boldsymbol{Matrix\ effect = \left(\frac{S_{matrix}}{S_{std}} - 1\right) \times 100\%} \qquad \textbf{Equation 5-3}$$

Where S_{matrix} was the slope of the curve constructed by PBS and placebo. S_{std} was the slope of the calibration curve in water.

5.4.6. Repeatability and intermediate precision

A 1 mg/mL Ac-SDKP solution in water was prepared and 10 replicates of the validation standard were injected to determine the instrumental precision. The result was reported as average, standard deviation, and relative standard deviation (RSD) of the retention time, peak area, and height. The acceptable criteria were within ± 1% of RSD for these parameters. Meanwhile, intermediate precision determined the intra-lab variations. Three solutions with concentrations of 0.5, 1.0 and 1.5 mg/mL Ac-SDKP in water were prepared and performed on two different HPLCs (Agilent 1200, Santa Clara, CA, USA) on two different days by two operators. The relative standard deviation for each operator and each instrument was determined and reported. The acceptable criterion was RSD within ± 2% [288].

5.4.7. Robustness

The robustness of the method was tested with deliberate alterations in the flow rate, $\%B_s$, temperature, and pH of the mobile phase to determine the capacity of the method to remain unaffected by variations in the method parameters. Variations of flow rate, $\%B_s$, temperature, and pH were selected as ± 0.2 mL/min, ± 1%, ± 5 ^oC and ± 0.1, respectively. Thus, buffers with pH of 2.4 and 2.6 were prepared. The robustness of the method was assessed using two aspects – the peak area and capacity factors of the analyte peak. For capacity factors, the predicted values were calculated from the chromatographic conditions of the deliberate alterations using the correlation established in the MODR. The assays were then performed in triplicate to obtain the experimental result. Percentage differences between the two values were calculated as described in **Equation 5-4**. Regarding the peak area, it is not an identified ATPs, so the percentage difference was calculated using **Equation 5-5**, between the peak area obtained in the optimal condition and conditions with deliberate alterations.

$$\%\,\boldsymbol{Difference} = \frac{\boldsymbol{Rf_{experimental} - Rf_{predicted}}}{\boldsymbol{Rf_{predicted}}} \times \mathbf{100}\% \qquad \textbf{Equation 5-4}$$

$$\%\,\boldsymbol{Difference} = \frac{\boldsymbol{Peak\ Area_{Alterations} - Peak\ Area_{opt.}}}{\boldsymbol{Peak\ Area_{opt.}}} \times \mathbf{100}\% \qquad \textbf{Equation 5-5}$$

Where $Rf_{predicted}$ and $Rf_{experimental}$ refer to the predicted and experimental capacity factor of the analyte peak, respectively. $Peak\ Area_{Alterations}$ and $Peak\ Area_{opt.}$ corresponded to the measured peak area for the analyte peak in the chromatographic conditions with deliberate alterations and the optimal condition, respectively.

5.5. Results and Discussion

5.5.1. Risk assessment

Risk identification in the HPLC method was illustrated in the Ishikawa fishbone diagram, as shown in **Figure 5-2**. Seven method parameters amongst the assessed CQA were evaluated as vital and subsequently selected as the input factors for the definitive screening design, namely starting solvent B concentration ($\%B_s$), solvent B concentration increment ($\%B_i$), flow rate (FR), temperature (T), injection volume (V), the run time (t) and pH of the buffer. As the method is intended to assay the peptide in various pharmaceutical dosage forms and matrices, which included the samples from *in vitro* drug release study, the use of phosphate buffer would be the most suitable and compatible with these samples. Thus, the buffer type was kept unchanged during the method development. Due to previous preliminary results altering the column choice, buffer strength and organic modifier worsened the ATPs, these parameters were also kept constant.

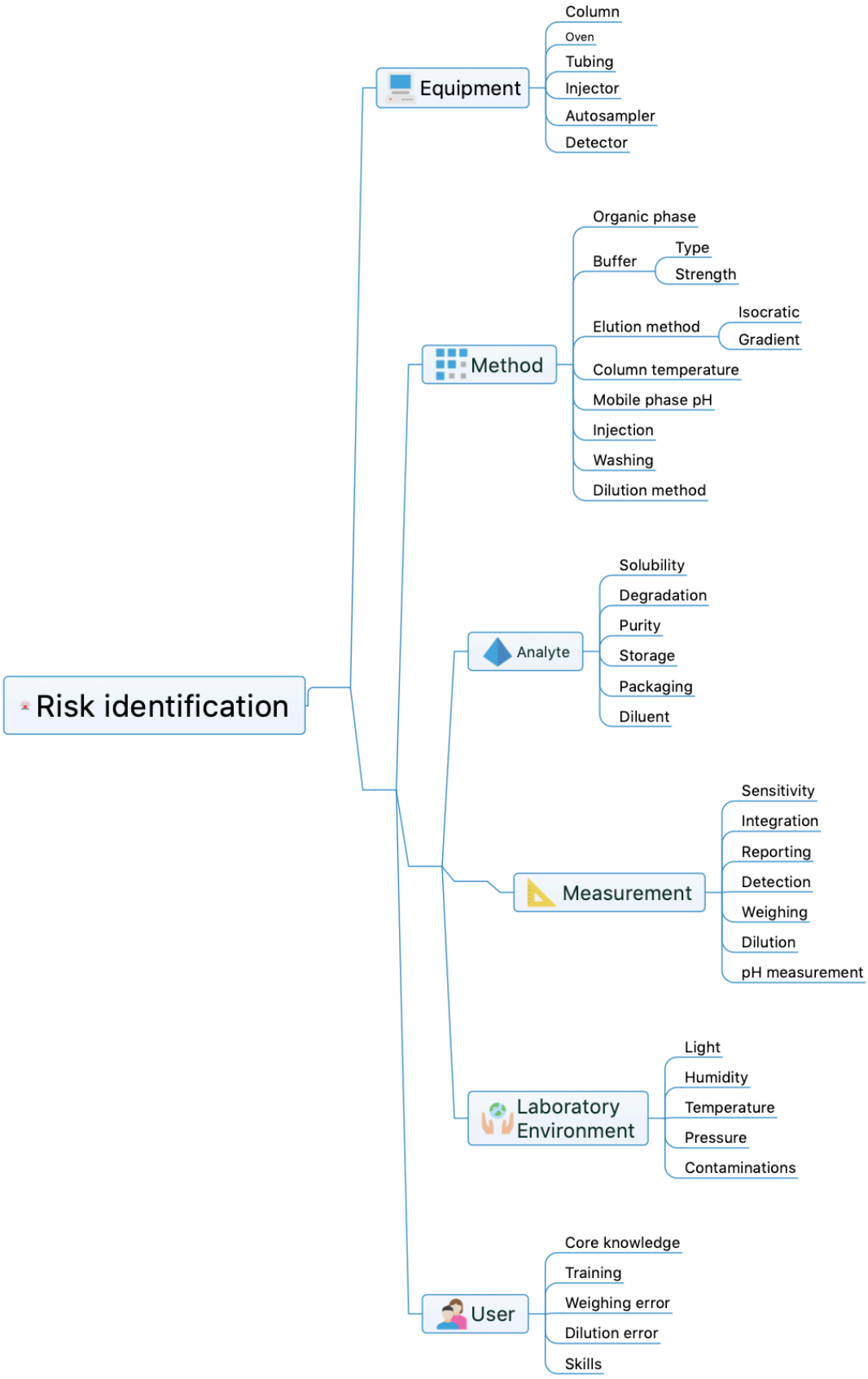

Figure 5-2. Fishbone diagram showing the risks proposed before the AQbD assisted HPLC method development for the peptide.

5.5.2. Definitive screening design

The effective factors screened in the definitive screening design for each variable (capacity factor, theoretical plate count, resolution and tailing factor) were estimated. The profilers for each factor were shown in **Figure 5-3**.

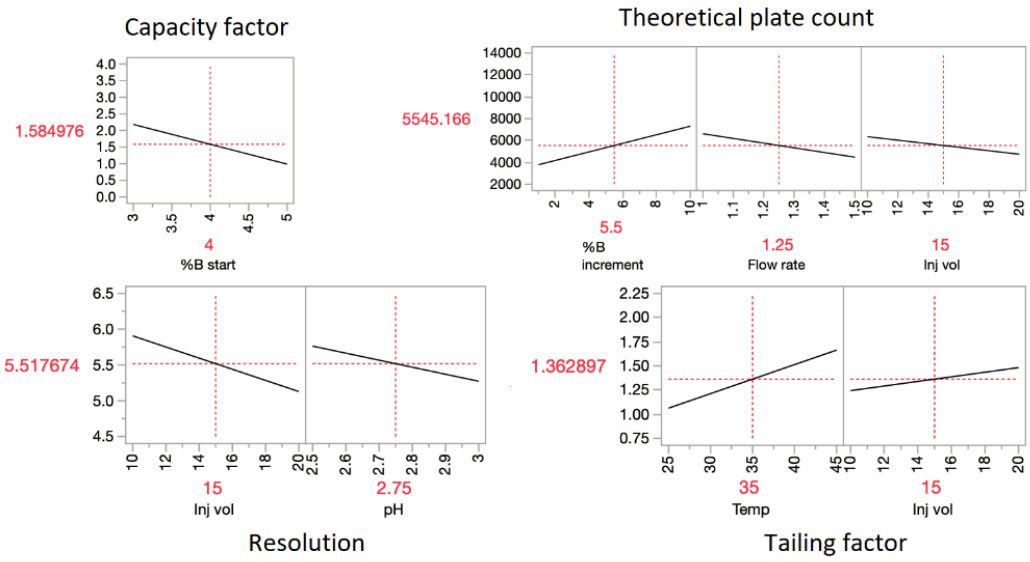

Figure 5-3. Profilers show the effect of the factors identified from the DSD on each independent variable. The predicted correlations were present as the solid black line in the profiler. The experimental conditions were mentioned on the x-axis of the profiler and in red, while the corresponding predicted nanogel properties were present in red on the y-axis.

The capacity factor was estimated to be dependent on the $\%B_s$, with the capacity factor decreasing with the $\%B_s$. Increasing $\%B_s$ would decrease the polarity of the starting mobile phase, eluting the analyte earlier. Meanwhile, the peak resolution correlated to the injection volume and the pH of the buffer, with peak resolution decreasing with both the injection volume and the pH of the buffer. Reduced injection volume would minimize band broadening, allowing better peak separation between the analyte peak and the adjacent peak. The correlation was observed because of mass overloading in the column, which will be discussed in **Section 5.5.5**. Lowering the pH altered the ionization state of the peptide, as the pH of the buffer was close to the isoelectric point. Furthermore, the tailing factor was

dependent on the temperature and injection volume, with tailing worsened with both factors. With increased injection volume, the band broadening was more pronounced with more diffusion and mass transfer at the edge of the peak. Interestingly, the tailing of the peak was promoted when the temperature increased, as the column temperature influences the kinetics and transport properties of the analytes. The diffusivity of the analyte was enhanced because the viscosity of the mobile phase decreased at a higher temperature. Nevertheless, theoretical plate count depended on the $\%B_i$, flow rate and injection volume. The efficacy of the retention was reduced with the flow rate and injection volume, as a higher flow rate reduced the time for interaction between the analyte and column. Injection volume usually increased the peak height and area. However, as the column was mass-overloaded, the tailing increased and the band was broadened, increasing the width of the peak. Interestingly, the %B increment promoted the efficiency of the analyte retention, probably due to the reduced width of the peak. In short, these independent factors were found to impact the ATPs, and thus selected for the optimisation via response surface methodology.

5.5.3. Central composite design

5.5.3.1. Statistical analysis

The response surface model for each dependent response, namely capacity factor, resolution, tailing factor, and the number of theoretical plates was constructed with a polynomial equation. A one-way analysis of variance (ANOVA) and lack of fit test was performed on the RSM for each individual dependent variable to determine the statistical significance and the goodness of fit of these models, respectively. The null hypothesis of the ANOVA is that these models do not correlate with the data set. The results of the ANOVA and lack of fit tests are reported in **Table 5-4**. *p*-values obtained in the ANOVA test for all the models were smaller than 0.05, demonstrating the significance of these models. Terms with linear effects, interactions, and quadratic effects included in the polynomial equations were also shown in **Table 5-4**, with the significance of these terms evaluated individually. Furthermore, the *p*-values in the lack of fit tests for all models were larger than 0.05, which indicated these relationships were a good fit for the data set. Thus, the results showed that the models established in the RSM were correlated strongly with the

data set and were well-fitted. The predictive capacity of these models within the design space is maintained.

Table 5-4. ANOVA and lack of fit test results for the CCD models for various independent variables. The significance for the effect of individual, quadratic and interaction terms of the independent terms predicted to impact the responses were also determined. Statistical significance was set as Prob. > F being smaller than 0.05.

Independent variables	Source of variations	Degree of freedom	Sum of squared	Mean squares	F value	Prob.> F	Significance
Capacity factor	**Model**	15	4.320	0.288	179.988	<0.0001	**Significant**
	$\%B_s$	1	1.541		962.936	<0.0001	*s*
	$\%B_i$	1	0.624		390.114	<0.0001	*s*
	pH	1	1.541		59.855	<0.0001	*s*
	FR	1	0.624		10.094	0.0080	*s*
	T	1	0.096		972.321	<0.0001	*s*
	$\%B_s$ x %Bi	1	0.016		115.204	<0.0001	*s*
	$\%B_i$ x pH	1	1.556		4.651	0.052	*ns*
	$\%B_s$ x FR	1	0.184		6.573	0.0248	*s*
	$\%B_i$ x FR	1	0.007		15.312	0.0021	*s*
	pH x FR	1	0.011		12.568	0.0040	*s*
	$\%B_s$ x T	1	0.025		29.792	0.0001	*s*
	$\%B_i$ x T	1	0.020		78.763	<0.0001	*s*
	pH x T	1	0.048		8.220	0.0142	*s*
	$\%B_i^2$	1	0.126		4.074	0.0665	*ns*
	T^2	1	0.013		6.431	0.0261	*s*
	Residual	12	0.019	0.002			
	Lack of fit	11	0.019	0.002	49.787	0.1101	**Not significant**
	Pure error	1	0.000	0.000			
Resolution	**Model**	5	2.227	0.445	25.493	<0.001	**Significant**
	$\%B_s$	1	0.216		12.354	0.0020	*s*
	$\%B_i$	1	0.162		9.251	0.0060	*s*
	pH	1	1.514		86.634	<0.0001	*s*
	FR	1	0.201		11.517	0.0026	*s*
	$\%B_s$ x $\%B_i$	1	0.135		7.710	0.0110	*s*
	Residual	22	0.384	0.018			
	Lack of fit	19	0.332	0.017	1.01	0.5824	**Not significant**
	Pure error	3	0.052	0.017			
Tailing factor	**Model**	12	3.653	0.304	256.251	<0.001	**Significant**
	$\%B_s$	1	0.035		29.757	<0.0001	*s*
	$\%B_i$	1	0.155		130.113	<0.0001	*s*
	pH	1	0.156		131.318	<0.0001	*s*
	FR	1	0.065		54.663	<0.0001	*s*
					2610.63		*s*
	T	1	3.102		1	<0.0001	
	$\%B_s$ x $\%B_i$	1	0.017		14.111	0.0019	*s*
	$\%B_i$ x pH	1	0.009		7.514	0.0152	*s*
	$\%B_s$ x FR	1	0.005		4.001	0.0639	*ns*

	pH x FR	1	0.004		3.007	0.1034	*ns*
	$\%B_s$ x T	1	0.016		13.723	0.0021	*s*
	$\%B_i$ x T	1	0.074		62.214	<0.0001	*s*
	T^2	1	0.017		13.965	0.0020	*s*
	Residue	15	0.018	0.001			
	Lack of fit	14	0.018	0.001	14.292	0.2048	**Not significant**
	Pure error	1	0.000	0.000			
Theoretical plate	**Model**	10	51632727.000	5163273.000	95.538	<0.001	**Significant**
	$\%B_s$	1	611939.000		11.323	0.0037	*s*
	$\%B_i$	1	36053121.000		667.105	<0.0001	*s*
	pH	1	404378.000		7.482	0.0141	*s*
	FR	1	7260544.000		134.345	<0.0001	*s*
	T	1	1209578.000		22.381	0.0002	*s*
	$\%B_s$ x $\%B_i$	1	938304.000		17.362	0.0006	*s*
	$\%B_s$ x FR	1	547589.000		10.132	0.0054	*s*
	$\%B_i$ x FR	1	3642030.000		67.390	<0.0001	*s*
	$\%B_i$ x T	1	368962.000		6.827	0.0182	*s*
	T^2	1	596281.000		11.033	0.0040	*s*
	Residual	17	918750.000	54044.000			
	Lack of fit	16	688502.200	43031.000	0.187	0.9657	**Not significant**
	Pure error	1	230247.820	230248.000			

Where $\%B_s$ is the starting solvent B concentration, $\%B_i$ is the solvent B concentration increment, FR is the flow rate and T is temperature. *s* and *ns* were denoted for statistically significant and not significant, respectively.

5.5.4. Method Operable design region (MODR)

The method operable design region (MODR) was determined by overlaying the contour plots, based on the criteria set for the ATPs, which are derived from the ICH Q2 (R1) guideline, with Rf and Rs ≥ 2, Tf ≤ 1.5 and N ≥ 2,000. The overlay contour plots were fixed with the optimal chromatographic conditions, with the MODR portrayed in **Figure 5-4**. The white region referred to the MODR, while the coloured region denoted the region that failed with one or more criteria set in the ATPs.

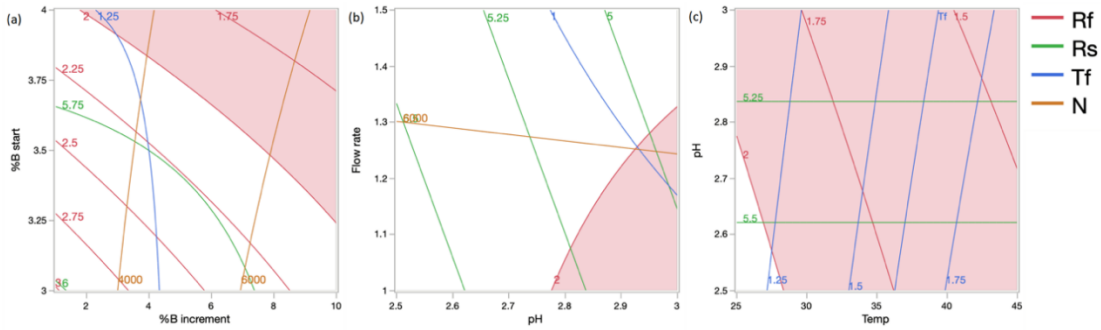

Figure 5-4. The overlay contour plots show the MODR. Only two factors were displayed at a time - (a) $\%B_s$ and $\%B_i$, (b) flow rate and temperature, and (c) pH and temperature, while the other factors were fixed at the optimal condition. The lines in the figure are the contour grid, with assorted colours for respective chromatographic responses.

5.5.4.1. Capacity factor

The capacity factor (Rf or k) indicates the retention of the analyte in the column about the dead volume (t_0). All the chromatographic runs in **Table 5-2** possessed capacity factors above 1, which indicated that the retention of the analyte in the column is sufficient, and the specificity of the analyte is achieved under these chromatographic conditions. All factors, except the quadratic term of $\%B_i$ and the interaction term between $\%B_i$ x pH, were statistically significant in the ANOVA test as presented in **Table 5-4**. Increasing in all linear terms resulted in a reduction of the capacity factor, as the interactions between the sorbent and analytes were weakened and thus the retention in the column was reduced. In contrast, all the statistically significant interaction terms possessed positive effects on the capacity factor, which

indicated that there are synergies between the linear factors and these synergistic interactions attenuate the reduction of capacity factors at a high level the linear factors. Quadratic terms of the temperature also possessed a positive coefficient, which demonstrated that the effect of temperature was not linear and the effect of temperature on capacity factor was enervated at high temperature, as shown in **Figure 5-5**, likely because of simultaneous altering of the chemical and mechanical factors in the kinetics of the analyte in the column in elevated column temperature. The results revealed that lowering these parameters could promote the interaction between the peptide and the column and thus increase the capacity factor.

$$\boldsymbol{Capacity\ factor\ (k) = 13.5123 - 0.3975 \times \%B_i - 1.4860 \times \%B_s - 2.3494 \times FR - 1.5078 \times pH - 0.14864 \times T + 0.002 \times \%B_i^2 + 0.0006 \times T^2 + 0.0477 \times \%B_s \times \%B_i + 0.03479 \times \%B_i \times FR + 0.0192 \times \%B_i \times pH + 0.0020 \times \%B_i \times T + 0.2051 \times \%B_s \times FR + 0.0109 \times \%B_s \times T + 0.5673 \times FR \times pH + 0.0115 \times pH \times T}$$

Equation 5-6

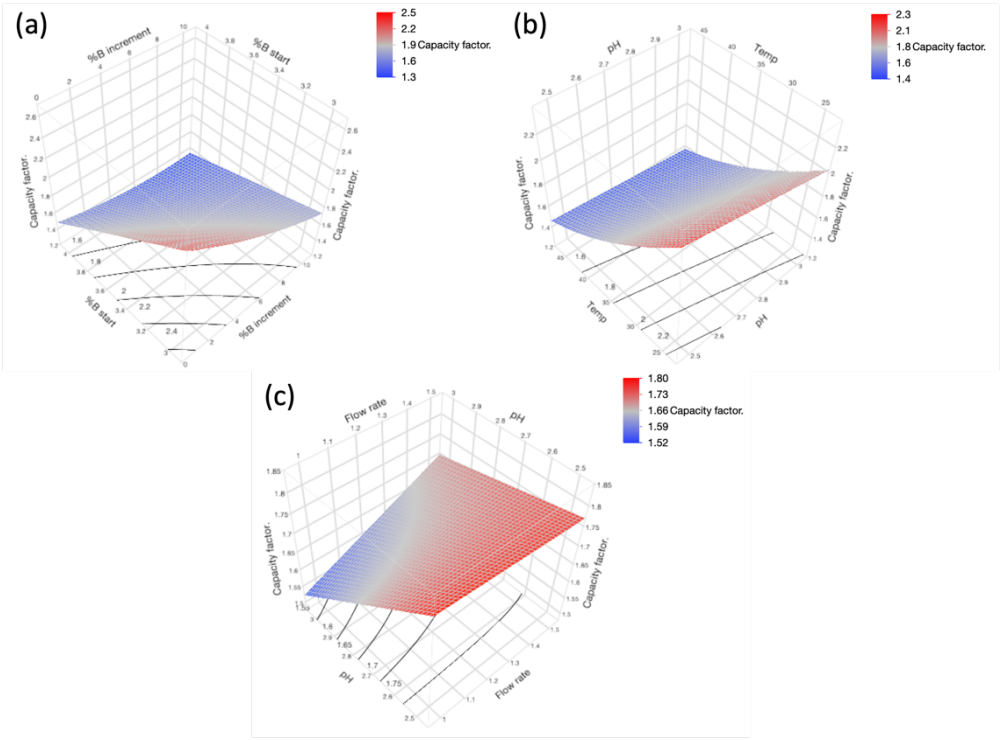

Figure 5-5. Response surface models predict the effect of (a) $\%B_s$ and $\%B_i$, (b) pH and temperature and (c) flow rate on the capacity factor of the analyte peak.

5.5.4.2. Resolution

Resolution is a measure of the separation between two peaks in a chromatogram in terms of distance and width [291]. In this study, the resolution measured the separation between the peak of interest and the closest adjacent peak using the half-height method. The adjacent peak was at the retention time of 5.935 minutes as shown in **Figure 5-10 (a)**. The measured resolution for all chromatographic runs in the design matrix was above 4, which indicated that the separations between the peak of interest and the adjacent peak were sufficient. The response surface plots for resolution are shown in **Figure 5-6**. $\%B_s$, $\%B_i$, flow rate, and pH were found to have significant but negative effects on the resolution, as the coefficients for these terms were negative in **Equation 5-7**. Increasing flow rate and steepness of the gradient generally decreased the resolution as both narrowed the peak spacing in the chromatogram [292]. Altering the pH was more complex, as it changed both selectivity and retention, which both subsequently impact the resolution. However, the response surface plots showed that the overall effect of pH was negative, which

indicates that the resolution decreases with the pH of the buffer for this peptide. In contrast, the use of higher organic solvent composition reduced the retention of the peptide as it decreased the polarity of the mobile phase and thus the peak spacing. Meanwhile, the interaction term between $\%B_s$ and $\%B_i$ was also found to be significant, which indicated that there is a synergism between $\%B_s$ and $\%B_i$ in changing the resolution.

$$\boldsymbol{Resolution = 10.7083 - 0.1638 \times \%B_i - 0.4433 \times \%B_s - 0.4229 \times FR - 1.1600 \times pH + 0.0408 \times \%B_s \times \%B_i} \qquad \textbf{Equation 5-7}$$

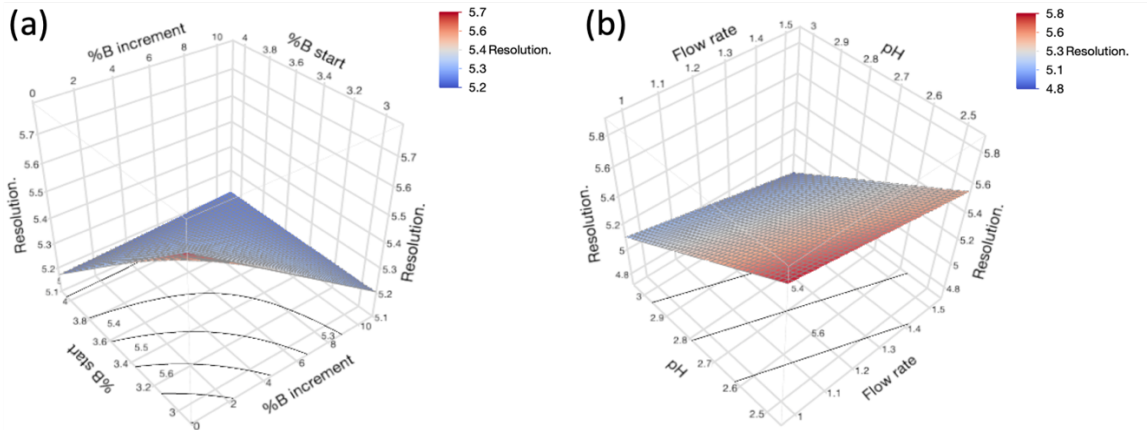

Figure 5-6. Response surface models predicting the effect of (a) $\%B_s$ and $\%B_i$, (b) pH and flow rate on the resolution.

5.5.4.3. Tailing factor

The tailing factor refers to the coefficient of peak symmetry in United States Pharmacopeia (USP) and the acceptable tailing factor is between 0.9 to 1.2. Only a quarter of the chromatographic conditions in **Table 5-2** possessed a tailing factor in between the acceptable criteria. The ANOVA study in **Table 5-4** demonstrated all the linear terms of the factors were significant, with $\%B_i$ and pH reducing the tailing and vice versa for $\%B_s$, FR, and T. Increase in $\%B_i$, specifically the gradient steepness, refocused the peak and minimised the peak tailing. Interestingly, increasing pH reduced the tailing factor, most likely due to the pH being close to the isoelectric point of the peptide. Increasing the flow rate resulted in higher tailing factors, which is potentially due to increased mass transfer and diffusion of the analytes at a higher flow rate. Elevating the column temperature also led to a higher

tailing factor, as the column temperature influences the kinetics and transport properties of the analytes. The diffusivity of the analyte was enhanced because the viscosity of the mobile phase decreased at a higher temperature. Nonetheless, the correlation between flow rate, temperature, and $\%B_s$ with the tailing factor is poorly understood. Several interactions between $\%B_s$ x $\%B_i$, $\%B_i$ x pH, $\%B_i$ x T, $\%B_s$ x T, and the quadratic term of temperature, as shown in **Figure 5-7**, were also found to be significant in controlling the tailing factor. However, it is difficult to identify the causes between the interaction terms and tailing factor as peak tailing is occurred due to multiple retention mechanisms of the analyte in the column. The peptide used in this study interacts via nonspecific hydrophobic interactions with the C18 chain and polar interactions with the ionised residue of the silanol groups. In addition, there are also interactions between the analytes as the peptide remains predominantly cationic at pH 2.5-3.0, where the repulsion between the analyte resulted in mass overloading of the column. Another possible explanation is that peak broadening was a consequence of the cationic peptides repulsing each other in the stationary phase.

$$\boldsymbol{Tailing\ factor = -0.6694 - 0.0758 \times \%B_i + 0.2281 \times \%B_s + 0.8999 \times FR - 0.1890 \times pH + 0.1077 \times T - 0.0005 \times T^2 + 0.0144 \times \%B_s \times \%B_i + 0.0210 \times \%B_i \times pH - 0.0015 \times \%B_i \times T - 0.1379 \times \%B_s \times FR - 0.0064 \times \%B_s \times T - 0.2391 \times FR \times pH} \quad \textbf{Equation 5-8}$$

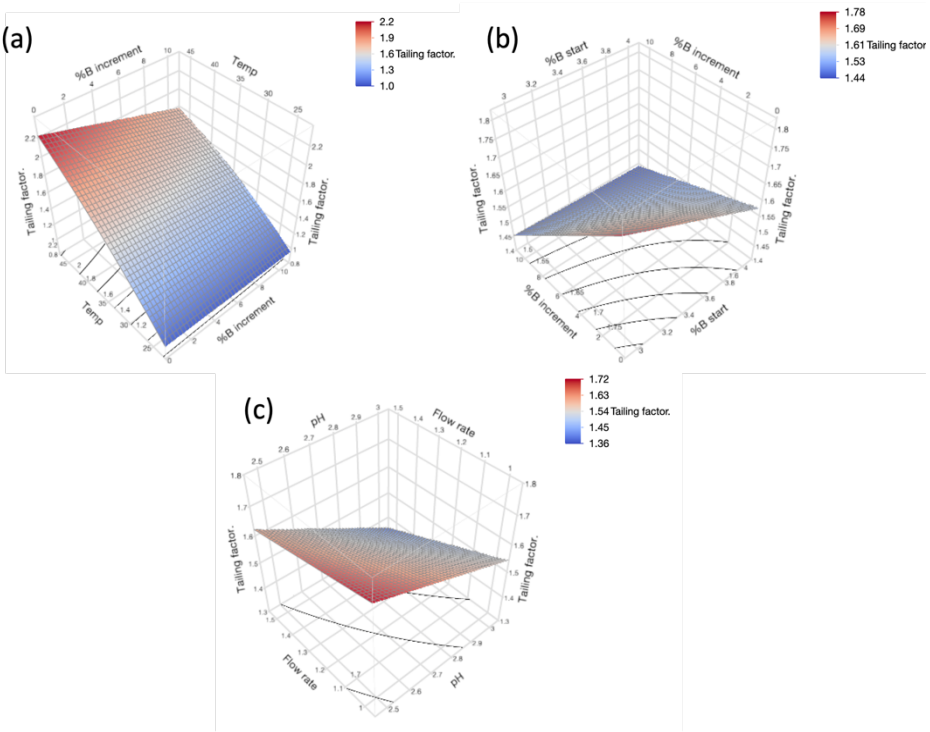

Figure 5-7. Response surface models predict the effect of (a) temperature, (b) $\%B_s$ and $\%B_i$, and (c) pH and flow rate on the tailing factor of the analyte peak.

5.5.4.4. Theoretical plate counts

The number of theoretical plates is an indication of the column efficiency. All factors identified in **Table 5-4** were statistically significant in controlling the number of theoretical plates. The response surface plots for theoretical plate counts are shown in **Figure 5-8**. %Bs, flow rate, temperature, and pH were found to have significant but negative effects on the theoretical plate counts, as the coefficients for these terms were negative in **Equation 5-9.** Increasing all these factors reduced the column efficiency, as the retention time was reduced and the standard deviation of the measured peak in the unit of time was also altered [293]. Conversely, $\%B_i$ was also significant and possessed a positive effect on the number of theoretical plates. The result demonstrated that steepening the gradient slope within the design space improved the column efficiency, which is likely due to refocusing of the peak with the steeper gradient. Several interaction terms, namely $\%B_i$ x $\%B_s$, $\%B_i$ x FR, $\%B_s$ x T, and $\%B_s$ x FR, were found statistically significant in the ANOVA, where the former three terms and the last term had negative and positive effects on the theoretical plate counts, respectively. Another quadratic term of temperature was also statistically significant, with the peak trough identified at about 35 ^{o}C.

$$\boldsymbol{Theoretical\ plate = 12125.0877 + 1339.4269 \times \%B_i - 1626.7860 \times \%B_s - 5387.884586 \times FR - 599.5389 \times pH - 168.7069 \times T + 3.0456 \times T^2 - 107.6290 \times \%B_i \times \%B_s - 424.0912 \times \%B_i \times FR - 3.3746 \times \%B_i \times T + 1479.9857 \times \%B_s \times FR}$$ **Equation 5-9**

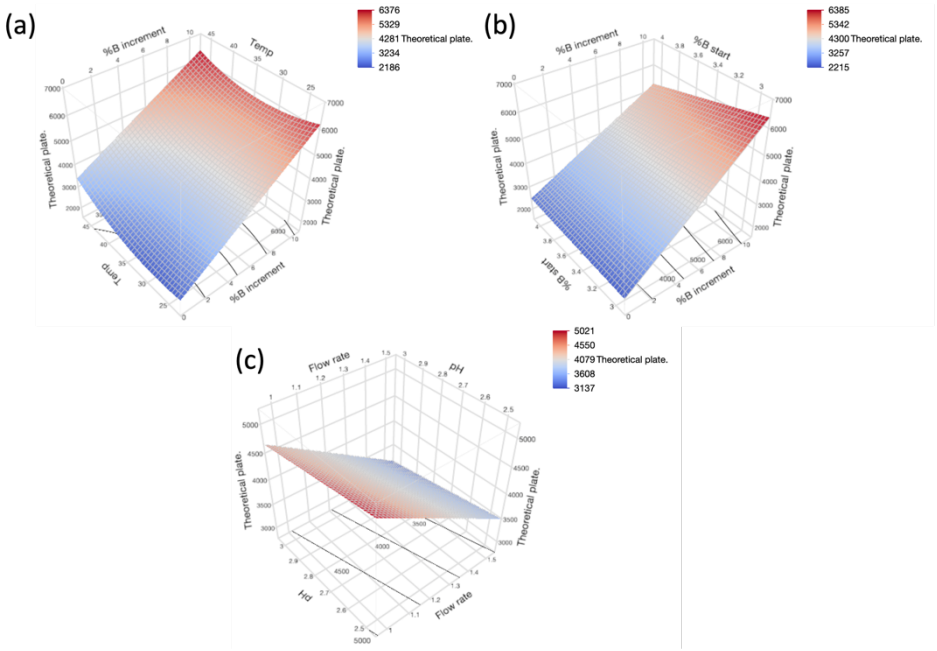

Figure 5-8. Response surface models predict the effect of (a) temperature, (b) starting % solvent B and %B increment, and (c) pH and flow rate on the number of theoretical plates.

5.5.5. Multiple response optimisation

The optimal fabricating condition was determined by multiple response optimisation (MRO) as shown in **Figure 5-9**, aiming to achieve the largest capacity factor, resolution and theoretical plate, and the lowest tailing factor. The optimal running condition for Ac-SDKP utilises phosphate buffer at pH 2.5 and acetonitrile as mobile phases, which starts at 3% acetonitrile and increases to 9.7% over 15 mins at a flow rate of 1 mL/min. The injection volume was initially fixed at 20 µL, to maximise the ranges of detection and quantitation. The predicted capacity factor, resolution, tailing factor and theoretical plate running at the optimal chromatographic condition were 2.400, 5.779, 1.22, and 5,778 respectively while the experimental results were 2.138,

5.970, 1.15, and 5,680, respectively. The measured values were -10.9%, 3.3%, -5.7%, and -1.7% different from the predicted values for capacity factor, resolution, tailing factor and theoretical plate, respectively. Although there were discrepancies between the measured and predicted values for all responses, the results still demonstrated that these models had the sufficient predictive ability.

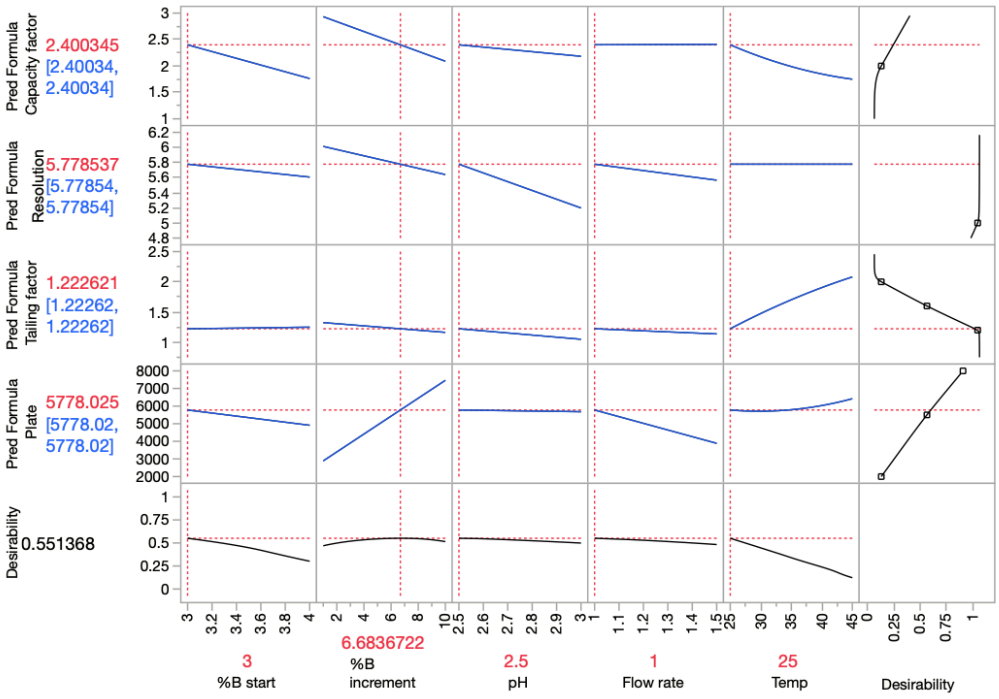

Figure 5-9. Interaction profilers show the optimal chromatographic condition with the predicted parameters. $\%B_i$ was rounded up to 9.7% in the final method as the HPLC program could only handle up to 1 decimal place. The overall desirability for the optimal chromatographic condition was 0.551.

However, mass overloading was observed in the column using the injection volume of 20 µL, with the peak fronting observed. The peak shifts exceeded the relative retention time window of 2.5%, at the lower concentrations of the calibration curve with the red arrow pointed in **Figure 5-10 (a)**. This was likely to be due to the repulsion between the cationic peptide on the stationary phase and preventing the occupancy of the high-energy sites in the deeper C18 layer by the solute [294], as the peptide remains cationic at pH 2.5. Moreover, the broad and asymmetrical peak observed in the chromatogram could also be explained by the slow sorption-

desorption kinetics of the silanols of the stationary phase [295]. Therefore, the injection volume was finally reduced to 10 µL, to further minimise the shifting of the retention time. The retention time shift was still present with the injection volume of 10µL, but the shift was much attenuated and maintained within 2.5% of variation as shown in **Figure 5-10 (b)**. It was noted that the reduction of the injection volume had impacts on the ATPs, mainly reducing the tailing factor, as the peak area was reduced and there was less mass overloading on the column. Moreover, it also impacted the capacity factor slightly, attenuating the shift of the peak retention time. Despite these impacts on the ATPs, it was vital to reduce the mass overloading on the column, avoiding the diminishments of the efficiency and the assay sensitivity. Hence, the injection volume was adjusted after the DOE optimisation, as a mitigation to the mass overloading.

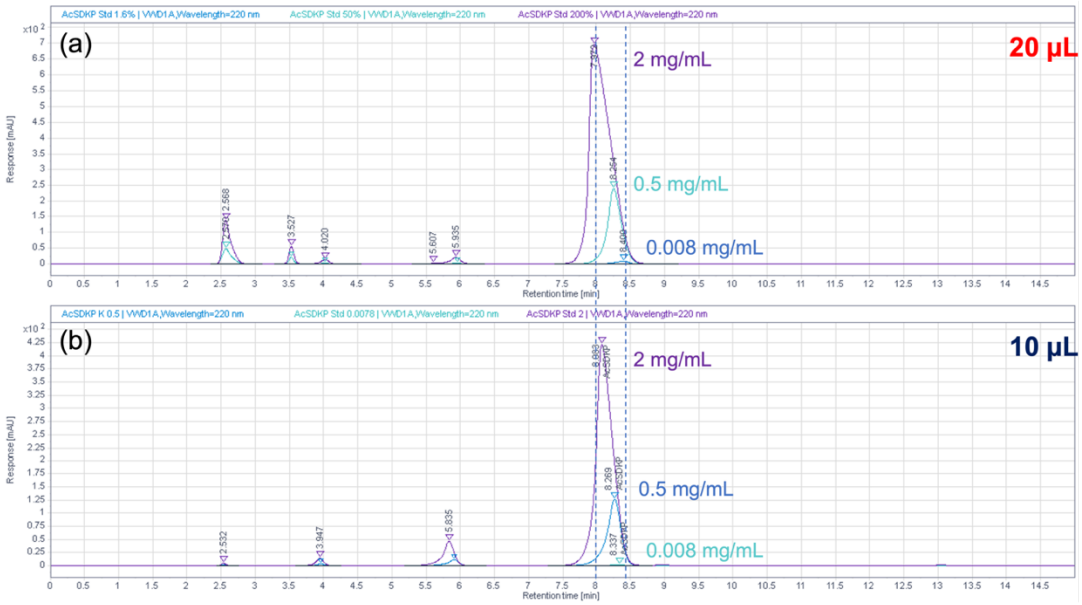

Figure 5-10. Chromatograms of three calibration standard solutions in the calibration curve ranged from 8 µg/mL, 0.5 and 2mg/mL at two different injection volumes of (a) 20 µL and (b) 10 µL; mobile phase flow rate 1 mL/min; a linear gradient (ACN: 3% to 9.7% in 15 minutes); VWD detector wavelength 220 nm; column temperature 25 ºC. The figure showed that the peak shifts were attenuated, and all the peaks were within the 2.5% window after halving the injection volume to 10 µL. Variations in retention times between runs are expected, thus 2.5% was set as the acceptable window in this method due to the robustness of the method and quality by design.

5.6. Method validation

5.6.1. Specificity

The specificity of the method was evaluated by comparing the chromatograms of the blank solution, PBS solution, matrix sample solution, validation standard solution, and sample solutions in PBS and matrix sample. Thus, 10 μL of these solutions were injected into the HPLC system individually, and the chromatograms are shown in **Figure 5-11**. In the chromatograms for the solutions containing the peptide, as present in **Figure 5-11 (a) to (c)**, the analyte was eluted as a single peak and well separated from other peaks presented. No co-eluting peak at the retention time of the peptide was observed, which indicated that the analyte peak was pure, and the method was specific. In **Figure 5-11 (d) to (f)**, no peak of analyte was present for the matrix sample, blank and pure PBS solutions, which also elucidated that the other components in the sample did not interfere with the peak of the analyte. The presence of other peaks in **Figure 5-11 (a) and (c)** likely corresponded to the contaminants, potentially incorporated during the sample preparations. The peak at 3.986 minutes observed in **Figure 5-11 (b)** likely referred to the impurities presented in the validation standard while the peak at 5.955 minutes was likely due to the presence of a contaminant.

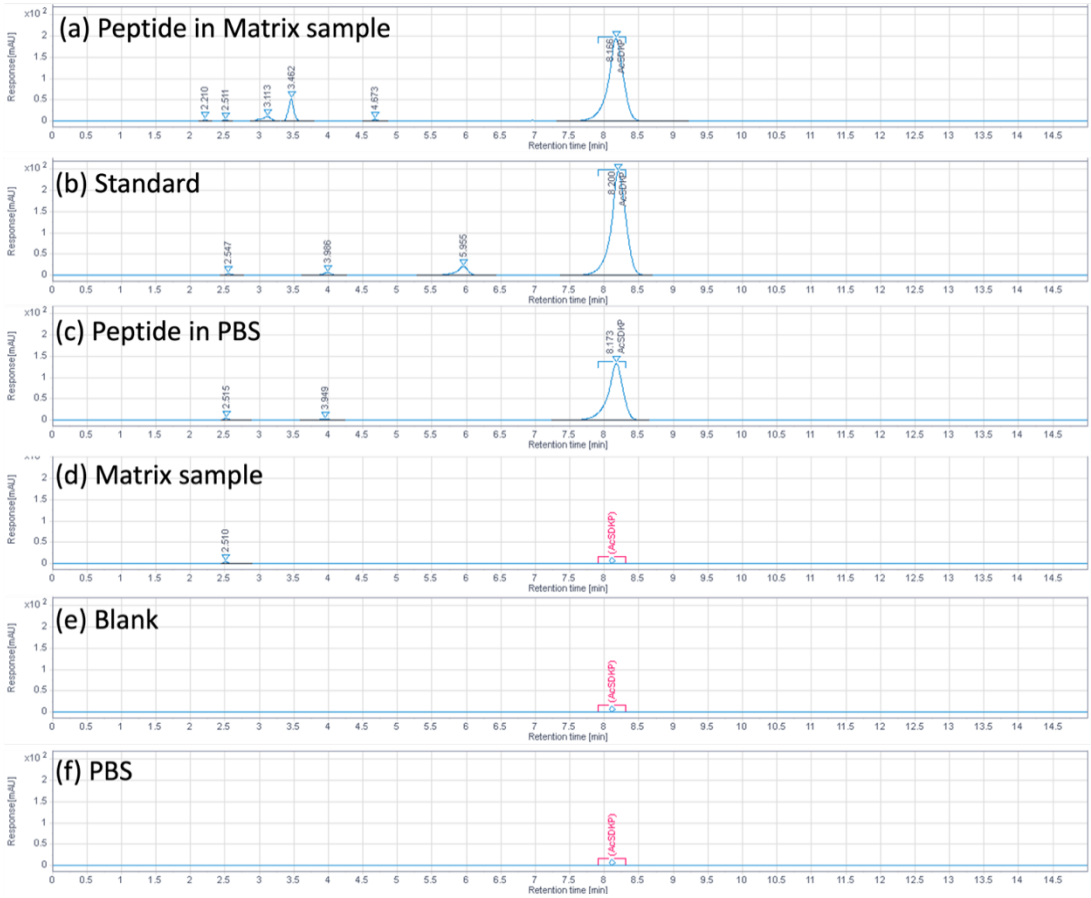

Figure 5-11. Chromatograms of (a) the peptide in matrix sample, (b) the standard solution in water, (c) peptide samples in PBS, (d) peptide-free matrix sample, (e) blank solution (i.e., Water), (f) PBS. No peak was observed in peptide-free matrix sample, blank solution, and PBS, which demonstrated no peptide was detected. The retention time for the peptide in matrix sample, water and PBS were similar.

5.6.2. System suitability

A system suitability test was performed with a 1 mg/mL validation standard solution on two different HPLC systems. A total of 6 injections of the standard were injected into the column. The capacity factor, resolution, tailing factor, theoretical plates, and relative standard deviations (RSD) for retention time and peak area were determined and presented as the average in **Table 5-5.**

Table 5-5. System suitability results of the proposed HPLC method on two different HPLC systems. The results demonstrated both HPLC were suitable for performing analysis of the peptide.

System suitability parameters	Acceptable criterion	HLPC 1	HPLC 2
Retention time	RSD ≤ 1%	0.1%	0.5%
Peak area	RSD ≤ 1%	0.2%	0.8%
Capacity factor (k)	k ≥ 2.0	2.237	2.256
Resolution (Rs)	Rs ≥ 2.0	6.881	6.409
Tailing factor (T)	T ≤ 1.5	0.90	0.93
Theoretical plates (N)	N ≥ 2000	7349	7283

5.6.3. Linearity and range

The calibration curve was established with 13 concentrations, with the solution with the lowest concentration of 3.9 µg/mL being undetectable. Therefore, the range of the assay method is between 7.8 µg/mL to 2 mg/mL. The correlation coefficient of the calibration was 0.9993, which was acceptable under the criterion. The result elucidated a good correlation between the peak area and the concentration within the range. The regression equation was shown as **Equation 5-10**. The range established in this method was much higher compared to the reported LC-MS/MS or EIA methods, where the range of these methods was between 0.5 and 100 ng/mL [270,272,274].

$$\boldsymbol{y = 3685x + 5.2019} \qquad \textbf{Equation 5-10}$$

5.6.4. Limit of detection and limit of quantification

The LOD and LOQ were determined from **Equation 5-1**and **Equation 5-2** using the standard deviation of y-intercept in the calibration curve as σ. The LOD and LOQ were 5.5 and 16.8 µg/mL, respectively.

5.6.5. Accuracy

Accuracy was reported as the recovery percentage of the known peptide added to both phosphate buffer saline (PBS) as a placebo and a matrix solution (M). The matrix solution was the diafiltrate of the chitosan-TPP nanogels solution. The method involved spiking the PBS and M with Ac-SDKP in water at three different

concentrations (0.75, 1.00 and 1.50 mg/mL), with the results shown in **Table 5-6**. The % recovery obtained in the spiking of the sample with PBS was higher than in the M. The matrix solution is predominantly water and salt, as the Amicon ultra filter trapped all nanoparticles during the centrifugation, where PBS also contained phosphate. The matrix effects of the M and PBS were determined by **Equation 5-3**, with the values of -0.9 ± 2.8% and 5.1 ± 3.8% for MS and PBS, respectively.

Table 5-6. Results of accuracy tests for determination of peptide Ac-SDKP in phosphate buffer saline and matrix solution samples. The RSD for both spiked samples fulfilled the criterion, which showed that peptide quantification in both samples was accurate.

Spiked samples	Concentrations (mg/mL)	Purity (% Area)	Area	Percentage recovery		Criterion
			RSD (%)	Average (%)	RSD (%)	
PBS	0.75	96.6 ± 0.4	3.7	82.2	3.7	RSD <10%
	1.00	97.1 ± 0.0	0.3	108.7	0.3	
	1.50	97.8 ± 0.2	0.2	161.0	0.2	
M	0.75	91.1 ± 0.2	2.3	75.6	2.3	
	1.00	91.1 ± 0.0	1.2	100.6	1.2	
	1.50	91.1 ± 0.1	1.2	150.0	1.2	

However, the matrix effects for M and PBS were not statistically significantly different from water according to the ANOVA as shown in **Figure 5-12**, and thus the matrix effects of the M and PBS are negligible. Despite the low purity of the peptide used due to the cost, the purity of the peptide was measured at over 91% in all spiked samples regardless of the matrix or PBS solution used, which agrees with the manufacturer's reported value of 90%. The result showed that the method remains robust, albeit the less pure peptide was used in the method development and validation, where the %area would reflect the purity of the analytes tested.

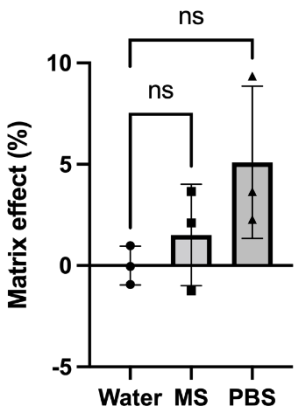

Figure 5-12. Matrix effects of the matrix solution (M) and phosphate buffer saline (PBS) on the chromatographic method. Analysis of variance (ANOVA) was performed to determine the statistical significance of the matrix effects for M and PBS. ns refers to *p*-value > 0.05.

5.6.6. Precision – Repeatability and intermediate precision

The average, SD and RSD of the retention time, peak area, and height for the 10 replicates in repeatability measurement were presented in **Table 5-7**, with the experimental RSD for all parameters below 1% and fulfilling the criteria. The result elucidated that the method is precise and the intra-day variation on the instrument was minimal.

In contrast, the intermediate precision assessed the method's resistance to different instrumentation, time of analysis, and analyst to the initial method developed. The RSDs for the inter-day precisions for both analysts 1 and 2 and on both Agilent Infinity 1260 and 1200 HPLC systems were lower than the limit of 2%, which indicated that the method was resistant to variations in the analyst and time. Ms Satinder Sembi has kindly performed the analysis as analyst 2. The instrumental RSD, which included all runs on that instrument regardless of the day and analyst, was also smaller than the criterion and thus demonstrated that the method was precise and repeatable in different instrumental systems.

Table 5-7. Intermediate precision and repeatability of the method.

Instrument	**HPLC 1 (Agilent 1260)**			**HPLC 2 (Agilent 1200)**			
Intermediate precision (n = 3)							
Concentrations (mg/mL)	**0.5**	**1.0**	**1.5**	**0.5**	**1.0**	**1.5**	**Criterion**
Operator 1 inter-day RSD	0.37%	0.26%	0.75%	0.93%	1.64%	0.69%	RSD <2%
Operator 2 inter-day RSD	1.32%	1.37%	1.32%	0.1%	0.46%	0.15%	RSD <2%
Instrument RSD	1.26%	1.04%	0.88%	0.16%	0.36%	0.11%	RSD <2%
Repeatability (n = 10)	**Average**	**RSD (%)**					**Criterion**
Resolution	8.203	0.12					RSD<1%
Area	3749.4	0.22					RSD<1%
Height	242.09	0.92					RSD<1%

5.6.7. Robustness

The robustness of the method was evaluated by deliberate alterations of the temperature, $\%B_s$, $\%B_i$, flow rate, and pH, as shown in **Table 5-8**. For the capacity factor of the analyte peak, they are first predicted based on the correlations established in the method operable design space and subsequently compared with the experimental result. The percentage difference between the predicted and experimental results was less than 7.5% for most of the alterations, which were set as the acceptance criteria. However, changing the flow rate had a notable impact on the capacity factor of the peak of an analyte, exceeding the 10% difference between the predicted and experimental results. The result indicated that controlling the flow rate (i.e., Linear velocity) is the most crucial method to avoid any impact on the ATPs. Temperature, $\%B_s$, and pH were found to impact the capacity factor of the analyte peak, but their effects could largely be modelled by the correlation established. Altering the temperature resulted in shifts of the retention as the temperature impacts the analyte diffusivity, the viscosity [296], dielectric constant [297], and surface tension of the mobile phase, where the analyte diffusivity improved and the rest of the factors decreased under the elevated temperature, resulting in the decrease of the solute elution. Nevertheless, modifying $\%B_s$ does not affect the interaction between the analyte and the stationary phase, as $\%B_s$ refers to the starting % of the organic

solvent in the mobile phase. Thus, with the same eluting gradient, the retention time changes with the $\%B_s$ inversely and linearly. The pH of the buffer is another factor crucial to determining the ionization of the peptide, where the pH of the buffer was close to the isoelectric point of the peptide. Therefore, any change in the pH of the buffer would affect the ionisation of the peptide and subsequently the capacity factor.

Table 5-8. Deliberate variations in analytical conditions to determine the robustness of the HPLC-UV assay method. The varied factors were bolded and italicised.

Trial	Opt.	A	B	C	D	E	F	G	H
T (°C)	25	***20***	***30***	25	25	25	25	25	25
%Bs	3	3	3	***2***	***4***	3	3	3	3
%Bi	6.7	6.7	6.7	6.7	6.7	6.7	6.7	6.7	6.7
FR (mL/min)	1	1	1	1	1	***0.8***	***1.2***	1	1
pH	2.5	2.5	2.5	2.5	2.5	2.5	2.5	***2.4***	***2.6***
Predicted Rf	2.400	2.657	2.193	3.100	1.723	2.428	2.395	2.464	2.359
Experimental Rf	2.261± 0.001	2.479 ± 0.001	2.105 ± 0.003	3.042 ± 0.004	1.856 ± 0.001	2.955 ± 0.002	2.107 ± 0.007	2.312 ± 0.004	2.255 ± 0.002
% Difference	6.1%	7.2%	4.2%	1.9%	-7.1%	-17.8%	13.6%	6.6%	4.6%
Area	3687.6 ± 8.7	3688.5 ± 2.3	3696.7 ± 1.9	3702.8 ± 1.8	3696.7 ±0.6	4607.4 ± 4.8	3731.6 ± 2.3	3703.2 ± 0.1	3762.5 ± 0.1
% Difference (vs Opt.)	N/A	0.0%	0.2%	0.4%	0.2%	24.9%	1.2%	0.4%	2.0%

Regarding the peak area, as it is not an ATPs defined above, the percentage difference was calculated between the results obtained in the optimal condition and altered conditions. ANOVA was performed to determine whether the differences between the peak area obtained from these conditions were significant, as shown in **Figure 5-13**. The acceptable criteria were set as a percentage difference of 2% between the peak area obtained from the optimal and altered conditions. The result indicated that the differences were significant, especially when $\%B_s$ was increased by 1%, and when flow rate and buffer pH were changed. The peak area measured in these conditions was larger as compared to the original method. However, the degree of differences was small, with less than 2% for most of the other alterations, revealing the robustness of the model. Similarly, decreasing the flow rate by 10% significantly increased the peak area of the analyte peak by approximately 25%,

which demonstrated the importance of controlling the flow rate in the method. A reduction in flow rate also indicated a slower velocity through the detection flow cell, of which each molecule contributed more to the measured absorbance at the set detector sensitivity (0.1 AUFS) [298]. Noteworthy, the flow rate in 0.8 mL/min was not in the method operable design region, as the latter was in between 1 and 1.5 mL/min. Thus, this discrepancy also revealed the significance of performing the method within the MODR, and any extrapolation outside the MODR was not feasible. Increasing the flow rate to 1.2 mL/min, which was in the MODR, altered the peak area to a much lesser degree, with only a 1.2% difference from that of optimal condition. Furthermore, increasing the pH to 2.6 also impacted the peak area, but the percentage difference calculated was 2.0%. The increase was likely due to more interactions between the solute and stationary phase when the pH of the buffer increased. Moreover, pH 2.6 is closer to the isoelectric point of the peptide (estimated to be pH 3), where more peptides were neutral in charge and interacted more strongly with the stationary phase. Conversely, the peak area measured with pH 2.4 buffer was significantly different from the proposed method, but the percentage difference was much smaller. The result demonstrated that pH 2.6 is likely the cut-off pH for the method without altering the accuracy. Overall, the result indicated that the method is robust within the MODR.

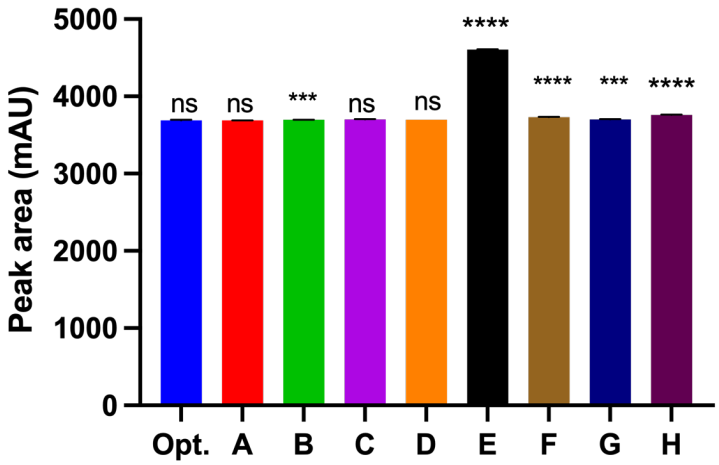

Figure 5-13. Robustness of method in terms of peak area with the variations in temperature (A & B), starting %B (C & D), flow rate (E & F), and pH (G & H). A one-way ANOVA was performed to determine if the variations result in a significant difference in the retention time and peak area. Dunnett's test was performed to compare all variations to the standard method. *** p-value < 0.001, **** p-value < 0.0001 and ns denoted not significant. Each data point is presented as average, while the error bar refers to the standard deviation, which might be too small to be observed in the figure.

5.7. Conclusion

In this chapter, a robust and accurate HPLC-UV method was developed for the quantification of Ac-SDKP using an analytical quality by design approach. The method was optimised via the Design of Experiment to identify the optimal chromatographic condition, where the obtained capacity factor, resolution, tailing factor, and theoretical plate counts fulfilled the ICH guidelines. The validated chromatography condition utilises phosphate buffer at pH 2.5 and acetonitrile as mobile phases, which starts at 3% acetonitrile and increases to 9.7% over 15 mins at a flow rate of 1 mL/min at 25 ºC. The injection volume is set at 10 µL and the VWD detector wavelength is 220 nm. The new analytical method is advantageous because it utilises standard HPLC settings and does not involve the use of expensive equipment or procedures, such as LC-MS/MS or ELISA. The method is particularly well-suited to pharmaceutical research and the development of dosage forms for

peptides as it could detect peptides at high concentrations covering the range for the experimental therapeutic doses and with low running costs. Therefore, this work is a prerequisite for the last chapter, which was aimed at developing Ac-SDKP-loaded nanogels. As the assay method was validated with spiking PBS and filtrate from nanogels as the matrix, the method would be used for determining the encapsulation efficiency of the nanogels and quantifying the samples from drug release studies of the nanogels.

Chapter 6

Developing Guanidylated Chitosan-TPP Nanogels as a Novel Drug Carrier System for Intrapericardial Delivery of Peptides

6. Developing guanidylated chitosan-TPP nanogels as a novel drug carrier for intrapericardial peptide delivery

6.1. Introduction

Biomolecules, including genes, proteins, and peptides, are fragile and susceptible to degradation from heat, enzymes, and hydrolysis. One way to protect these payloads is to encapsulate them in polymeric particles before delivery, which includes nanogels. In this study, the peptide Ac-SDKP was encapsulated in nanogels aiming for intrapericardial delivery. The key attributes of a successful intrapericardial nanogel formulation are that they are small enough to be injected through a needle and are monodisperse. The encapsulation of the peptide should also be efficient, and the activity of the peptide be retained after the encapsulation. In addition, peptides are sensitive to pH, as the amide bonds are susceptible to hydrolysis. Therefore, the peptide-loaded nanogels should be fabricated under mild conditions and at a close to neutral pH.

Since chitosan precipitates at pH 6 due to the deprotonation of the amine group, it was predicted that a new nanogel system would be required for use at a higher pH. Three amino acids possess basic side chains at neutral pH, namely lysine, histidine, and arginine. Several proteins bind to the DNA via the interaction between the cationic side chains of lysine and arginine and phosphate backbone on the DNA [299,300]. Thus, the functionalisation of chitosan with lysine or arginine could potentially overcome the precipitation issue at high pH, as the pKa of the amine and guanidino group is higher than the fabrication pH of 5.5 or 7, preventing the precipitation of the polymer. As a result, a guanidinoacetic acid-functionalised chitosan (CS-GAA) was developed for fabricating the nanogels at higher pH in this chapter. Guanidinoacetic acid (GAA) is a metabolite of glycine and is a natural precursor of creatine via methylation. Conjugation of GAA to chitosan could potentially make the polymer soluble at neutral pH and interact stronger with the phosphate-containing crosslinkers.

In **Chapter 3**, several correlations between size, PDI and zeta potential of the nanogels were established with the molecular descriptors in the beta-blocker family. This chapter applied these correlations to a different structurally similar drug pair, where lisinopril was first used as a surrogate for nanogel optimization (due to the prohibitive cost of the peptide) to determine the optimal condition. Subsequently, lisinopril was replaced with the peptide Ac-SDKP and the peptide-loaded nanogels were fabricated using the same formulation. The structures of both drugs are shown in **Figure 6-1**. Although the guanidine groups were conjugated on the chitosan, it was presumed that the interaction between the guanidylated chitosan with the drugs and crosslinkers would not change. Therefore, the properties of the Ac-SDKP could potentially be estimated from the correlations established in **Chapter 3**. Since the processing factors could also impact the properties of the nanogel the processing factors were either kept unchanged or included in the optimization process.

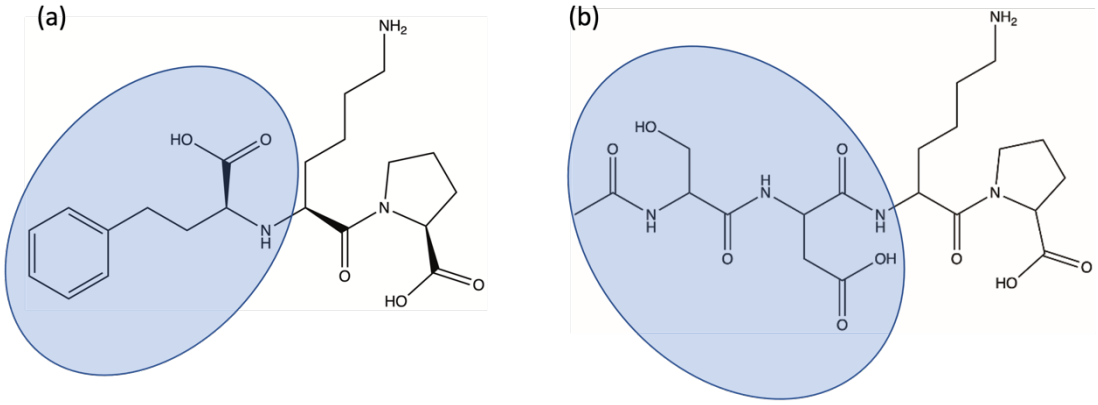

Figure 6-1. Structures of (a) lisinopril and (b) Ac-SDKP, with the distinct region shown in blue.

In this chapter, the first aim was to develop a novel nanogel system that could be fabricated at a pH closer to the physiological pH. The success criteria for the formulation were set as size ≤ 500 nm, PDI ≤ 0.3 (measured by the Zetasizer), ZP ≥ 15 mV, and EE ≥ 50%. The second aim was to fabricate Ac-SDKP-loaded nanogel with the formulation optimization process performed using a structurally similar drug – lisinopril. The ability to extrapolate the correlations established in propranolol-loaded nanogels was tested. Raw materials are defined as the starting materials in this chapter. They were characterised using various techniques alongside the guanidylated chitosan, and its nanogels. Finally, the last aim of this chapter was

to determine a suitable dose to evaluate the effect and function of the Ac-SDKP-loaded CS-GAA nanogel.

6.2. Materials and Methods

6.2.1. Materials

Low molecular weight chitosan (LMW with a molecular weight of 50-190 kDa according to the manufacturer), N-hydroxysuccinimide (NHS) and guanidine acetic acid (GAA; glycocyamine) were purchased from Sigma Aldrich (St Louise, MO, USA). Sodium triphosphate pentabasic (TPP) was purchased from Fluka (Buchs, Switzerland) while lisinopril dihydrate (lisinopril), deuterium oxide, and deuterium chloride were acquired from Acros Organics (Geel, Belgium). 1-Ethyl-3-(3-dimethylaminopropyl) carbodiimide hydrochloride (EDC) was purchased from Tokyo Chemical Industry (Tokyo, Japan). Cellulose-based dialysis bag (MWCO 3,000 Da), tetramethylethylenediamine (TEMED) and hydrochloric acid was obtained from Fisher Scientific (Waltham, MA, USA). Sodium hydroxide pellets were acquired from VWR (Radnor, PA, USA). Antifibrotic peptide - N-acetyl-seryl-aspartyl-lysyl-proline (Ac-SDKP) was custom-made by the Chinese Peptide Company (Hangzhou, PRC), with a purity of 90-94%. All chemicals were at analytic grade and used as supplied. HPLC grade water was obtained from PURELAB® Chorus 2+ machine (ELGA LabWater, High Wycombe, UK). High glucose Dulbecco's Modified Eagle's Medium with Glutamax (DMEM), fetal bovine serum (FBS), 5% streptomycin-penicillin solution and 0.05% trypsin-EDTA solution were purchased from ThermoFisher Scientific (Gibco; Waltham, MA, USA). Trypan blue was purchased from Sigma Aldrich (St Louis, MO, USA). T75 cell culture flasks and clear flat-bottomed 96-well plates were purchased from Grenier Bio-One (Kremsmünster, Austria).

6.2.2. Synthesis of guanidylated chitosan

Guanidylated chitosan, also known as chitosan-guanidine acetic acid conjugate or chitosan-glycocyamine conjugate (CS-GAA), was produced by conjugating the LMW chitosan with guanidine acetic acid (GAA) via EDC/NHS coupling reaction adapted from the method developed by Liu *et al*. [301]. LMW chitosan was used instead of MMW chitosan as the viscosity and molecular weight were lower in

LMW chitosan, which allows better mixing during the functionalization process and smaller particles to form compared to MMW chitosan. Briefly, 0.1 g of glycocyamine and 0.5 g of LMW chitosan were first dissolved in 25 mL TEMED/HCl buffer solution at pH 4.7. NHS (0.07 g) and EDC (0.3 g) were added to the solution and stirred using a 12 mm stirrer bar and at 600 rpm for 24 hours at ambient temperature in the dark. The mechanism of coupling was shown in **Figure 6-2**. The conjugate was purified by dialysis, where the solution was added into a dialysis tube with both ends tied and clamped. Dialysis was performed over 5 days and the water was replaced daily. The product was then quench-cooled in dry ice and lyophilised for 2 days. The identity of the conjugate was confirmed by FTIR.

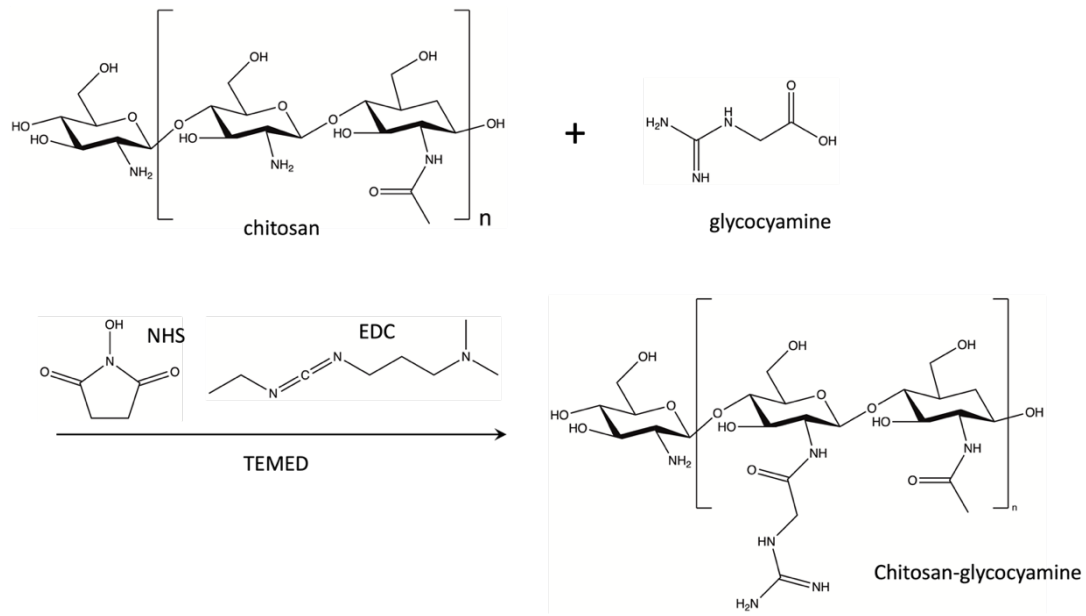

Figure 6-2. Mechanism of conjugating glycocyamine to chitosan via EDC/NHS coupling. (Created with ChemDraw 20.1)

6.2.3. Fabrication of lisinopril-loaded guanidylated chitosan TPP nanogels

Lisinopril-loaded guanidylated chitosan nanogel was prepared by the ionic crosslinking method. Lisinopril nanogels were fabricated according to the matrices established by the Design of Experiment approach, with the experimental conditions of each formulation stated in **Table 6-1** and **Table 6-2**. Guanidylated chitosan was first dissolved in 0.1 M hydrochloric acid solution until it formed a clear solution, followed by adjustment to the final pH with 0.1M sodium hydroxide solution. The chitosan-glycocyamine solution was filtered through a 0.22 µm syringe filter before

use. Lisinopril dihydrate was weighed and dissolved in the chitosan-glycocyamine solution before the addition of the TPP solution. Meanwhile, various amounts of TPP were dissolved in deionised water to prepare different concentrations and filtered with a 0.22 μm syringe filter. An equal amount of TPP solution was added to the chitosan solution at a rate of 2 mL/min under stirring at ambient or elevated temperatures. The solution was then stirred at 300 or 600 rpm for 1 hour in a 14 mL glass vial using a 12 mm magnetic stirrer. The prepared nanogels were then kept in a fridge at 4 ^{o}C for further characterisation. All nanogels were prepared and tested in triplicate.

6.2.4. Screening design

Plackett-Burman design was used to screen the key factors that influence four key criteria in a successful nanogel formulation, namely size, PDI, ZP, and EE. Seven independent variables were screened in the study, namely guanidylated chitosan concentration (GC), guanidylated chitosan-TPP ratio (GT), guanidylated chitosan-drug ratio (GD), temperature (T), pH of guanidylated chitosan, rotating speed (SR), and duration (D). A total of 14 experimental runs were performed in triplicate to construct the Plackett-Burman design, where the composite matrix was constructed using JMP 15 (SAS Institute, Cary, NC, USA).

Table 6-1. Independent and dependent variable and the experimental design matrix of Plackett-Burman design. The nanogel properties were represented as the mean value obtained from three independent experiments (n = 3).

Pattern	GC (%)	GD	GT	T (ºC)	pH	SR (rpm)	D (hour)	Size (nm)	PDI	ZP (mV)	EE (%)
+−−−+−−	0.3	0.5	4	25	7	300	1	375.3	0.846	19.94	31.8
+−+++−−	0.3	0.5	8	50	7	300	1	538.3	1.000	30.76	64.2
++−−−+−	0.3	2	4	25	5.5	600	1	10000	1.000	4.46	31.2
−−−+−−+	0.1	0.5	4	50	5.5	300	3	3522.3	0.761	8.38	12.3
−+++−−−	0.1	2	8	50	5.5	300	1	207	0.367	24.21	0.5
−+−−+−+	0.1	2	4	25	7	300	3	142	0.241	15.66	0.0
−−+−+++	0.1	0.5	8	25	7	600	3	4920.3	0.211	27.98	16.0
−+−+++−	0.1	2	4	50	7	600	1	280	0.687	12.00	0.0
−−+−−+−	0.1	0.5	8	25	5.5	600	1	105.7	0.260	11.44	14.0
+−−+−++	0.3	0.5	4	50	5.5	600	3	10000	1.000	10.62	28.8
+++−−−+	0.3	2	8	25	5.5	300	3	300.5	0.646	25.37	15.7
+++++++	0.3	2	8	50	7	600	3	542.7	1.000	25.44	20.8

6.2.5. Response surface methodology

Response surface methodology was used to determine the optimal condition for preparing lisinopril-loaded CS-GAA nanogels. A face-centred cubic (FCC) central composite design (CCD) was used in the optimisation, which was formed by four factors as identified in the Plackett-Burman design and at three levels, namely the guanidylated chitosan concentration (GC), the guanidylated chitosan-TPP mass ratio (GT), the guanidylated chitosan-drug ratio (GD), and temperature (T). A total of 27 experimental runs were performed in triplicate to construct the response surface model. The composite matrix was constructed using JMP 15 (SAS Institute, Cary, NC, USA). The four properties of nanogels (Size, ZP, PDI, and EE), which contribute to being a successful drug carrier, were again determined as the dependent variables.

A stepwise least square regression was used to fit the polynomial model to the data individually for each dependent variable. A 5-fold cross-validation was performed to validate the model for all dependent variables. A one-way analysis of variance (ANOVA) test and lack of fit test was conducted to determine the statistical significance and goodness of fit for the model respectively, at a confidence interval

(*CI*) of 95%. Response surfaces were plotted to visualise the relationship between independent and dependent variables. A p-value < 0.05 is considered statistically significant.

Table 6-2. Independent and dependent variables and the experimental design matrix of CCD design. The nanogel properties were represented as the mean value obtained from three independent experiments (n = 3).

Pattern	Independent variables				Dependent variables			
	GC	GT	GD	T	Size (nm)	PDI	ZP (mV)	EE (%)
−+−+	0.15	7	0.5	50	501.0	0.117	27.52	32.7
++−+	0.25	7	0.5	50	6826.3	0.432	10.47	29.3
+−++	0.25	5	1	50	441.0	0.245	23.45	26.8
++++	0.25	7	1	50	6785.3	0.333	11.81	31.8
−+−−	0.15	7	0.5	25	398.3	0.001	30.00	28.3
0000	0.2	6	0.75	37.5	421.0	0.001	35.64	26.8
+−−−	0.25	5	0.5	25	560.0	0.001	32.38	31.6
+−+−	0.25	5	1	25	383.0	0.001	30.33	26.3
+++−	0.25	7	1	25	10000	0.069	13.19	32.7
−+++	0.15	7	1	50	482.3	0.001	22.12	19.7
000A	0.2	6	0.75	50	512.0	0.333	28.76	22.6
−−−−	0.15	5	0.5	25	463.3	0.165	25.35	31.3
−++−	0.15	7	1	25	466.3	0.001	25.49	13.4
+−−+	0.25	5	0.5	50	10000	0.001	11.74	31.5
A000	0.25	6	0.75	37.5	3697.7	0.333	27.69	24.3
a000	0.15	6	0.75	37.5	1018.0	0.001	22.30	15.0
0A00	0.2	7	0.75	37.5	279.3	0.333	29.24	13.5
0000	0.2	6	0.75	37.5	380.3	0.001	26.57	16.6
0000	0.2	6	0.75	37.5	853.3	0.001	33.74	28.9
−−−+	0.15	5	0.5	50	847.0	0.624	13.54	26.4
00A0	0.2	6	1	37.5	629.0	0.313	29.99	33.9
000a	0.2	6	0.75	25	719.0	0.508	35.08	26.2
++−−	0.25	7	0.5	25	7286.7	1.000	8.25	30.3
−−+−	0.15	5	1	25	399.9	0.667	22.85	24.3
0a00	0.2	5	0.75	37.5	6960.3	0.667	14.86	36.4
−−++	0.15	5	1	50	539.3	0.001	9.94	0.0
00a0	0.2	6	0.5	37.5	6794.7	0.001	20.25	56.0

Key: -, 0 and + refer to low, medium, and high levels respectively, while a and A denote the axial points.

6.2.6. Multiple response optimisation

Multiple response optimisation was employed to determine the optimal condition for fabricating lisinopril-loaded nanogels, as discussed in **Section 3.2.4**. The running

conditions with the highest overall desirability were deemed as the optimal condition and were determined by JMP 15. Nanogels were then fabricated under the optimal conditions in triplicate, with the dependent variables measured experimentally and compared with the predicted values to validate the models. Nanogels produced were then freeze-dried and characterised.

6.2.7. Fabrication of Ac-SDKP-loaded guanidylated chitosan TPP nanogels

The Ac-SDKP-loaded nanogels were produced under the optimal condition identified above, with Ac-SDKP replacing lisinopril in the formulation. The fabrication condition was 0.161% GC, GT of 7, GD of 0.5 and T at 50 ºC. Nanogels produced were freeze-dried and characterised. The properties of nanogels were determined using the same methods discussed below.

6.2.8. Characterisation techniques for raw materials and freeze-dried nanogels

6.2.8.1. Thermogravimetric analysis

The analysis was conducted as described in **Section 2.2.3.1**.

6.2.8.2. Differential scanning calorimetry

1-3 mg of sample was added to an aluminium pan, which was sealed with a non-hermetic lid (Tzero, TA instrument, New Castle, DE, USA). A hole was punctured in the lid to release the vaporized solvent and moisture during heating. The analysis was carried out using a Q2000 differential scanning calorimeter (TA Instruments, New Castle, DE, USA). The calorimeter was calibrated for temperature using an indium standard before the experiment. Ac-SDKP and GAA were heated from 0 ºC to 170 and 350 ºC at a temperature ramp of 10 ºC/min and under a flow of 50 mL/min nitrogen gas. Other samples were heated directly from 0 ºC to 200 ºC. Data were recorded with the TA Advantage software package and analysed using TA Universal Analysis.

6.2.8.3. Fourier transform infrared spectroscopy (FTIR)

Analysis was performed using the same method described in **Section 2.2.3.3**.

6.2.8.4. Solid X-ray diffraction

XRD patterns were performed using the same method described in **Section 2.2.3.4**.

6.2.8.5. Confirming the conjugation of GAA on chitosan using ^{1}H nuclear magnetic resonance spectroscopy (NMR)

The conjugation of GAA on the chitosan was confirmed with NMR. ^{1}H NMR spectrums of chitosan, CS-GAA, and CS-GAA nanogels were obtained using a 400 MHz NMR spectrometer (Bruker, Billerica, MA, USA), at a temperature of 25 ^{o}C. The relaxation time was set at 2 s. 10 mg of chitosan and guanidylated chitosan was dissolved in 2 mL of 2% deuterium chloride (DCl) in deuterium oxide (D_2O) while the nanogels sample was dissolved in 2 mL of D_2O. The solutions were then transferred into a 5mm glass NMR tube. Results were analysed using TopSpin software (Bruker, Billerica, MA, USA), with the integrals of the peaks being automatically determined.

6.2.9. Characterisation techniques for nanogels

6.2.9.1. Transmission electron microscopy

The shape and morphology of the CS-GAA nanogels were characterised using an FEI CM120 Bio Twin Transmission Electron Microscope (TEM) (Hillsboro, Oregon, United State). 1 µL of the nanogel sample was dropped onto 200-mesh carbon lacey-coated copper grids, followed by air-drying at room temperature for a few minutes. The excess solution was removed using filter paper. The sample was not stained. Particle size distribution was performed using Fiji [302].

6.2.9.2. Dynamic light scattering (DLS) and electrophoretic light scattering (ELS)

The hydrodynamic diameter and polydispersity index of the nanogels were measured in a medium-throughput approach using a Dynapro II plate dynamic light scattering detector (Wyatt Technology, Santa Barbara, CA, USA) at 25 ^{o}C. A disposable 96-well black clear-bottomed polystyrene plate was employed in the analysis, with 100 µL of nanogels added to each well. Any observable bubble was pierced with a needle and the plate was centrifuged to remove any smaller bubble. Size and polydispersity of the lisinopril and Ac-SDKP loaded nanogels were also analysed using both Dynapro II and Zetasizer Ultra (Malvern Panalyticals, Malvern, United

Kingdom) dynamic light scattering detector, as the latter is the gold standard for DLS. The measurements with Zetasizer were performed at 25 ^{o}C using a backscatter angle of 173^{o}, using a polystyrene cuvette. Zeta potentials were measured using a Zetasizer Ultra with U-shaped capillary cells (DTS 1070, Malvern Panalyticals, Malvern, United Kingdom). The results were measured in triplicate obtained from three independent experiments.

6.2.9.3. Encapsulation efficiency of lisinopril and Ac-SDKP in chitosan/TPP nanogels

The unloaded drug in the nanogel solution was separated by centrifugal filtration (aka. diafiltration). 0.5 mL of the propranolol-loaded nanogel solutions were loaded into a 0.5 mL Amicon diafiltration tube (MWCO 3,000; Merck Millipore, Billerica, MA, USA). The solutions were then centrifuged using at 14,000 X g for 30 minutes at 4 ^{o}C using a refrigerated mini centrifuge (Heraeus Fresco 17, Thermo Scientific, Waltham, USA), the filtrate was isolated and assayed by high-performance liquid chromatography, and the details of the quantification are discussed below. The drug concentrations were calculated using the pre-determined calibration curves for lisinopril, while EE for Ac-SDKP was calculated using **Equation 5-10**. The experiment was repeated three times and the results were presented as mean ± SD.

Quantification of lisinopril was performed on an Agilent 1260 Infinity liquid chromatography system (Santa Clara, CA, USA), equipped with a Variable Wavelength Detector (VWD) using the assay method described in the USP 43 NF 38 monograph for lisinopril [303]. Briefly, a Kinetex C8 core-shell column (Phenomenex, Torrance, CA, USA), with a particle size of 5 µm, dimensions of 4.6 mm column diameter and 250 mm in length was used in the analysis. Lisinopril was eluted using an isocratic method, where the flow rate was fixed at 1 mL/min and the column temperature was maintained at 50 ^{o}C. The VWD was set at 210 nm, while the injection volume used was 20 µL. Phosphate buffer at pH 5.0 and acetonitrile was used as the mobile phases. To prepare the phosphate buffer, 2.76 g of monobasic sodium phosphate was dissolved in 900 mL of HPLC grade water in a 1 L volumetric flask, with the pH adjusted to pH 5.0 with sodium hydroxide solution. The buffer was filtered through a 0.22 µm polyethersulfone Steristop^{TM} vacuum

bottle-top filter. The buffer was then used immediately upon preparation or stored under refrigeration in borosilicate glass bottles for a maximum period of 24 hours.

Chromatographic analysis of the peptide was performed on the same system using a Zorbax Eclipse Plus reverse phase C18 column (Agilent, Santa Clara, CA, USA), with a particle size of 5 μm, dimensions of 4.6 mm column diameter and 250 mm in length was used in the analysis. The analysis was performed using the method developed and validated in **Chapter 5**. The VWD was set at a wavelength of 220 nm and the column temperature was maintained at 25 ºC. The peptide was eluted using a gradient method as shown in **Table 5-3**, at a flow rate of 1 mL/min with phosphate buffer at pH 2.5 and acetonitrile used as the mobile phase. The injection volume was set at 10 μL. A post-time of 5 minutes at 97% solvent A and 3% solvent B was used after each run to re-equilibrate the column. To prepare the phosphate buffer, 1.36 g of monobasic potassium phosphate was dissolved in 900 mL of HPLC grade water in a 1 L volumetric flask, with the pH adjusted to pH 2.5 with a phosphoric acid solution. The buffer was filtered through a 0.22 μm vacuum bottle-top filter as discussed above.

6.2.10. Drug release of lisinopril and Ac-SDKP loaded in Chitosan-TPP nanogels

Dissolution tests of lisinopril nanogels were performed in 50 mL PBS (10 mM, pH 7.4) solution with continuous stirring at 37 ºC over 72 hours. 2 mL of the nanogels solutions were first loaded into an Amicon diafiltration tube and centrifuged as described above to remove the free drug. Then, the nanogels were resuspended in 1.5 mL water and loaded into a cellulose dialysis bag (3,500 MWCO, volume/cm = 1.91, Fischer Scientific, Waltham, MA, USA) with both ends tied, followed by submerging into PBS. 1 mL aliquots were withdrawn at certain time points and an equal volume of fresh preheated PBS solution was added to maintain a constant volume. Lisinopril was assayed by HPLC as described above, with 150 μL of the sample added into an HPLC vial with a 200 μL conical glass insert. Drug concentrations were calculated using pre-determined calibration curves. The experiment was replicated independently three times and the results were presented as the mean value ± standard deviation.

Owing to the poor detection of the peptide, 4 mL of the nanogels solutions were centrifuged in the Amicon filter tube to remove the non-encapsulated peptide. Then, the nanogels were resuspended in 1.5 mL of water and loaded into a cellulose dialysis bag (MWCO 3,500, volume/cm = 1.91, Fischer Scientific, Waltham, MA, USA) with both ends tied, followed by submerging into 20 mL PBS. 20 mL was chosen as this is the lower end of the volume of pericardial fluid under normal circumstances and the dialysis bag can be fully submerged at this volume. 0.5 mL aliquots were withdrawn at certain time points and an equal volume of fresh preheated PBS solution was added to maintain a constant volume. The peptide was assayed by HPLC as described above, using the same vial and insert. Drug concentrations were calculated using pre-determined calibration curves. The experiment was replicated independently three times and the results were presented as the mean value ± standard deviation.

6.2.11. *In vitro* cell culture conditions

6.2.11.1. *Epicardial cells and L929 fibroblasts*

Both cells were cultured in a complete medium consisting of Dulbecco's modified Eagle's medium-high glucose (DMEM) with 2 mM glutamate and supplemented with 10% (v/v) heat-inactivated fetal bovine serum (FBS), and 1% (v/v) streptomycin-penicillin solution (100X). Cells were grown in T75 flasks. They were incubated in a PHCbi carbon dioxide incubator (MCO-170AICD; PHC, Tokyo, Japan) at 37 ºC and 5% carbon dioxide. When confluency of 70-80% was reached, the cells were first washed with PBS and then passaged by treating with 1.5 mL of a 0.025% trypsin-EDTA solution for 5 minutes. 5 mL of complete medium was added to suspended cells to inhibit the activity of trypsin, followed by centrifugation at 1,000 x g for 5 minutes (Eppendorf; Hamburg, Germany). the cell pellet was resuspended in a complete medium and divided 1:3-1:4 into fresh flasks. Epicardial cells between passages 1 and 5 were used while the passage number of L929 was between 9 and 13 in this study.

6.2.12. MTT assay

MTT assay was performed using a CellTiter 96 Non-radioactive cell proliferation assay kit (Promega, Madison, WI, USA). The assay kit was performed as described in the protocol by the manufacturer. When the cells reached ~80% confluence, they were detached using a trypsin-EDTA solution, washed, and counted using a Luna-II automated cell counter (Logos Biosystem, Anyang, South Korea) and trypan blue. The cell suspension was adjusted to 12,000 cells/mL and 180 µL of the cell suspension was added into each well of a clear flat-bottom 96-well plate to achieve 10,000 cells per well. The cells were allowed to equilibrate in the wells for 24 hours before incubation with the nanogels and individual ingredients. Solutions of the nanogels and raw materials were filtered through a 0.22µm syringe filter for sterilisation. After 24 hours, the culture medium was removed from the wells and replaced with equal volumes of complete medium containing nanogel or raw materials at various concentrations from 0.625 µg/mL to 2.5 mg/mL for 24 hours with or without TGF-β1. The media containing the test materials (100 µL) was incubated in the well for 24-72 hours. 15 µL of the MTT dye solution was added to each well. The plate was then incubated at 37 ^{o}C for 4 hours, followed by the addition of 100 µL of the solubilisation/stop solution. The plate was then incubated at 37 ^{o}C overnight to dissolve the formazan. Absorbance at 570 nm was measured using a SpectraMax M2e spectrophotometer (Molecular Devices Inc., Sunnyvale, CA, USA). The reference wavelength was 630 nm. The background absorbance was also measured with empty wells containing the media, dye solution and solubilisation/stop solution. The cell metabolic activity was calculated according to **Equation 4-2**.

6.3. Results and Discussion

6.3.1. Plackett-Burman design

The factors with the main effect were first screened in the Plackett-Burman design for each nanogel property (size, PDI, ZP, and EE). However, unlike the definitive screening design used in **Chapter 3**, the Plackett-Burman design was unable to determine any interaction or quadratic effect, in return for a fewer number of experimental runs. Thus, this design is only capable of determining the main effects only. The effects of the factors were estimated by half-normal probability plots,

where the unimportant factors tend to have near-zero effects and a normal distribution centred near zero. In contrast, the key factors have effects away from zero and a normal distribution centred at true large effect values, in other words, a non-zero value. The half-normal plots for each nanogel property were shown in **Figure 6-3**. The further the point from the line, the higher the estimated effect for that factor. In **Figure 6-3 (a)**, none of the variables was estimated to impact the size of the nanogels, while guanidylated chitosan concentration (GC), guanidylated chitosan TPP ratio (GT) and temperature (T) were likely to influence the PDI of nanogels as shown in **Figure 6-3 (b)**. Furthermore, ZP was likely to be dependent on the guanidylated chitosan-TPP ratio (GT) and the pH of the solution, presented in **Figure 6-3 (c)**. Nevertheless, the guanidylated chitosan drug ratio (GD) and guanidylated chitosan concentration (GC) were expected to affect the encapsulation efficiency in the nanogels as presented in **Figure 6-3 (d)**. The results indicated that these factors had main effects on the properties of nanogels and would be used in constructing the central composite design for further optimization.

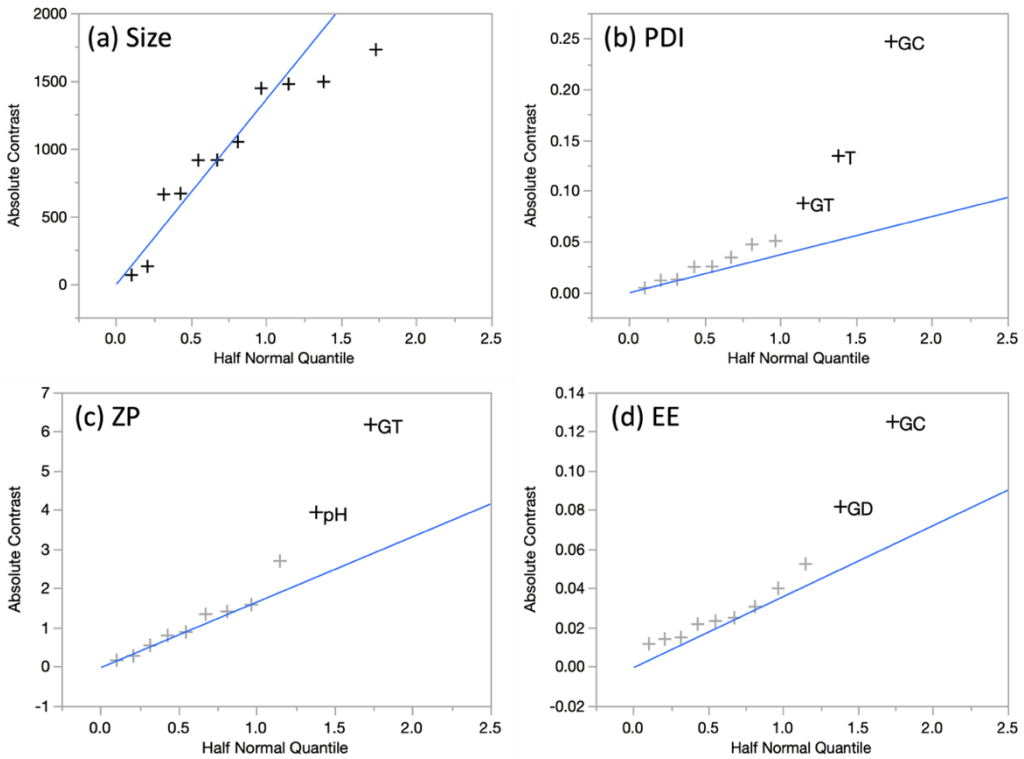

Figure 6-3. Half normal plots show the factors which were estimated to have effects on each independent variable. The further the point from the blue line, the higher the effect is estimated. The variables estimated with effects were in black.

6.3.2. Central composite design

The estimated parameters were then used to construct a model via stepwise regression, with a 5-fold cross-validation. The factors included GC, GD, GT, and T. pH of the solution was fixed at pH 5.5 to minimise the number of factors in the model and the number of experimental runs required. A one-way analysis of variation (ANOVA) and lack of fit test was then performed on the linear regression models for each individual dependent variable to determine the statistical significance and the goodness of fit of these models on the training set. The results of the ANOVA and lack of fit tests are reported in **Table 6-3**. *p*-values obtained in the ANOVA test for all the models were smaller than 0.05, demonstrating the significance of the correlations between the training set and the models. Furthermore, the *p*-values in the lack of fit tests for all models were larger than 0.05, which indicate these models were a good fit for the training set data. Thus, these models can predict the properties of nanogels.

Table 6-3. ANOVA and lack of fit test results for the GCD models for various independent variables. Significance for the effect of individual, quadratic and interaction terms of the independent terms predicted to impact the responses were also determined. Statistically significance was set as Prob. > F being smaller than 0.05.

Independent variables	Source of variations	Degree of freedom	Sum of squared	Mean squares	F value	Prob.> F	Significance
Size	**Model**	3	19930940	6643647	3.860	0.0226	**Significant**
	GC	1	8266178		4.803	0.0388	*s*
	GT	1	4960935		2.882	0.1030	*ns*
	GC x GT	1	6703827		3.895	0.0606	*ns*
	Residual	23	39586401	1721148			
	Lack of fit	5	7320413	1464083	0.8168	0.5533	**Not significant**
	Pure error	18	32265988	1792555			
PDI	**Model**	3	0.5605713	0.186857	3.0878	0.0471	**Significant**
	GC	1	0.04461071		0.7372	0.3994	*ns*
	GT	1	0.00111864		0.0185	0.8930	*ns*
	GC x GT	1	0.51484192		8.5077	0.0078	*s*
	Residual	23	1.3918327	0.060514			
	Lack of fit	5	0.2712320	0.054246	0.8713	0.5194	**Not significant**
	Pure error	18	1.1206007	0.062256			
ZP	**Model**	6	1343.8727	225.812	8.8916	<0.0001	**Significant**
	GC	1	49.33556		1.9623	0.1766	*ns*
	GT	1	2.24014		0.0891	0.7684	*ns*
	T	1	224.50805		8.9297	0.0073	*s*
	GC x GT	1	479.93856		19.0893	0.0003	*s*
	GT x T	1	139.41706		5.5452	0.0289	*s*
	GT^2	1	459.43334		18.2737	0.0004	*s*
	Residual	20	502.8344	25.142			
	Lack of fit	8	234.99500	29.3744	1.3161	0.3222	**Not significant**
	Pure error	12	267.83943	22.3200			
EE	**Model**	7	0.16877552	0.024111	5.1467	0.0021	**Significant**
	GC	1	0.03001250	6.4065		0.0204	*s*
	GD	1	0.04351250	9.2882		0.0066	*s*
	T	1	0.00309422	0.6605		0.4265	*ns*
	GC x GD	1	0.01974025	4.2138		0.0541	*ns*
	GC^2	1	0.02890046	6.1691		0.0225	*s*
	GD^2	1	0.06418553	13.7011		0.0015	*s*
	T^2	1	0.00819363	1.7490		0.2017	*ns*
	Residual	19	0.08900900	0.004685			
	Lack of fit	7	0.02263980	0.003234	0.5868	0.7425	**Not significant**
	Pure error	12	0.06636920	0.005531			

Where GC is guanidylated chitosan concentration, GT is guanidylated chitosan TPP ratio, GD is guanidylated chitosan drug ratio, and T is temperature.

6.3.3. Effect of factors on the nanogels

6.3.3.1. Hydrodynamic size

The hydrodynamic sizes of the nanoparticles in **Table 6-1** and **Table 6-2** were in a range of 142 – 10,000 nm. Two out of the whole batch were larger than 10,000 nm (i.e., 10 μm), as the formulations precipitated and thus exceeded the detection limit of 10,000 nm. Several formulations with sizes between 1,000 and 10,000 nm were obtained, whilst most of the formulations were smaller than 1 μm in diameter. Noteworthy, the hydrodynamic size measured with the Dynapro II plate DLS is different from that measured with the Malvern Zetasizer, as the algorithms used to calculate hydrodynamic size and polydispersity are proprietary and vary between manufacturers. A Dynapro II plate DLS was used instead of the standard Malvern Zetasizer Ultra, which has been employed in the previous chapters, owing to the high throughput capacity of Dynapro. The samples were loaded in a black 96- or even 384-well plate and the samples can be measured using a sequence. In contrast, individual polystyrene cuvettes were used for sample measurements while the samples and cuvette loading are all manual handling. Thus, 96 or 384 measurements could be performed in an automated mode with the Dynapro II, which is efficient and suitable for optimising the nanogels formulation using the Design of Experiment. Moreover, the Dynapro II plate DLS offers another advantage over the Zetasizer, with a smaller sample volume used. Although a different DLS detector was used in this chapter, the extensive range of size obtained in the results revealed that the guanidylated chitosan TPP nanogel is highly dependent on the formulations. In the definitive screening design, no factor was estimated to have significant effects on the hydrodynamic size of nanogels, as presented in **Figure 6-3**.

In the central composite design, guanidylated chitosan concentration (GC), guanidylated chitosan-TPP ratio (GT) and their interaction were estimated to impact the hydrodynamic size of the lisinopril-loaded guanidylated chitosan nanogels. However, only GC was shown to have a significant effect on the hydrodynamic size of the nanogel, as shown in **Table 6-3**, while the other factor terms were not. The result reveals that the hydrodynamic size increased with GC, as shown in **Figure 6-4**, where the number of nuclei was likely unchanged and nanogels grew bigger

with higher polymer concentration. Moreover, conjugation with glycocyamine also strengthened the interaction with the crosslinker, making the nanogels more susceptible to precipitation during fabrication. The result was different from that observed in propranolol-loaded chitosan TPP nanogels in **Chapter 3**, where the quadratic effect of the chitosan-TPP ratio was reported in addition to the terms identified in the guanidylated chitosan-TPP nanogels. Moreover, all terms were significant in chitosan-TPP nanogels. The difference was likely multi-factorial. First, a different polymer-crosslinker ratio was used, with the ratio of 3-5 and 5-7 used in chitosan-TPP nanogel and guanidylated chitosan-TPP nanogels, respectively. Furthermore, the interaction between polymer and crosslinkers was strengthened with the guanidine group, which might interact differently with the crosslinker, compared to the chitosan TPP nanogels. Moreover, the stronger interaction also indicated that the guanidylated chitosan nanogels were more susceptible to precipitation during stirring, especially at high polymer and crosslinkers concentrations, distorting the model and masking the quadratic effect. Nevertheless, as the Dynapro II was used instead of Zetasizer, the algorithm to measure size was different and thus the sizes of the nanogels should not be compared directly.

$$\boldsymbol{Size = 19191.309 - 103964.139 \times GC - 4288.325 \times GT + 24894.875 \times GC \times GT}$$ **Equation 6-1**

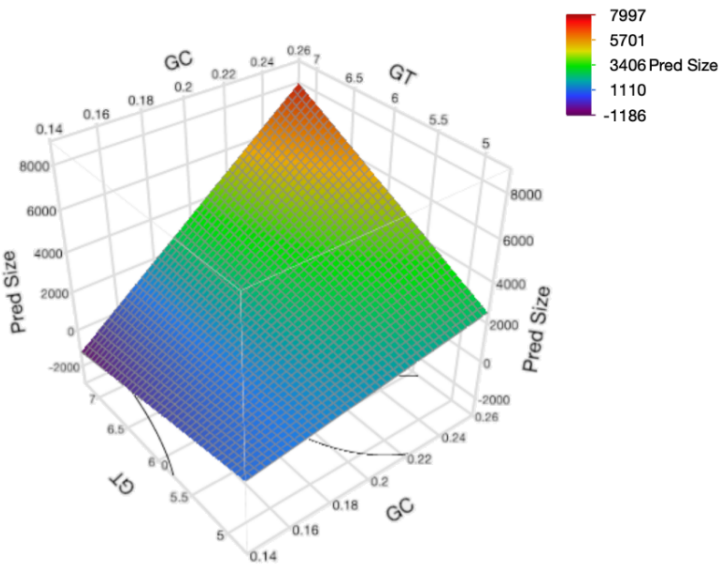

Figure 6-4. Response surface models predicting the effect of guanidylated chitosan concentration (GC) and guanidylated chitosan TPP ratio (GT) on the size of the lisinopril-loaded nanogels. The nanogels size was estimated to increase with GC and GT. Synergism in nanogel size was also observed between GC and GT.

6.3.3.2. PDI

The PDI is a measure of the homogeneity of the nanoparticles in terms of size distribution [250], which is a value between 0 to 1 for the Dynapro II plate reader DLS. Hence, the smaller the PDI, the more uniform the size of the nanogels. The PDI of the nanogels shown in **Table 6-2** was between 0.001 and 1.000, of which half of the formulations were smaller than 0.3. The main effects of guanidylated chitosan concentration and the guanidylated chitosan-TPP ratio were found to be insignificant on the PDI of the nanogels. Interestingly, the interaction effect between these two factors was significant, as shown in **Table 6-3**. Thus, the individual terms for GC and GT were included in the equation. The result indicated that the PDI is not dependent on the guanidylated chitosan concentration and polymer-crosslinker ratio individually. Importantly, there was a synergism between the two terms. The PDI of the nanogels were high at both low GC and GT, as well as high GC and GT. Low PDI was observed at high GC with low GT and vice versa. The observations demonstrated that the PDI was likely related to the degree of crosslinking. Less crosslinking was formed at low GC and high GT, as well as high GC and low GT, where the mass of the polymer was more than that of the crosslinker. On the other

hand, the nanogels were likely to precipitate at high GC and low GT, resulting in a very wide particle size distribution and higher polydispersity. At low GT and low GC, the polymer was not in excess, and thus more crosslinking was formed. However, the degree of crosslinking was not sufficient to cause nanogels to precipitate, resulting in large size distribution and polydispersity. Compared to the propranolol-loaded chitosan TPP nanogels in **Chapter 3**, the synergism between GC and GT was more prominent. The results showed that conjugation with the glycocyamine altered the interaction between chitosan and crosslinker TPP, requiring a fine balance between the polymer and crosslinker concentrations.

$$\boldsymbol{PDI = 4.383 - 20.530 \times GC - 0.725 \times GT + 3.588 \times GC \times GT}$$

Equation 6-2

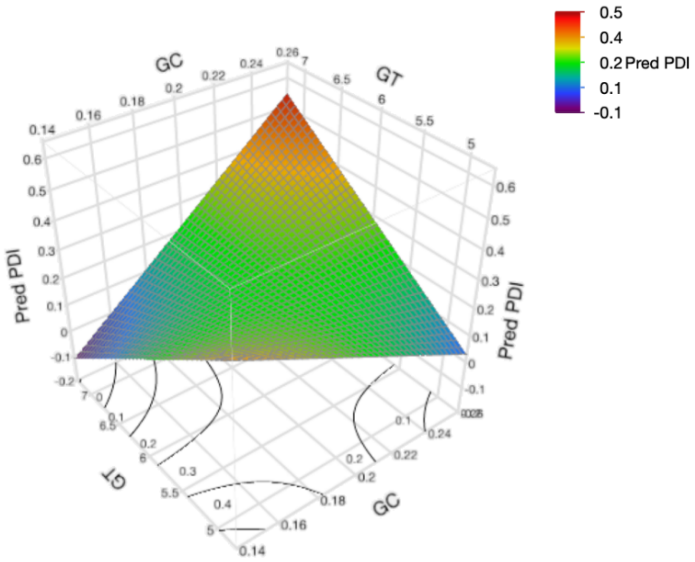

Figure 6-5. Response surface models predicting the effect of guanidylated chitosan concentration (GC) and guanidylated chitosan TPP ratio (GT) on the PDI of the lisinopril-loaded nanogels. PDI decreased with increasing GC and GT, but there was synergism between GC and GT, where high PDI was observed where both GC and GT were simultaneously either at low or high levels.

6.3.3.3. Zeta potential

The nanogels are formed by ionic gelation between cationic guanidylated chitosan and anionic crosslinkers TPP, where chitosan is used in excess compared to the crosslinkers. Moreover, the guanidine group on the chitosan possess a pKa of 13.

Therefore, the nanogels are generally positively charged. The ZP of nanogels is an important indicator of the colloidal stability of the nanogels, as the agglomeration of nanogels is attenuated by the electronic repulsion [251,252]. Nanogels with ZP values of 30 mV are generally stable in suspension due to the sufficient electronic repulsion between particles [253]. Zeta potentials of the nanogels from the training set as shown in **Table 6-2**, were in a range of 8.25 to 35.64 mV, where only five nanogels formulations were stable due to the surface charge in the suspension.

The temperature was found to have a significant effect on the ZP of the nanogels, with an inverted relationship to the ZP as shown in the equation. It is likely due to the diffusibility of the polymer solution being lower at high temperatures, allowing more interaction between the polymer and the crosslinker. As the chitosan was guanidylated, the interaction was stronger and more crosslinking was formed, neutralising the surface net charge. Thus, the zeta potential measured reduced with temperature. Moreover, low ZP was usually observed in the nanogels with large particle sizes, as shown in **Table 6-2**. Two interaction terms - GT and GC, T and GT also had a statistically significant effect on the ZP, with ZP decreasing with the interaction between GC and GT and increasing with the interaction between T and GT. However, their individual terms did not significantly impact the ZP of nanogels. These terms had to be included in the equation as their interaction term was included. The quadratic term of GT was inversely related to the ZP of the nanogels, where the peak was identified at about 6 to 6.5. At low GT, in other words, high TPP concentration, more interactions between guanidylated chitosan and TPP resulted in a reduction in the net surface charge. At high GT, which means the low TPP concentration was used, the polymer was in excess which in theory increased the ZP. However, the results showed the opposite trend where ZP was lower at high GT. The proposed explanation is that TPP might become the nuclei for the guanidylated chitosan to interact and condense to form the core particle under this condition. The hydrophobic part of the guanidylated chitosan might be exposed on the surface and form the shell, reducing the adsorption of ions and lowering the ZP.

$$\boldsymbol{ZP = -345.106 + 624.114 \times GC - 1.699 \times T + 117.706 \times GT - 8.751 \times GT^2 - 109.538 \times GC \times GT + 0.236 \times T \times GT}$$ **Equation 6-3**

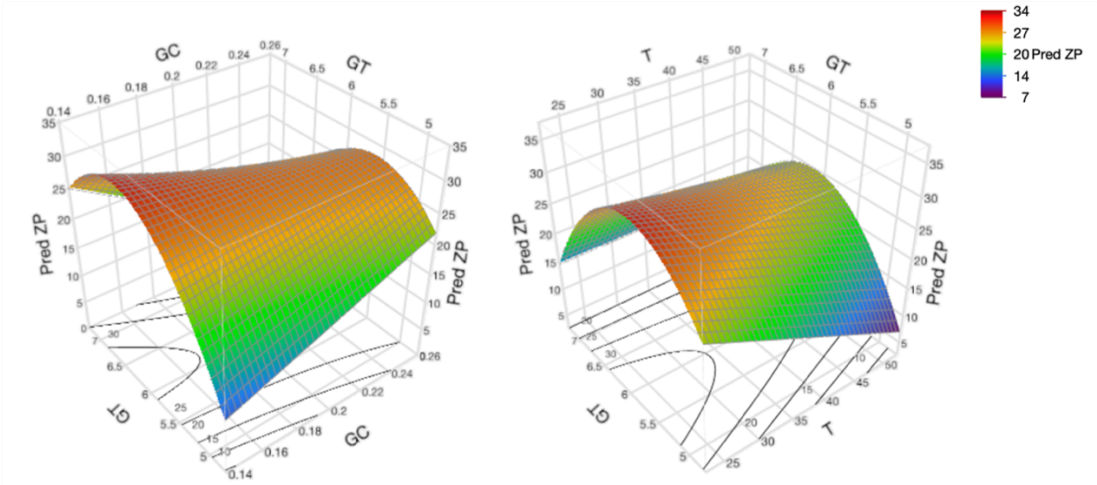

Figure 6-6. Response surface models predicting the effect of (right) temperature (T), (left) guanidylated chitosan concentration (GC) and guanidylated chitosan TPP ratio (GT) on the ZP of the lisinopril-loaded nanogels.

6.3.3.4. Encapsulation efficiency

The EE of lisinopril in the guanidylated chitosan nanogels formulations after varying the fabrication factors was between 0% to 56%, as shown in **Table 6-2**. The results indicated the encapsulation process of lisinopril was altered by varying the fabrication factors, and thus the encapsulation efficiency was quite different. In concordance with the previous chapter, encapsulation was inefficient because of the charge repulsions between the cationic chitosan and lisinopril at pH 5.5. Lisinopril has two carboxylic acids and two amine groups (one each for primary and secondary amines), with the respective pKa shown in **Figure 6-7**. At pH 5.5, the carboxylic acids and two amine groups were protonated. Thus, the drug carried two positive charges, which repulsed the guanidine group on the chitosan. However, as with propranolol-loaded nanogels, a portion of the lisinopril was still encapsulated in the nanogels.

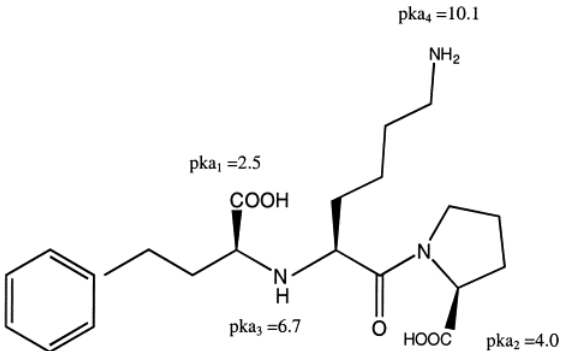

Figure 6-7. The structure of lisinopril with the pKa is shown for each acid and base group [304].

The individual and quadratic terms of temperature, the individual, quadratic and interaction terms of GC and GD were all predicted to affect the EE in the stepwise regression. However, according to **Table 6-3**, only the individual and quadratic terms of GC and GD were found to have a significant effect on the EE, but not their interactions. Although the correlation between terms was not statistically significant (p = 0.0541), a link could still be observed in the surface plot in **Figure 6-8**, where the EE was high with 0.2% GC and with GD of 0.5 or 1. In **Chapter 3**, the individual term of chitosan concentration and the chitosan-TPP ratio was found to significantly impact the EE of chitosan-TPP nanogels, where the amount of propranolol was irrelevant to the EE. Conversely, in guanidylated chitosan nanogel, the quadratic effects of the GC and GD were observed in **Figure 6-8**, with the peak trough of GD at about 0.7 and the peak of GC at 0.2. The guanidylated chitosan-TPP ratio did not alter the EE. Relatively high EE was observed when either a low or high amount of lisinopril was added. The potential explanation was that when more lisinopril was added, the repulsion between the drug and polymer was stronger, which led to a decrease in EE initially. However, despite the stronger repulsion between the drug and polymer at high GD, more drugs were physically trapped in the mash by probability as the concentration of lisinopril in the solution was higher, overcoming the drop of EE due to repulsion. Thus, the EE rebounded when the GD decreased from 0.7 to 0.5. Although a double amount of lisinopril was used, only about a 10% increase in EE was predicted, elucidating the strong repulsion between polymer and drug. Furthermore, EE peaked at a GC of 0.2, which was possibly due to insufficient loading when the polymer concentration was low. When the polymer concentration was high, the repulsion between lisinopril and the polymer intensified

and lowered the EE. The results revealed that there is a fine balance between the amount of lisinopril added and the guanidylated chitosan for optimal EE. The repulsion with the drugs was more severe after conjugating chitosan with glycocyamine. Moreover, the individual and quadratic effects of temperature on the EE were also not significant. The result indicated that the effect of temperature on the EE of the nanogels was minimal.

$$EE = -0.036 + 14.964 \times GC - 4.392 \times GD + 0.025 \times T - 40.638 \times GC^2 + 2.422 \times GD^2 + +0.001 \times T^2 + 2.810 \times GC \times GD \qquad \textbf{Equation 6-4}$$

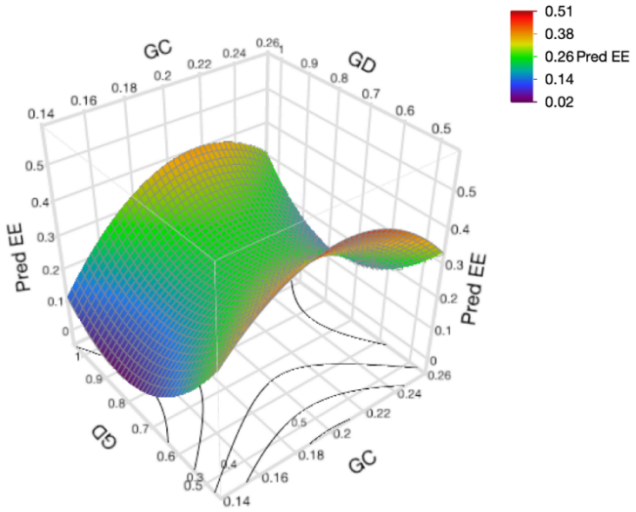

Figure 6-8. Response surface models predicting the effect of guanidylated chitosan concentration (GC) and guanidylated chitosan drug ratio (GD) on the EE of the lisinopril-loaded nanogels.

6.3.4. Multiple response optimisation

The optimal fabrication condition was determined by multiple response optimisation (MRO) as shown in **Figure 6-9**, aiming to achieve the highest EE, and the lowest Z-average and PDI. Desirable ZP was set over 15 mV. The optimal fabrication for nanogel production utilised 0.162% guanidylated chitosan, a guanidylated chitosan to TPP ratio of 7, and guanidylated chitosan to drug ratio of 0.5. The solution was stirred at a temperature of 50 °C and a stirring speed of 600 rpm. The predicted size, PDI, ZP, and EE of nanogels produced at the optimal condition were 512.3 nm, 0.043, 25.7 mV, and 36.9% respectively while the measured results of the nanogels

were 279.5 ± 20.1 nm, 0.256 ± 0.072, 19.1 ± 2.3 mV, and 54.7 ± 3.1%. The measured values were -45.8%, -492%, -34.6%, and 34.1% different from the predicted values, respectively. The high discrepancies between the measured and predicted values for all parameters demonstrate that other factors impacted these properties but were not included in the models. The size and PDI of the nanogels measured with Zetasizer were 260.8 ± 9.2 and 0.233 ± 0.015, respectively. The results demonstrated that the lisinopril-loaded nanogels fulfilled all success criteria set at the beginning of this chapter.

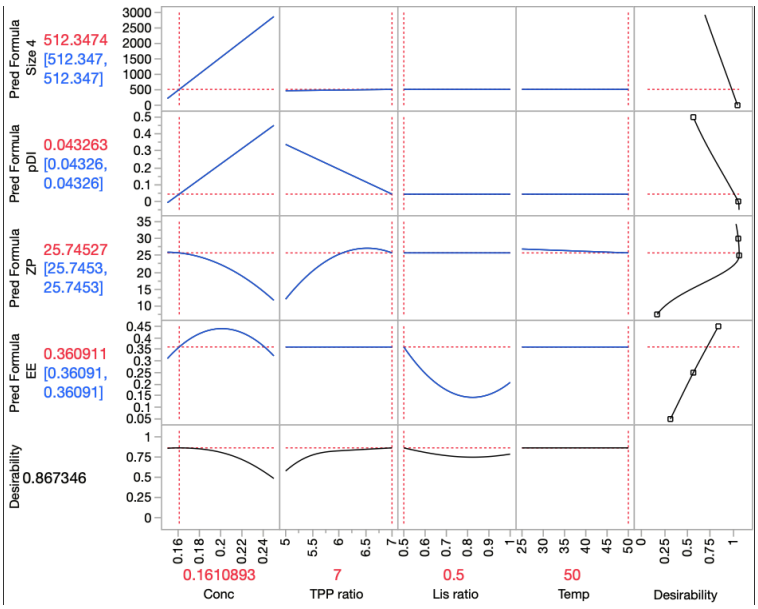

Figure 6-9. Prediction tool shows the relationship between the parameters and the outcome and the optimal condition for nanogel fabrications. The optimal experimental condition was shown in red on the x-axis of the profiler, while the corresponding nanogel properties and overall desirability were shown on the y-axis.

6.3.5. Ac-SDKP loaded nanogels

The Ac-SDKP loaded CS-GAA nanogels were fabricated with the condition described above, with the measured size, PDI, ZP, and EE shown in **Table 6-4**. The size of the peptide-loaded nanogels was smaller than that of the lisinopril-loaded counterpart, but the lisinopril nanogels were less polydisperse. The zeta potential of both nanogels was comparable, while the encapsulation efficiency was lower with the Ac-SDKP-loaded nanogels. The observed differences between the properties of lisinopril- and Ac-SDKP-loaded nanogels echoed the important influence of drug

loading on the nanogel properties. The result only partly fulfilled the success criteria, with the size and ZP reaching the set criteria. The size and ZP of the Ac-SDKP loaded nanogels measured by Zetasizer were ≤ 500 nm and ≥ 15 mV, respectively. The PDI of Ac-SDKP-loaded nanogels was larger than 0.3, while the encapsulation efficiency was lower than the success criteria of 50%.

Table 6-4. Properties and the fabrication condition of the Ac-SDKP loaded CS-GAA nanogels. Size and PDI were measured with two different dynamic light scattering instruments, which use different algorithms to calculate size and PDI. The values of size were agreed upon between the two instruments, but a large discrepancy was present between the two PDI values.

Instrument	GC (%)	GT	GD	T (°C)	Size (nm)	PDI	ZP (mV)	EE (%)
Zetasizer	0.161	7	0.5	50	130.0 ± 9.7	0.434 ± 0.085	19.5 ± 0.8	39.2 ± 6.1
Dynapro II					139.3 ± 20.6	1.000 ± 0.000		

Multiple correlations between the molecular descriptor and the properties of nanogels (size, PDI and ZP) were predicted in **Chapter 3** for structural similar drugs. Both Ac-SDKP and lisinopril have similar structures and thus were used to evaluate whether the correlations observed applied to a different family of drugs and a new nanogel carrier. The prediction of the nanogel properties was based on extrapolation from the correlations, as the values for Ac-SDKP and lisinopril in **Table 6-5** exceeded the ranges reported in the correlation plots (**Figure 3-6**). The size of beta-blocker-loaded nanogels decreased with XLogP. As Ac-SDKP has a lower XLogP than lisinopril, it was predicted that the Ac-SDKP-loaded nanogels were larger. However, the result measured using Zetasizer was the opposite, with Ac-SDKP-loaded nanogels smaller in size. The discrepancy was probably due to one amine group less in Ac-SDKP, which reduced the repulsion between polymer and drugs, contracting the nanogels. As for PDI, two correlations were established, with PDI increased linearly with TopoDiameter and exponentially with bpol. The bpol and TopoDiameter were larger with Ac-SDKP than lisinopril, thus the PDI of the Ac-SDKP-loaded nanogels were expected to be higher. The measured result matched this expectation. Finally, the ZP of nanogels correlated with apol and bpol in a negative exponential manner, WPATH and ALogP in a quadratic manner, and

decreased linearly with TopoDiameter. As the WPATH, apol, bpol and TopoDiameter of Ac-SDKP were higher than those of lisinopril, while the ALogP was lower with Ac-SDKP, extrapolation of all correlations pointed to a decrease of ZP in Ac-SDKP-loaded nanogels, compared to the lisinopril counterpart. However, the experimental results for both nanogels were comparable. The discrepancy could be related to the use of CS-GAA instead of chitosan in this study. Conjugation of GAA on the chitosan might have disrupted the interactions with TPP and drugs, altering the surface net charge and thus the ZP of the nanogels. The results demonstrated the poor prediction accuracy for extrapolating the correlations onto another family of drugs and the new nanogel carrier. However, with the existing results, it is impossible to determine if either a new family of drugs or a new nanogel carrier or both caused the discrepancy in the prediction, and hence further investigation should be performed to determine the root cause of the discrepancy.

Table 6-5. Selected molecular descriptors of Ac-SDKP and lisinopril, which were demonstrated in Chapter 3 varying the size, PDI and ZP of nanogels loaded with structurally similar drugs. These descriptors were calculated by PaDEL and are present as single values.

Drugs	Molecular descriptors					
	apol	bpol	WPATH	TopoDiameter	ALogP	XLogP
Ac-SDKP	69.92217	45.12383	3599	14	-6.2179	-5.369
Lisinopril	64.94058	38.74342	2362	13	-4.3984	1.106

6.4. Characterisation of raw materials and freeze-dried nanogels

6.4.1. Thermogravimetric analysis

The TGA thermogram of raw materials used in guanidylated chitosan-TPP nanogel fabrication is shown in **Figure 6-10**. Chitosan exhibited a two-step decomposition profile, with the initial degradation starting at around 40 ^{o}C and ending at around 85 ^{o}C, owing to the vaporization of adsorbed and bound water from the chitosan [215]. The second stage of degradation associated with a rapid and dramatic drop in weight occurred at 280 ^{o}C and continued up to 320 ^{o}C, with about half of the weight loss. However, conjugation of the chitosan to the GAA reduced the thermal stability. The first decomposition started at 40 ^{o}C and ended at 110 ^{o}C with about 10% weight loss observed, which demonstrated more bound water was adsorbed on the polymer after

the conjugation. The second degradation started at about 200 ºC and ended at 250 ºC, which was lower than chitosan. The results revealed that conjugation with GAA might weaken the interaction between polymers and lower the thermal stability. Moreover, it could also be the degradation of GAA on the polymer as there was an obvious degradation step at 270 ºC in the GAA. The decomposition temperature of GAA was slightly lower than the reported value of 281 ºC [305], which might indicate the presence of impurities or a less stable polymorphic form. Furthermore, lisinopril exhibited multi-step decomposition profiles, with the two obvious weight losses observed under 120 ºC. The first weight loss was 4.1% observed at 82 ºC, while the second weight loss was 4.4% at 107 ºC. Both results were similar to those reported in the literature. These weight losses were likely due to two-step dehydration of the lisinopril dihydrate [306]. There were another three decomposition steps observed at 172, 200 and 268 ºC, where the weight losses for each stage were 2.5%, 7.3% and 35.6% respectively. These weight losses were likely due to the decomposition of lisinopril. As for Ac-SDKP, three decomposition steps were observed. The first weight loss was 4.3% from 40 to 110 ºC, which was likely due to evaporation of the free and bound water. The second stage started at 168 ºC and ended at 250 ºC, with 17.0% of weight loss, while the third degradation step started at 250 ºC and did not end at 400 ºC. The second stage could be due to degradations of the acetyl group and hydrochloride, which was equal to about 15.2% of weight loss. The third step might be related to the decomposition of the peptide backbones.

In contrast, multiple decomposition stages were observed for the drug-free, lisinopril- and Ac-SDKP-loaded nanogels. The drug-free CS-GAA nanogel exhibited 3 degradation steps, with the first step from 40 to 75 ºC with 9% of weight loss, as a result of the evaporation of free water adsorbed in the freeze-dried samples. The second degradation was from 75 to 160 ºC with 9% weight loss due to removal of bound water, while 45% weight loss was observed in the third degradation from 200 to 300 ºC, which was likely due to degradation of GAA conjugated to the polymer. In contrast, only two decomposition steps were observed in Ac-SDKP-loaded CS-GAA nanogels, with 12% weight loss resulting from the evaporation of the free and bound water from 40 to 160 ºC. Another 16% of the weight was lost in the second

decomposition from 160 to 250 ºC, which was likely due to degradation of GAA only the chitosan. As most of the weight in the nanogels was the peptide, the weight loss was smaller as the proportion of GAA in the sample was lower than in free CS-GAA nanogels. Finally, a constant loss of weight of the lisinopril-loaded nanogels was observed until the temperature was 260 ºC, where an obvious drop in weight was observed. Alike other freeze-dried nanogels, the drop was likely due to the decomposition of the GAA conjugated on the polymer. However, further weight loss was observed as the temperature increased.

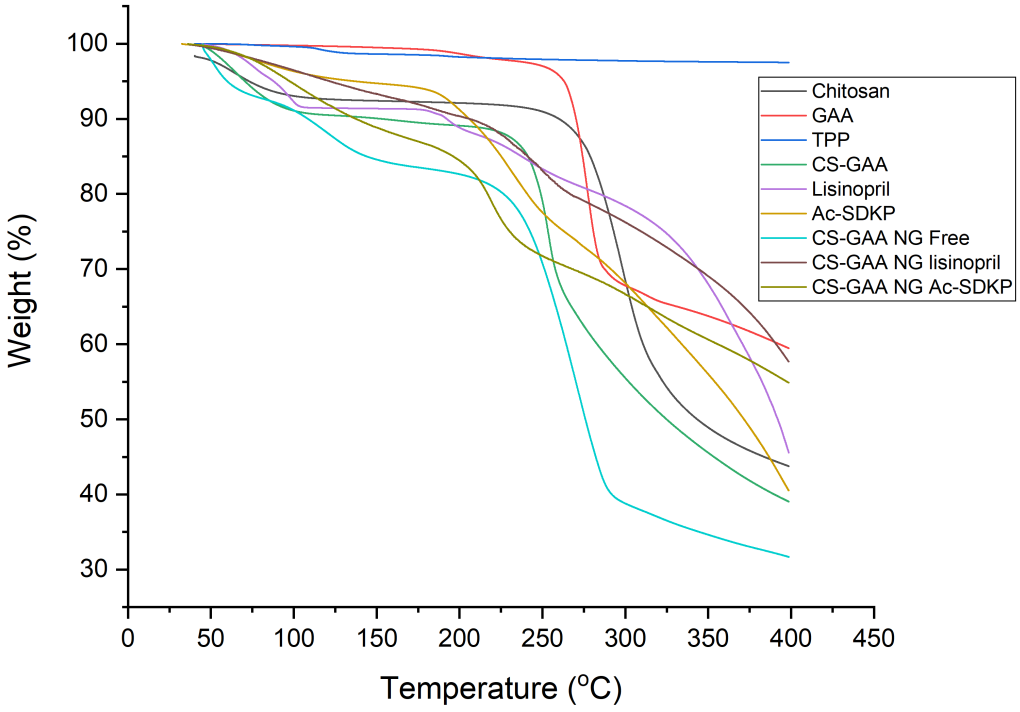

Figure 6-10. TGA thermogram of the raw materials and freeze-dried guanidylated chitosan TPP. Multi-stage degradations were observed for all samples, except for TPP, where no degradation was observed for the temperature range used.

6.4.2. Differential scanning calorimetry

DSC thermograms of lisinopril dihydrate, Ac-SDKP, TPP, chitosan, freeze-dried drug-loaded and drug-free nanoparticles using a single heating method are shown in **Figure 6-11**. Lisinopril dihydrate shows two board asymmetric peaks at 89.5 and 137.0 ºC, where both peaks were likely due to desolvation. Sorrenti *et al.* reported

that the temperatures for desolvation were 61.9 and 90.4 ºC and there should be two peaks that corresponded to each hydrate [307]. However, the temperature for desolvation in the experimental results was much higher than the reported result, despite a similar pattern of the thermogram being obtained. Thus, a possible explanation is that the two desolvation peaks were merged into one which was observed at 89.5 ºC and the second peak was shifted to 137 ºC. The second peak at 137 ºC was not reported in any literature and the minimal weight loss was shown in the TGA thermogram in **Figure 6-10**. Thus, it could be the second desolvation peak, melting of a polymorph or impurity, but further analysis is required. The peak at 180.9 ºC corresponded to the melting peak of the desolvated lisinopril, which was close to the value of 187.1 ºC reported by Sorrenti *et al*. [307]. No melting peak is observed for chitosan and Ac-SDKP, which demonstrated that the materials are amorphous. Broad peaks at 97.1 ºC in chitosan and 110.0 ºC in Ac-SDKP were likely due to the vaporization of the moisture adsorbed or bound to chitosan and the peptide. TPP exhibits two endothermic peaks at 114.7 ºC and 190.5 ºC. A larger temperature range (up to 300.0 ºC) is required to see the full profile as an endothermic peak is observed at around 200.0 ºC. The melting point for TPP was 622.0 ºC, which exceeded the maximum temperature that the Tzero pan could handle. A sharp peak was also observed at about 270.0 ºC for glycocyamine, which was 11.2 ºC lower than the reported melting point of 281.2 ºC [305]. The result echoed the TGA result, where the onset of decomposition temperature was lower in the measured sample. The results indicated the possibility of polymorphism of glycocyamine or the presence of impurities in the measured sample.

A broad peak was observed in the diffractogram of CS-GAA at 125 ºC, which was likely due to the removal of the bound water in the conjugate. Compared to chitosan, the temperature for water evaporation was higher, which indicated that the water was bounded strongly to the conjugate, as the guanidine group could interact with water via ion-dipole interactions in addition to hydrogen bonds while only the latter was present in chitosan. Similar board peaks were present in drug-free and Ac-SDKP-loaded nanogels at around 73.9 ºC, which indicated that the water is also contained in the samples. However, the drug-free nanogels had a higher degree of bound water than Ac-SDKP-loaded nanogels, as the intensity of the former was higher. In short,

the results confirmed the amorphous nature of the freeze-dried nanogels and CS-GAA conjugate.

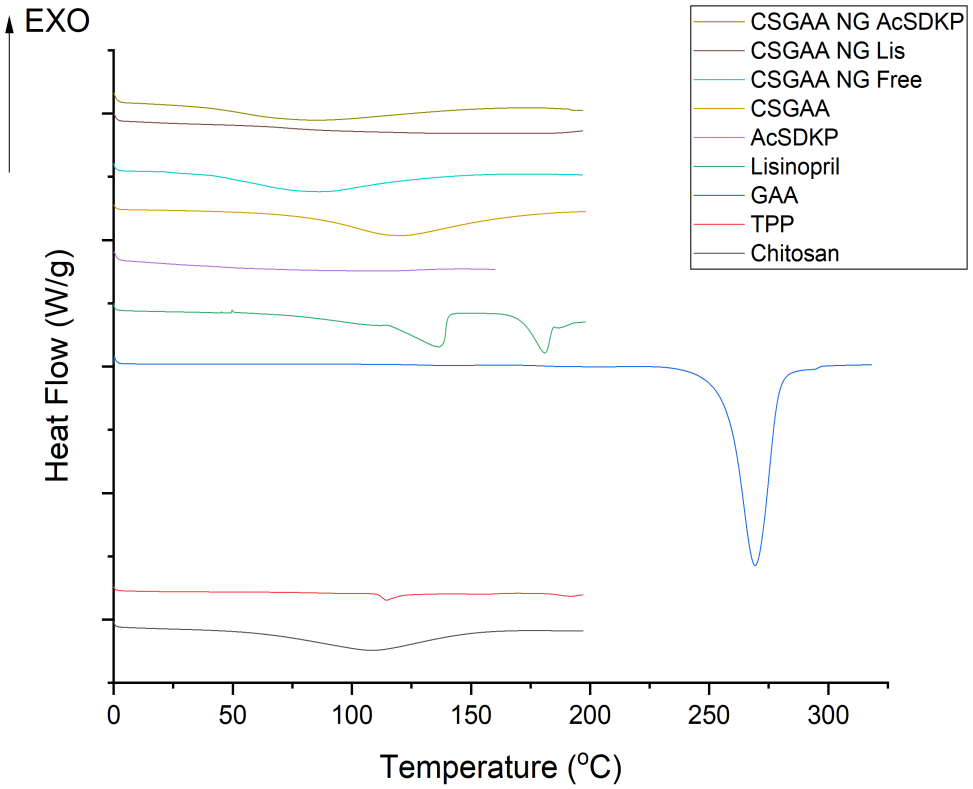

Figure 6-11. DSC thermogram of the raw materials used in the fabrication of CS-GAA nanogels, freeze-dried drug-free and drug-loaded CS-GAA nanogels using a single heating method. All samples, except GAA and Ac-SDKP, were heated between 0 to 200 °C. A lower temperature range (0 to 170 °C) was selected for Ac-SDKP as the peptide started to degrade at 168 °C. On the contrary, the melting point for GAA is 300 °C according to the MSDS. Therefore, a higher temperature limit of 320 °C was set. A sharp melting peak was observed for GAA, confirming the crystalline nature. Board peaks were observed for chitosan, Ac-SDKP, CS-GAA, drug-free and drug-loaded nanogels, which corresponded to evaporation of free and bound water. The result demonstrated these samples were amorphous.

6.4.3. Fourier transform infrared spectroscopy

Figure 6-12 shows the IR spectrum of the individual components of the nanogels, as well as drug-free, lisinopril- and Ac-SDKP-loaded nanogels. In the spectra of

chitosan, strong bands around 3290 and 3356 cm^{-1} are associated with O-H and N-H stretching and intermolecular hydrogen bonds, while the peak at around 2870 cm^{-1} corresponds to asymmetric C-H stretching. A small peak at 1397 cm^{-1} is related to the O-H bending, whereas the N-acetylation of chitosan was confirmed with the band at 1642-1650 cm^{-1} and 1323 cm^{-1}, which are the C=O stretching of amide and C-N stretching of amide respectively, as well as the peak at around 1590 cm^{-1} which corresponds to the N-H bending. The strong bands at 1027-1068 cm^{-1} are associated with the C-O-C anti-asymmetric stretching [308]. The spectra agree with the result reported in the literature [218,219]. As for TPP, the band at 3326 cm^{-1} corresponds to the O-H stretching while the band at 1135 and 1209 cm^{-1} is associated with O-P=O and P=O stretching, respectively [221]. A sharp peak at 1094 cm^{-1} corresponds to P-O stretching. In the FTIR spectrum of Ac-SDKP, a band at 2936 and 1722 cm^{-1} corresponds to the C-H and C=O stretching, respectively. Peaks at 1622, 1447 and 1043 cm^{-1} are associated with the N-H bending in the amine group, O-H stretching in the carboxylic acid group, and C-O in the side chain of serine, respectively. C-N stretching could be observed with peaks at 1180 and 1220 cm^{-1}. Unlike Ac-SDKP, the N-H, O-H and C-H stretching are found at 3550, 3292 and 2919 cm^{-1} respectively and no intermolecular hydrogen bond is observed in the spectrum of lisinopril. The C=O stretching in the group and N-H bending are at 1651 and 1568 cm^{-1}, respectively. C-N stretching in the amine group is identified at 1231 cm^{-1}. Regarding the spectrum of GAA, the O-H and N-H stretching are observed from 2976 to 3380 cm^{-1} and no intermolecular hydrogen bonds are observed due to the absence of the broad hump. Peaks for C-H stretching and the C=O stretching are at 2808 and 1663 cm^{-1}. The characteristic peaks for GAA are the two peaks at 1621 and 1573 cm^{-1}, which correspond to the C=N stretching and N-H bending in the guanidino group.

After conjugation of GAA to chitosan, additional peaks at 1634 and 1530 cm^{-1} are observed, which correspond to the C=N in the guanidino group and N-H bending, respectively. The result agreed with the literature and indicated the successful conjugation of GAA on the chitosan [301]. The peak for O-H bending and stretching are shifted slightly to 1379 and 3348 cm^{-1}, respectively. The C-O-C stretching could still be observed after the conjugation, with a strong peak at 1070 cm^{-1}. As for the

lyophilised CS-GAA nanogels, similar peaks at around 1630 and 1538 cm^{-1} were observed in both drug-loaded and drug-free nanogels which also correspond to the C=N stretching and N-H bending in the guanidino groups. The broad peak at about 3200 cm^{-1} corresponds to the O-H stretching with intramolecular hydrogen bonds. The symmetric C-H stretching was not obvious in the spectra of CS-GAA, but a peak was observed around 2940 cm^{-1} in all lyophilised nanogels samples. For the drug-loaded nanogels, some characteristic peaks are observed in the spectrum which is related to the drug. For example, the peak at 1389 cm^{-1} and two peaks in the fingerprint region at 700 and 746 cm^{-1} were related to lisinopril. Peaks in 1718 and 1446 cm^{-1} in the spectrum of Ac-SDKP loaded nanogels are contributed by Ac-SDKP, where similar peaks in 1772 and 1446 cm^{-1} are observed for the C=O and O-H stretching in Ac-SDKP. The sharp peak at 1155-1185 and 1224 cm^{-1} were present in the drug-free and drug-loaded nanogels, which are indicative of the P=O bond in TPP within the nanogel structure, albeit shifted from 1209 cm^{-1} in TPP alone as a consequence of the interaction with CS-GAA. Moreover, the C-O-C stretching of the saccharide backbone of chitosan is shifted to 1039, 1032 and 1042 cm^{-1} in the drug-free, lisinopril-loaded and Ac-SDKP-loaded nanogels respectively from 1087 cm^{-1}. In conclusion, the IR spectrum confirms the presence of the individual components in the CS-GAA nanogels. Structural change of the nanogels after encapsulation of the drug was not observed.

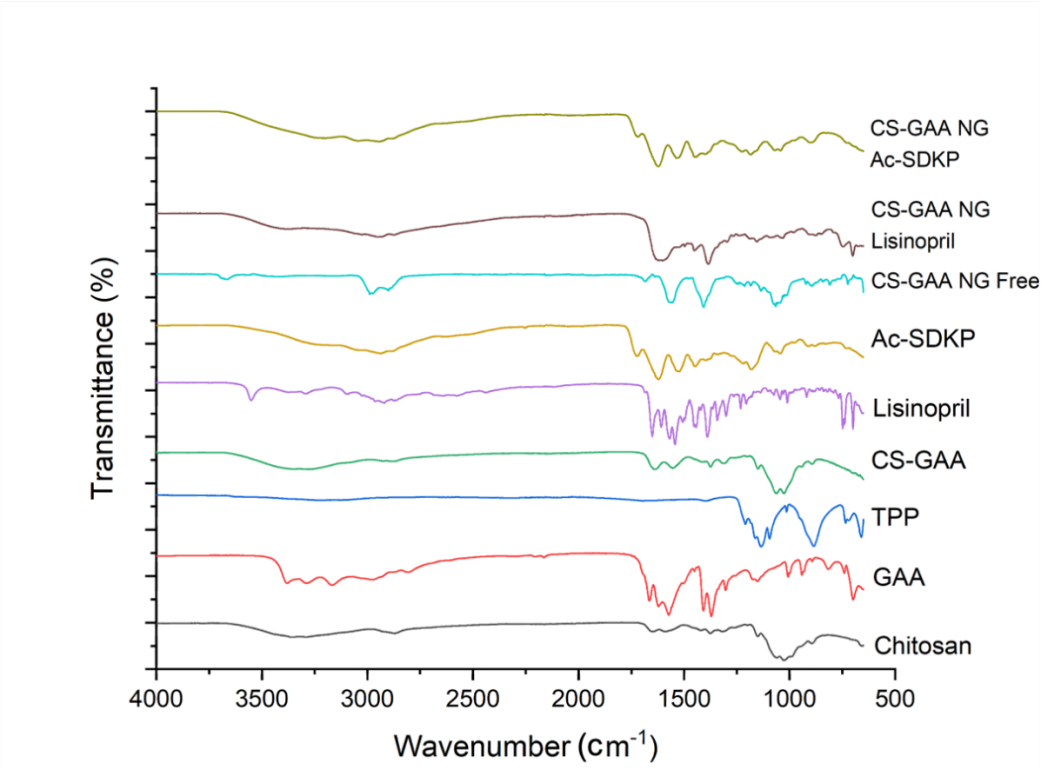

Figure 6-12. FTIR spectrum showing the components of the formulation individually, freeze-dried drug-free nanogels, lisinopril-loaded and Ac-SDKP-loaded nanogels

6.4.4. X-ray powder diffraction

The physical forms of raw materials and freeze-dried nanogels were assessed by XRD, with the results shown in **Figure 6-13**. Lisinopril dihydrate is a crystalline material, with strong peaks at $2\theta = 7.5^{o}$, 12.5^{o}, $13{,}4^{o}$ 16.3^{o}, 19.7^{o}, 22.5^{o}, 24.5^{o}, 26.5^{o} and 28^{o}. The results were remarkedly similar to the PXRD reported by Fujii *et al*. in their synchrotron-DSC study of lisinopril dihydrate [309], but the peak at $2\theta = 16.3^{o}$ was much smaller in terms of intensity compared to the reported result. Combined with the TGA and DSC results, it might indicate the presence of another polymorphic form or the presence of impurities. X-ray diffraction patterns of chitosan exhibited broad peaks at $2\theta = 10°$ and $2\theta = 20°$. The result is also in agreement the with XRD analysis of other grades of chitosan reported in the literature and indicates that the chitosan has a low degree of crystallinity rather than is amorphous [222,223]. TPP is crystalline, with sharp peaks observed in the diffractogram. Three peaks at $2\theta = 23.7^{o}$, 24.1^{o} and 24.7^{o} are observed in the

diffractogram, which are the characteristic peaks for phase II TPP [225]. GAA is crystalline, with Bragg's reflections observed. Sharp peaks were observed at 2θ = 20 °, 20.6 °, 23 °, 23.6 °, 24 °, 25 °, and 26°. On the other hand, a broad hump was observed in the diffractograms of Ac-SDKP and CS-GAA at about 2θ = 20.5° and 22° respectively, which indicated that both Ac-SDKP and CS-GAA were amorphous. Conjugation of crystalline GAA with chitosan likely disrupted the packing of chitosan, eradicating the low degree of crystallinity that chitosan originally possess.

The nanogels exhibited a mixture of mostly amorphous materials and a small amount of crystalline material, especially in the drug-free CS-GAA nanogels. The hump observed at $2\theta = 20°$ in chitosan disappeared, which agrees with the previous literature [226,227]. However, no Bragg reflection but a smaller hump at $2\theta = 10°$ were observed in all lyophilised nanogels, regardless of the drug loading. The intensity in drug-free nanogels was lower than the drug-loaded counterparts, but all of them were much lower compared to unreacted chitosan. The disappearances indicated that the crosslinked chitosan was mostly amorphous, and the crystallinity was lost due to the crosslinking with TPP, as a structure with a dense network of TPP crosslinked chitosan was formed [228]. However, additional peaks with low intensities were observed at $2\theta = 28$ °, 38 °, and 39.5°, which are likely due to a small amount of TPP crystal present in the sample, but they were shifted slightly from those in the diffractogram of TPP. The intensity of these peaks was weaker than those observed in TPP due to the smaller amount of TPP present in the nanogels. However, their intensities were higher than the drug-loaded counterparts as the proportion of TPP in the drug-free nanogels was approximately double that of the drug-loaded counterparts. Only a small halo at $2\theta = 27.5°$ was seen in the drug-loaded nanogels, which was related to the TPP in the nanogels. Hence, the freeze-dried propranolol-loaded nanogels were a solid dispersion of amorphous crosslinked chitosan-TPP structure with a small degree of crystallinity from its components.

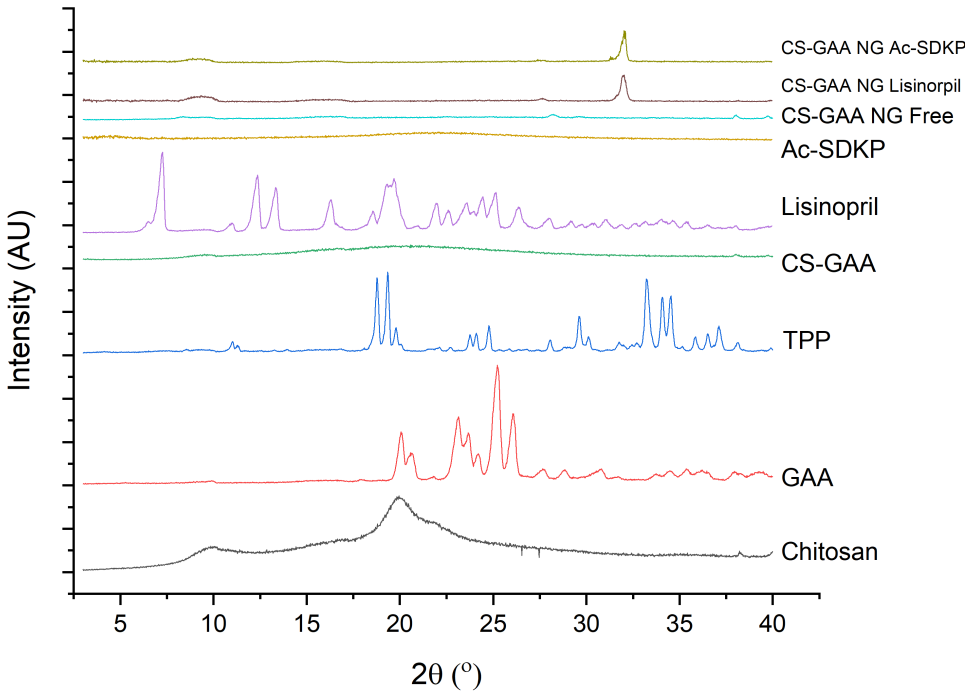

Figure 6-13. X-ray powder diffraction patterns of the various raw materials used in guanidylated chitosan-TPP nanogels fabrication and lyophilised nanogels. The results demonstrated that GAA, TP and lisinopril were crystalline materials.

6.4.5. Determination of deacetylation efficiency of chitosan using ^{1}H nuclear magnetic resonance

A 400 MHz ^{1}H NMR spectrum of the chitosan, CS-GAA, and CS-GAA nanogels was measured at 25 °C and a 2-second relaxation time was shown in **Figure 6-14**, with the solvent (HOD) proton resonating at 4.7040 ppm. As the NMR was performed at ambient temperature, the chemical shifts of some protons in chitosan overlapped with the solvent peak (HOD), such as the H1 of deacetylated monomer (H1D). The H2 and H3-6 could be observed in the NMR spectrum of chitosan at 3.0662 and 3.6359-3.8023 ppm, respectively. The peak at 1.9390 ppm corresponded to the three protons in the acetyl group of acetylated monomers (HAc).

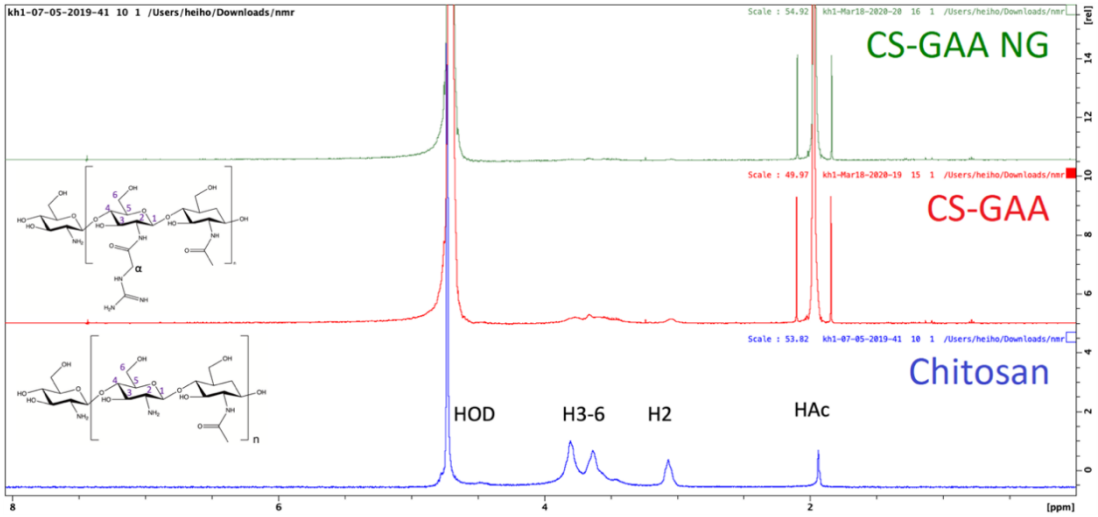

Figure 6-14. A ^{1}H NMR spectrum of the chitosan, guanidylated chitosan and the drug free nanogels at 60 °C.

After conjugation with GAA, the peaks of H2 and H3-6 were not obvious in CS-GAA under a similar scale. The single peak at 2.1009 ppm was likely the overlapping of a peak for the two hydrogens at the α carbon on the conjugates without coupling and the peak of HAc. The duplets at 1.8367 and 2.1009 ppm were the peaks when protons on the α carbon coupled with the proton on the adjacent nitrogen in the guanidine group, which could be occurred at room temperature. A similar spectrum was observed for the CS-GAA nanogels, but the intensities for the peaks of H2 and H3-6 were attenuated after crosslinking with TPP.

6.4.6. Transmission electron microscopy (TEM)

TEM images of the Ac-SDKP-loaded CS-GAA nanogel are shown in **Figure 6-15 (a-c)**. The former two images were taken at a scale of 100 nm, while the last image was taken at a scale of 500 nm. The nanogel appeared as spherical or oval objects. The average size of the Ac-SDKP-loaded nanogel at the dried state was 116.6 ± 45.6 nm, which is close to the measured z-average of 139.3 ± 2.0.6 nm and 130.0 ± 9.7 nm measured with Dynapro II and Zetasizer Ultra respectively. However, the number of particles in each image was limited and thus the size distribution was measured on 41 particles from three TEM images as shown in **Figure 6-15 (a-c)**, where the particles are visible from the background or have a distinct boundary. The large standard deviation showed a wide size distribution, which echoed the high PDI measured in dynamic light scattering via both machines.

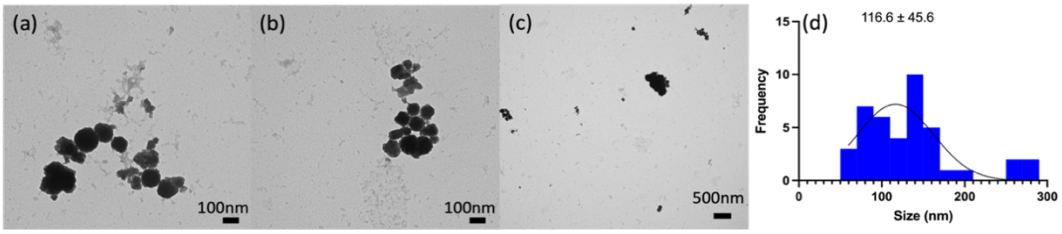

Figure 6-15. (a-c) TEM images of the Ac-SDKP-loaded CS-GAA nanogels at different scales and (d) the size distribution of the Ac-SDKP-loaded CS-GAA nanogels measured according to the particles with distinct boundaries (n = 41) observed in the TEM images using Fiji. Average size and SD were reported above the histogram.

6.4.7. Drug release study

The *in-vitro* drug release test uses PBS (pH 7.4) to simulate the release at physiological pH. A burst release of encapsulated lisinopril and Ac-SDKP can be observed in the first 8 and 5 hours respectively, as in **Figure 6-16**. A similar release profile was observed between the lisinopril- and Ac-SDKP-loaded nanogels in the first 5 hours, which indicated the same release mechanism of the drug from the nanogels. As Ac-SDKP and lisinopril are structurally alike, they are likely to interact with the guanidylated chitosan and TPP similarly. Both lisinopril and Ac-SDKP possess a similar molecular weight of 405.5 and 487.5 g/mol respectively, where they could leach out from the voids of the nanogels. In addition, it is known that the nanogels properties were partly dependent on the formulation, where the same formulation was used for both nanogels. Therefore, the release profiles were similar, and a quick release was observed. Nearly all Ac-SDKP was released in 24 hours, but only 70% of lisinopril was released from the nanogels.

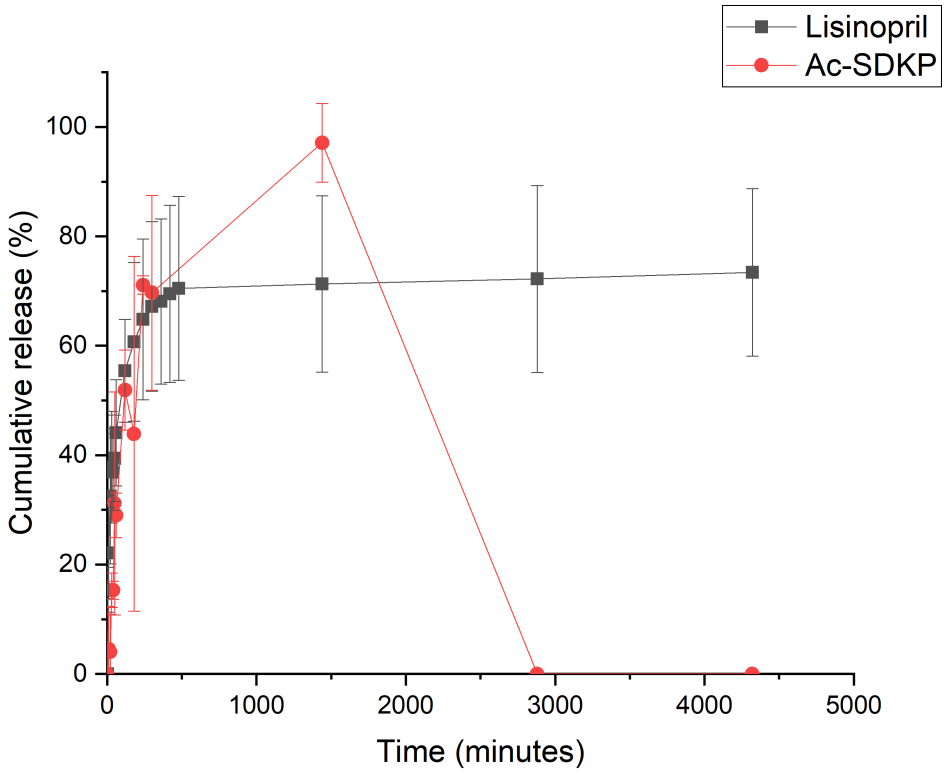

Figure 6-16. *In vitro* drug release from both lisinopril- and Ac-SDKP-loaded guanidylated chitosan nanogels over 72 hours. Data are obtained from three independent experiments and represented as mean ± SD. The cumulative release of Ac-SDKP in the PBS plunged to 0% at 48 and 72 hours, which was likely due to the degradation of the peptide over time in the PBS. In other words, the amount of parent peptide detected at 48 and 72 hours were below the detection and quantification limits of the HPLC method. Hydrolysis of the peptide bonds is likely the cause of degradation, as the X-asp-Y sequence in the peptide are more liable than other peptide bonds [1].

However, after 24 hours, the drug concentration from lisinopril-loaded CS-GAA nanogels levelled off, whilst the cumulative release from Ac-SDKP-loaded-CS-GAA nanogels plunged to 0. In other words, the concentration was below the lower limits of detection and quantitation of 5.5 and 16.87 µg/mL respectively in the method. It is likely due to the hydrolysis of Ac-SDKP in PBS into two dipeptides - (Ac-SD and KP) or a pair of amino acid and tripeptide (Ac-S with DKP or Ac-SDK with P). Interestingly, PBS promoted the fragmentation of peptides [310]. Two extra sharp peaks were observed at the dead time (t0) in the chromatogram in **Figure 6-17**,

which might correspond to these peptide fragments. However, the identities of these peaks should be confirmed via LC-MS. The results demonstrated that encapsulating the peptide in nanogels failed to protect the peptide from degradation, as the peptide likely leached out through the voids in the nanogels.

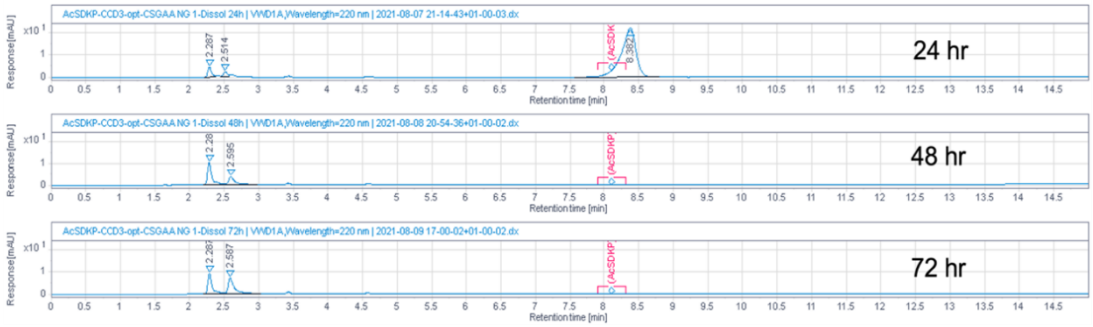

Figure 6-17. HPLC chromatogram of the samples was obtained at 24, 48, and 72 hours during the dissolution tests. The peak of interest at about 8 minutes disappeared at 48 and 72 hours, which indicated no peptides were detected in the sample. Two peaks were observed at about 2.2 and 2.5 minutes, with higher intensity compared to those observed at 24 hours. The result demonstrated that the peptide was likely degraded into two compounds, which had weaker interaction with the column and were eluted early.

6.4.8. MTT assay

TGF-β is an important proliferative signal that activates downstream signalling cascades that result in the transformation of fibroblasts into myofibroblasts and fibrosis. Epicardial cells are also able to transdifferentiate into myofibroblasts. TGF-β promotes the production and secretion of extracellular matrix including collagens and stimulates the expression of α-SMA [61]. Thus, it is an important signal leading to fibrosis post-MI injury. Peptide Ac-SDKP is thought to suppress the TGF-β/Smad signalling, attenuating the epithelial-mesenchymal transition (EMT) and fibroblast proliferation [61]. Instead of using 5 or 10 nM Ac-SDKP in other studies, the suitable concentration that suppresses the metabolic activity of fibroblasts without affecting those of epicardial cells was determined using the MTT assay with epicardial cells and L929 fibroblasts. The use of peptide-loaded nanogels was aimed to suppress fibrosis, instead of inhibiting the metabolic activity of the resident cells. Thus, it is crucial to ensure that the concentration does not impact the epicardial

cells, especially when they are the first layer in contact with the nanogels and were shown to be sensitive in **Chapter 4**.

Metabolic activity of fibroblast is partly towards the breakdown and resynthesis of protein and lipid, as well as to the excretion of extracellular matrix [311]. Therefore, the metabolic activity of fibroblast is a potential marker for the excretion of extracellular matrix and biosynthesis such as α -SMA and collagen. As a result, the cell metabolic activity determined with MTT assay under the conditions with and without TGF-β could be used to determine a suitable concentration for further study on the ability of the peptide to attenuate the excretion of extracellular matrix, the epithelial-mesothelial transition of the epicardial cells, and suppress the fibroblast proliferation. 5 ng/mL of TGF-β1 was selected based on the concentration used in the study conducted by Peng *et al.*, to facilitate further investigations on the α-SMA expression, collagen synthesis and Smad using western blot [312]. According to the *in vitro* release study, the peptide level was not detectable at 48 and 72 hours, where the peptide level was below the detection and quantitation limits of the HPLC-UV quantitation method. It was likely due to the peptide fragmentation in PBS [310]. Consequently, the MTT assay was only performed after incubation for 24 hours, as the stability of the peptide over 24 hours in the culture media was not warranted.

Peptide Ac-SDKP did not show any concentration-dependent inhibition of metabolism on the epicardial cells, as the metabolic activity levelled off at between 90-100% across all concentrations tested under the conditions without and with TGF-β1, respectively. However, the cell metabolic activity of the epicardial cells was significantly promoted with the presence of TGF-β1 across all tested concentrations. For L929 fibroblasts, Ac-SDKP exhibited concentration-dependent metabolic inhibition, with the response dropping below 100% at the concentration of 2.5 mg/mL without exposure to TGF-β1. Conversely, the metabolic activity was below 100% when the Ac-SDKP concentrations were higher than 0.62 mg/mL with 5 ng/mL TGF-β1. The metabolic activity was lower for cells incubated with TGF-β1 at concentrations above 0.156 mg/mL than the counterparts without TGF-β1. However, according to the multiple comparison test, the difference in metabolic activity was statistically significant at only two concentrations (0.62 and 1.25

mg/mL). The results indicated the different responses to the peptide were cell specific. In general, the peptide suppressed the cell metabolism only at a very high concentration of 2.5 mg/mL but promoted cell growth at lower concentrations, especially in the epicardial cells. The suppression of fibroblast metabolism at concentrations > 0.156 mg/mL (320 μM) was limited, which echoed the finding of Peng *et al*. in human cardiac fibroblasts which only used 1-10 nM Ac-SDKP [312].

With regards to the Ac-SDKP nanogels, a dose-dependent effect was observed with both L929 and epicardial cells, where cell metabolic activity was the lowest at 1.218 mg/mL. Unlike cell proliferation being promoted after incubating with Ac-SDKP and TGF-β1, the cell proliferation in response to Ac-SDKP nanogels was not obvious. The cell metabolic activity was maintained at the same level as the control in both cell lines after incubating with Ac-SDKP nanogels and TGF-β1. At concentrations of 0.152 mg/mL and above, the Ac-SDKP nanogels significantly lowered cell metabolic activity of epicardial cells in the presence of TGF-β1, but the reduction was not significant for concentrations lower than 0.152 mg/mL. In comparison, the degree of suppression in L929 was more prominent after 24-hour incubation with TGF- β1 and the nanogels. However, the difference in cell metabolic activity between the presence and absence of TGF-β1 was only significant at three concentrations – 0.005, 0.019 and 0.152 mg/mL. Reduction of the cell metabolic activity only in the presence of TGF- β1. It should be noted that the concentrations used in the experiments were the total weight of freeze-dried nanogels, and thus the equivalent concentration of Ac-SDKP present in the nanogels was 0.003, 0.012 and 0.097 mg/mL, respectively. Thus, compared to the Ac-SDKP only in **Figure 6-18 (b)**, the metabolic suppression at concentrations closest to these values was not significant, which indicated that the effect of the peptide at the nanoscale was likely strengthened. Therefore, the effect of proliferation suppression on L929 was shown at lower equivalent Ac-SDKP concentrations in nanogels.

Epicardial cells were found to be more susceptible to metabolic suppression by the drug-free CS-GAA nanogels, which were positively charged and could potentially disrupt the phospholipid bilayers of the cells. However, the inhibition was only observed at concentrations of 0.443 mg/mL for both cells, but the suppression in

epicardial cells was more obvious. The results reflect the observations in **Chapter 4** and the epicardial cell metabolic inhibition. Under the presence of TGF-β1, the average cell metabolic activity of epicardial cells and L929 was lower than under the absence of TGF-β1 when incubating with the drug-free nanogels, but the differences were statistically significant only at several concentrations as shown in **Figure 6-18 (e-f)**. However, the epicardial cells and L929 were over 100% viable at these concentrations, which indicated that the drug-free nanogels were not cytotoxic to the cells.

To determine a suitable concentration of Ac-SDKP-loaded nanogels, the key criterion of selection is that no inhibition of metabolic activity is observed in the epicardial cells while the metabolism of fibroblast is suppressed simultaneously. Three concentrations fulfilled the criterion according to the multiple comparison test, namely, 0.005, 0.019 and 0.152 mg/mL. A significant reduction in metabolic activity of L929 was shown after the incubation with 0.005 mg/mL Ac-SDKP nanogels (equivalent to 6.52 μM of Ac-SDKP) and TGF- β1 for 24 hours, whilst the epicardial cells remained 100% viable. On the other hand, at 0.019 and 0.152 mg/ml (equivalent to 24.8 and 198.4 μM) of Ac-SDKP nanogels, although the cell metabolic activity of both epicardial cells and fibroblast were suppressed, the epicardial cells were still over 100% viable. Therefore, these three concentrations were explored further to evaluate the effect of the Ac-SDKP and its nanogels at various concentrations on the epithelial mesothelial transition, trans-differentiation of fibroblast into myofibroblast, and the production of collagen, which will be discussed in future works.

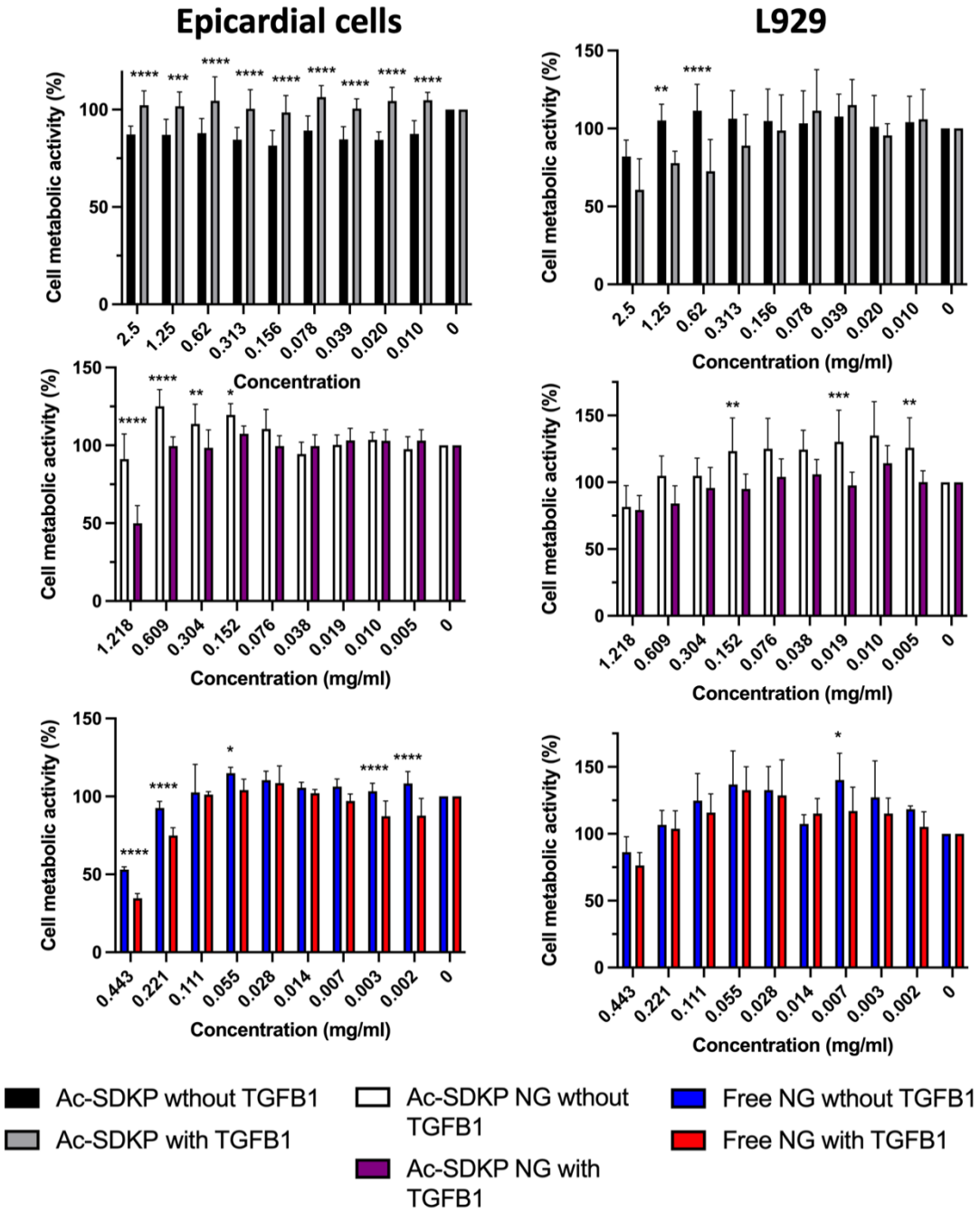

Figure 6-18. Relative cell viability of the epicardial cells and L929 after 24-hour incubation with (a-b) Ac-SDKP, (c-d) Ac-SDKP-loaded nanogels and (e-f) drug-free nanogels with and without 5 ng/mL TGF- β1. *Šidák* test was used to compare the cell viability with and without the presence of TGF- β1. * Denoted $p \leq 0.05$, ** referred to $p \leq 0.01$, *** meant $p \leq 0.001$, and **** referred to $p < 0.0001$.

6.5. Conclusion

In this chapter, a novel nanogel system was developed to produce nanogels at a more neutral pH. Guanidinoacetic acid was conjugated to the chitosan to make the chitosan soluble at physiological pH for loading an anti-fibrotic peptide Ac-SDKP, minimising the degradation due to a low pH environment. Conjugation was performed via EDC/NHS reaction. As the peptide is expensive, formulation optimisation was performed using the structurally similar drug lisinopril. The important formulation and processing parameters were first selected from the Plackett-Burman design and used to construct the response surface methodology. Properties of the lisinopril-loaded nanogels fabricated at the optimal condition fulfilled all success criteria, with size ≤ 500nm, PDI ≤ 0.3, ZP ≥ 15 mV, and EE ≥ 50%. Subsequently, Ac-SDKP-loaded nanogels were fabricated according to the same condition. However, the success criteria were partly fulfilled with the Ac-SDKP-loaded nanogels, with PDI and EE of 0.434 and about 40% respectively. Properties of the Ac-SDKP loaded nanogels were determined but there was a discrepancy between the measured result and the expectation based on extrapolating the correlations established in **Chapter 3**, where the nanogels are expected to be larger, more polydisperse and with a lower ZP. However, only the PDI followed the extrapolation, but the size was smaller and a similar ZP was measured. The results indicated that the correlations might not be suitable for extrapolating to other families of drugs or a different nanogels system or both.

Moreover, the novel CS-GAA polymer and its nanogels were characterised with several physical characterisation methods, to understand the properties of these materials. The FTIR and NMR results demonstrated the successful conjugation of the GAA on the chitosan. Furthermore, the release study illustrated that the conjugation of GAA did not impact the release of the peptide. The peptide was released immediately and throughout the first 24 hours, but the cumulative release plunged to 0% at 48 and 72 hours, likely due to the promoted degradation of peptide in PBS. In the cell studies, the use of nanogels reduced the peptide concentration required to suppress the metabolic activity of fibroblasts under the presence of TGF-β1. Three concentrations of Ac-SDKP-loaded nanogels were identified in cell studies, which did not impact the cell metabolic activity of epicardial cells and

simultaneously attenuated the proliferation of L929 fibroblast. These concentrations are suitable for use in future to determine the effects of the nanogels on preventing the epithelial-mesenchymal transition, collagen production and transdifferentiation of fibroblasts into myofibroblasts.

Chapter 7

Conclusions and Future Works

7. Conclusions and Future works

7.1. Conclusions

Intrapericardial delivery is an alternative route for delivering therapeutics to the heart. Encouraging results have been reported when using this route for delivery of cells, drugs, and protein for a variety of conditions, resulting in regeneration of myocardium after acute myocardial infarction, mitigating cardiac arrhythmias or preventing platelet aggregation and restenosis after reperfusion via the coronary artery. Minimally invasiveness intrapericardial delivery is likely to offer advantageous pharmacokinetic profiles and localised therapy to the heart, which could fill the unmet needs for targeted cardiac delivery. However, these techniques also restrict the choice of formulations. Nanogels have been applied in numerous experimental settings and for different purposes, offering potentially favourable injectability and ease of fabrication. Thus, the formulation of nanogels for intrapericardial delivery of therapeutic agents was the focus of this thesis.

The key outcomes from this research included demonstrating the predictability of the nanogels properties and optimising the formulation and fabrication process of drug-loaded nanogel. This study also demonstrated the potential application of the models on structural similar drugs and elucidated the drug loading mechanism in nanogels. The third outcome was developing a novel, simple and robust HPLC-UV method for the anti-fibrotic peptide Ac-SDKP, which is suitable for pharmaceutical assessment. Last but not least, a novel guanidylated chitosan-TPP nanogels was developed for delivering the peptide Ac-SDKP and the cytotoxicity of the nanogels was tested on epicardial cells and other cell lines. The findings for each chapter are summarised and as follows.

7.1.1. Modelling the properties of the nanogels and prediction of drug-loading and release with structural activity relationship

In **Chapter 2**, propranolol-loaded chitosan-TPP nanogels were fabricated and characterised to demonstrate the fabrication method, set-up and assay method were fit for purpose. In **Chapter 3**, prediction models for the properties of propranolol-loaded nanogels were constructed using a Design of Experiment approach. First, the effects of three formulation factors - chitosan concentration, chitosan-TPP ratio and

chitosan-propranolol ratio on the four key criteria of a successful nanogel formulation were determined, namely Z-average (size), polydispersity index (PDI), zeta potential (ZP), and encapsulation efficiency (EE). The optimal formulation of 0.1% chitosan concentration, a chitosan-TPP ratio of 3 and a chitosan-propranolol ratio of 0.5 was predicted. The Z-average and PDI of the optimum nanogel formulation were 75.5 ± 2.2 nm and 0.211 respectively, which were close to the predicted values. However, ZP and the EE have not been predicted as the predictability of these models were weak, indicating the importance of performing a test set and other unexplored factors controlling these parameters. The results demonstrated the size and PDI of the nanogels could be modelled and predicted.

To evaluate the application of these prediction models to different drugs, the nanogels loaded with other drugs were fabricated at the optimal condition in the model with 12 structurally distinct and 6 structurally similar drugs, and the size, PDI and ZP of the nanogels were measured. These properties were distinct from the predicted value, which indicated that the DOE models must be refined when a new drug is used. Despite the different payloads in the nanogels, the measured properties of nanogels were similar, which revealed that the nanogel properties are partly dependent on the formulation. Nevertheless, relationships were found between structurally related drugs and performance parameters, hence there is a dependence on the molecular structure which could potentially be solved for a wider range of drugs. Firstly, the size of beta-blocker-loaded nanogels decreased with XLogP of the drug, while the PDI of nanogels increased linearly with TopoDiameter and exponentially with the bpol of the drug. Finally, the ZP of nanogels negatively and exponentially correlated with apol and bpol, quadratically related to WPATH and AlogP, and decreased linearly with TopoDiameter. These outcomes also show that encapsulation and formation processes are indeed drug-dependent and are not simply a matter of incorporation into the inter-chain voids. This is the first study that reported that the interaction between the nanogels and drugs are intrinsic mechanisms for encapsulation that also govern the properties of nanogels, paving a solid foundation for further formulation developments using nanogels.

A definitive screening design was used to screen and optimize the important fabricating factors that influenced the hydrodynamic size, PDI, ZP and the EE of the

nanogels. Five out of ten processing factors were shown to significantly affect the properties of propranolol-loaded nanogels, namely temperature, stirrer size, the addition rate of the crosslinker and volume of the glass container. Moreover, the chitosan grade and the choice of crosslinkers also significantly impacted the properties of nanogels. As chitosan is a natural polymer, the properties of chitosan (i.e., molecular weight and deacetylation efficiency) vary between batches and manufacturers, which also adds complexity to reproducing the nanogels with expected properties from reported methods. Lastly, the optimal formulation condition of nanogels was established from the definitive screening study, utilising MMW chitosan and TPP. The additional rate for TPP solution was set at 2 mL/min while the solution was then stirred at a temperature of 50 ºC, stirring speed of 600 rpm. The volume of the glass vial used was 28 mL while the stirrer size was 20 mm. This is a novel study evaluating the effects of processing factors during fabrication on the nanogel properties systematically. The results indicated the importance of controlling the processing factors in the fabrication process and demonstrated that the scaling-up of the nanogels fabrication process is not simply via increasing the volume pro-rata. The process has to be investigated individually to prepare the respective target volume of nanogels.

7.1.2. Evaluation of the biocompatibility of the propranolol-loaded nanogels

In **Chapter 4**, propranolol was shown to suppress cell metabolic activity of epicardial cells, H9c2 cardiomyoblasts and L929 fibroblasts. The results also indicated the significantly higher sensitivity of epicardial cells to propranolol cytotoxicity, which highlights the importance of using location-specific cells (i.e., epicardial cells for modelling intrapericardial delivery) in the screening of new drug formulations. Time-dependent and dose-dependent inhibition of cell metabolic activity and proliferation was demonstrated with propranolol on epicardial cells. Finally, cytotoxicity of propranolol, drug-free nanogels and propranolol-loaded nanogels were tested on the epicardial cells. The result indicated that the use of biocompatible nanogels reduced the effect of propranolol on cells, with inhibition of cell metabolism observed at higher equivalent propranolol concentrations, demonstrating that it is advantageous to use nanogels as a carrier.

7.1.3. HPLC-UV assay method development and validation for anti-fibrotic peptide Ac-SDKP

Owing to the metabolic suppression of propranolol at concentrations likely to be delivered, an anti-fibrotic peptide Ac-SDKP was selected to be the new payload in the nanogels. The existing quantification methods for the peptide are liquid chromatography-tandem mass spectrometry (LC-MS/MS) and enzyme-linked immunosorbent assay (ELISA), but they are not ideal for formulation development, where detection of high dose-equivalent concentrations is required. In **Chapter 5**, a novel HPLC-UV assay method for the peptide was developed using an analytical Quality by Design (AQbD) approach, which could detect and quantify high concentrations. The method was developed based on the principles in ICH Q8-10 guidelines and was subsequently validated according to the ICH Q2 (R1) guideline. The holistic approach involves multiple stages, namely identification of the ATPs and CQA, risk assessments, Design of Experiment, determination of the method operable design region (MODR), establishing control measures, and continuous monitoring. Four key chromatographic responses – capacity factor, resolution, tailing factor and theoretical plate count were selected as the outputs. Various chromatographic parameters were first screened and selected to construct the response surface design. The optimised chromatography conditions utilised 10 mM phosphate buffer at pH 2.5 and acetonitrile as mobile phases, starting at 3% acetonitrile and 97% buffer and increasing to 9.7% acetonitrile and 90.3% buffer over 15 mins at 25 ^{o}C and a flow rate of 1 mL/min. The injection volume and VWD wavelengths were 10 µL and 220 nm, respectively. In short, the method offered a cost-effective, simple, and accurate quantification assay for the peptide, but the drawback of the method was that the LOD and LOQ were compromised. Therefore, the method developed is likely to provide a complementary approach to the existing quantification methods, especially when quantifying the peptide at higher concentrations. This method is the first reported HPLC-UV assay method for peptide Ac-SDKP that is capable of quantitation at relatively high concentrations and is compatible with phosphate buffer, which could facilitate the future development of the peptide in clinics.

7.1.4. Fabrication of CS-GAA nanogels at higher pH to enable encapsulation of Ac-SDKP

As the new payload was a peptide, which is fragile and pH-sensitive, nanogels were required to be fabricated at a more basic or neutral pH to attenuate the hydrolysis of the peptide. However, chitosan is not soluble at neutral pH and functionalisation of the polymer was required to achieve this. Thus, guanidinoacetic acid was conjugated via EDC/NHS coupling to the chitosan, making the chitosan soluble at physiological pH for loading an anti-fibrotic peptide Ac-SDKP. As the peptide is expensive, the formulation optimisation was performed using the structurally similar drug lisinopril, based on the correlations established in **Chapter 3** between nanogels properties and properties of drugs with structural similarity. Important formulation and processing parameters were first selected from the Plackett-Burman design and used to construct the response surface methodology. Ac-SDKP loaded CS-GAA nanogels were then fabricated according to the optimal conditions predicted. A discrepancy in the properties of the Ac-SDKP-loaded nanogels, as compared to the result based on extrapolating the correlations established in **Chapter 3**. The Ac-SDKP-loaded nanogels were expected to be larger, more polydisperse and with lower ZP. However, only the PDI followed the extrapolation, whilst the size was smaller and ZP was comparable. The results indicated that the correlations might not be suitable for extrapolating to other families of drugs or a different nanogels system or both, but further investigation is required for a solid conclusion. Moreover, the novel CS-GAA polymer and its nanogels were characterised with several physical characterisation methods, to understand the properties of these materials. The *in vitro* drug release study was performed using the quantification assay described in **Chapter 5**, with the released peptide from the nanogels fragmented after 24 hours owing to the PBS used. The MTT assay showed that the use of nanogels reduced the peptide concentration required to suppress the metabolism of fibroblast under the presence of TGF-β1. Three concentrations of Ac-SDKP-loaded nanogels were identified in cell studies, which did not impact the metabolic activity of epicardial cells and simultaneously attenuated that of L929 fibroblast. These concentrations are candidates for future research to determine the effects of the nanogels on preventing the epithelial-mesenchymal transition, collagen production and transdifferentiation of fibroblasts into myofibroblasts.

7.2. Future works

The research reported in this thesis has identified an Ac-SDKP-loaded nanogel formulation that warrants further investigations in intrapericardial delivery for the treatment of myocardial infarction. Further experiments will need to explore the effects and distribution of the Ac-SDKP-loaded nanogels. Therefore, additional directions are proposed for the next steps towards achieving this overarching goal in the future.

7.2.1. Effects of the Ac-SDKP-loaded nanogels

Further experiments are needed to establish the biological effects and behaviour of the nanogels. A biodegradation test should be performed to understand the fate and degradation of the nanogels. Moreover, the swelling behaviour of the nanogels should be explored further.

Secondly, the activity of the peptide after encapsulating in the nanogels should be tested. As Ac-SDKP is thought to suppress the TGF-β/Smad signalling, attenuating the epithelial-mesenchymal transition (EMT) and fibroblast proliferation [61], the effect of Ac-SDKP on associated cellular pathways would provide a good indication of whether the peptide activity is preserved after loading in the nanogels. Western blots could be performed to determine the expression of α-smooth muscle actin, Smad 2 & 7, and collagen in fibroblasts after incubating the Ac-SDKP nanogels and TGF-β1. These are markers for the transdifferentiation of fibroblasts into myofibroblasts, activation of Smad signalling, and secretion of extracellular matrix, respectively. Cardiac fibroblasts should be used instead of L929 as the latter are immortalised areolar fibroblasts. The ability of the peptide to suppress the epicardial mesenchymal transition could be performed, as outlined above. Lastly, the peptide-loaded nanogels could be injected intrapericardially into animal models of myocardial infarction to evaluate the cardioprotective effects of the Ac-SDKP-loaded nanogels *in vivo*.

7.2.2. *In vitro* and *in vivo* distribution of the nanogels

To understand the uptake, distribution, and fate of nanogels delivered into the pericardium, a Transwell uptake study could be performed using the epicardial and H9c2 cells, simulating the layer-by-layer structure in the cardiac wall. The feasibility of trans-endocytosis or permeation of nanogels through the epicardial cells was evaluated, as shown in **Figure 7-1**. The fluorescently labelled nanogel will be first added into the medium contained in the insert, where the EMCs are grown on the membrane. Confocal microscopy could be performed on the epicardial cells and H9c2 cells to detect the uptake of nanogels in the layer-by-layer setting. This would be a qualitative study. The fluorescently labelled nanogels could also be injected directly into the pericardium of an animal. The depth of penetration and distribution of the labelled nanogels in the cardiac wall could be investigated using either *in situ* imaging methods or immunofluorescence imaging of explanted tissue.

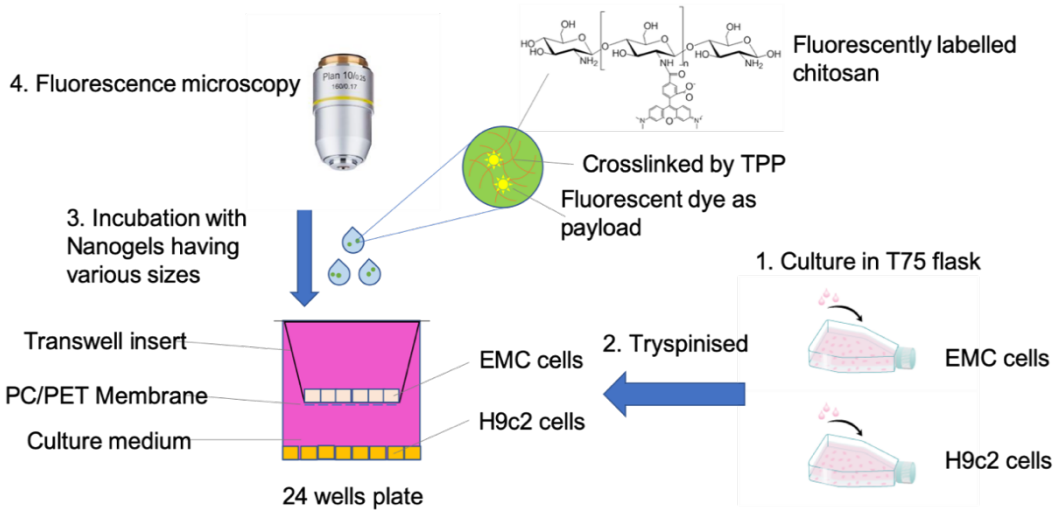

Figure 7-1. A schematic diagram showing the steps in tracking the deposition of nanogels using the in-vitro H9c2 and epicardial cells model

References

[1] Zapadka KL, Becher FJ, Gomes dos Santos AL, Jackson SE. Factors affecting the physical stability (aggregation) of peptide therapeutics. Interface Focus 2017;7:20170030.

[2] World Health Organization. WHO - The top 10 causes of death. 24 Maggio 2018;2018:1–7. http://www.who.int/en/news-room/fact-sheets/detail/the-top-10-causes-of-death.

[3] Rolfes C, Howard S, Goff R, A. P. Localized Drug Delivery for Cardiothoracic Surgery. Curr. Concepts Gen. Thorac. Surg., InTech; 2012. https://doi.org/10.5772/48577.

[4] Kühn B, Del Monte F, Hajjar RJ, Chang YS, Lebeche D, Arab S, et al. Periostin induces proliferation of differentiated cardiomyocytes and promotes cardiac repair. Nat Med 2007;13:962–9. https://doi.org/10.1038/nm1619.

[5] Polizzotti BD, Arab S, Kühn B. Intrapericardial delivery of gelfoam enables the targeted delivery of periostin peptide after myocardial infarction by inducing fibrin clot formation. PLoS One 2012;7:e36788. https://doi.org/10.1371/journal.pone.0036788.

[6] Ladage D, Yaniz-Galende E, Rapti K, Ishikawa K, Tilemann L, Shapiro S, et al. Stimulating Myocardial Regeneration with Periostin Peptide in Large Mammals Improves Function Post-Myocardial Infarction but Increases Myocardial Fibrosis. PLoS One 2013;8:e59656. https://doi.org/10.1371/journal.pone.0059656.

[7] Ladage D, Turnbull IC, Ishikawa K, Takewa Y, Rapti K, Morel C, et al. Delivery of gelfoam-enabled cells and vectors into the pericardial space using a percutaneous approach in a porcine model. Gene Ther 2011;18:979–85. https://doi.org/10.1038/gt.2011.52.

[8] Browne SE. Cardiovascular diseases. Practitioner 1984;228. http://www.who.int/news-room/fact-sheets/detail/cardiovascular-diseases-(cvds).

[9] British Heart Foundation. BHF CVD statistics. Br Hear Found 2021;2018:8. https://www.google.com/url?sa=t&rct=j&q=&esrc=s&source=web&cd=&ved=2ahUKEwiLiamF1Nz1AhXaQUEAHcwxB5IQFnoECAgQAw&url=https%

3A%2F%2Fwww.bhf.org.uk%2F-%2Fmedia%2Ffiles%2Fresearch%2Fheart-statistics%2Fbhf-cvd-statistics---uk-factsheet.pdf&usg=AOvVaw1dOumSZ3VTf.

[10] Mendis S, Puska P, Norrving B. Global atlas on cardiovascular disease prevention and control. World Health Organization; 2011.

[11] Lusis AJ. Atherosclerosis. Nature 2000;407:233–41. https://doi.org/10.1038/35025203.

[12] Fitridge R, Thompson M. Mechanisms of vascular disease: a reference book for vascular specialists. University of Adelaide Press; 2011.

[13] Bäck M, Hansson G. Basic Mechanisms of Atherosclerosis. Chronic Coron. Artery Dis. A Companion to Braunwald's Hear. Dis., 2018, p. 45–54. https://doi.org/10.1016/B978-0-323-42880-4.00004-2.

[14] Narula J, Rosenzweig A. Mechanisms of cell death in heart failure. Heart Fail 2004;32:45–59. https://doi.org/10.1201/b14176-6.

[15] Whelan RS, Kaplinskiy V, Kitsis RN. Cell death in the pathogenesis of heart disease: Mechanisms and significance. Annu Rev Physiol 2009;72:19–44. https://doi.org/10.1146/annurev.physiol.010908.163111.

[16] Chiong M, Wang Z V., Pedrozo Z, Cao DJ, Troncoso R, Ibacache M, et al. Cardiomyocyte death: Mechanisms and translational implications. Cell Death Dis 2011;2:e244. https://doi.org/10.1038/cddis.2011.130.

[17] Potts MB, Vaughn AE, McDonough H, Patterson C, Deshmukh M. Reduced Apaf-1 levels in cardiomyocytes engage strict regulation of apoptosis by endogenous XIAP. J Cell Biol 2005;171:925–30. https://doi.org/10.1083/jcb.200504082.

[18] Gui L, Liu B, Lv G. Hypoxia induces autophagy in cardiomyocytes via a hypoxia-inducible factor 1-dependent mechanism. Exp Ther Med 2016;11:2233–9. https://doi.org/10.3892/etm.2016.3190.

[19] Marambio P, Toro B, Sanhueza C, Troncoso R, Parra V, Verdejo H, et al. Glucose deprivation causes oxidative stress and stimulates aggresome formation and autophagy in cultured cardiac myocytes. Biochim Biophys Acta - Mol Basis Dis 2010;1802:509–18. https://doi.org/10.1016/j.bbadis.2010.02.002.

[20] Pinto AR, Ilinykh A, Ivey MJ, Kuwabara JT, D'antoni ML, Debuque R, et al. Revisiting cardiac cellular composition. Circ Res 2016;118:400–9.

https://doi.org/10.1161/CIRCRESAHA.115.307778.

[21] Shinde A V., Frangogiannis NG. Fibroblasts in myocardial infarction: A role in inflammation and repair. J Mol Cell Cardiol 2014;70:74–82. https://doi.org/10.1016/j.yjmcc.2013.11.015.

[22] Frangogiannis NG. The inflammatory response in myocardial injury, repair, and remodelling. Nat Rev Cardiol 2014;11:255–65. https://doi.org/10.1038/nrcardio.2014.28.

[23] Talman V, Ruskoaho H. Cardiac fibrosis in myocardial infarction—from repair and remodeling to regeneration. Cell Tissue Res 2016;365:563–81. https://doi.org/10.1007/s00441-016-2431-9.

[24] Kong P, Christia P, Frangogiannis NG. The pathogenesis of cardiac fibrosis. Cell Mol Life Sci 2014;71:549–74. https://doi.org/10.1007/s00018-013-1349-6.

[25] Ma ZG, Yuan YP, Wu HM, Zhang X, Tang QZ. Cardiac fibrosis: New insights into the pathogenesis. Int J Biol Sci 2018;14:1645–57. https://doi.org/10.7150/ijbs.28103.

[26] Frangogiannis NG. Regulation of the inflammatory response in cardiac repair. Circ Res 2012;110:159–73. https://doi.org/10.1161/CIRCRESAHA.111.243162.

[27] Testa M, Yeh M, Lee P, Fanelli R, Loperfido F, Berman JW, et al. Circulating levels of cytokines and their endogenous modulators in patients with mild to severe congestive heart failure due to coronary artery disease or hypertension. J Am Coll Cardiol 1996;28:964–71. https://doi.org/10.1016/S0735-1097(96)00268-9.

[28] Mitchell MD, Laird RE, Brown RD, Long CS. IL-1β stimulates rat cardiac fibroblast migration via MAP kinase pathways. Am J Physiol - Hear Circ Physiol 2007;292:H1139–47. https://doi.org/10.1152/ajpheart.00881.2005.

[29] Saxena A, Chen W, Su Y, Rai V, Uche OU, Li N, et al. IL-1 Induces Proinflammatory Leukocyte Infiltration and Regulates Fibroblast Phenotype in the Infarcted Myocardium. J Immunol 2013;191:4838–48. https://doi.org/10.4049/jimmunol.1300725.

[30] Desmouliere A, Geinoz A, Gabbiani F, Gabbiani G. Transforming growth factor-β1 induces α-smooth muscle actin expression in granulation tissue myofibroblasts and in quiescent and growing cultured fibroblasts. J Cell Biol

1993;122:103–11. https://doi.org/10.1083/jcb.122.1.103.

[31] Van Den Borne SWM, Diez J, Blankesteijn WM, Verjans J, Hofstra L, Narula J. Myocardial remodeling after infarction: The role of myofibroblasts. Nat Rev Cardiol 2010;7:30–7. https://doi.org/10.1038/nrcardio.2009.199.

[32] Curley D, Lavin Plaza B, Shah AM, Botnar RM. Molecular imaging of cardiac remodelling after myocardial infarction. Basic Res Cardiol 2018;113:10. https://doi.org/10.1007/s00395-018-0668-z.

[33] Deb A, Ubil E. Cardiac fibroblast in development and wound healing. J Mol Cell Cardiol 2014;70:47–55. https://doi.org/10.1016/j.yjmcc.2014.02.017.

[34] Willems IEMG, Havenith MG, De Mey JGR, Daemen MJAP. The α-smooth muscle actin-positive cells in healing human myocardial scars. Am J Pathol 1994;145:868–75.

[35] NICE. My Myocardial infarction with ST ocardial infarction with ST-segment -segment ele elevation: acute management vation: acute management Clinical guideline. NICE Guid 2013;2018:28. https://www.nice.org.uk/guidance/cg167.

[36] NICE. Myocardial infarction: cardiac rehabilitation and prevention of further cardiovascular disease. Clin Guidel [CG172] 2013;2018:Key priorities for implementation. https://www.nice.org.uk/guidance/cg172/chapter/Key-priorities-for-implementation.

[37] Bergmann O, Bhardwaj RD, Bernard S, Zdunek S, Barnabé-Heide F, Walsh S, et al. Evidence for cardiomyocyte renewal in humans. Science (80-) 2009;324:98–102. https://doi.org/10.1126/science.1164680.

[38] Poss KD, Wilson LG, Keating MT. Heart regeneration in zebrafish. Science (80-) 2002;298:2188–90. https://doi.org/10.1126/science.1077857.

[39] Godwin JW, Debuque R, Salimova E, Rosenthal NA. Heart regeneration in the salamander relies on macrophage-mediated control of fibroblast activation and the extracellular landscape. Npj Regen Med 2017;2:22. https://doi.org/10.1038/s41536-017-0027-y.

[40] Porrello ER, Mahmoud AI, Simpson E, Johnson BA, Grinsfelder D, Canseco D, et al. Regulation of neonatal and adult mammalian heart regeneration by the miR-15 family. Proc Natl Acad Sci U S A 2013;110:187–92. https://doi.org/10.1073/pnas.1208863110.

[41] Madonna R, Van Laake LW, Davidson SM, Engel FB, Hausenloy DJ, Lecour

S, et al. Position Paper of the European Society of Cardiology Working Group Cellular Biology of the Heart: cell-based therapies for myocardial repair and regeneration in ischemic heart disease and heart failure. Eur Heart J 2016;37:1789–98.

[42] Yin VP, Lepilina A, Smith A, Poss KD. Regulation of zebrafish heart regeneration by miR-133. Dev Biol 2012;365:319–27. https://doi.org/10.1016/j.ydbio.2012.02.018.

[43] Cao W, Shi P, Ge JJ. miR-21 enhances cardiac fibrotic remodeling and fibroblast proliferation via CADM1/STAT3 pathway. BMC Cardiovasc Disord 2017;17:88. https://doi.org/10.1186/s12872-017-0520-7.

[44] Gabisonia K, Prosdocimo G, Aquaro GD, Carlucci L, Zentilin L, Secco I, et al. MicroRNA therapy stimulates uncontrolled cardiac repair after myocardial infarction in pigs. Nature 2019;569:418–22. https://doi.org/10.1038/s41586-019-1191-6.

[45] Zhao B, Tumaneng K, Guan KL. The Hippo pathway in organ size control, tissue regeneration and stem cell self-renewal. Nat Cell Biol 2011;13:877–83. https://doi.org/10.1038/ncb2303.

[46] Miesfeld JB, Link BA. Establishment of transgenic lines to monitor and manipulate Yap/Taz-Tead activity in zebrafish reveals both evolutionarily conserved and divergent functions of the Hippo pathway. Mech Dev 2014;133:177–88. https://doi.org/10.1016/j.mod.2014.02.003.

[47] Heallen T, Morikawa Y, Leach J, Tao G, Willerson JT, Johnson RL, et al. Hippo signaling impedes adult heart regeneration. Dev 2013;140:4683–90. https://doi.org/10.1242/dev.102798.

[48] Lin Z, Von Gise A, Zhou P, Gu F, Ma Q, Jiang J, et al. Cardiac-specific YAP activation improves cardiac function and survival in an experimental murine MI model. Circ Res 2014;115:354–63. https://doi.org/10.1161/CIRCRESAHA.115.303632.

[49] Hertig CM, Kubalak SW, Wang Y, Chien KR. Synergistic roles of neuregulin-1 and insulin-like growth factor-I in activation of the phosphatidylinositol 3-kinase pathway and cardiac chamber morphogenesis. J Biol Chem 1999;274:37362–9. https://doi.org/10.1074/jbc.274.52.37362.

[50] Grego-Bessa J, Luna-Zurita L, del Monte G, Bolós V, Melgar P, Arandilla A, et al. Notch Signaling Is Essential for Ventricular Chamber Development.

Dev Cell 2007;12:415–29. https://doi.org/10.1016/j.devcel.2006.12.011.

[51] Chen M, Bi LL, Wang ZQ, Zhao F, Gan XD, Wang YG. Time-dependent regulation of neuregulin-1β/ErbB/ERK pathways in cardiac differentiation of mouse embryonic stem cells. Mol Cell Biochem 2013;380:67–72. https://doi.org/10.1007/s11010-013-1658-y.

[52] Bersell K, Arab S, Haring B, Kühn B. Neuregulin1/ErbB4 Signaling Induces Cardiomyocyte Proliferation and Repair of Heart Injury. Cell 2009;138:257–70. https://doi.org/10.1016/j.cell.2009.04.060.

[53] Gemberling M, Karra R, Dickson AL, Poss KD. Nrg1 is an injury-induced cardiomyocyte mitogen for the endogenous heart regeneration program in zebrafish. Elife 2015;2015:e05871. https://doi.org/10.7554/eLife.05871.

[54] Xiang MSW, Kikuchi K. Endogenous Mechanisms of Cardiac Regeneration. Int Rev Cell Mol Biol 2016;326:67–131. https://doi.org/10.1016/bs.ircmb.2016.04.002.

[55] Doppler SA, Deutsch M-A, Lange R, Krane M. Cardiac regeneration: current therapies—future concepts. J Thorac Dis 2013;5:683.

[56] Friedman SL. Fighting Cardiac Fibrosis with CAR T Cells. N Engl J Med 2022;386:1576–8.

[57] Fan Z, Guan J. Antifibrotic therapies to control cardiac fibrosis. Biomater Res 2016;20:1–13.

[58] Leask A. Potential therapeutic targets for cardiac fibrosis: TGFβ, angiotensin, endothelin, CCN2, and PDGF, partners in fibroblast activation. Circ Res 2010;106:1675–80.

[59] Rasoul S, Carretero OA, Peng H, Cavasin MA, Zhuo J, Sanchez-Mendoza A, et al. Antifibrotic effect of Ac-SDKP and angiotensin-converting enzyme inhibition in hypertension. J Hypertens 2004;22:593–603. https://doi.org/10.1097/00004872-200403000-00023.

[60] Mnguni AT, Engel ME, Borkum MS, Mayosi BM. The Effects of Angiotensin Converting Enzyme Inhibitors (ACE-I) on human nacetyl- seryl-aspartyl-lysyl-proline (Ac-SDKP) Levels: A systematic review and meta-analysis. PLoS One 2015;10:e0143338. https://doi.org/10.1371/journal.pone.0143338.

[61] Kumar N, Yin C. The anti-inflammatory peptide Ac-SDKP: Synthesis, role in ACE inhibition, and its therapeutic potential in hypertension and

cardiovascular diseases. Pharmacol Res 2018;134:268–79. https://doi.org/10.1016/j.phrs.2018.07.006.

[62] Gao X, Xu H, Zhang B, Tao T, Liu Y, Xu D, et al. Interaction of N-acetyl-seryl-aspartyl-lysyl-proline with the angiotensin-converting enzyme 2–angiotensin-(1–7)–Mas axis attenuates pulmonary fibrosis in silicotic rats. Exp Physiol 2019;104:1562–74. https://doi.org/10.1113/EP087515.

[63] González GE, Rhaleb NE, Nakagawa P, Liao TD, Liu Y, Leung P, et al. N-acetyl-seryl-aspartyl-lysyl-proline reduces cardiac collagen cross-linking and inflammation in angiotensin II-induced hypertensive rats. Clin Sci 2014;126:85–94. https://doi.org/10.1042/CS20120619.

[64] Zhu L, Yang XP, Janic B, Rhaleb NE, Harding P, Nakagawa P, et al. Ac-SDKP suppresses TNF-α-induced ICAM-1 expression in endothelial cells via inhibition of iκB kinase and NF-κB activation. Am J Physiol - Hear Circ Physiol 2016;310:H1176–83. https://doi.org/10.1152/ajpheart.00252.2015.

[65] Zuo Y, Chun B, Potthoff SA, Kazi N, Brolin TJ, Orhan D, et al. Thymosin β4 and its degradation product, Ac-SDKP, are novel reparative factors in renal fibrosis. Kidney Int 2013;84:1166–75. https://doi.org/10.1038/ki.2013.209.

[66] Sanchez-Mas J, Lax A, Asensio-Lopez MC, Fernandez-Del Palacio MJ, Caballero L, Garrido IP, et al. Galectin-3 expression in cardiac remodeling after myocardial infarction. Int J Cardiol 2014;172:e98–101. https://doi.org/10.1016/j.ijcard.2013.12.129.

[67] Peng H, Carretero OA, Brigstock DR, Oja-Tebbe N, Rhaleb NE. Ac-SDKP Reverses Cardiac Fibrosis in Rats with Renovascular Hypertension. Hypertension 2003;42:1164–70. https://doi.org/10.1161/01.HYP.0000100423.24330.96.

[68] Conte E, Fagone E, Gili E, Fruciano M, Iemmolo M, Pistorio MP, et al. Preventive and therapeutic effects of thymosin β4 N-terminal fragment Ac-SDKP in the bleomycin model of pulmonary fibrosis. Oncotarget 2016;7:33841–54. https://doi.org/10.18632/oncotarget.8409.

[69] Nakagawa P, Romero CA, Jiang X, Ambrosio MD, Bordcoch G, Peterson EL, et al. Ac-SDKP decreases mortality and cardiac rupture after acute myocardial infarction. PLoS One 2018;13:e0190300. https://doi.org/10.1371/journal.pone.0190300.

[70] Song M, Jang H, Lee J, Kim JH, Kim SH, Sun K, et al. Regeneration of

chronic myocardial infarction by injectable hydrogels containing stem cell homing factor SDF-1 and angiogenic peptide Ac-SDKP. Biomaterials 2014;35:2436–45. https://doi.org/10.1016/j.biomaterials.2013.12.011.

[71] Srebnik HH. Formation of Heart and Great Vessels. Concepts Anat., Springer; 2002, p. 61–8. https://doi.org/10.1007/978-1-4615-0857-1_10.

[72] Kluge T, Hovig T. THE ULTRASTRUCTURE OF HUMAN AND RAT PERICARDIUM: 2. Intercellular Spaces and Junctions. Acta Pathol Microbiol Scand 1967;71:547–63. https://doi.org/10.1111/j.1699-0463.1967.tb05176.x.

[73] Ishihara T, Ferrans VJ, Jones M, Boyce SW, Kawanami O, Roberts WC. Histologic and ultrastructural features of normal human parietal pericardium. Am J Cardiol 1980;46:744–53. https://doi.org/10.1016/0002-9149(80)90424-5.

[74] Ernst S, Sanchez-Quintana D, Ho SY. Anatomy of the Pericardial Space and Mediastinum: Relevance to Epicardial Mapping and Ablation. Card Electrophysiol Clin 2010;2:1–8. https://doi.org/10.1016/j.ccep.2009.11.003.

[75] Chinchoy E, Ujhelyi MR, Hill AJ, Skadsberg ND, Iaizzo PA. The pericardium. In: Iaizzo PA, editor. Handb. Card. Anatomy, Physiol. Devices, Totowa, NJ: Humana Press; 2005, p. 101–10. https://doi.org/10.1007/978-1-59259-835-9_7.

[76] Takada K, Otsuki Y, Magari S. Lymphatics and pre-lymphatics of the rabbit pericardium and epicardium with special emphasis on particulate absorption and milky spot-like structures. Lymphology 1991;24:116–24.

[77] Michailova KN, Usunoff KG. Serosal membranes (pleura, pericardium, peritoneum). Normal structure, development and experimental pathology. vol. 183. Springer Science & Business Media; 2006.

[78] Jöbsis PD, Ashikaga H, Wen H, Rothstein EC, Horvath KA, McVeigh ER, et al. The visceral pericardium: Macromolecular structure and contribution to passive mechanical properties of the left ventricle. Am J Physiol - Hear Circ Physiol 2007;293:H3379–87. https://doi.org/10.1152/ajpheart.00967.2007.

[79] Rodriguez ER, Tan CD. Structure and Anatomy of the Human Pericardium. Prog Cardiovasc Dis 2017;59:327–40. https://doi.org/10.1016/j.pcad.2016.12.010.

[80] Hutchinson SJ. Pericardial Diseases : Clinical Diagnostic Imaging Atlas.

Elsevier Health Sciences; 2009.

[81] Czum JM, Silas AM, Althoen MC. Evaluation of the Pericardium with CT and MR. ISRN Cardiol 2014;2014:1–11. https://doi.org/10.1155/2014/174908.

[82] Choi YW, Park CS, Jeon YS, Bae IY, Choi SG, Koo JH, et al. CT Measurement of Normal Pericardial Thickness in Adults on Computed Tomography. J Korean Radiol Soc 1998;39:289. https://doi.org/10.3348/jkrs.1998.39.2.289.

[83] Bull RK, Edwards PD, Dixon AK. CT dimensions of the normal pericardium. Br J Radiol 1998;71:923–5. https://doi.org/10.1259/bjr.71.849.10195005.

[84] Sechtem U, Tscholakoff D, Higgins CB. MRI of the abnormal pericardium. Am J Roentgenol 1986;147:245–52. https://doi.org/10.2214/ajr.147.2.245.

[85] Ben-Horin S, Shinfeld A, Kachel E, Chetrit A, Livneh A. The composition of normal pericardial fluid and its implications for diagnosing pericardial effusions. Am J Med 2005;118:636–40. https://doi.org/10.1016/j.amjmed.2005.01.066.

[86] Vesely TM, Cahill DR. Cross-sectional anatomy of the pericardial sinuses, recesses, and adjacent structures. Surg Radiol Anat 1986;8:221–7. https://doi.org/10.1007/BF02425071.

[87] Vogiatzidis K, Zarogiannis SG, Aidonidis I, Solenov EI, Molyvdas PA, Gourgoulianis KI, et al. Physiology of pericardial fluid production and drainage. Front Physiol 2015;6:62. https://doi.org/10.3389/fphys.2015.00062.

[88] Sevre K. Handbook of cardiac anatomy, physiology, and devices. vol. 15. Springer Science & Business Media; 2006. https://doi.org/10.1080/08037050500369058.

[89] Yune HY, Klatte EC. Mediastinal venography. Subselective transfemoral catheterization technique. Radiology 1972;105:285–91. https://doi.org/10.1148/105.2.285.

[90] Yuan Z, Boulanger B, Flessner M, Johnston M. Relationship between pericardial pressure and lymphatic pericardial fluid transport in sheep. Microvasc Res 2000;60:28–36. https://doi.org/10.1006/mvre.2000.2239.

[91] Shabetai R. The Pericardium (Developments in Cardiovascular Medicine) 2003.

[92] D'Avila A, Neuzil P, Thiagalingam A, Gutierrez P, Aleong R, Ruskin JN, et

al. Experimental efficacy of pericardial instillation of anti-inflammatory agents during percutaneous epicardial catheter ablation to prevent postprocedure pericarditis. J Cardiovasc Electrophysiol 2007;18:1178–83. https://doi.org/10.1111/j.1540-8167.2007.00945.x.

[93] Xiang F, Guo X, Chen W, Wang J, Zhou T, Huang F, et al. Proteomics analysis of human pericardial fluid. Proteomics 2013;13:2692–5. https://doi.org/10.1002/pmic.201200317.

[94] Gomes RADS, Teodoro LDGVL, Lopes ICR, Bersanetti PA, Carmona AK, Hial V. Enzima conversora de angiotensina no líquido pericárdico: Estudo comparativo com a atividade sérica. Arq Bras Cardiol 2008;91:172–8. https://doi.org/10.1590/S0066-782X2008001500006.

[95] Mallat Z, Philip I, Lebret M, Chatel D, Maclouf J, Tedgui A. Elevated levels of 8-iso-prostaglandin F(2α) in pericardial fluid of patients with heart failure: A potential role for in vivo oxidant stress in ventricular dilatation and progression to heart failure. Circulation 1998;97:1536–9. https://doi.org/10.1161/01.CIR.97.16.1536.

[96] Benhaiem-Sigaux N, Mina E, Sigaux F, Lambré CR, Valensi F, Allégret C, et al. Characterization of human pericardial macrophages. J Leukoc Biol 1985;38:709–21. https://doi.org/10.1002/jlb.38.6.709.

[97] Bui QT, Gertz ZM, Wilensky RL. Intracoronary delivery of bone-marrow-derived stem cells. Stem Cell Res Ther 2010;1:29. https://doi.org/10.1186/scrt29.

[98] Perin EC, Silva G V, Fernandes MR, Munger T, Pandey A, Sehra R, et al. First experience with remote left ventricular mapping and transendocardial cell injection with a novel integrated magnetic navigation-guided electromechanical mapping system. EuroIntervention 2007;3:142–8.

[99] Dib N, Khawaja H, Varner S, McCarthy M, Campbell A. Cell therapy for cardiovascular disease: A comparison of methods of delivery. J Cardiovasc Transl Res 2011;4:177–81. https://doi.org/10.1007/s12265-010-9253-z.

[100] Dib N, Menasche P, Bartunek JJ, Zeiher AM, Terzic A, Chronos NA, et al. Recommendations for Successful Training on Methods of Delivery of Biologics for Cardiac Regeneration. A Report of the International Society for Cardiovascular Translational Research. JACC Cardiovasc Interv 2010;3:265–75. https://doi.org/10.1016/j.jcin.2009.12.013.

[101] Abu Arab T, Rafik R, El Etriby A. Efficacy and Safety of Local Intracoronary Drug Delivery in Treatment of No-Reflow Phenomenon: A Pilot Study. J Interv Cardiol 2016;29:496–504. https://doi.org/10.1111/joic.12318.

[102] Ayers GM, Rho TH, Ben-David J, Besch HR, Zipes DP. Amiodarone instilled into the canine pericardial sac migrates transmurally to produce electrophysiologic effects and suppress atrial fibrillation. J Cardiovasc Electrophysiol 1996;7:713–21. https://doi.org/10.1111/j.1540-8167.1996.tb00579.x.

[103] Vereckei A, Gorski JC, Ujhelyi M, Mehra R, Zipes DP. Intrapericardial ibutilide administration fails to terminate pacing-induced sustained atrial fibrillation in dogs. Cardiovasc Drugs Ther 2004;18:269–77. https://doi.org/10.1023/B:CARD.0000041246.13952.b4.

[104] Branco É, Fioretto ET, Cabral R, Palmera CAS, Gregores GB, Stopiglia AJ, et al. Homing miocárdico tras infusión intrapericárdica de células mononucleares de médula ósea. Arq Bras Cardiol 2009;93:e50–3. https://doi.org/10.1590/S0066-782X2009000900021.

[105] Rob Hermans JJ, Van Essen H, Struijker-Boudier HAJ, Johnson RM, Theeuwes F, Smits JFM. Pharmacokinetic advantage of intrapericardially applied substances in the rat. J Pharmacol Exp Ther 2002;301:672–8. https://doi.org/10.1124/jpet.301.2.672.

[106] Lerner-Tung MB, Chang AYC, Ong LS, Kreiser D. Pharmacokinetics of intrapericardial administration of 5-fluorouracil. Cancer Chemother Pharmacol 1997;40:318–20. https://doi.org/10.1007/s002800050663.

[107] Garcia JR, Campbell PF, Kumar G, Langberg JJ, Cesar L, Deppen JN, et al. Minimally Invasive Delivery of Hydrogel-Encapsulated Amiodarone to the Epicardium Reduces Atrial Fibrillation. Circ Arrhythm Electrophysiol 2018;11:e006408. https://doi.org/10.1161/CIRCEP.118.006408.

[108] Van Brakel TJ, Hermans JJR, Accord RE, Schotten U, Smits JFM, Allessie MA, et al. Effects of intrapericardial sotalol and flecainide on transmural atrial electrophysiology and atrial fibrillation. J Cardiovasc Electrophysiol 2009;20:207–15. https://doi.org/10.1111/j.1540-8167.2008.01318.x.

[109] Marcano J, Campos K, Rodriguez V, Handy K, Brewer MA, Cohn WE. Intrapericardial delivery of amiodarone rapidly achieves therapeutic levels in the atrium. Heart Surg. Forum, vol. 16, 2013, p. E279-86.

https://doi.org/10.1532/hsf98.2013188.

[110] Laham RJ, Rezaee M, Post M, Xu X, Sellke FW. Intrapericardial administration of basic fibroblast growth factor: Myocardial and tissue distribution and comparison with intracoronary and intravenous administration. Catheter Cardiovasc Interv 2003;58:375–81. https://doi.org/10.1002/ccd.10378.

[111] Fukushima S, Varela-Carver A, Coppen SR, Yamahara K, Felkin LE, Lee J, et al. Direct intramyocardial but not intracoronary injection of bone marrow cells induces ventricular arrhythmias in a rat chronic ischemic heart failure model. Circulation 2007;115:2254–61. https://doi.org/10.1161/CIRCULATIONAHA.106.662577.

[112] Miyazaki T, Zipes DP. Pericardial prostaglandin biosynthesis prevents the increased incidence of reperfusion-induced ventricular fibrillation produced by efferent sympathetic stimulation in dogs. Circulation 1990;82:1008–19. https://doi.org/10.1161/01.CIR.82.3.1008.

[113] Miyazaki T, Pride HP, Zipes DP. Prostaglandins in the pericardial fluid modulate neural regulation of cardiac electrophysiological properties. Circ Res 1990;66:163–75. https://doi.org/10.1161/01.RES.66.1.163.

[114] Miyazaki T, Pride HP, Zipes DP. Modulation of cardiac autonomic neurotransmission by epicardial superfusion. Effects of hexamethonium and tetrodotoxin. Circ Res 1989;65:1212–9. https://doi.org/10.1161/01.RES.65.5.1212.

[115] Fei L, Baron AD, Henry DP, Zipes DP. Intrapericardial delivery of L-arginine reduces the increased severity of ventricular arrhythmias during sympathetic stimulation in dogs with acute coronary occlusion: Nitric oxide modulates sympathetic effects on ventricular electrophysiological properti. Circulation 1997;96:4044–9. https://doi.org/10.1161/01.CIR.96.11.4044.

[116] Frobert A, Valentin J, Cook S, Lopes-Vicente J, Giraud MN. Cell-based therapy for heart failure in rat: Double thoracotomy for myocardial infarction and epicardial implantation of cells and biomatrix. J Vis Exp 2014:e51390. https://doi.org/10.3791/51390.

[117] Laakmann S, Fortmüller L, Piccini I, Grote-Wessels S, Schmitz W, Breves G, et al. Minimally invasive closed-chest ultrasound-guided substance delivery into the pericardial space in mice. Naunyn Schmiedebergs Arch Pharmacol

2013;386:227–38. https://doi.org/10.1007/s00210-012-0815-2.

[118] McDermott DA, Meller ST, Gebhart GF, Gutterman DD. Use of an indwelling catheter for examining cardiovascular responses to pericardial administration of bradykinin in rat. Cardiovasc Res 1995;30:39–46. https://doi.org/10.1016/S0008-6363(95)00013-5.

[119] Wang W, Mei YQ, Yuan XH, Feng XD. Clinical efficacy of epicardial application of drug-releasing hydrogels to prevent postoperative atrial fibrillation. J Thorac Cardiovasc Surg 2016;151:80–5. https://doi.org/10.1016/j.jtcvs.2015.06.061.

[120] Feng XD, Wang XN, Yuan XH, Wang W. Effectiveness of biatrial epicardial application of amiodarone-releasing adhesive hydrogel to prevent postoperative atrial fibrillation. J Thorac Cardiovasc Surg 2014;148:939–43. https://doi.org/10.1016/j.jtcvs.2014.05.049.

[121] Cannata A, Petrella D, Russo CF, Bruschi G, Fratto P, Gambacorta M, et al. Postsurgical intrapericardial adhesions: Mechanisms of formation and prevention. Ann Thorac Surg 2013;95:1818–26. https://doi.org/10.1016/j.athoracsur.2012.11.020.

[122] Becker JM, Dayton MT, Fazio VW, Beck DE, Stryker SJ, Wexner SD, et al. Prevention of postoperative abdominal adhesions by a sodium hyaluronate-based bioresorbable membrane: A prospective, randomized, double-blind multicenter study. J Am Coll Surg 1996;183:297–306.

[123] Vrijland WW, Tseng LNL, Eijkman HJM, Hop WCJ, Jakimowicz JJ, Leguit P, et al. Fewer intraperitoneal adhesions with use of hyaluronic acid-carboxymethylcellulose membrane: A randomized clinical trial. Ann Surg 2002;235:193–9. https://doi.org/10.1097/00000658-200202000-00006.

[124] Diamond MP, Bieber E, Coddington C, Franklin R, Grunert G, Gunn D, et al. Reduction of adhesions after uterine myomectomy by Seprafilm membrane (HAL-F): A blinded, prospective, randomized, multicenter clinical study. Fertil Steril 1996;66:904–10. https://doi.org/10.1016/s0015-0282(16)58716-0.

[125] Laham RJ, Rezaee M, Post M, Novicki D, Sellke FW, Pearlman JD, et al. Intrapericardial delivery of fibroblast growth factor-2 induces neovascularization in a porcine model of chronic myocardial ischemia. J Pharmacol Exp Ther 2000;292:795–802.

[126] Macris MP, Igo SR. Minimally invasive access of the normal pericardium:

Initial clinical experience with a novel device. Clin Cardiol 1999;22:36–9. https://doi.org/10.1002/clc.4960221310.

[127] Seferovic PM, Ristic AD, Maksimovic R, Petrovic P, Ostojic M, Simeunovic S, et al. Initial clinical experience with PerDUCER® device: Promising new tool in the diagnosis and treatment of pericardial disease. Clin Cardiol 1999;22:30–5. https://doi.org/10.1002/clc.4960221309.

[128] Kolettis TM, Kazakos N, Katsouras CS, Niokou D, Pappa L, Koulouras V, et al. Intrapericardial drug delivery: Pharmacologic properties and long-term safety in swine. Int J Cardiol 2005;99:415–21. https://doi.org/10.1016/j.ijcard.2004.03.004.

[129] Saksena S, Marchlinski FE. Interventional Cardiac Electrophysiology: A Multidisciplinary Approach. Cardiotext Publishing; 2014.

[130] De Carlini, Caterina C.; Maggiolini S. Pericardiocentesis in cardiac tamponade : indications and practical aspects Cardiac tamponade Effect of pericardiocentesis Indications of pericardiocentesis Contraindications Post-procedure management. E-Journal Cardiol Pract 2018;15:2018.

[131] Rupp H, Rupp TP, Alter P, Jung N, Pankuweit S, Maisch B. Intrapericardial procedures for cardiac regeneration by stem cells: Need for minimal invasive access (AttachLifter) to the normal pericardial cavity. Herz 2010;35:458–66. https://doi.org/10.1007/s00059-010-3382-7.

[132] Maisch B, Ristić AD, Seferovic PM, Spodick DH. Intrapericardial treatment of autoreactive myocarditis with triamcinolon: Successful administration in patients with minimal pericardial effusion. Herz 2000;25:781–6. https://doi.org/10.1007/PL00001997.

[133] Uchida Y, Yanagisawa-Miwa A, Nakamura F, Yamada K, Tomaru T, Kimura K, et al. Angiogenic therapy of acute myocardial infarction by intrapericardial injection of basic fibroblast growth factor and heparin sulfate: An experimental study. Am Heart J 1995;130:1182–8. https://doi.org/10.1016/0002-8703(95)90140-X.

[134] Waxman S, Moreno R, Rowe KA, Verrier RL. Persistent primary coronary dilation induced by transatrial delivery of nitroglycerin into the pericardial space: A novel approach for local cardiac drug delivery. J Am Coll Cardiol 1999;33:2073–7. https://doi.org/10.1016/S0735-1097(99)00131-X.

[135] Waxman S, Lovell EG, Verier RL. New technique for rapid, safe transvenous

access into the pericardial space: a novel approach for local cardiac drug delivery. J Am Coll Cardiol 1998;31:462. https://doi.org/10.1016/s0735-1097(98)80362-8.

[136] Kumar K, Nguyen K, Waxman S, Nearing BD, Wellenius GA, Zhao SX, et al. Potent antifibrillatory effects of intrapericardial nitroglycerin in the ischemic porcine heart. J Am Coll Cardiol 2003;41:1831–7. https://doi.org/10.1016/S0735-1097(03)00340-1.

[137] Waxman S, Pulerwitz TC, Rowe KA, Quist WC, Verrier RL. Preclinical safety testing of percutaneous transatrial access to the normal pericardial space for local cardiac drug delivery and diagnostic sampling. Catheter Cardiovasc Interv 2000;49:472–7. https://doi.org/10.1002/(SICI)1522-726X(200004)49:4<472::AID-CCD28>3.0.CO;2-Y.

[138] Pulerwitz TC, Waxman S, Rowe KA, Quist WC, Lipinska I, Verrier RL. Transatrial access to the normal pericardial space for local cardiac therapy: Preclinical safety testing with aspirin and pulmonary artery hypertension. J Interv Cardiol 2001;14:493–8. https://doi.org/10.1111/j.1540-8183.2001.tb00364.x.

[139] Verrier RL, Waxman S, Lovett EG, Moreno R. Transatrial access to the normal pericardia space: A novel approach for diagnostic sampling, pericardiocentesis, and therapeutic interventions. Circulation 1998;98:2331–3. https://doi.org/10.1161/01.CIR.98.21.2331.

[140] Koruth JS, Aryana A, Dukkipati SR, Pak HN, Kim YH, Sosa EA, et al. Unusual complications of percutaneous epicardial access and epicardial mapping and ablation of cardiac arrhythmias. Circ Arrhythmia Electrophysiol 2011;4:882–8. https://doi.org/10.1161/CIRCEP.111.965731.

[141] Lim HS, Sacher F, Cochet H, Berte B, Yamashita S, Mahida S, et al. Safety and prevention of complications during percutaneous epicardial access for the ablation of cardiac arrhythmias. Hear Rhythm 2014;11:1658–65. https://doi.org/10.1016/j.hrthm.2014.05.041.

[142] Neves D, Silva G, Morais G, Ferreira N, Carvalho M, Ribeiro VG, et al. Computed tomography-guided pericardiocentesis–A single-center experience. Rev Port Cardiol 2016;35:285–90.

[143] Sosa E, Scanavacca M. Epicardial mapping and ablation techniques to control ventricular tachycardia. J Cardiovasc Electrophysiol 2005;16:449–52.

https://doi.org/10.1046/j.1540-8167.2005.40710.x.

[144] Sosa E, Scanavacca M, D'Avila A, Pilleggi F. A New Technique to Perform Epicardial Mapping in the Electrophysiology Laboratory. J Cardiovasc Electrophysiol 1996;7:531–6. https://doi.org/10.1111/j.1540-8167.1996.tb00559.x.

[145] Laham RJ, Simons M, Hung D. Subxyphoid access of the normal pericardium: A novel drug delivery technique. Catheter Cardiovasc Interv 1999;47:109–11. https://doi.org/10.1002/(SICI)1522-726X(199905)47:1<109::AID-CCD24>3.0.CO;2-3.

[146] Tsang TSM, Freeman WK, Sinak LJ, Seward JB. Echocardiographically guided pericardiocentesis. Mayo Clin. Proc., vol. 73, Elsevier; 1998, p. 647–52. https://doi.org/10.1016/s0025-6196(11)64888-x.

[147] GARCIA-FERNANDEZ MA. Echocardiography in Pericardial Diseases. Echocardiography 1986;3:453–453. https://doi.org/10.1111/j.1540-8175.1986.tb00219.x.

[148] CALLAHAN JA, SEWARD JB, TAJIK AJ. Cardiac Tamponade: Pericardiocentesis Directed by Two-Dimensional Echocardiography. Mayo Clin. Proc., vol. 60, Elsevier; 1985, p. 344–7. https://doi.org/10.1016/S0025-6196(12)60541-2.

[149] Maggiolini S, Gentile G, Farina A, De Carlini CC, Lenatti L, Meles E, et al. Safety, Efficacy, and Complications of Pericardiocentesis by Real-Time Echo-Monitored Procedure. Am J Cardiol 2016;117:1369–74. https://doi.org/10.1016/j.amjcard.2016.01.043.

[150] Lakhter V, Aggarwal V, Bashir R, O'Murchu B, Cohen HA, O'Neill BP. Pericardiocentesis under Continuous Ultrasonographic Guidance Using a 7 cm Micropuncture Needle. J Invasive Cardiol 2016;28:397–402.

[151] Melvan JN, Madden D, Vasquez JC, DeLaRosa J. Computed Tomography-guided Pericardiocentesis: An alternative approach for accessing the pericardium. Hear Lung Circ 2016;25:725–8. https://doi.org/10.1016/j.hlc.2016.01.004.

[152] Syed F, Slaughter R, Tjahjadi C, Hansen M, Raffel O. Computed Tomography Guided Pericardiocentesis in Adults: A Single Centre Experience of 44 Procedures. Hear Lung Circ 2011;20:S165. https://doi.org/10.1016/j.hlc.2011.05.411.

[153] Hoey ETD, Mankad K. Computed tomography-guided pericardiocentesis: utility in the management of malignant pericardial effusion. Am J Emerg Med 2010;28:388.e1-388.e3. https://doi.org/10.1016/j.ajem.2009.07.015.

[154] Maisch B, Bethge C, Drude L, Hufnagel G, Herzum M, Schonian U. Pericardioscopy and epicardial biopsy new diagnostic tools in pericardial and perimyocardial disease. Eur Heart J 1994;15:68–73. https://doi.org/10.1093/eurheartj/15.suppl_c.68.

[155] Maisch B, Ristić AD, Rupp H, Spodick DH. Pericardial access using the PerDUCER and flexible percutaneous pericardioscopy. Am J Cardiol 2001;88:1323–6. https://doi.org/10.1016/S0002-9149(01)02101-4.

[156] Richardson ES, Rolfes C, Woo OS, Elmquist WF, Benditt DG, Iaizzo PA. Cardiac responses to the intrapericardial delivery of metoprolol: Targeted delivery compared to intravenous administration. J Cardiovasc Transl Res 2012;5:535–40. https://doi.org/10.1007/s12265-011-9315-x.

[157] Moreno R, Waxman S, Rowe K, Verrier RL. Intrapericardial β-adrenergic blockade with esmolol exerts a potent antitachycardic effect without depressing contractility. J Cardiovasc Pharmacol 2000;36:722–7. https://doi.org/10.1097/00005344-200012000-00006.

[158] Van Brakel TJ, Hermans JJR, Janssen BJ, Van Essen H, Botterhuis N, Smits JFM, et al. Intrapericardial delivery enhances cardiac effects of sotalol and atenolol. J Cardiovasc Pharmacol 2004;44:50–6. https://doi.org/10.1097/00005344-200407000-00007.

[159] Maslov MY, Edelman ER, Pezone MJ, Wei AE, Wakim MG, Murray MR, et al. Myocardial drug distribution generated from local epicardial application: Potential impact of cardiac capillary perfusion in a swine model using epinephrine. J Control Release 2014;194:257–65. https://doi.org/10.1016/j.jconrel.2014.09.012.

[160] Lovich MA, Wei AE, Maslov MY, Wu PI, Edelman ER. Local epicardial inotropic drug delivery allows targeted pharmacologic intervention with preservation of myocardial loading conditions. J Pharm Sci 2011;100:4993–5006. https://doi.org/10.1002/jps.22681.

[161] Maslov MY, Edelman ER, Wei AE, Pezone MJ, Lovich MA. High concentrations of drug in target tissues following local controlled release are utilized for both drug distribution and biologic effect: An example with

epicardial inotropic drug delivery. J Control Release 2013;171:201–7. https://doi.org/10.1016/j.jconrel.2013.06.038.

[162] Lovich MA, Edelman ER. Mechanisms of transmural heparin transport in the rat abdominal aorta after local vascular delivery. Circ Res 1995;77:1143–50. https://doi.org/10.1161/01.RES.77.6.1143.

[163] Le KN, Hwang CW, Tzafriri AR, Lovich MA, Hayward A, Edelman ER. Vascular regeneration by local growth factor release is self-limited by microvascular clearance. Circulation 2009;119:2928–35. https://doi.org/10.1161/CIRCULATIONAHA.108.823609.

[164] Hollenberg M, Dougherty J. Lymph flow and 131I-albumin resorption from pericardial effusions in man. Am J Cardiol 1969;24:514–22. https://doi.org/10.1016/0002-9149(69)90494-9.

[165] Szokodi I, Horkay F, Kiss P, Selmeci L, Merkely B, Kékesi V, et al. Characterization and stimuli for production of pericardial, fluid atrial natriuretic peptide in dogs. Life Sci 1997;61:1349–59. https://doi.org/10.1016/S0024-3205(97)00680-2.

[166] Lehtonen LA, Antila S, Pentikäinen PJ. Pharmacokinetics and Pharmacodynamics of Intravenous Inotropic Agents. Clin Pharmacokinet 2004;43:187–203. https://doi.org/10.2165/00003088-200443030-00003.

[167] Blázquez R, Sánchez-Margallo FM, Crisóstomo V, Báez C, Maestre J, Álvarez V, et al. Intrapericardial delivery of cardiosphere-derived cells: An immunological study in a clinically relevant large animal model. PLoS One 2016;11:e0149001. https://doi.org/10.1371/journal.pone.0149001.

[168] Xiao YF, Sigg DC, Ujhelyi MR, Wilhelm JJ, Richardson ES, Iaizzo PA. Pericardial delivery of omega-3 fatty acid: A novel approach to reducing myocardial infarct sizes and arrhythmias. Am J Physiol - Hear Circ Physiol 2008;294:H2212–8. https://doi.org/10.1152/ajpheart.91502.2007.

[169] Matthews KG, Devlin GP, Stuart SP, Jensen JA, Doughty RN, Conaglen J V., et al. Intrapericardial IGF-I improves cardiac function in an ovine model of chronic heart failure. Hear Lung Circ 2005;14:98–103. https://doi.org/10.1016/j.hlc.2005.02.002.

[170] Li X, Mikrani R, Li C, Naveed M, Liu Z, Abbas M, et al. An epicardial delivery of nitroglycerine by active hydraulic ventricular support drug delivery system improves cardiac function in a rat model. Drug Deliv Transl

Res 2020;10:23–33. https://doi.org/10.1007/s13346-019-00656-9.

[171] Hagberg RC, Safi HJ, Sabik J, Conte J, Block JE. Improved intraoperative management of anastomotic bleeding during aortic reconstruction: Results of a randomized controlled trial. Am Surg 2004;70:307–11.

[172] Liechty WB, Scheuerle RL, Vela Ramirez JE, Peppas NA. Uptake and function of membrane-destabilizing cationic nanogels for intracellular drug delivery. Bioeng Transl Med 2019;4:17–29. https://doi.org/10.1002/btm2.10120.

[173] Ryu JH, Hong S, Lee H. Bio-inspired adhesive catechol-conjugated chitosan for biomedical applications: A mini review. Acta Biomater 2015;27:101–15. https://doi.org/10.1016/j.actbio.2015.08.043.

[174] Jiang T, Deng M, James R, Nair LS, Laurencin CT. Micro- and nanofabrication of chitosan structures for regenerative engineering. Acta Biomater 2014;10:1632–45. https://doi.org/10.1016/j.actbio.2013.07.003.

[175] Hu KJ, Hu JL, Ho KP, Yeung KW. Screening of fungi for chitosan producers, and copper adsorption capacity of fungal chitosan and chitosanaceous materials. Carbohydr Polym 2004;58:45–52. https://doi.org/10.1016/j.carbpol.2004.06.015.

[176] Bellich B, D'Agostino I, Semeraro S, Gamini A, Cesàro A. "The good, the bad and the ugly" of chitosans. Mar Drugs 2016;14:99. https://doi.org/10.3390/md14050099.

[177] Wang H, Qian J, Ding F. Recent advances in engineered chitosan-based nanogels for biomedical applications. J Mater Chem B 2017;5:6986–7007. https://doi.org/10.1039/c7tb01624g.

[178] Pereira P, Pedrosa SS, Correia A, Lima CF, Olmedo MP, González-Fernández Á, et al. Biocompatibility of a self-assembled glycol chitosan nanogel. Toxicol Vitr 2015;29:638–46. https://doi.org/10.1016/j.tiv.2014.11.004.

[179] Zhaveh S, Mohsenifar A, Beiki M, Khalili ST, Abdollahi A, Rahmani-Cherati T, et al. Encapsulation of Cuminum cyminum essential oils in chitosan-caffeic acid nanogel with enhanced antimicrobial activity against Aspergillus flavus. Ind Crops Prod 2015;69:251–6. https://doi.org/10.1016/j.indcrop.2015.02.028.

[180] Lee J, Lee C, Kim TH, Lee ES, Shin BS, Chi SC, et al. Self-assembled glycol chitosan nanogels containing palmityl-acylated exendin-4 peptide as a long-acting anti-diabetic inhalation system. J Control Release 2012;161:728–34.

https://doi.org/10.1016/j.jconrel.2012.05.029.

[181] Arteche Pujana M, Pérez-Álvarez L, Cesteros Iturbe LC, Katime I. Biodegradable chitosan nanogels crosslinked with genipin. Carbohydr Polym 2013;94:836–42. https://doi.org/10.1016/j.carbpol.2013.01.082.

[182] Pujana MA, Pérez-Álvarez L, Iturbe LCC, Katime I. Water soluble folate-chitosan nanogels crosslinked by genipin. Carbohydr Polym 2014;101:113–20. https://doi.org/10.1016/j.carbpol.2013.09.014.

[183] Arteche Pujana M, Perez-Alvarez L, Cesteros Iturbe LC, Katime I. PH-sensitive chitosan-folate nanogels crosslinked with biocompatible dicarboxylic acids. Eur Polym J 2014;61:215–25. https://doi.org/10.1016/j.eurpolymj.2014.10.007.

[184] Lanzalaco S, Armelin E. Poly(N-isopropylacrylamide) and copolymers: A review on recent progresses in biomedical applications. Gels 2017;3:36. https://doi.org/10.3390/gels3040036.

[185] Duan C, Zhang D, Wang F, Zheng D, Jia L, Feng F, et al. Chitosan-g-poly(N-isopropylacrylamide) based nanogels for tumor extracellular targeting. Int J Pharm 2011;409:252–9. https://doi.org/10.1016/j.ijpharm.2011.02.050.

[186] Shen X, Zhang L, Jiang X, Hu Y, Guo J. Reversible surface switching of nanogel triggered by external stimuli. Angew Chemie - Int Ed 2007;46:7104–7. https://doi.org/10.1002/anie.200701368.

[187] Ahirrao SP, Gide PS, Shrivastav B, Sharma P. Ionotropic Gelation: A Promising Cross Linking Technique for Hydrogels. Res Rev J Pharm Nanotechnol 2014;2:1–6.

[188] Parhi R. Cross-linked hydrogel for pharmaceutical applications: A review. Adv Pharm Bull 2017;7:515–30. https://doi.org/10.15171/apb.2017.064.

[189] Chen Y, Ballard N, Bon SAF. Waterborne polymer nanogels non-covalently crosslinked by multiple hydrogen bond arrays. Polym Chem 2013;4:387–92. https://doi.org/10.1039/c2py20615c.

[190] Ding F, Mou Q, Ma Y, Pan G, Guo Y, Tong G, et al. A Crosslinked Nucleic Acid Nanogel for Effective siRNA Delivery and Antitumor Therapy. Angew Chemie - Int Ed 2018;57:3064–8. https://doi.org/10.1002/anie.201711242.

[191] Mi FL, Shyu SS, Peng CK. Characterization of ring-opening polymerization of genipin and pH-dependent cross-linking reactions between chitosan and genipin. J Polym Sci Part A Polym Chem 2005;43:1985–2000.

https://doi.org/10.1002/pola.20669.

[192] Rinaudo M. New way to crosslink chitosan in aqueous solution. Eur Polym J 2010;46:1537–44. https://doi.org/10.1016/j.eurpolymj.2010.04.012.

[193] Sacco P, Furlani F, de Marzo G, Marsich E, Paoletti S, Donati I. Concepts for Developing Physical Gels of Chitosan and of Chitosan Derivatives. Gels 2018;4:67. https://doi.org/10.3390/gels4030067.

[194] Vina-Vilaseca A, Bender-Sigel J, Sorkina T, Closs EI, Sorkin A. Protein kinase C-dependent ubiquitination and clathrin-mediated endocytosis of the cationic amino acid transporter CAT-1. J Biol Chem 2011;286:8697–706. https://doi.org/10.1074/jbc.M110.186858.

[195] Kovács T, Kárász A, Szöllosi J, Nagy P. The density of GM1-enriched lipid rafts correlates inversely with the efficiency of transfection mediated by cationic liposomes. Cytom Part A 2009;75:650–7. https://doi.org/10.1002/cyto.a.20756.

[196] Ho HMK, Craig DQM, Day RM. Design of Experiment Approach to Modeling the Effects of Formulation and Drug Loading on the Structure and Properties of Therapeutic Nanogels. Mol Pharm 2022;19:602–15. https://doi.org/10.1021/acs.molpharmaceut.1c00699.

[197] Whiteley Z, Ho HMK, Gan YX, Panariello L, Gkogkos G, Gavriilidis A, et al. Microfluidic synthesis of protein-loaded nanogels in a coaxial flow reactor using a design of experiments approach. Nanoscale Adv 2021;3:2039–55. https://doi.org/10.1039/d0na01051k.

[198] Schütz CA, Juillerat-Jeanneret L, Käuper P, Wandrey C. Cell response to the exposure to chitosan-TPP//alginate nanogels. Biomacromolecules 2011;12:4153–61. https://doi.org/10.1021/bm201231x.

[199] Huang Y, Lapitsky Y. Salt-assisted mechanistic analysis of chitosan/tripolyphosphate micro- and nanogel formation. Biomacromolecules 2012;13:3868–76. https://doi.org/10.1021/bm3014236.

[200] Ashrafi H, Azadi A. Chitosan-based hydrogel nanoparticle amazing behaviors during transmission electron microscopy. Int J Biol Macromol 2016;84:31–4. https://doi.org/10.1016/j.ijbiomac.2015.11.089.

[201] Azadi A, Hamidi M, Khoshayand MR, Amini M, Rouini MR. Preparation and optimization of surface-treated methotrexate-loaded nanogels intended for brain delivery. Carbohydr Polym 2012;90:462–71.

https://doi.org/10.1016/j.carbpol.2012.05.066.

[202] Azadi A, Rouini MR, Hamidi M. Neuropharmacokinetic evaluation of methotrexate-loaded chitosan nanogels. Int J Biol Macromol 2015;79:326–35. https://doi.org/10.1016/j.ijbiomac.2015.05.001.

[203] Debache K, Kropf C, Schütz CA, Harwood LJ, Käuper P, Monney T, et al. Vaccination of mice with chitosan nanogel-associated recombinant NcPDI against challenge infection with Neospora caninum tachyzoites. Parasite Immunol 2011;33:81–94. https://doi.org/10.1111/j.1365-3024.2010.01255.x.

[204] Harisa GI, Badran MM, AlQahtani SA, Alanazi FK, Attia SM. Pravastatin chitosan nanogels-loaded erythrocytes as a new delivery strategy for targeting liver cancer. Saudi Pharm J 2016;24:74–81. https://doi.org/10.1016/j.jsps.2015.03.024.

[205] McCullough KC, Bassi I, Milona P, Suter R, Thomann-Harwood L, Englezou P, et al. Self-Replicating replicon-rna delivery to dendritic cells by chitosan-Nanoparticles for translation in vitro and in vivo. Mol Ther - Nucleic Acids 2014;3:e173. https://doi.org/10.1038/mtna.2014.24.

[206] Schmitt F, Lagopoulos L, Käuper P, Rossi N, Busso N, Barge J, et al. Chitosan-based nanogels for selective delivery of photosensitizers to macrophages and improved retention in and therapy of articular joints. J Control Release 2010;144:242–50. https://doi.org/10.1016/j.jconrel.2010.02.008.

[207] Buschmann MD, Merzouki A, Lavertu M, Thibault M, Jean M, Darras V. Chitosans for delivery of nucleic acids. Adv Drug Deliv Rev 2013;65:1234–70. https://doi.org/10.1016/j.addr.2013.07.005.

[208] Al-Kassas R, Wen J, Cheng AEM, Kim AMJ, Liu SSM, Yu J. Transdermal delivery of propranolol hydrochloride through chitosan nanoparticles dispersed in mucoadhesive gel. Carbohydr Polym 2016;153:176–86. https://doi.org/10.1016/j.carbpol.2016.06.096.

[209] Goycoolea FM, Lollo G, Remuñán-López C, Quaglia F, Alonso MJ. Chitosan-alginate blended nanoparticles as carriers for the transmucosal delivery of macromolecules. Biomacromolecules 2009;10:1736–43. https://doi.org/10.1021/bm9001377.

[210] Halász G, Gyüre B, Jánosi IM, Szabó KG, Tél T. Vortex flow generated by a magnetic stirrer. Am J Phys 2007;75:1092–8.

https://doi.org/10.1119/1.2772287.

[211] Acheson DJ. Elementary Fluid Dynamics. J Acoust Soc Am 1991;89:3020–3020. https://doi.org/10.1121/1.400751.

[212] Katopodes ND. Vorticity Dynamics. In: Katopodes NDBT-F-SF, editor. Free. Flow, Butterworth-Heinemann; 2019, p. 516–65. https://doi.org/10.1016/b978-0-12-815489-2.00007-1.

[213] Kamat V, Bodas D, Paknikar K. Chitosan nanoparticles synthesis caught in action using microdroplet reactions. Sci Rep 2016;6:1–4.

[214] Lavertu M, Xia Z, Serreqi AN, Berrada M, Rodrigues A, Wang D, et al. A validated 1H NMR method for the determination of the degree of deacetylation of chitosan. J Pharm Biomed Anal 2003;32:1149–58. https://doi.org/10.1016/S0731-7085(03)00155-9.

[215] Yeh JT, Chen CL, Huang KS, Nien YH, Chen JL, Huang PZ. Synthesis, characterization, and application of PVP/chitosan blended polymers. J Appl Polym Sci 2006;101:885–91. https://doi.org/10.1002/app.23517.

[216] Gedam AH, Dongre RS. Adsorption characterization of Pb(ii) ions onto iodate doped chitosan composite: equilibrium and kinetic studies. RSC Adv 2015;5:54188–201. https://doi.org/10.1039/c5ra09899h.

[217] Fernandes JBM, Celestino MT, Tavares MIB, Freitas ZMF, Dos Santos EP, Júnior ER, et al. The development and characterization of propranolol tablets using tapioca starch as excipient. An Acad Bras Cienc 2019;91. https://doi.org/10.1590/0001-3765201920180094.

[218] Queiroz MF, Melo KRT, Sabry DA, Sassaki GL, Rocha HAO. Does the use of chitosan contribute to oxalate kidney stone formation? Mar Drugs 2015;13:141–58. https://doi.org/10.3390/md13010141.

[219] Vino AB, Ramasamy P, Shanmugam V, Shanmugam A. Extraction, characterization and in vitro antioxidative potential of chitosan and sulfated chitosan from Cuttlebone of Sepia aculeata Orbigny, 1848. Asian Pac J Trop Biomed 2012;2:S334–41. https://doi.org/10.1016/S2221-1691(12)60184-1.

[220] Chaturvedi K, Umadevi S, Vaghani S. Floating matrix dosage form for propranolol hydrochloride based on gas formation technique: Development and in vitro evaluation. Sci Pharm 2010;78:927–39. https://doi.org/10.3797/scipharm.0909-02.

[221] Loutfy SA, Salaheldin TA, Ramadan MA, Farroh KY, Abdallah ZF, Eloahed

TYA. Synthesis, characterization and cytotoxic evaluation of graphene oxide nanosheets: In vitro liver cancer model. Asian Pacific J Cancer Prev 2017;18:955–61. https://doi.org/10.22034/APJCP.2017.18.4.955.

[222] Kumar S, Dutta PK, Koh J. A physico-chemical and biological study of novel chitosan-chloroquinoline derivative for biomedical applications. Int J Biol Macromol 2011;49:356–61. https://doi.org/10.1016/j.ijbiomac.2011.05.017.

[223] Kumar S, Koh J. Physiochemical and optical study of chitosan-terephthaldehyde derivative for biomedical applications. Int J Biol Macromol 2012;51:1167–72. https://doi.org/10.1016/j.ijbiomac.2012.09.001.

[224] Faham S, Watanabe A, Besserer GM, Cascio D, Specht A, Hirayama BA, et al. The crystal structure of a sodium galactose transporter reveals mechanistic insights into Na+/sugar symport. Science (80-) 2008;321:810–4. https://doi.org/10.1126/science.1160406.

[225] Sadeghi F, Fayazi A. Analysis of crystalline structure of sodium tripolyphosphate: Effect of pH of solution and calcination conditions. Ind Eng Chem Res 2012;51:1093–8. https://doi.org/10.1021/ie202064e.

[226] Ali MEA, Aboelfadl MMS, Selim AM, Khalil HF, Elkady GM. Chitosan nanoparticles extracted from shrimp shells, application for removal of Fe(II) and Mn(II) from aqueous phases. Sep Sci Technol 2018;53:2870–81. https://doi.org/10.1080/01496395.2018.1489845.

[227] Sivakami MS, Gomathi T, Venkatesan J, Jeong HS, Kim SK, Sudha PN. Preparation and characterization of nano chitosan for treatment wastewaters. Int J Biol Macromol 2013;57:204–12. https://doi.org/10.1016/j.ijbiomac.2013.03.005.

[228] Vaezifar S, Razavi S, Golozar MA, Karbasi S, Morshed M, Kamali M. Effects of Some Parameters on Particle Size Distribution of Chitosan Nanoparticles Prepared by Ionic Gelation Method. J Clust Sci 2013;24:891–903. https://doi.org/10.1007/s10876-013-0583-2.

[229] de Alvarenga ES, Pereira de Oliveira C, Roberto Bellato C. An approach to understanding the deacetylation degree of chitosan. Carbohydr Polym 2010;80:1155–60. https://doi.org/10.1016/j.carbpol.2010.01.037.

[230] Vårum KM, Antohonsen MW, Grasdalen H, Smidsrød O. Determination of the degree of N-acetylation and the distribution of N-acetyl groups in partially N-deacetylated chitins (chitosans) by high-field n.m.r. spectroscopy.

Carbohydr Res 1991;211:17–23. https://doi.org/10.1016/0008-6215(91)84142-2.

[231] Hirai A, Odani H, Nakajima A. Determination of degree of deacetylation of chitosan by 1H NMR spectroscopy. Polym Bull 1991;26:87–94. https://doi.org/10.1007/BF00299352.

[232] Watt RP, Khatri H, Dibble ARG. Injectability as a function of viscosity and dosing materials for subcutaneous administration. Int J Pharm 2019;554:376–86. https://doi.org/10.1016/j.ijpharm.2018.11.012.

[233] Kou L, Sun J, Zhai Y, He Z. The endocytosis and intracellular fate of nanomedicines: Implication for rational design. Asian J Pharm Sci 2013;8:1–10. https://doi.org/10.1016/j.ajps.2013.07.001.

[234] Benmerah A, Lamaze C. Clathrin-coated pits: vive la difference? Traffic 2007;8:970–82.

[235] Tang J, Li L, Howard CB, Mahler SM, Huang L, Xu ZP. Preparation of optimized lipid-coated calcium phosphate nanoparticles for enhanced in vitro gene delivery to breast cancer cells. J Mater Chem B 2015;3:6805–12. https://doi.org/10.1039/c5tb00912j.

[236] Huang M, Ma Z, Khor E, Lim LY. Uptake of FITC-chitosan nanoparticles by A549 cells. Pharm Res 2002;19:1488–94. https://doi.org/10.1023/A:1020404615898.

[237] Ma Z, Lim LY. Uptake of Chitosan and Associated Insulin in Caco-2 Cell Monolayers: A Comparison between Chitosan Molecules and Chitosan Nanoparticles. Pharm Res 2003;20:1812–9. https://doi.org/10.1023/B:PHAM.0000003379.76417.3e.

[238] Vicario-De-la-torre M, Forcada J. The potential of stimuli-responsive nanogels in drug and active molecule delivery for targeted therapy. Gels 2017;3:16. https://doi.org/10.3390/gels3020016.

[239] Instruments M. Zeta potential: An Introduction in 30 minutes. Zetasizer Nano Serles Tech Note MRK654-01 2011;2:1–6.

[240] Chandrasekaran B, Abed SN, Al-Attraqchi O, Kuche K, Tekade RK. Computer-Aided Prediction of Pharmacokinetic (ADMET) Properties. Dos. Form Des. Parameters, vol. 2, Elsevier; 2018, p. 731–55. https://doi.org/10.1016/B978-0-12-814421-3.00021-X.

[241] Roy K, Kar S, Das RN. Chemical Information and Descriptors. In: Roy K,

Kar S, Das RNBT-U the B of Q for A in PS and RA, editors. Underst. Basics QSAR Appl. Pharm. Sci. Risk Assess., Boston: Academic Press; 2015, p. 47–80. https://doi.org/10.1016/b978-0-12-801505-6.00002-8.

[242] Yap CW. PaDEL-descriptor: An open source software to calculate molecular descriptors and fingerprints. J Comput Chem 2011;32:1466–74. https://doi.org/10.1002/jcc.21707.

[243] Moriwaki H, Tian YS, Kawashita N, Takagi T. Mordred: A molecular descriptor calculator. J Cheminform 2018;10:4. https://doi.org/10.1186/s13321-018-0258-y.

[244] Steinbeck C, Han Y, Kuhn S, Horlacher O, Luttmann E, Willighagen E. The Chemistry Development Kit (CDK): An open-source Java library for chemo- and bioinformatics. J Chem Inf Comput Sci 2003;43:493–500. https://doi.org/10.1021/ci025584y.

[245] Mauri A, Consonni V, Pavan M, Todeschini R. DRAGON software: An easy approach to molecular descriptor calculations. Match 2006;56:237–48.

[246] Landrum G. RDKit: Open-source cheminformatics 2006. https://www.rdkit.org/.

[247] Harrington EC. The desirability function. Ind Qual Control 1965;21:494–8.

[248] Derringer G, Suich R. Simultaneous Optimization of Several Response Variables. J Qual Technol 1980;12:214–9. https://doi.org/10.1080/00224065.1980.11980968.

[249] Gao L, Wan AJ. Preparation of probucol loaded chitosan nanoparticles and in vitro release study. Chinese J New Drugs 2009;18:1892–6.

[250] Bera B. Nanoporous Silicon Prepared by Vapour Phase Strain Etch and Sacrificial Technique. Int J Comput Appl 2015;Micro:42–5.

[251] Hosseinzadeh H, Atyabi F, Dinarvand R, Ostad SN. Chitosan-Pluronic nanoparticles as oral delivery of anticancer gemcitabine: Preparation and in vitro study. Int J Nanomedicine 2012;7:1851–63. https://doi.org/10.2147/IJN.S26365.

[252] Gan Q, Wang T. Chitosan nanoparticle as protein delivery carrier-Systematic examination of fabrication conditions for efficient loading and release. Colloids Surfaces B Biointerfaces 2007;59:24–34. https://doi.org/10.1016/j.colsurfb.2007.04.009.

[253] Mohanraj VJ, Chen Y. Nanoparticles-a review. Trop J Pharm Res

2006;5:561–73.

[254] Srivastava G, Walke S, Dhavale D, Gade W, Doshi J, Kumar R, et al. Tartrate/tripolyphosphate as co-crosslinker for water soluble chitosan used in protein antigens encapsulation. Int J Biol Macromol 2016;91:381–93. https://doi.org/10.1016/j.ijbiomac.2016.05.099.

[255] Rouvray DH, King RB. Topology in chemistry : discrete mathematics of molecules. Elsevier Science; 2002.

[256] Hussain Z, Sahudin S. Preparation, characterisation and colloidal stability of chitosan-tripolyphosphate nanoparticles: Optimisation of formulation and process parameters. Int J Pharm Pharm Sci 2016;8:297–308.

[257] Sacco P, Paoletti S, Cok M, Asaro F, Abrami M, Grassi M, et al. Insight into the ionotropic gelation of chitosan using tripolyphosphate and pyrophosphate as cross-linkers. Int J Biol Macromol 2016;92:476–83. https://doi.org/10.1016/j.ijbiomac.2016.07.056.

[258] Cai Y, Lapitsky Y. Formation and dissolution of chitosan/pyrophosphate nanoparticles: is the ionic crosslinking of chitosan reversible? Colloids Surfaces B Biointerfaces 2014;115:100–8.

[259] ISO ISO. ISO 10993-5:2009 (2009): Biological evaluation of medical devices—Part 5: Tests for in vitro cytotoxicity; German version EN ISO 10993-5:2009. Int Organ Stand Geneva 2009.

[260] Witek P, Korga A, Burdan F, Ostrowska M, Nosowska B, Iwan M, et al. The effect of a number of H9C2 rat cardiomyocytes passage on repeatability of cytotoxicity study results. Cytotechnology 2016;68:2407–15. https://doi.org/10.1007/s10616-016-9957-2.

[261] Wada AM, Smith TK, Osler ME, Reese DE, Bader DM. Epicardial/mesothelial cell line retains vasculogenic potential of embryonic epicardium. Circ Res 2003;92:525–31. https://doi.org/10.1161/01.RES.0000060484.11032.0B.

[262] Eid H, Larson DM, Springhorn JP, Attawia MA, Nayak RC, Smith TW, et al. Role of epicardial mesothelial cells in the modification of phenotype and function of adult rat ventricular myocytes in primary coculture. Circ Res 1992;71:40–50. https://doi.org/10.1161/01.RES.71.1.40.

[263] Boncler M, Rózalski M, Krajewska U, Podswdek A, Watala C. Comparison of PrestoBlue and MTT assays of cellular viability in the assessment of anti-

proliferative effects of plant extracts on human endothelial cells. J Pharmacol Toxicol Methods 2014;69:9–16. https://doi.org/10.1016/j.vascn.2013.09.003.

[264] Ma Z, Hu Y, Jiang G, Hou J, Liu R, Lu Y, et al. Spontaneous generation of germline characteristics in mouse fibrosarcoma cells. Sci Rep 2012;2:1–10. https://doi.org/10.1038/srep00743.

[265] Sukhatme V, Bouche G, Meheus L, Sukhatme VP, Pantziarka P. Repurposing Drugs in Oncology (ReDO) - Nitroglycerin as an anti-cancer agent. Ecancermedicalscience 2015;9. https://doi.org/10.3332/ecancer.2015.568.

[266] Wei WJ, Shen CT, Song HJ, Qiu ZL, Luo QY. Propranolol sensitizes thyroid cancer cells to cytotoxic effect of vemurafenib. Oncol Rep 2016;36:1576–84. https://doi.org/10.3892/or.2016.4918.

[267] Bota M, Fischer-Fodor E, Bochiș O, Cenariu M, Popa G, Blag C, et al. Combined effect of propranolol, vincristine and bevacizumab on HUVECs and BJ cells. Exp Ther Med 2018;17:307–15. https://doi.org/10.3892/etm.2018.6925.

[268] Ezan E, Carde P, Le Kerneau J, Ardouin T, Thomas F, Isnard F, et al. Pharmacokinetics in healthy volunteers and patients of NAc-SDKP (seraspenide), a negative regulator of hematopoiesis. Drug Metab Dispos 1994;22:843–8.

[269] INNOVAGEN. {PepCalc}.com - {Peptide} calculator. Https://PepcalcCom/ 2015:2019-09–10. https://pepcalc.com/ (accessed November 11, 2021).

[270] Junot C, Theodoro F, Thierry J, Clement G, Wdzieczak-Bakala J, Ezan E. Development of an enzyme immunoassay for a stable amidated analog of the hemoregulatory peptide Acetyl-Ser-Asp-Lys-Pro. J Immunoass Immunochem 2001;22:15–31. https://doi.org/10.1081/IAS-100102895.

[271] Pradelles P, Frobert Y, Créminon C, Liozon E, Massé A, Frindel E. Negative regulator of pluripotent hematopoietic stem cell proliferation in human white blood cells and plasma as analysed by enzyme immunoassay. Biochem Biophys Res Commun 1990;170:986–93. https://doi.org/10.1016/0006-291X(90)90489-A.

[272] Inoue K, Ikemura A, Tsuruta Y, Tsutsumiuchi K, Hino T, Oka H. On-line solid-phase extraction LC-MS/MS for the determination of Ac-SDKP peptide in human plasma from hemodialysis patients. Biomed Chromatogr 2012;26:137–41. https://doi.org/10.1002/bmc.1636.

[273] Mesmin C, Cholet S, Blanchard A, Chambon Y, Azizi M, Ezan E. Mass spectrometric quantification of AcSDKP-NH 2 in human plasma and urine and comparison with an immunoassay. Rapid Commun Mass Spectrom 2012;26:163–72. https://doi.org/10.1002/rcm.5326.

[274] Inoue K, Ikemura A, Tsuruta Y, Watanabe K, Tsutsumiuchi K, Hino T, et al. Quantification of N-acetyl-seryl-aspartyl-lysyl-proline in hemodialysis patients administered angiotensin-converting enzyme inhibitors by stable isotope dilution liquid chromatography-tandem mass spectrometry. J Pharm Biomed Anal 2011;54:765–71. https://doi.org/10.1016/j.jpba.2010.10.009.

[275] Junot C, Pruvost A, Créminon C, Grognet JM, Benech H, Ezan E. Characterization of immunoreactive acetyl-Ser-Asp-Lys-Pro in human plasma and urine by liquid chromatography-electrospray mass spectrometry. J Chromatogr B Biomed Sci Appl 2001;752:69–75. https://doi.org/10.1016/S0378-4347(00)00520-X.

[276] Sharma U, Rhaleb NE, Pokharel S, Harding P, Rasoul S, Peng H, et al. Novel anti-inflammatory mechanisms of N-Acetyl-Ser-Asp-Lys-Pro in hypertension-induced target organ damage. Am J Physiol - Hear Circ Physiol 2008;294:H1226–32. https://doi.org/10.1152/ajpheart.00305.2007.

[277] Singh H, Khurana LK, Singh R. Pharmaceutical Development. Pharm Med Transl Clin Res 2017:33–46. https://doi.org/10.1016/B978-0-12-802103-3.00003-1.

[278] Elder D, Teasdale A. ICH Q9 Quality Risk Management. ICH Qual Guidel 2017:579–610. https://doi.org/10.1002/9781118971147.ch21.

[279] Pogány J. ICH pharmaceutical quality system Q10. WHO Drug Inf 2008;22:177–81.

[280] Raman NVVSS, Mallu UR, Bapatu HR. Analytical Quality by Design Approach to Test Method Development and Validation in Drug Substance Manufacturing. J Chem 2015;2015. https://doi.org/10.1155/2015/435129.

[281] Peraman R, Bhadraya K, Padmanabha Reddy Y. Analytical quality by design: A tool for regulatory flexibility and robust analytics. Int J Anal Chem 2015;2015. https://doi.org/10.1155/2015/868727.

[282] Lloyd DK, Bergum J. Application of quality by design (QbD) to the development and validation of analytical methods. Specif Drug Subst Prod Dev Valid Anal Methods 2013;405:29–72. https://doi.org/10.1016/B978-0-

08-098350-9.00003-5.

[283] Singh V. Textbook of Anatomy Vol.1 Upper Limb and Thorax. vol. 1. Elsevier Health Sciences; 2014.

[284] Bhutani H, Kurmi M, Singh S, Beg S, Singh B. Quality by design (QbD) in analytical sciences: An overview. Pharma Times 2014;46:71–5.

[285] Patel KY, Dedania ZR, Dedania RR, Patel U. QbD approach to HPLC method development and validation of ceftriaxone sodium. Futur J Pharm Sci 2021;7:1–10. https://doi.org/10.1186/s43094-021-00286-4.

[286] Krishna MV, Dash RN, Jalachandra Reddy B, Venugopal P, Sandeep P, Madhavi G. Quality by Design (QbD) approach to develop HPLC method for eberconazole nitrate: Application oxidative and photolytic degradation kinetics. J Saudi Chem Soc 2016;20:S313–22. https://doi.org/10.1016/j.jscs.2012.12.001.

[287] U.S. Food & Drug Administration. QbD Considerations for Analytical Methods - FDA Perspective. IFPAC Annu. Meet., 2013.

[288] Agency EM. European Medicines Agency: An unacceptable choice. Prescrire Int 2011;20:278.

[289] da Silva Guedes J, da Silva Guedes ML. Quantificação do indicador de Nelson de Moraes (curva de mortalidade proporcional). Rev Saude Publica 2006;40:951–61. https://doi.org/10.1590/s0034-89102006000700002.

[290] Naseef H, Moqadi R, Qurt M. Development and validation of an HPLC method for determination of antidiabetic drug alogliptin benzoate in bulk and tablets. J Anal Methods Chem 2018;2018. https://doi.org/10.1155/2018/1902510.

[291] McNaught AD, Wilkinson A. Compendium of Chemical Terminology. vol. 80. Blackwell Science Oxford; 2014.

[292] Dolan JW. Flow-rate and peak spacing. LC-GC Eur 2003;16:252–5.

[293] Barth HG. Chromatography Fundamentals, Part V: Theoretical Plates: Significance, Properties, and Uses 2018.

[294] Wang C, Guo Z, Long Z, Zhang X, Liang X. Overloading study of basic compounds with a positively charged C18 column in liquid chromatography. J Chromatogr A 2013;1281:60–6. https://doi.org/10.1016/j.chroma.2013.01.074.

[295] Peris-García E, García-Alvarez-Coque MC, Carda-Broch S, Ruiz-Angel MJ.

Effect of buffer nature and concentration on the chromatographic performance of basic compounds in the absence and presence of 1-hexyl-3-methylimidazolium chloride. J Chromatogr A 2019;1602:397–408. https://doi.org/10.1016/j.chroma.2019.06.061.

[296] Greibrokk T, Andersen T. High-temperature liquid chromatography. J Chromatogr A 2003;1000:743–55.

[297] Wenclawiak BW, Giegold S, Teutenberg T. High-temperature liquid chromatography. Anal Lett 2008;41:1097–105.

[298] Dwight R. Effect of Flow Rate on UV Detection in Liquid Chromatography. LCGC North Am 2019;37:846–50.

[299] Frigyes D, Alber F, Pongor S, Carloni P. Arginine–phosphate salt bridges in protein–DNA complexes: a Car–Parrinello study. J Mol Struct THEOCHEM 2001;574:39–45.

[300] Yusufaly TI, Li Y, Singh G, Olson WK. Arginine-phosphate salt bridges between histones and DNA: Intermolecular actuators that control nucleosome architecture. J Chem Phys 2014;141:10B610_1. https://doi.org/10.1063/1.4897978.

[301] Liu WG, Zhang JR, Cao ZQ, Xu FY, Yao KD. A chitosan-arginine conjugate as a novel anticoagulation biomaterial. J Mater Sci Mater Med 2004;15:1199–203. https://doi.org/10.1007/s10856-004-5672-1.

[302] Schindelin J, Arganda-Carreras I, Frise E, Kaynig V, Longair M, Pietzsch T, et al. 714 Saalfeld S, Schmid B, Tinevez JY, White DJ, Hartenstein V, Eliceiri K, Tomancak P, Cardona A. 2012. 715 Fiji: an open-source platform for biological-image analysis. Nat Methods n.d.;9:676–82.

[303] Convention USP. USP 43- NF 38. United States Pharmacopoeial Convention; 2019.

[304] Bouabdallah S, Trabelsi H, Bouzouita K, Sabbah S. Reversed-phase liquid chromatography of lisinopril conformers. J Biochem Biophys Methods 2002;54:391–405. https://doi.org/10.1016/S0165-022X(02)00140-9.

[305] Vraneš M, Ostojić S, Tot A, Papović S, Gadžurić S. Experimental and computational study of guanidinoacetic acid self-aggregation in aqueous solution. Food Chem 2017;237:53–7. https://doi.org/10.1016/j.foodchem.2017.05.088.

[306] Wang SL, Lin SY, Chen TF. Thermal-dependent dehydration process and

intramolecular cyclization of lisinopril dihydrate in solid state. Chem Pharm Bull 2000;48:1890–3. https://doi.org/10.1248/cpb.48.1890.

[307] Sorrenti M, Catenacci L, Cruickshank DL, Caira MR. Lisinopril dihydrate: Single-Crystal X-Ray structure and physicochemical characterization of derived solid forms. J Pharm Sci 2013;102:3596–603. https://doi.org/10.1002/jps.23660.

[308] Song J, Feng H, Wu M, Chen L, Xia W, Zhang W. Preparation and characterization of arginine-modified chitosan/hydroxypropyl methylcellose antibacterial film. Int J Biol Macromol 2020;145:750–8. https://doi.org/10.1016/j.ijbiomac.2019.12.141.

[309] Fujii K, Uekusa H, Itoda N, Yonemochi E, Terada K. Mechanism of dehydration-hydration processes of lisinopril dihydrate investigated by ab initio powder X-ray diffraction analysis. Cryst Growth Des 2012;12:6165–72. https://doi.org/10.1021/cg3013377.

[310] Bell LN. Peptide stability in solids and solutions. Biotechnol Prog 1997;13:342–6. https://doi.org/10.1021/bp970057y.

[311] Lemons JMS, Coller HA, Feng XJ, Bennett BD, Legesse-Miller A, Johnson EL, et al. Quiescent fibroblasts exhibit high metabolic activity. PLoS Biol 2010;8:e1000514. https://doi.org/10.1371/journal.pbio.1000514.

[312] Peng H, Carretero OA, Peterson EL, Rhaleb NE. Ac-SDKP inhibits transforming growth factor-β1-induced differentiation of human cardiac fibroblasts into myofibroblasts. Am J Physiol - Hear Circ Physiol 2010;298:H1357–64. https://doi.org/10.1152/ajpheart.00464.2009.